Doctoral Dissertation

博士論文

Direct photon production at low transverse momentum in proton-proton collisions at $\sqrt{s} = 13$ TeV

(重心系エネルギー 13 TeV 陽子+陽子衝突における
低横運動量直接光子生成)

A Dissertation Submitted for Degree of Doctor of Science

November 2023

令和 5 年 11 月博士 (理学) 申請

Department of Physics, Graduate School of Science,

The University of Tokyo

東京大学大学院理学系研究科物理学専攻

Hikari Murakami

村上　ひかり

Abstract

Direct photons are unique probes to study quark-gluon plasma (QGP) created in ultra-relativistic heavy-ion collisions, as they are emitted from the whole stages of the space-time evolution with negligible final state interaction. They carry undistorted medium information such as thermodynamic properties.

Direct photon measurements in pp collisions serve as a vacuum baseline for the studies in heavy-ion collisions and can be used as a test of perturbative QCD (pQCD) calculation. On the other hand, recent measurements in pp collisions with high event activity exhibit similarities to heavy-ion collisions, such as collective phenomena of hadrons. This motivates a search for the thermal photons and the creation of the QGP in small systems to better understand the underlying dynamics in such collisions. This thesis presents direct photon production in pp collisions at $\sqrt{s} = 13$ TeV in minimum-bias and high-multiplicity event multiplicity classes to test pQCD and search thermal photons in small systems.

This work is performed via the internal conversion technique, the ratio of direct to inclusive photons can be extracted from the dielectron continuum. Compared to the previous study, the statistical and systematic uncertainties were significantly improved and the direct-photon signal was extracted in the range $1 < p_{\mathrm{T}} < 6$ GeV/c, for both event multiplicity classes. It was found that direct photon yields in inelastic and high-multiplicity pp collisions show clear multiplicity dependence.

The obtained results were compared with theoretical predictions. One is the next-to-leading-order (NLO) pQCD calculation with two different parton distribution functions and fragmentation functions and the other is the theoretical model assuming thermal radiation from the QGP in small systems. The latter predicts thermal contribution even in inelastic collisions and the model gave a better description of the minimum-bias result at $p_{\mathrm{T}} < 3$ GeV/c, though both models are consistent with the data within uncertainties. The minimum-bias result was found to be consistent with both pQCD predictions but the QGP-like model gives a slightly better description.

For the comparison with the high-multiplicity result, theoretical prediction needs to consider charged-particle multiplicity dependence. To this purpose, NLO pQCD contribution was empirically scaled with the ratio of mean charged-particle multiplicity at mid-rapidity between inelastic and high-multiplicity events as there is no theoretical prediction. The QGP-like model predicts thermal contribution increases as charged-particle multiplicity goes higher. Compared with these predictions, it was found that the high-multiplicity result was consistent with both standalone empirically

scaled prompt photons and the sum of the thermal and prompt photons, similar to the minimum-bias result.

The p_{T}-integrated direct-photon yield as a function of charged-particle multiplicity was reported. We integrated direct photon p_{T} spectra in the range $1 < p_{\mathrm{T}} < 3$ GeV/c, where we expect the direct photons to be dominated by thermal photons. The data shows multiplicity dependence and is consistent with the theoretical prediction within uncertainty and favors the QGP-like model.

The results are compared with other results from LHC energies. A smooth evolution of direct photon yields as a function of multiplicity was observed, which implies that particle multiplicity is one of the key quantities of direct photon production. If we extend theoretical prediction in Pb–Pb collisions towards the lower charged-particle multiplicity, the lowest edge of the total contribution is very close to the high-multiplicity data in pp collisions. At the same time, the line of prompt photons underestimates the high-multiplicity data. These observations support the statement made in the discussion about direct photon p_{T} spectra.

Contents

List of Figures

List of Tables

Chapter 1

Introduction

1.1 Quantum Chromodynamics (QCD)

Quantum Chromodynamics (QCD) is non-Abelian gauge theory of interactions between quarks and gluons [1]. The most outstanding feature of QCD is *asymptotic freedom*, which causes interaction between quarks and gluons become weaker as momentum transfer increases [2]. Due to this nature, coupling constant α_s of the strong interaction depends on the momentum scale of the interaction (Fig. 1.1). The important consequence of asymptotic freedom is that processes at large momentum transfer can be computed in a perturbation expansion in α_s [3], as only lower orders contribute significantly. In contrast, for the calculations of processes at low momentum, perturbative QCD (pQCD) breaks down as higher orders become dominant [4]. At a non-perturbative regime, where α_s is large, very attractive phenomena which close to the essence of strong interactions appear. One is *color confinement* [6], which leads to the fact that quarks and gluons are not isolated and confined into hadrons, and therefore not directly observed. Another feature is the spontaneous breaking of chiral symmetry [7], responsible for the emergence of hadron mass, e.g. protons and neutrons have much larger mass ($\sim$ 1 GeV) compared to the one from their constituent quarks which have only few MeV. Therefore, to describe these phenomena, theoretical approaches such as Lattice QCD (LQCD) [8–10] and Effective Field Theories [11–13] are practical solutions. LQCD is a formalism of quantized gauge field theory on a discrete lattice in four-dimensional Euclidean space-time, introduced by Wilson [14], which serves first-principle results on QCD.

1.2 Quark Gluon-Plasma (QGP)

The states of matter can be illustrated in a phase diagram as a function of the temperature T and the baryon chemical potential μ_B as shown in the left of Fig. 1.2. It is predicted that under extremely high temperature and/or density, QCD matter can undergo a phase transition from ordinary hadrons to a new state of matter, called Quark Gluon-Plasma (QGP), where quarks and gluons are deconfined [15]. According

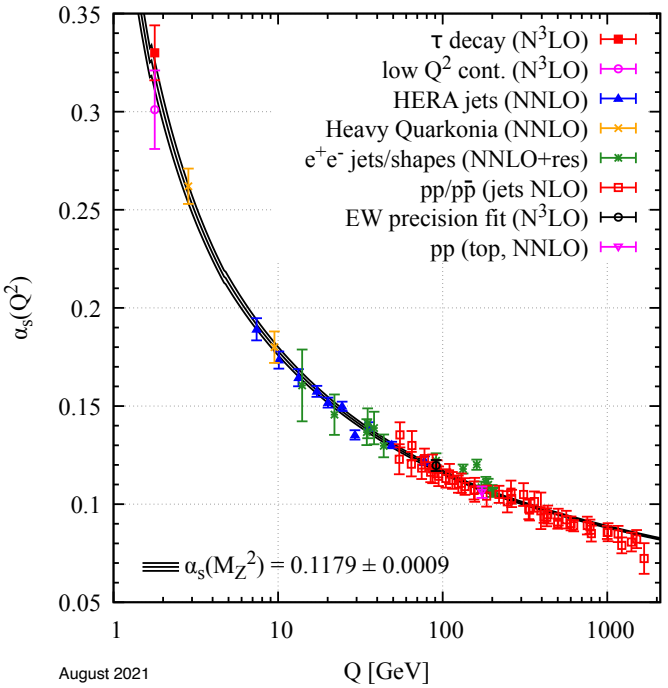

Figure 1.1: Summary of measurements of α_s as a function of the energy scale Q. The respective degree of QCD perturbation theory used in the extraction of α_s is indicated in brackets (NLO: next-to-leading order, NNLO: next-to-next-to leading order, NNLO: NNLO matched with resumed next-to-leading logs, N3LO:next-to-NNLO) [5].

to LQCD simulation, QGP can be formed at extremely high temperatures ($T = 150 \sim 160$ MeV) [16]. This can be seen in Fig. 1.2 (right), the transition is a rapid but smooth crossover around the critical temperature. It is conjectured that the QGP is a matter that existed in the early universe in $\sim 10^{-6}$ seconds after the Big Bang. Hence, if such matter can be created in a laboratory, space-time evolution and the emergence of hadrons in the early universe can be studied in a laboratory.

In order to create extremely high temperature and density conditions, high-energy heavy-ion collisions are considered as an ideal way. This is because the size of the colliding nuclei is large, and many particles are being produced in a short time-scale after the collisions. It is essential to undergo the multiple interactions among produced partons and particles, and the system needs to reach a state of (local) thermal equilibrium, to define thermodynamic quantities like temperature, pressure, or energy density. That means the system's lifetime must be longer than the inverse rate of interactions, which allows particles to interact and drive the system towards equilibrium [18].

Figure 1.3 is a sketch of the evolution of the system created in relativistic heavy-ion collisions. Soon after the head-on collision, a huge amount of energy is released in a tiny volume, and scattering between partons occurs. The stage is called pre-

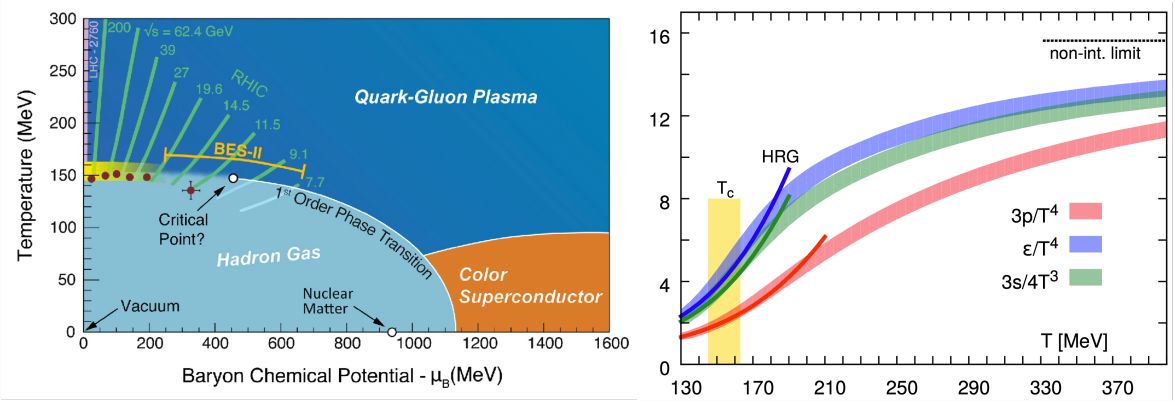

Figure 1.2: Left: Sketch of the QCD phase diagram [17]. Right: Pressure, energy density, and entropy density suitably normalized to the 4th (3rd for the latter) power of the temperature, from the Lattice QCD calculations of the HotQCD Collaboration [16]. The dark lines show the prediction of the Hadron Resonance Gas model, the horizontal line corresponds to the ideal gas limit for the energy density. The vertical band indicates the cross-over transition region.

equilibrium. After the subsequent multiple scattering of partons, the system reaches local equilibrium. The system consists of quark and gluon, is formed and the evolution can be described by relativistic hydrodynamics. The system expands further and cools down, when the temperature drops below the critical value, hadronization of partons occurs. This phase is called chemical freeze-out with the system being transformed into a hadron gas.

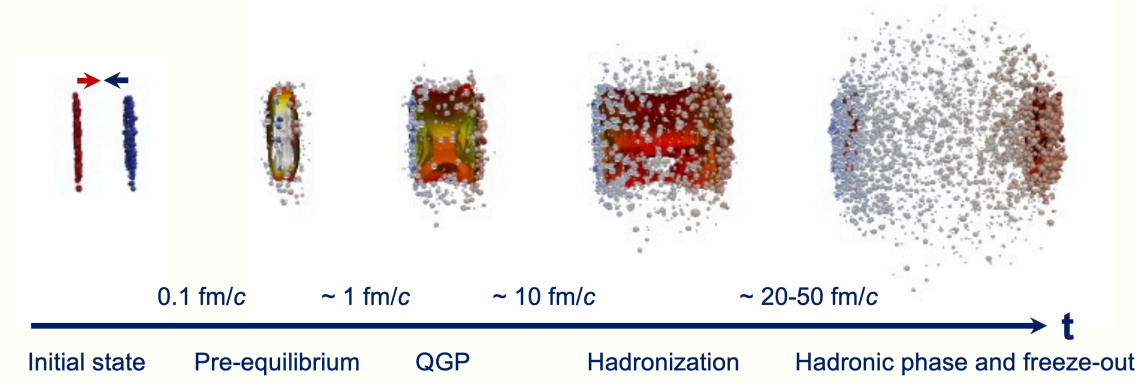

Figure 1.3: Evolution of the system created in high-energy heavy-ion collisions. Time is advancing from the left to the right. (The sketch is based on the simulations by the MADAI collaboration [19])

The picture of space-time evolution can be better interpreted by extensive studies

that include proton-proton and proton-nucleus collision experiments as well as heavy-ion collisions. Experiments in these smaller colliding systems are important as pp collision serves as a vacuum baseline and cold nuclear matter effects can be studied via proton-nucleus collisions. These studies help to distinguish between QGP-relevant and irrelevant effects.

Numerous high-energy heavy-ion collision experiments were conducted at the Relativistic Heavy Ion Collider (RHIC) and the Large Hadron Collider (LHC) to create and study the QGP. As a result, strong results indicating the creation of the QGP have been obtained. To give some examples, this includes energy loss of color probes [20,21], sequential suppression of quarkonium states [22,23], and electromagnetic radiation consistent with high initial temperatures of several hundred MeV [24,25]. Also, it was very surprising that the data shows anisotropic flow and this observation is well described by relativistic hydrodynamics [26].

The most important and valuable observable for the study of the QGP is real or virtual photons. This is because electromagnetic radiation of direct photons is direct evidence of the creation of the thermalized system. Figure 1.4 shows direct photon p_{T} spectra in proton-proton and nucleus-nucleus collisions measured by PHENIX at RHIC (left) and by ALICE at the LHC (right). Looking at the PHENIX result, the pQCD calculation is consistent with the pp data within the theoretical uncertainties for $p_{\mathrm{T}} > 2$ GeV/c. The Au–Au data are above the nuclear overlap function T_{AA} scaled pp fit which indicates the direct photon at low p_{T} range increases faster than the binary NN collision. The excess is evaluated with an exponential fit with the inverse slope parameter T, which corresponds to the effective temperature of the medium. Extracted T reaches $T_{\mathrm{eff}} = 239 \pm 25^{\mathrm{stat}} \pm 7^{\mathrm{syst}}$ MeV, which corresponds to 4 trillion degrees Celsius. Similar direct photon excess was observed at the LHC by ALICE and the extracted temperature was $T_{\mathrm{eff}} = 304 \pm 11^{\mathrm{stat}} \pm 40^{\mathrm{syst}}$ MeV. It turned out that the medium created at LHC was hotter than at RHIC.

1.3 High-Multiplicity Proton-Proton Collisions

In recent years, collective phenomena [30, 38–41] in high-multiplicity proton–proton and proton–ion collisions have been found and attracted great interest of the heavy-ion community, as they exhibit surprising similarities with those found in heavy-ion collisions (Fig. 1.5). Another important discovery is the strangeness enhancement [42], a smooth evolution of strangeness particle production with event multiplicity, which is originally considered as a signature of the formation of the QGP in nucleus-nucleus collisions (Fig. 1.6). Moreover, not only light-flavour hadrons, heavy-flavor hadrons such as D-meson and J/ψ production show multiplicity dependence [43, 44]. Given that the creation of the QGP is always discussed by assuming the absence of those phenomena in proton-proton and proton-nucleus collisions, these discoveries is forcing a paradigm shift in this field. They opened the big question: *Is a QGP formed in small systems ?*. To answer this question a number of measurements have been carried out: hadronic

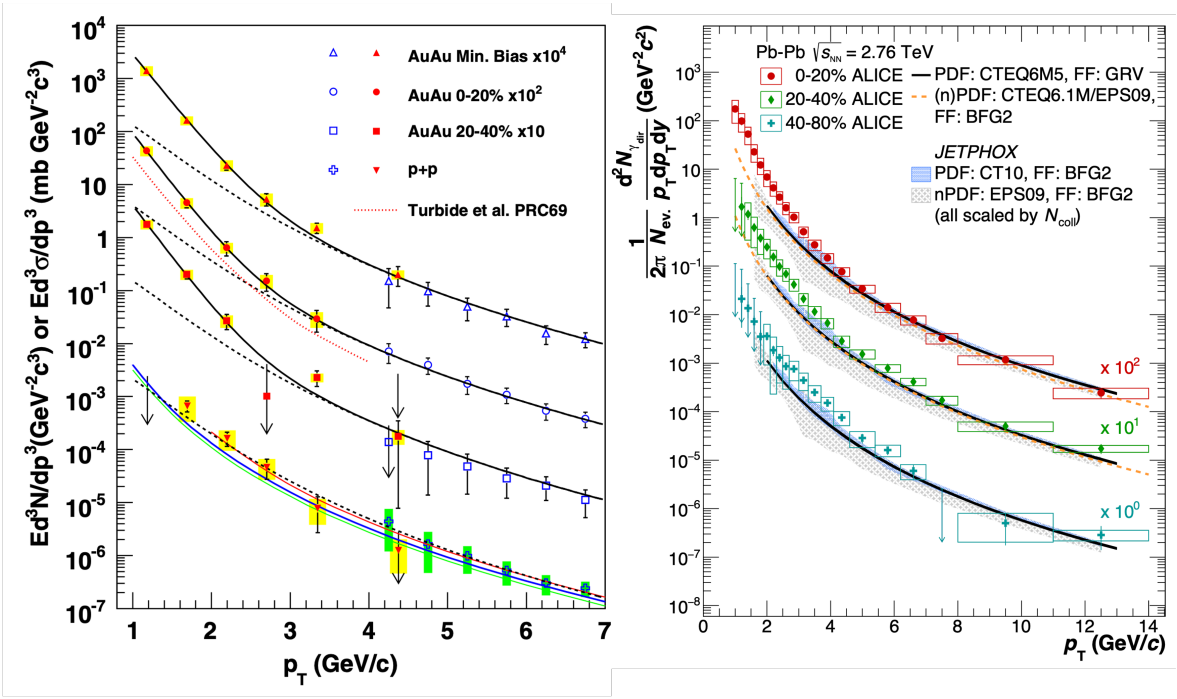

Figure 1.4: Left: Invariant cross section (pp) and invariant differential yield (Au–Au) of direct photons as a function of p_{T}. The filled points and open points are from two different analyses, [24] and [27,28], respectively. The three curves on the pp data represent NLO pQCD calculations, and the dashed curves show a modified power-law fit to the pp data, scaled by T_{AA}. The dashed (black) curves are exponential plus the T_{AA} scaled pp fit. The dotted (red) curve near the 0-20% centrality data is a theory calculation [29]. Right: Direct photon spectra in Pb–Pb collisions at $\sqrt{s_{\mathrm{NN}}}$ = 2.76 TeV for the 0-20% (scaled by a factor 100), the 20-40% (scaled by a factor 10) and 40-80% centrality classes compared to NLO pQCD predictions for the direct photon yield in pp collisions at the same energy, scaled by the number of binary nucleon collisions for each centrality class [25].

anisotropic flow, the mass ordering of the identified particle v_2, particle interferometry in small systems, multiplicity dependence of charged-particle jet production and so on (see Refs. [45–47]). Nevertheless, the situation is not conclusive and measurement of electromagnetic radiation is being awaited.

1.4 Direct Photons in Small Systems

The most important but missing inputs are direct photons and dileptons. They are unique probes as they are emitted without final state interactions and take over medium properties. In heavy-ion collisions, the thermal radiation of direct photons which con-

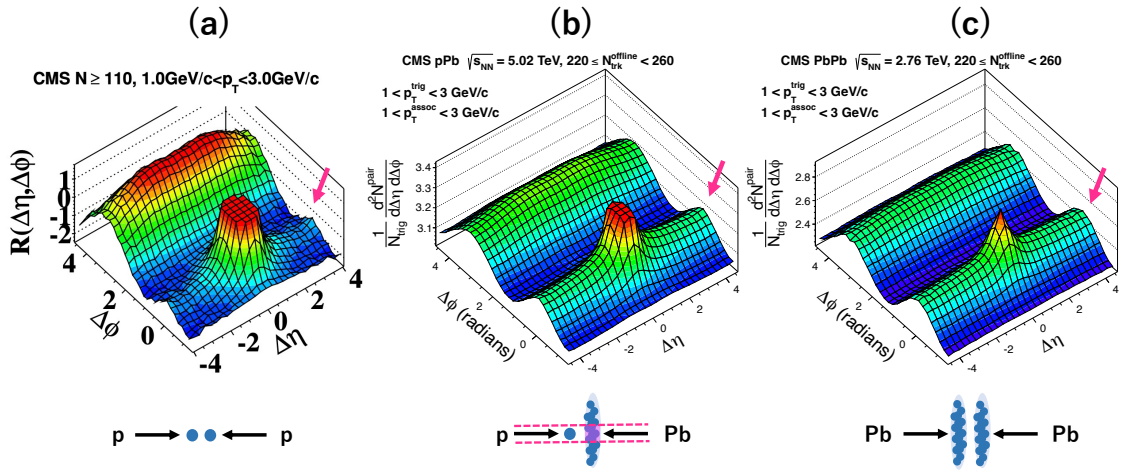

Figure 1.5: Two-particle correlation functions for 7 TeV pp (a) [30], 5.02 TeV p-Pb (b), and 2.76 TeV PbPb (c) collisions [31]. The arrow shows the long-range correlations at small $\Delta\phi$. The structure called "ridge" in heavy-ion collisions is interpreted as a consequence of the hydrodynamic flow of the produced strongly interacting medium. The structure evolves from pp to Pb–Pb collisions.

tributes to low transverse momentum[1] was conceived as direct evidence of the creation of hot QGP. If a thermalized system is created in small systems, it should give rise to the thermal radiation of (virtual) direct photons as well. However, to single out and quantify the thermal contribution, precise knowledge of other contributions such as prompt photons is essential. Therefore, direct photon production is studied in both minimum bias and high-multiplicity pp collisions. In this context, the former serves as a vacuum baseline with respect to the latter.

In addition, as shown in Fig. 1.7, there is an interesting result of the PHENIX experiment. It is integrated photon yield ($p_{\mathrm{T}} > 1$ GeV/c) as a function of charged particle multiplicity. Data points from pp and heavy-ion collisions in various collision systems are shown. Whereas all the A+A points are on the dotted lines, pp and N_{coll} scaled pQCD calculations are on a different line which is parallel to the dotted line. The data points from pAu and dAu collisions are plotted in the middle and seem to fill the gap smoothly. If these results may indicate the onset of the QGP, it is natural to study the thermal radiation in pp collisions at $\sqrt{s} = 13$ TeV, whose charged particle-multiplicity covers from ~ 7 to ~ 30.

1.5 Previous Experimental Result

ALICE measured direct photon in pp collisions at $\sqrt{s} = 13$ TeV using the data from the early year of Run 2. The analysis employed virtual photon method and extracted

[1]The defnitions of kinematic variables used in this thesis can be found in Appendix A.

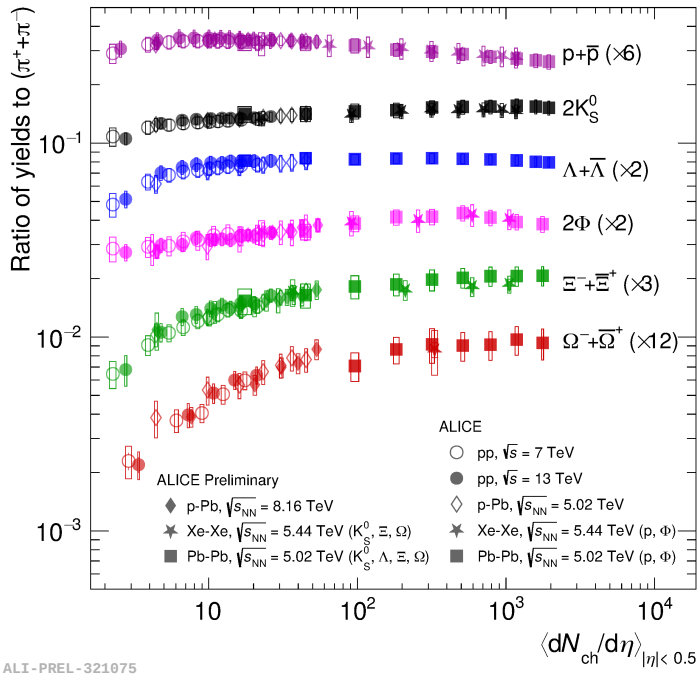

Figure 1.6: p_{T}-integrated yields of strange and multi-strange hadrons over $\pi^+ + \pi^+$ as a function of $\mathrm{d}N_{\mathrm{ch}}/\mathrm{d}\eta$, measured in high-multiplicity pp collisions at $\sqrt{s} = 7$ TeV in $|\eta| < 0.5$. The error bars show the statistical uncertainty, whereas the empty and dark-shaded boxes show the total systematic uncertainty and the contribution uncorrelated across multiplicity bins, respectively. The data are compared to Monte Carlo calculations [32–34] and to results obtained in Pb-Pb and p-Pb collisions with ALICE [35–37].

direct photon fraction r which defined as the ratio of direct photons γ_{dir} to inclusive photons γ_{incl} which is sum of direct and decay photons ($\gamma_{\mathrm{incl}} = \gamma_{\mathrm{dir}} + \gamma_{\mathrm{decay}}$). Figure. 1.8 shows the fraction as a function of transverse momentum p_{T} in inelastic (left) and high-multiplicity (right) pp collisions. If $r = 0$, $\gamma_{\mathrm{incl}} = \gamma_{\mathrm{decay}}$ which indicates there are no direct photons and all of them are from hadron decays such as $\pi^0 \to \gamma\gamma$ and $\eta \to \gamma\gamma$. In that study, no significant direct-photon signals were observed due to large statistical and systematic uncertainties in both minimum-bias and high-multiplicity event analysis. Therefore, this study aims to extract direct-photon signals in pp collisions, using increased statistics from whole Run 2 years (2016–2018) and better knowledge of decay backgrounds.

Compared to the previous study, the following major improvements were utilized in this study. First, the statistics of experimental datasets were increased, i.e., 4.4 (3.8) times larger event statistics were used in inelastic and high-multiplicity pp collisions. Second, cocktail input spectra such as π^0 and η meson are taken from measurements [54]. Fig. 1.9 shows invariant cross sections for neutral meson production in

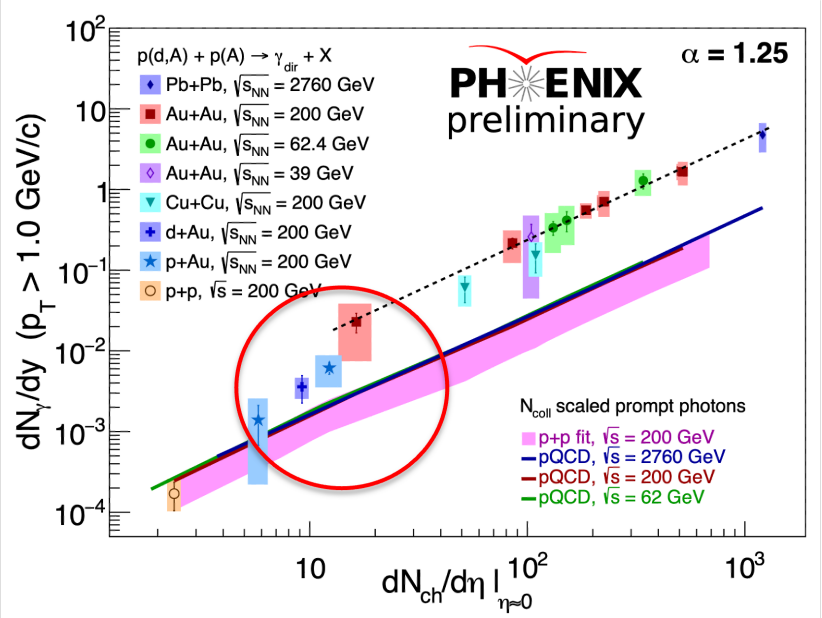

Figure 1.7: Preliminary result of integrated direct-photon yield ($p_{\mathrm{T}} > 1$ GeV/c) as a function of charged particle multiplicity dN_{ch}/η at midrapidity [48] in various collision systems. The data points from PHENIX [49], ALICE [25] experiments are compared with $\mathrm{N_{coll}}$ scaled pQCD calculations for pp collisions at $\sqrt{s} = 200$ GeV [50].

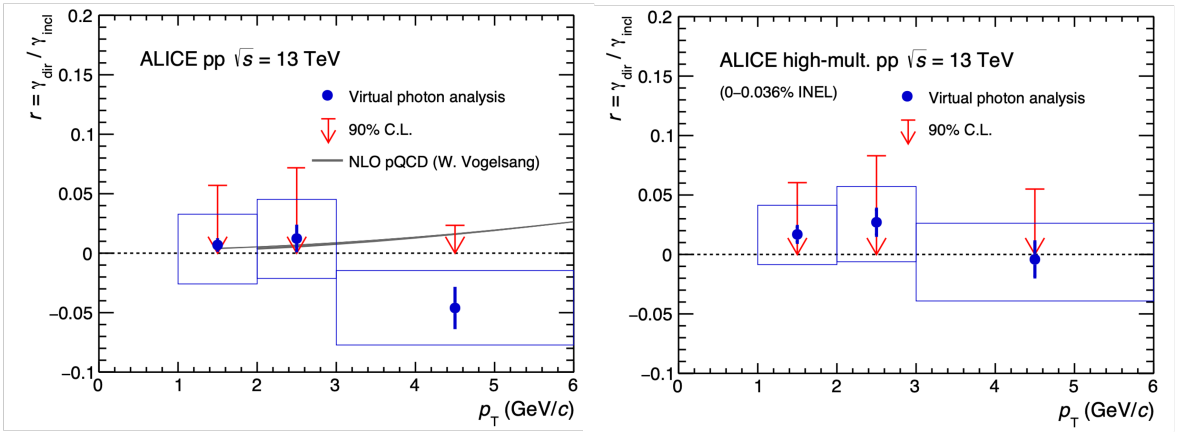

Figure 1.8: Fraction of direct photon as a function of p_{T} in inelastic and high-multiplicity event [51]. Statistical and systematic uncertainties are shown in bars and boxes. The upper limits in shown in red arrow are extracted at 90% confidence level (C.L.) using the Feldman-Cousins method [52]. The gray band shows NLO pQCD calculation taken from [53].

pp collisions at $\sqrt{s} = 13$ TeV. Third, as shown in Fig. 1.10, high-multiplicity neutral

mesons were also measured, which are the same event multiplicity class (0–0.1%) as used in this analysis. In addition, it is also important that the η/π^0 ratios were studied as well. These measurements were not available in the previous study and caused large systematic uncertainties of direct photon signal.

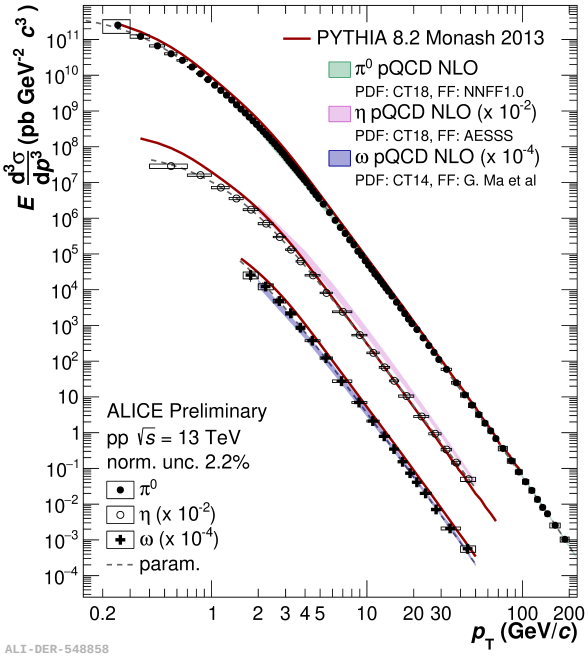

Figure 1.9: Invariant cross sections for neutral meson production at midrapidity in pp collisions at $\sqrt{s} = 13$ TeV compared with theoretical predictions [54]. The neutral pion, η, and ω meson are measured at transverse momenta p_{T} in the range $0.2 < p_{\mathrm{T}} < 200$ GeV/c, $0.4 < p_{\mathrm{T}} < 50$ GeV/c and $2 < p_{\mathrm{T}} < 50$ GeV/c, respectively. The red line shows the theoretical prediction obtained using the PYTHIA8.2 [55] calculation with Monash 2013 tune [56]. The green (pink) band represents pQCD calculation at NLO using CT18 [57] PDF and NNFF1.0 [58] (AESSS [59]) FF for π^0 (η), and the purple band shows calculation at NLO using CT14 [60] PDF and ω fragmentation based on a broken SU(3) model [61] for ω meson.

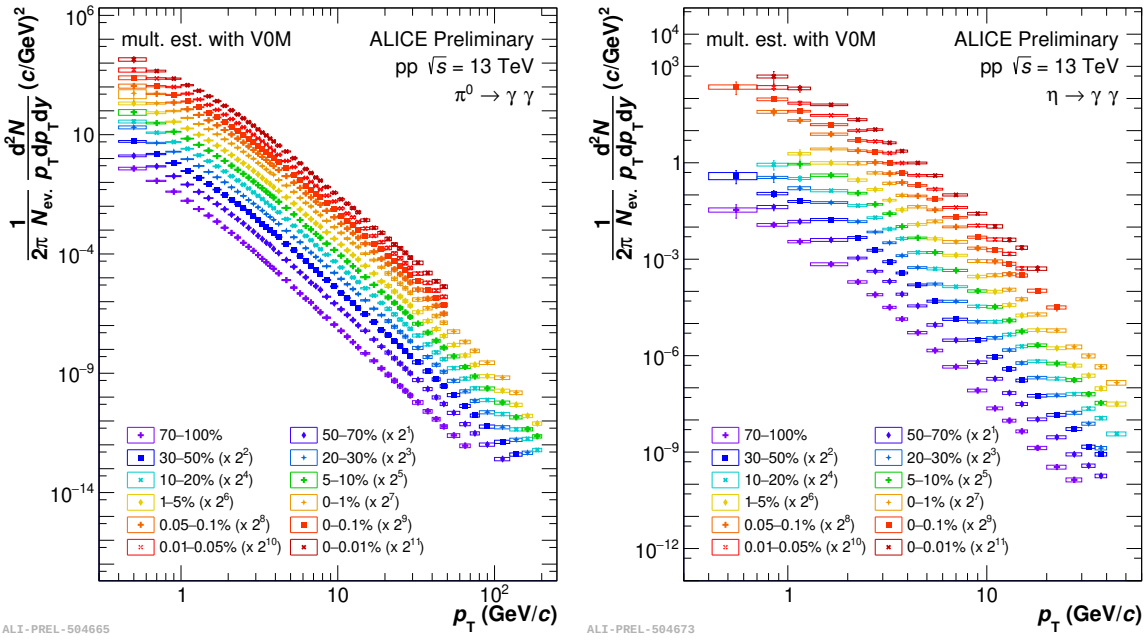

Figure 1.10: Invariant differential π^0 (left) and η (right) yields for different multiplicity classes in pp collisions at $\sqrt{s} = 13$ TeV. Statistical and systematic uncertainties are shown in bars and boxes. The red square points indicate π^0 and η meson measured in the 0–0.1% multiplicity class, which are used in this analysis. The neutral pion and η meson are measured at transverse momenta p_{T} in the range $0.4 < p_{\mathrm{T}} < 50$ GeV/c, $0.4 < p_{\mathrm{T}} < 25$ GeV/c, respectively.

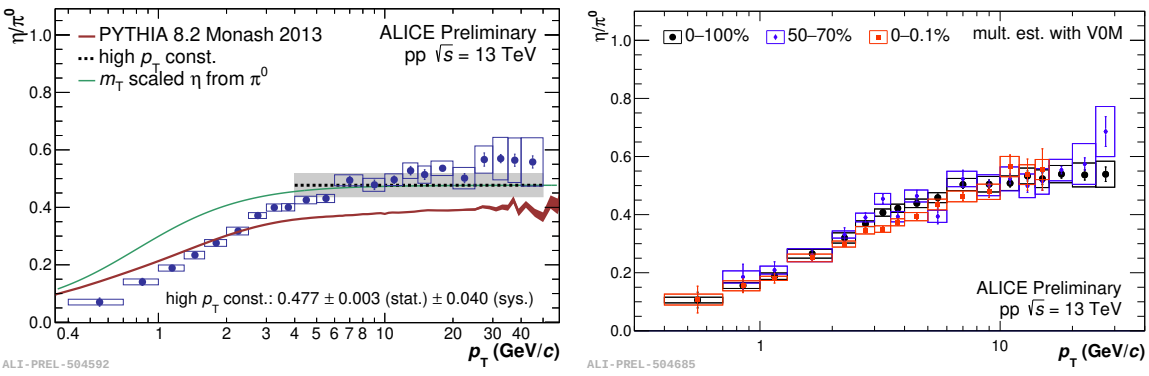

Figure 1.11: Left: η/π^0 ratio in pp collisions at $\sqrt{s} = 13$ TeV compared with PYTHIA8.2 calculation with Monash 2013 tune and m_{T} scaling. The η/π^0 is measured at transverse momenta p_{T} in the range $0.4 < p_{\mathrm{T}} < 50$ GeV/c. Right: η/π^0 ratio in high and low multiplicity classes in pp collisions at $\sqrt{s} = 13$ TeV. The red square points indicate η/π^0 ratio measured in the 0–0.1% multiplicity class, which is used in this analysis. The η/π^0 is measured at transverse momenta p_{T} in the range $0.4 < p_{\mathrm{T}} < 16$ GeV/c.

1.6 Organization of This Thesis

This work presents the study of dielectron and direct photon production in proton-proton collisions at $\sqrt{s} = 13$ TeV via an internal conversion technique (virtual photon method). The thesis is organized as follows: Chapter 1 gives an introduction, physics motivation, and previous experimental results. Chapter 2 describes the basics of photon measurement, i.e., source of photons and experimental technique. Chapter 3 describes the experimental setup including LHC and ALICE apparatus, and relevant detectors for this analysis together. The details of analysis is presented in Chapter 4. In Chapter 5, obtained results are discussed. Finally, Chapter 6 concludes the thesis.

1.7 Major Contributions

The major contributions of the author as an ALICE collaborator are as follows:

- Operation of data taking during LHC Run 2
- Quality Assurance of GEM foil for ALICE–TPC upgrade project for LHC Run 3 [62]
- Validation of material budget in ALICE detector using conversion photons to precise determination of ALICE material budget [63]
- Paper committee chair of the paper (under preparation) *"Direct photon production in inelastic and high-multiplicity proton-proton collisions at $\sqrt{s} = 13$ TeV"* on behalf of the ALICE Collaboration.

Chapter 2

Basics of Direct Photon Measurement

This chapter introduces the sources of direct photons and their measurement methods. In the field of heavy-ion physics, pp collisions were taken only as a vacuum baseline for interpreting results from heavy-ion collisions. In the case of photon production in pp collisions, the only possible contribution was prompt photons and no other contribution was considered to exist. The recent observations of collectivity in small systems have led to discussions on the production of thermal photons even in pp collisions [64] Referring to this, Sec. 2.1 describes the basics of the photon production mechanisms in high-energy hadron collisions. In Sec. 2.2, experimental techniques to measure low p_{T} direct photon are described.

2.1 Source of Photons

Photon is a powerful probe in heavy-ion collisions as they are produced at every stage of the collisions and emitted from the strongly interacting medium almost unaffected by final state interaction. This is due to the small coupling constant of the electromagnetic interaction. Figure 2.1 shows various photon sources in heavy-ion collisions. Photons of interest that do not originate from hadron decays are called direct photons. Direct photons consist of two categories. Prompt photons are produced in the hard process and used for testing pQCD calculations. Non-prompted photons are considered to be photons from physical sources other than pQCD, rather than photons from hard processes. Since photons are detected inclusively, it is not possible to distinguish between the different sources in the experiment. Thus, with the help of theory, these sources of direct photons are estimated and their relative contributions in the transverse momentum spectrum are investigated.

Typically, interactions that can be calculated in QCD are referred to as hard processes, which are characterized by either large momentum transfer or large transverse momentum. The spectrum of hard processes follows a power-low shape. The measurements of the direct photon at RHIC and the LHC are well described by pQCD calculations at higher p_{T} [65]. The expected behavior in heavy-ion collisions is a scal-

ing from pp cross section proportional to the number of nucleon-nucleon collisions. On the other hand, it is not clear how low transverse momentum pQCD is applicable since theoretical uncertainties are large at low p_{T}.

As mentioned above, the measurement of photons is a big experimental challenge as most photons arise from decays of neutral mesons. If a QGP droplet is created in high-multiplicity proton-proton collisions, analogously, one would assume direct photons in high-multiplicity proton-proton collisions can be classified similarly. Theoretically, it is predicted that thermal photons will increase in high-multiplicity pp collisions as shown in Fig. 2.2. If such photons are emitted, a sizeable enhancement of the direct photon signal should appear at $p_{\mathrm{T}} < 3$–4 GeV/c [64]. Major photon sources such as prompt, thermal, and decay photons are described below.

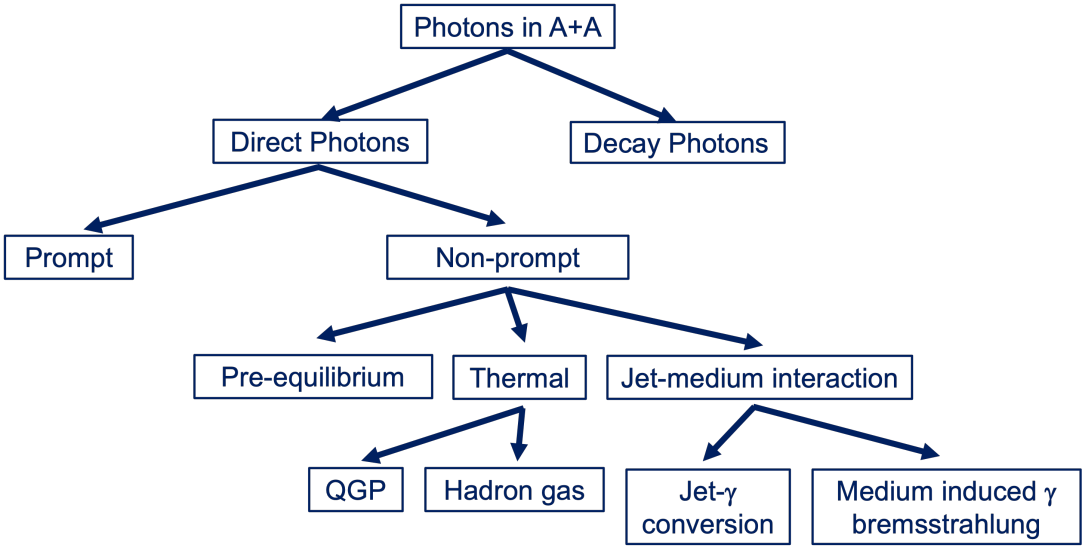

Figure 2.1: Known and expected photon sources in heavy-ion collisions.

2.1.1 Prompt photon

Prompt photons are defined as photons created in initial hard scatterings of incoming partons. The main production mechanisms are: (a) quark-gluon Compton scattering, (b) quark-antiquark annihilation and (c) bremsstrahlung from quark fragmentation [66]. Corresponding Feynman diagrams are illustrated in Figure 2.3. The production rates of prompt photons can be calculated in pQCD, therefore prompt photon is also called pQCD photon. The photon production cross section in proton-proton collisions can be written as [65]

$$E\frac{d^3\sigma_{\mathrm{pp}}}{d^3p} = \sum_{a,b,c,d} f_{a/p}(x_a, Q^2) \otimes f_{b/p}(x_b, Q^2) \otimes d\hat{\sigma}(Q^2) \otimes D_{\gamma/c}(z_c, Q^2), \tag{2.1}$$

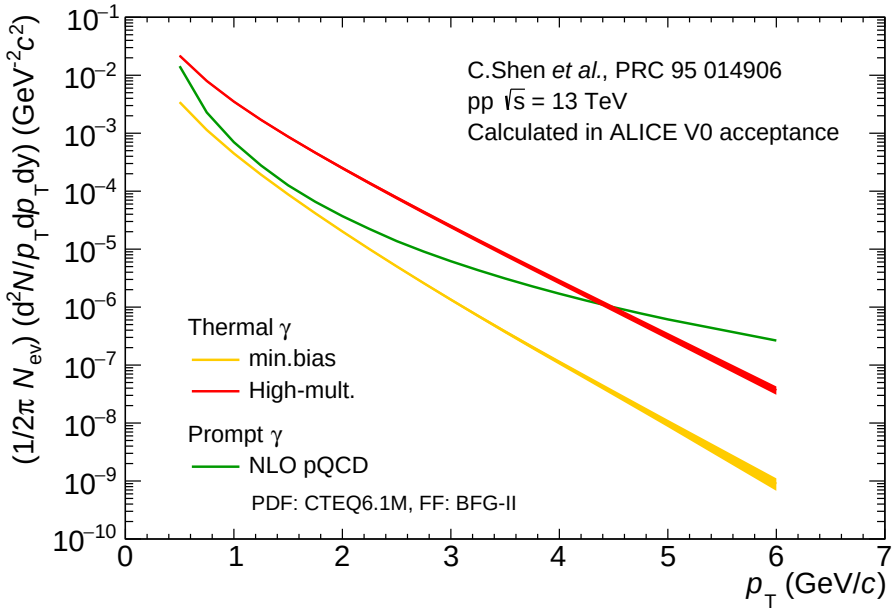

Figure 2.2: Theoretical prediction of direct photon production in pp collisions at $\sqrt{s}$ = 13 TeV [64]. The orange and red curves show thermal photon contribution in minimum-bias and high-multiplicity events, respectively. In the calculation, the charged-particle multiplicity is determined at forward rapidity which is consistent with the ALICE acceptance of the V0 detector. The high-multiplicity thermal-photon contribution shows clear enhancement compared to the one from minimum-bias events. This enhancement should be visible below p_{T} = 3–4 GeV/c, where the thermal-photon contribution is above the prompt-photon contribution as shown in the green line.

where $f_{i/p}(x_i, Q)$ with $i = a, b$ are parton distribution functions (PDF) of incoming partons a and b. These PDFs depend on the momentum transfer Q^2 and describe the probability to find parton i with momentum fraction x_i inside either of the colliding hadrons. The scale is typically chosen on the order of the transverse momentum of final state partons. The partonic cross-section $d\hat{\sigma}$ is evaluated as a perturbative expansion in the strong coupling constant $\alpha_s(Q)$. The term $D_{\gamma/c}(z_c, Q^2)$ is the parton-to-photon fragmentation function (FF) that governs the fragmentation of a scattered parton c to a photon with momentum fraction z, which emerges from the collinear fragmentation of a colored high p_{T} parton accompanied by hadrons. Prompt photons from the LO processes of (a) and (b) in Fig. 2.3 are final state objects and do not require the FF. In that sense, these photons are also called "direct" photons. The process of (c) can be interpreted as the NLO corrections to the LO in the perturbative expansion in powers of the strong coupling α_s. These photons behave as a high p_{T} colorless parton, and it is most likely to be well separated from hadrons.

With experimentally determined PDF and FF, pQCD calculations reproduce the

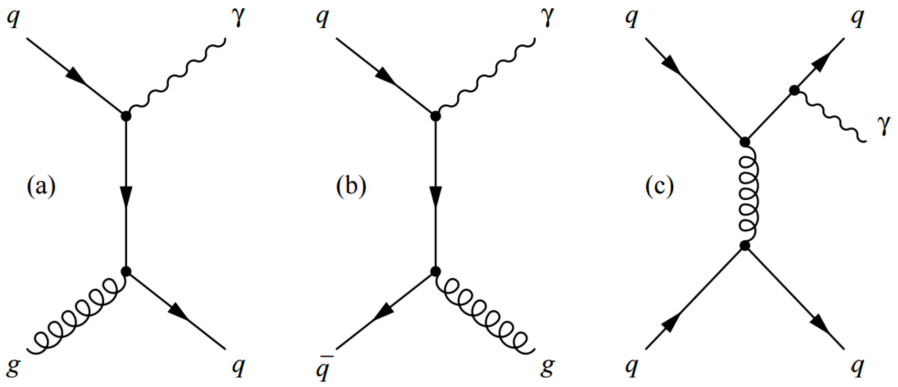

Figure 2.3: Leading Order (LO) and Next-to-Leading Order (NLO) diagrams of direct photon production in the initial scatterings: (a) quark-gluon Compton scattering, (b) quark-antiquark annihilation and (c) bremsstrahlung radiation from quark fragmentation [67].

measured direct photon spectra in proton-proton collisions by PHENIX at RHIC, and in proton-antiproton collisions by D0 at Tevatron [68]. According to theoretical analysis [69], at RHIC energy, direct (LO) photons are a dominant source of prompt photons compared to fragmentation photons above $p_{\mathrm{T}} \sim 3$ GeV/c, while at LHC energy, the contribution from fragmentation processes dominates prompt photons (Fig. 2.4).

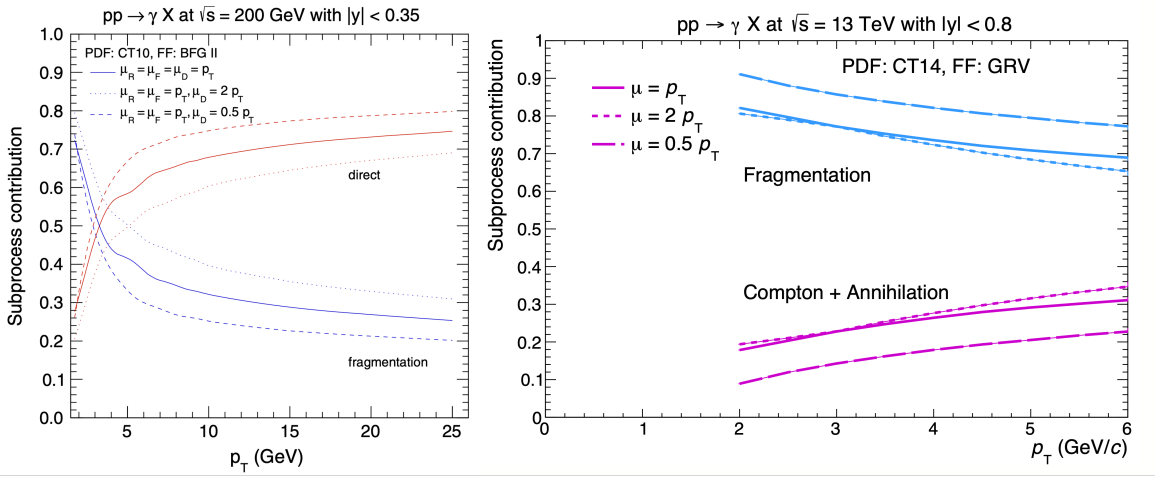

Figure 2.4: Fractional contributions of direct (LO) and fragmentational processes to inclusive photon production at RHIC [69] (left) and LHC [70] (right) energies as a function of p_{T} for the different choice of the photon fragmentation scale μ. At the LHC, fragmentation photon dominates inclusive photon.

2.1.2 Thermal photon

In contrast to hard photons, photons from a thermalized system can be used to diagnose the formation of a strongly interacting medium in heavy ion collisions. Soft photons can be produced through the same processes as hard photons shown in Fig. 2.3, but produced by the interactions of thermalized particles. They are emitted during the entire QGP evolution and the following hot hadron gas phase. An introductory review of thermal photon productions can be found in Ref. [71].

The thermal emission rate of photons with energy E and momentum p from the QGP is expressed as

$$E\frac{d^3R}{d^3p} = \frac{-2}{(2\pi)^3}\mathrm{Im}\Pi_\mu^{R,\mu}\frac{1}{e^{E/T}-1}, \tag{2.2}$$

where $\Pi_\mu^{R,\mu}$ is the retarded photon self-energy at a finite temperature T, R stands for the transition rate between the initial and final state. This equation is valid in the perturbative [72, 73] and non-perturbative [74] limits. According to the theoretical investigations, Eq.2.4 exhibits proportionality of the rate to the Boltzmann factor $\exp(-E/T)$. This means the transverse momentum spectrum of thermal photons has a similar spectral shape that is realized in thermal equilibrium in the medium.

Hot hadronic matter (hadron gas, HG) produced after the hadronization of the QGP, will also emit photons due to hadronic reactions. The most important hadronic constituents for photon production are π and ρ mesons, and elementary processes are $\pi^+\rho \to \pi^+\gamma$, $\pi^+\pi^- \to \rho\gamma$ and $\rho \to \pi^+\pi^-\gamma$ [75]. Certain models also include meson + meson and meson + baryon interactions in the hadronic phase [76]. As shown in Fig. 2.5, a theory predicts thermal photons from HG are dominant at $p_\mathrm{T} < 1$, while a suitable window for the study of thermal radiation from the QGP is $1 < p_\mathrm{T} < 3$ GeV/c [29].

2.1.3 Photons from other sources

In addition to prompt and thermal photons, for instance, emission of photons from pre-equilibrium stage [77], magnetic field effects [78–80] and the jet-medium interactions are expected. The pre-equilibrium phase is a phase created in an early stage soon after the first impact and lasts until the system reaches local thermalization towards the QGP, and photons can be produced in such a non-equilibrium phase. PHENIX experiment reported a possible sensitivity of the measurement to photons from earlier stages [81], but less conclusive compared to thermal photons. Photons induced from jet-medium interactions [82] are expected to contribute relatively higher transverse momentum region above 4 GeV/c.

2.1.4 Fraction of direct photons over decay photons

Theoretically expected fraction of direct photons over decay photons at below $p_\mathrm{T} = 3$ GeV/c is at most 10% in heavy-ion collisions. In pp collisions, the fraction is even

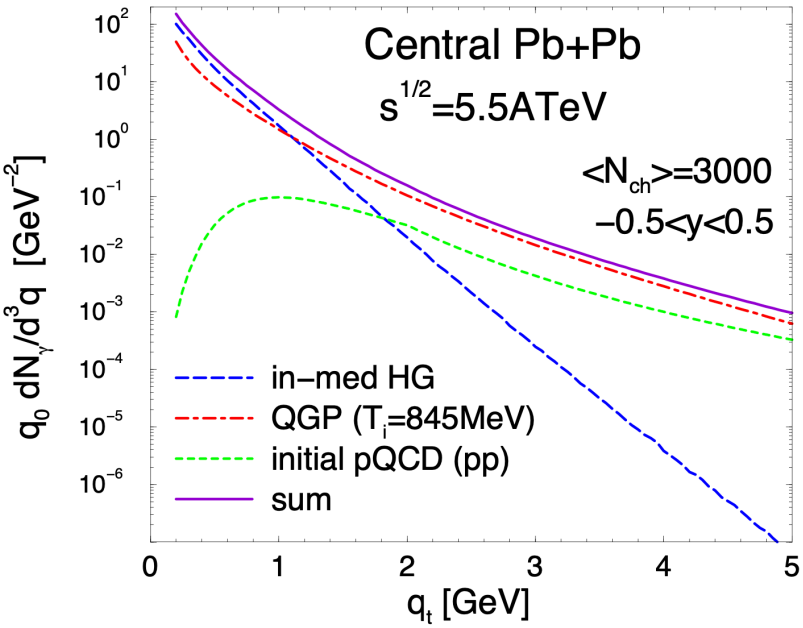

Figure 2.5: Theoretical prediction of direct-photon emission rate as a function of transverse momentum q_{T}, from various thermal sources in central Pb–Pb collisions at $\sqrt{s_{\mathrm{NN}}} = 5.5$ TeV [29]. The blue and red dashed lines show thermal-photon contribution from hot hadron gas (HG) and from the QGP, while the green dashed line shows prompt photon contribution from initial hard scatterings. Below $q_{\mathrm{T}} = 1$ GeV/c, thermal photons are dominated by the HG, while above $q_{\mathrm{T}} = 1$ GeV/c, ones from QGP are the largest source of thermal radiation.

smaller. At the LHC energies, this ratio is very close to a few % at 1-3 GeV/c, which shows how the measurements are difficult. Therefore, the direct-photon measurement is a big challenge.

Experimentally, direct photon signal is extracted in terms of the ratio defined as inclusive over decay photon as follows:

$$R_\gamma = \gamma_{\mathrm{incl}}/\gamma_{\mathrm{decay}}, \tag{2.3}$$

where γ_{incl} is sum of direct photon and decay photon, R_γ is called direct-photon excess ratio. By definition, $R_\gamma > 1$ indicates the existence of a direct-photon signal. Direct photon γ_{dir} is obtained from inclusive photon yield as

$$\gamma_{\mathrm{dir}} = (1 - \frac{1}{R_\gamma})\gamma_{\mathrm{incl}}. \tag{2.4}$$

Figure 2.6 shows R_γ as a function of p_{T} measured in Pb–Pb collisions at $\sqrt{s_{\mathrm{NN}}} =$ 2.76 TeV (left) and in pp collisions $\sqrt{s} = 8$ TeV (right), respectively. The results from

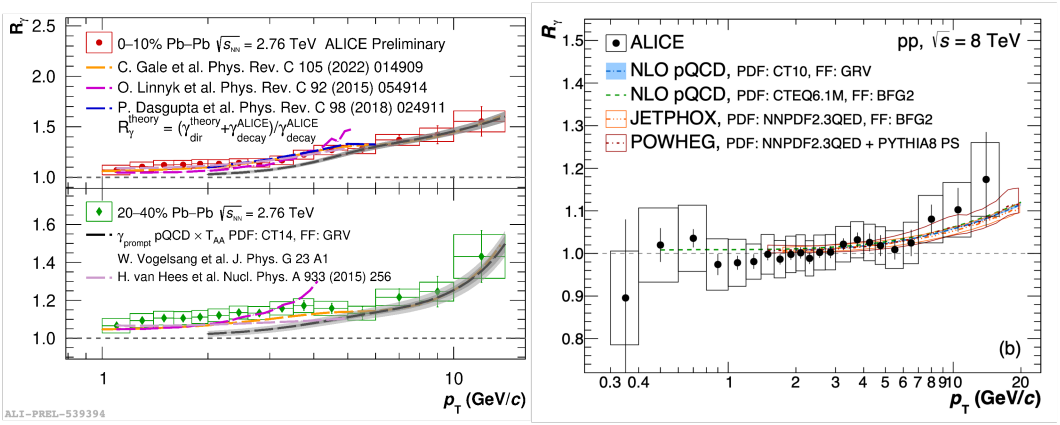

Figure 2.6: Left: Direct photon excess ratio R_γ as function of p_{T} in two different centrality classes. Results are compared with theoretical predictions [76, 77, 83–85]. The significance of the direct photon are: 0-10%: 3.1σ ($1.0 < p_{\mathrm{T}} < 1.8$ GeV/c) and 20-40%: 3.4σ ($1.0 < p_{\mathrm{T}} < 2.3$ GeV/c). Right: Direct photon excess ratios R_γ as a function of p_{T} in pp collisions at 8 TeV. Results are compared with theoretical predictions with CT10 [86–88] or CTEQ6.1M [89] proton PDF and GRV [90] or BFG2 [91] FF. In addition, a JETPHOX calculation [92] based on NNPDF2.3QED [93] proton PDF and BFG2 FF as well as a POWHEG calculation [92].

Pb–Pb collisions are compared with various theoretical predictions including prompt and thermal photons. The extracted R_γ in central Pb–Pb collisions is about 5% below $p_{\mathrm{T}} = 3$ GeV/c, which is compatible with the theoretical predictions. On the other hand, in pp collisions, expected R_γ at low p_{T} is almost unity, and the direct photon excess is covered by the large uncertainties. From the above, the extraction of the direct-photon signal in pp collisions requires a very precise measurement of the background photons to reduce systematic uncertainties.

2.2 Techniques of Direct Photon Measurement

Direct photons are measured in the form of real or virtual photons. In this study, direct photons are measured by the latter. In the following, real and virtual photon measurements are described together with their advantages and disadvantages.

2.2.1 Subtarction method

Real direct photons can be measured by statistically subtracting decay photon spectra from inclusive photon spectra. This technique was developed by WA98 collaboration [94] and PHENIX [27] and ALICE [25, 95] and was adopted in direct photon measurements as described in the previous section. In this technique, photons are

reconstructed using either electromagnetic calorimeters or electron pairs from photon conversions in the material. The π^0 and η mesons are measured in their two-photon decay channels. Decay photon contributions are estimated via Monte Carlo simulations and subtracted from the inclusive photon spectrum. As most of the decay photons arise from $\pi^0 \to \gamma\gamma$ and $\eta \to \gamma\gamma$, precise measurement of neutral mesons is crucial to extracting direct photon signals.

2.2.2 Internal conversion method

Direct photons can be measured via internal conversion technique, which was developed by PHENIX experiment [96]. Any source of real photons can emit a virtual photon which subsequently decays into low-mass e^+e^- pair, which is interpreted as a higher-order correction to that of real photons. Figure 2.7 shows the lowest order diagrams of the dielectron production via virtual-photon decays.

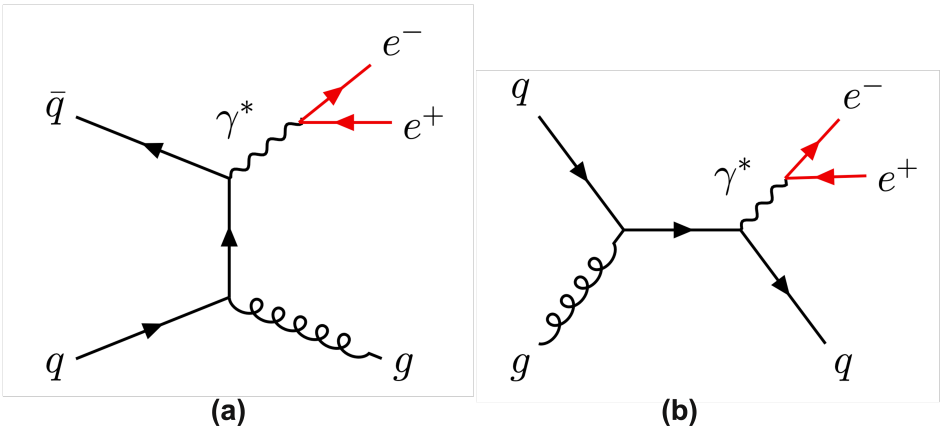

Figure 2.7: The lowest order diagrams for (a) quark-antiquark annihilation and (b) gluon Compton scattering with associated virtual photon decay into an e^+e^- pair.

The relation between real photon and the e^+e^- production is given by Kroll-Wada formulae [97, 98]:

$$\frac{\mathrm{d}^2 N_{\mathrm{ee}}}{\mathrm{d}m_{\mathrm{ee}}\mathrm{d}p_{\mathrm{T,ee}}} = \frac{2\alpha}{3\pi}\frac{1}{m_{\mathrm{ee}}} L(m_{\mathrm{ee}}) S(m_{\mathrm{ee}}, p_{\mathrm{T,ee}}) \frac{\mathrm{d}N_\gamma}{\mathrm{d}p_{\mathrm{T}}}, \tag{2.5}$$

$$L(m_{\mathrm{ee}}) = \sqrt{1 - \frac{4m_{\mathrm{e}}^2}{m_{\mathrm{ee}}^2}}\left(1 + \frac{2m_{\mathrm{e}}^2}{m_{\mathrm{ee}}^2}\right), \tag{2.6}$$

$$S(m_{\mathrm{ee}}, p_{\mathrm{T,ee}}) = |F_h(m_{\mathrm{ee}}^2)|^2 (1 - \frac{m_{\mathrm{ee}}^2}{m_h^2})^3. \tag{2.7}$$

Here, $\alpha \approx 1/137$ is the fine structure constant, m_{ee} is the invariant mass of e^+e^- pairs, m_{e} and m_h are the electron and hadron mass, respectively. The $S(m_{\mathrm{ee}}, p_{\mathrm{T,ee}})$ denotes

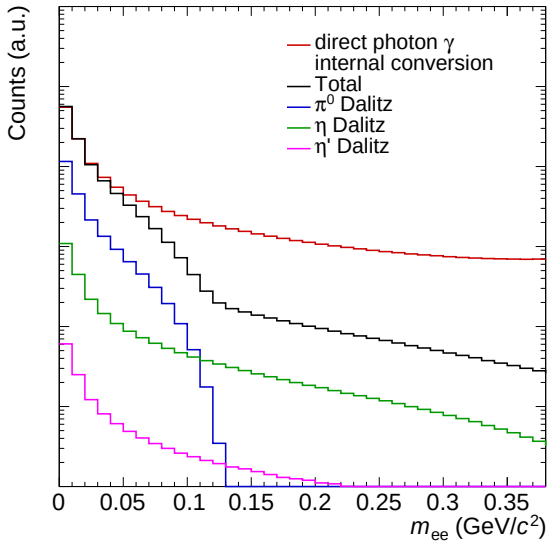

Figure 2.8: Invariant mass distribution from virtual photon from π^0, η and η' Dalitz decays and direct photon. The total contribution includes all Dalitz pairs i.e., (π^0, η, η', ω, ϕ), the contribution from direct photon is normalized to the total contribution below $m_{\rm ee} = 30$ MeV/c^2, to highlight difference of mass dependence.

the process-dependent factor that accounts for the differences between real and virtual photons such as form factors, phase space, and spectral functions. This equation holds for any process of emitting real photons, i.e., Compton scattering ($qg \rightarrow q\gamma$), Dalitz decays ($\pi^0, \eta \rightarrow {\rm e}^+{\rm e}^-\gamma$) and 2-photon decays from other hadrons. For high $p_{\rm T}$ ($p_{\rm T} \gg m_{\rm ee}$), the process dependence becomes negligible. The factor $S(m_{\rm ee}, p_{\rm T,ee})$ becomes 1 as $m_{\rm ee} \rightarrow 0$ or $m_{\rm ee}/p_{\rm T} \rightarrow 0$. For ($m_{\rm ee} \gg m_{\rm e}$), the factor $L(m_{\rm ee})$ also becomes very close to 1. Thus the relation is simplified and gives very characteristic $1/m_{\rm ee}$ dependence as follows

$$\frac{{\rm d}^2N_{\rm ee}}{{\rm d}m_{\rm ee}{\rm d}p_{\rm T,ee}} \simeq \frac{2\alpha}{3\pi}\frac{1}{m_{\rm ee}}\frac{{\rm d}N_\gamma}{{\rm d}p_{\rm T}}. \tag{2.8}$$

On the other hand, for Dalitz decays, as $S(m_{\rm ee}, p_{\rm T,ee})$ becomes 0 for $m_{\rm ee} \rightarrow m_h$ and Dalitz pair do not carry whole invariant mass. This leads to a rapid-falling shoulder shape and gives different mass dependence that of the virtual photon as shown in Fig. 2.8. By making use of these differences, the direct-photon signal can be separated from the background.

The signal extraction is performed assuming the equivalence between the fraction of real direct photons and the fraction of virtual direct photons with zero mass

$$r_{\rm dir} = \frac{N^\gamma_{\rm dir}}{N^\gamma_{\rm incl}} \equiv \frac{N^{\gamma^*}_{\rm dir}}{N^{\gamma^*}_{\rm incl}}\Big|_{m=0}, \tag{2.9}$$

the real direct photon fraction r can be extracted with a fit of the e^+e^- invariant mass distribution above π^0 mass with a virtual photon contribution plus hadron decays using the following expression:

$$d\sigma/dm_{ee} = r f_{dir}(m_{ee}) + (1-r) f_{LF}(m_{ee}) + f_{HF}(m_{ee}) \quad (2.10)$$

where $f_{LF}(m_{ee})$ and $f_{HF}(m_{ee})$ are contributions from light-flavour and heavy-flavour hadron decays, and the shape of the virtual direct photon $f_{dir}(m_{ee})$ is described by Eq. 2.8 in the range $p_T \gg m_{ee}$, where the quasi-real virtual photon region.

The advantage of this method is by selecting mass window above $m_{ee} > m_{\pi^0} \approx 135$ GeV/c^2, the signal-to-background ratio is significantly improved. The drawbacks of this method are the small internal conversion probability ($\sim \alpha \approx 1/137$) and rapidly decreasing cross section as a function of m_{ee} ($\sim 1/m_{ee}$).

This technique requires the knowledge of the backgrounds up to η mass region ($\sim$ 0.5 GeV/c^2). Therefore, the p_T and rapidity spectra of π^0 and η mesons are essential inputs. Moreover, at LHC energies the contribution from open heavy-flavor hadrons cannot be ignored and needs to be evaluated precisely. Below sources of background dielectrons are summarised.

Dalitz decays

Dalitz decays is a radiative leptonic decay of a neutral pseudo-scalar meson into a dilepton pair and either a photon [99] or a vector meson. Pseudo-scalar (π^0, η and η') and vector mesons (ω, ϕ, J/ψ) are prime examples of internal conversion. In these processes, a virtual photon, instead of a real photon, is emitted in the decay of a hadron and subsequently decays into an e^+e^- pair. In the case of Dalitz decays such as $\pi^0 \to \gamma$ e^+e^-, the relation between hadron production and the associated e^+e^- pair production is given by Eq. 2.8.

Semileptonic decays of open heavy-flavor hadrons

Electrons from semi-leptonic decay open heavy-flavor hadrons are important contributions to the dilepton production at LHC energies. Open-heavy flavor hadrons are particles made of at least a heavy (charm or beauty) quark and other lighter quarks. Below, a full process of heavy-quark production, hadronization, and semileptonic decay is briefly summarised.

Charm and beauty quarks are referred to as heavy quarks ($Q\bar{Q}$). Due to their large mass ($m_c \approx 1.27$ GeV/c^2 and $m_b \approx 4.18$ GeV/c^2), heavy-quark pairs ($c\bar{c}$ and $b\bar{b}$) are produced by only initial hard scattering, and their production can be calculated using pQCD even at low p_T. At leading order (LO), heavy quarks are produced via gluon fusion and quark-antiquark annihilation. At next-to-leading order (NLO), processes such as flavor excitation and gluon splitting are important (Fig. 2.9). Once a heavy-quark pair is produced, hadronization occurs and open-heavy flavor hadrons are created e.g. $D\bar{D}^0$. Then they weakly decay semileptonically ($D^0 \to K^- l^+ \nu_l$), which leads to

the creation of correlated l^+l^- pair (Figure 2.10). These dilepton pairs dominate the intermediate-mass region between ϕ meson and J/ψ ($1.1 < m_{ee} < 2.7$ GeV/c^2) as is discussed in Sec. 4.10 of Chapter 4.

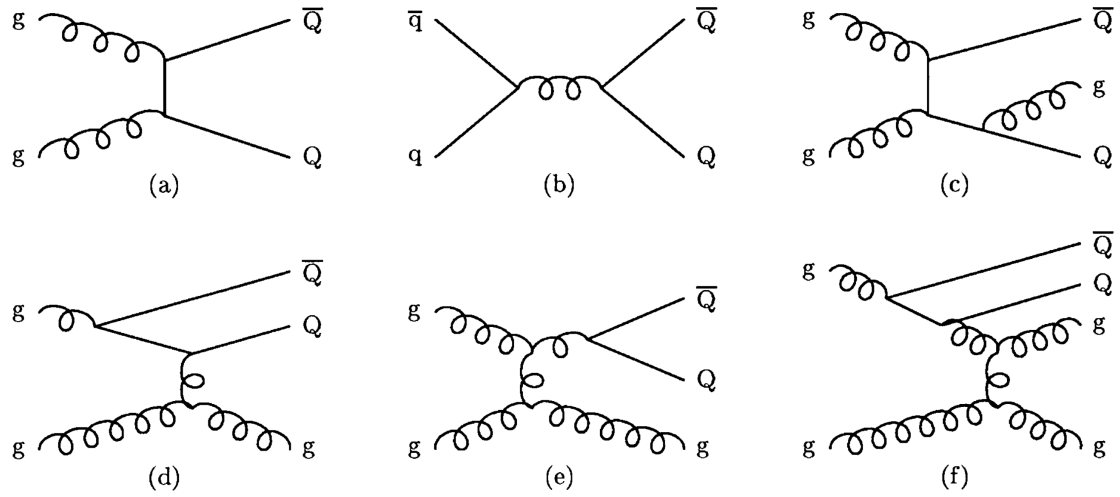

Figure 2.9: Examples of heavy-flavor production diagrams. (a) and (b) Leading order. (c) Pair creation (with gluon emission). (d) Flavor excitation. (e) Gluon splitting. (f) Events classified as gluon splitting but of flavor-excitation character [100]

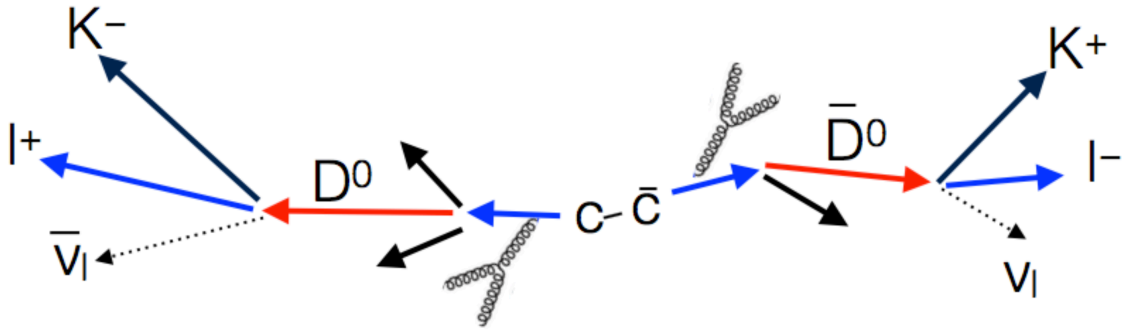

Figure 2.10: Skematic view of dilepton production from correlated semi-leptonic decays of open heavy-flavor hadrons.

Chapter 3

Experimental Setup

3.1 The Large Hadron Collider (LHC)

The Large Hadron Collider (LHC) [101] is the largest particle accelerator in the world, built by the European Organization for Nuclear Research (CERN) beneath the French-Swiss border near the city of Geneva. The LHC is a 27 km-long ring of superconducting magnets, installed in a tunnel originally used for the Large Electron-Positron Collider (LEP). It is designed to accelerate and collide proton beams at an energy of 7 TeV, which gives a total center-of-mass energy of 14 TeV, while 2.75TeV/nucleon Pb beams lead to a center-of-mass energy of 5.5 TeV. The proton and heavy-ion beams are divided into thousands and hundreds of bunches, respectively. Each bunch contains more than a hundred billion protons or tens of millions of lead nuclei. During Run 2 (2015 - 2018), the LHC increased the center-of-mass energy $\sqrt{s} = 13$ TeV in pp collisions and achieved the design luminosity of 10^{34} cm^{-2} s^{-1}. In Pb-ion collisions, the center-of-mass energy was reached up to $\sqrt{s_{\mathrm{NN}}} = 5.02$ TeV per nucleon pair with a peak luminosity of 10^{27} cm^{-2} s^{-1}. Design and performance of LHC during 2016-2018 in Run 2 are summarised in Table. 3.1. The LHC beams are produced and pre-accelerated in the CERN accelerator chain, so-called LHC injectors. Figure 3.1 shows an overview of CERN accelerator complex [102]. The injection chain for the protons starts at LINAC 2, where the H^+ ions are produced and accelerated to 50 MeV. After the LINAC 2, the beams are injected into the PS Booster. The booster consists of four storage rings, which make protons a single bunch. The bunches are accelerated to 1.4 GeV and transferred into the Proton Synchrotron (PS). The PS has several RF systems that can produce bunch structure via adiabatically switching frequencies among them. Then, the beams are extracted to the Super Proton Synchrotron (SPS) and further accelerated to 450 GeV, the injection energy of the LHC. The two beams are transported to the LHC via injection systems which are located at TI 1 for beam 1 and TI 2 for beam 2. The bunches are injected every 25 ns for pp collisions, and make up bunch trains - groups of bunches. In Run 2, the number of bunches reached $\sim$ 2500 bunches. When the injection process is completed, the energy is increased by ramping up the LHC magnets. Afterward, the beams are accelerated and squeezed to minimize β^*, which is the value of the beta function β at an interaction point. Finally, collisions of two

beams occur and experiment starts to data taking [103]. The two beams can collide only in the regions containing the four major experiments in ALICE, ATLAS, CMS and LHCb.

Table 3.1: Summary of beam and machine parameters during 2016-2018 in Run 2 compared to the LHC design values [104]. The β^* (m) and half Crossing angle (μrad) are at IP2 and the same as Run 1 [105]. The β^* is described in the text.

Parameter	Design	2018	2017	2016
Energy (TeV)	7.0	6.5	6.5	6.5
Bunch spacing (ns)	25	25	25	25
Number of bunches	2808	2556	2556 - 1868	2220
β^* (m)	0.55		10	
Bunch intensity (10^{11} ppb)	1.15	1.1	1.25	1.25
Emittance (μm)	3.75	1.8-2.2	1.8-2.2	1.8-2
Peak luminosity (10^{34} cm^{-2} s^{-1})	1.0	2.1	2.0	1.5
Harf Crossing angle (μrad)	142.5		710	

3.2 ALICE Detector Overview

ALICE (A Large Ion Collider Experiment) is one of the four major experiments at the LHC. The spectrometer is designed to study the strong interaction sector of the Standard Model and QGP, using the ultra-relativistic heavy-ion collisions.

Figure 3.2 shows the schematic view of ALICE apparatus during the LHC Run 2. In total, 19 detector systems are installed, each has its own different purposes and technologies, driven by the physics requirements and the experimental conditions expected at LHC. ALICE is optimized to have a good momentum resolution as well as excellent particle identification (PID) capability over a wide p_{T} range under very high multiplicity conditions in central Pb–Pb collisions ($\mathrm{d}N_{\mathrm{ch}}/\mathrm{d}\eta \sim 8000$). A detailed description of each detector and its performance is summarized in [105–108]. ALICE consists of two main parts, i.e., central barrel part which is housed in the solenoid magnet reused from L3 experiment, and the forward detector part. From the inside out, the central barrel detector comprises Inner Tracking System (ITS), Time-Projection Chamber (TPC), Transition Radiation (TRD), Time-of-Flight (TOF), Ring Imaging Cherenkov (HMPID) detectors, and two electromagnetic calorimeters (PHOS, EMCal and DCal). The forward detector includes the Photon Multiplicity Detector (PMD), the silicon Forward Multiplicity Detector (FMD), and the Muon spectrometer. The

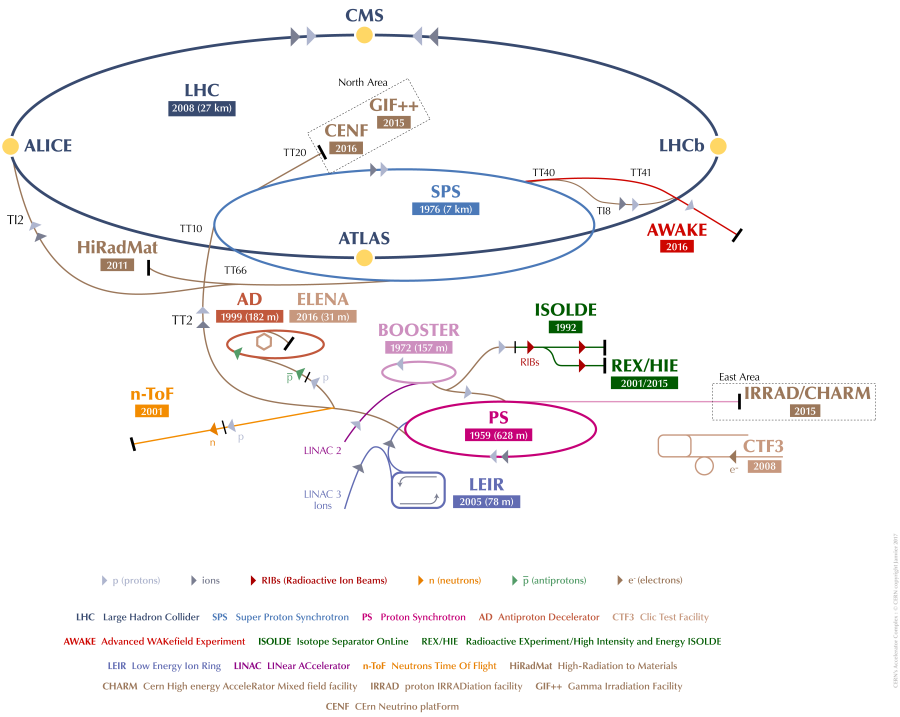

Figure 3.1: Schematic view of the CERN accelerrator complex [102].

Muon spectrometer consists of Muon tracker (MTR), Muon Wall, and Muon Trigger. In addition, small detectors (ZDC, PMD, FMD, T0, V0) are located at small angles for global event characterization and triggering. An array of scintillators (ACORDE) on top of the L3 magnet is used to trigger cosmic rays.

ALICE coordinate system

The ALICE coordinate system is a right-handed orthogonal coordinate, the interaction point 2 (IP2) is the origin of the coordinate system [109]. As shown in Fig. 3.3, the z axis is parallel to the beam direction, the x axis is perpendicular to the z axis and points to the accelerator center, the y axis is perpendicular to the beam axis and the x axis, pointing vertically up. The azimuthal angle φ, between the x- and y-axis, counts clockwise with the observer facing the A-side. The polar angle θ increases from the positive part of the z-axis towards the y-axis. Here we introduce a variable called rapidity, which is an essential quantity to characterize particle production. The rapidity is used to express approximate angles with respect to the beam axis which is

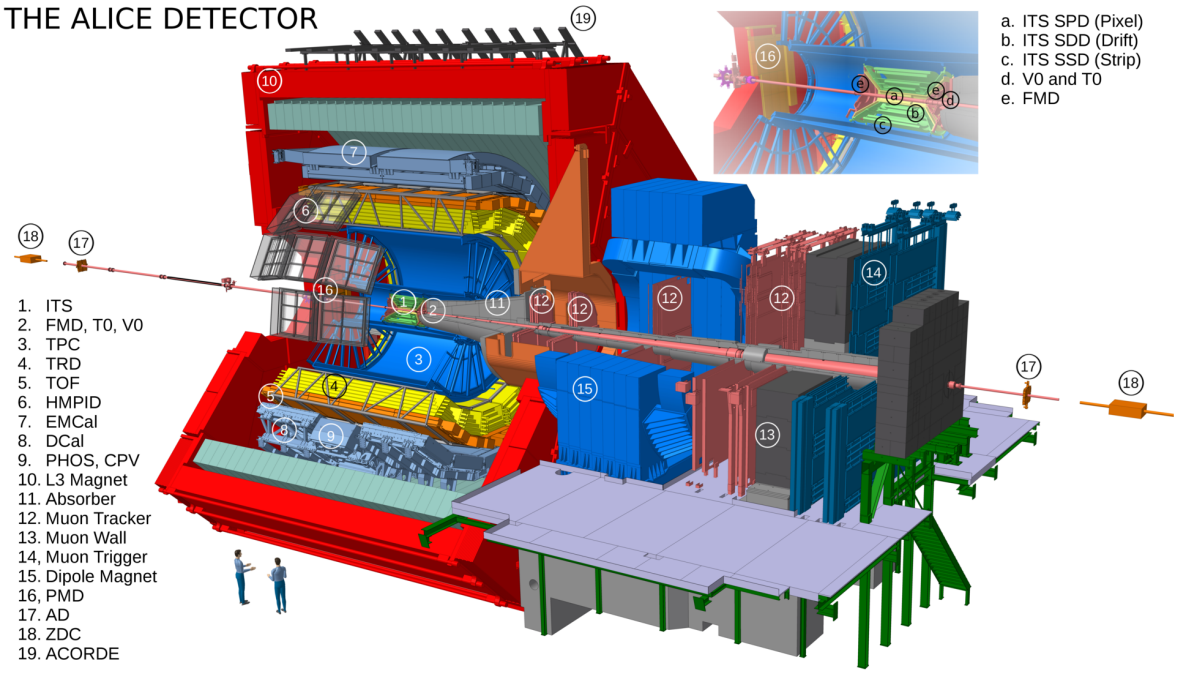

Figure 3.2: ALICE detector complex in LHC Run 2 [109].

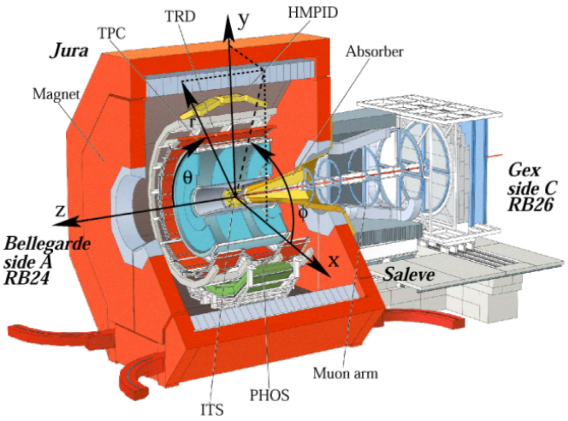

Figure 3.3: Global coordinate of ALICE detectors [110].

defined as

$$y = \frac{1}{2}\ln\frac{E + p_z}{E - p_z}, \tag{3.1}$$

where, E is the energy of the particle and p_z is the particle longitudinal momentum component, along with the z-axis. Since the rapidity requires knowledge of the mass of the particle, another variable called pseudorapidity $\eta = \ln[\tan(\theta/2)]$, with polar angle

θ is used. This quantity is equivalent to rapidity for massless particles.

To represent the detector position, the positive (negative) z is labeled A (C), these correspond to forward and backward rapidity, respectively. For example, Muon Tracker is placed at backward rapidity (C-side). In the following sections, only relevant detectors to this analysis: ITS, TPC, TRD, TOF, and V0 are explained.

3.2.1 Inner Tracking System

The Inner Tracking System (ITS) consists of six cylindrical layers of silicon detectors with two layers of; Silicon Pixel Detector (SPD), Silicon Drift Detector (SDD), and Silicon Strip Detector (SSD). It is located at radii between 4 and 43 cm, the outer radius is determined to make track matching with the TPC, and the inner radius is the minimum allowed by the beam pipe. All detectors cover the rapidity range of $|\eta| < 0.9$. The main tasks of the ITS are:

- Localise the primary vertex with a resolution better than 100 μm, to reconstruct the secondary vertices from the decays of hyperons and D and B mesons
- To track and identify particles with momentum below 200 MeV/c
- Improve the momentum and angular resolution for particles reconstructed by the Time-Projection Chamber (TPC)

Therefore, the ITS information is used for practically all physics topics addressed by the ALICE experiment. The geometrical dimensions and the technology used in the various layers of the ITS are summarised in Table 3.2. The choice of innermost and intermediate detectors which have different technologies are to achieve the required impact parameter resolution under high particle density. The four outer layers have analogue readout which can be used for particle identification via $\mathrm{d}E/\mathrm{d}x$ measurement in the non-relativistic region.

Another key component of the ITS detector is to keep minimize material budget as the momentum and impact parameter resolution of low-momentum particles are affected by multiple scattering in the detector material. From the point of view of dielectron analysis, the smaller material budget is of importance as the electrons from conversions are a source of the background. Figure 3.5 shows the thickness of material as a function of radius and azimuthal angle, the total material budget in the ITS is $\sim$ 8% of the radiation length X_0.

3.2.2 Time Projection Chamber

The TPC [111] is the main tracking device in the central barrel detector which provides charged particle momentum and particle identification. The choice of a TPC is suitable to achieve efficient and robust tracking, under high particle density for central Pb–Pb collision even after taking into consideration of the limitation of high rate capabilities. The TPC covers full azimuth and a pseudorapidity interval $|\eta| < 0.9$, which can ensure

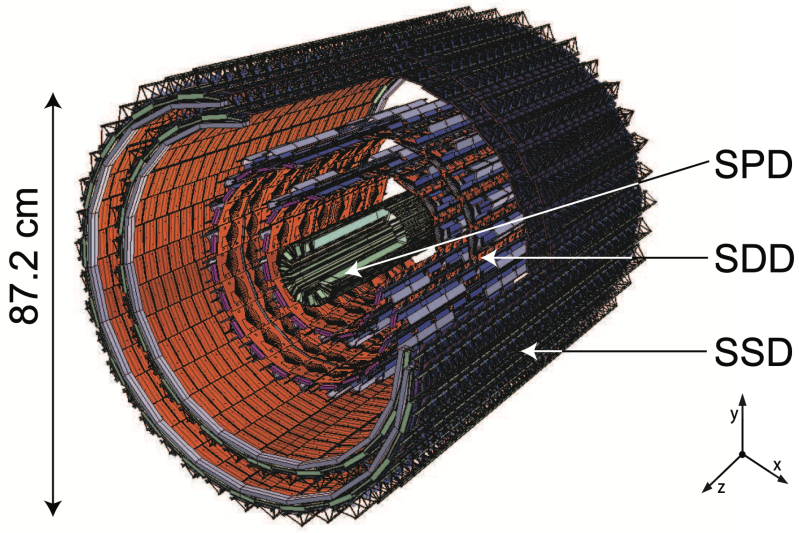

Figure 3.4: Layout of ITS system

Table 3.2: Geometrical dimensions, active areas and number of channels of each ITS layers.

Layer	Type	r (cm)	± z (cm)	Area (m^3)	Channels
1	pixel	3.9	14.1	0.07	3276800
2	pixel	7.6	14.1	0.14	6553600
3	drift	15.0	22.2	0.42	43008
4	drift	23.9	29.7	0.89	90112
5	strip	38.0	43.1	2.20	1148928
6	strip	43.0	48.9	2.80	1459200

reliable performance at order of 10000 charged particles. Figure 3.6, shows a schematic view of the ALICE TPC. The TPC is a cylinder gaseous chamber with radial and longitudinal dimensions of 85 cm $< r <$ 247 cm and -250 cm $< z <$ 250 cm, whose axis is aligned with the beam axis and is parallel to the solenoidal magnetic field. The detector is filled with a counting gas which was Ar–CO_2 gas mixture (with abundances of 88%–12%) in 2016 and 2018, and Ne–CO_2–N_2 (90%–10%–5%) in 2017. The choice of the gas and its mixture is made by considering diffusion characteristics, ion mobility, drift velocity and operational stability. A central electrode in the middle of the detector is charged to -100 kV, and electrons drift with a drift velocity of 2.7 cm/μs to both end plates in a uniform electric field of 400 V/cm.

Figure 3.7 shows the working principle of a TPC around the end plate region for position measurement. The TPC is equipped with Multi-Wire Proportional Chambers (MWPCs) for the readout, located at its end plates. In a MWPC, different potentials are applied to a set of wire planes (cathode plane and anode plane), resulting in a

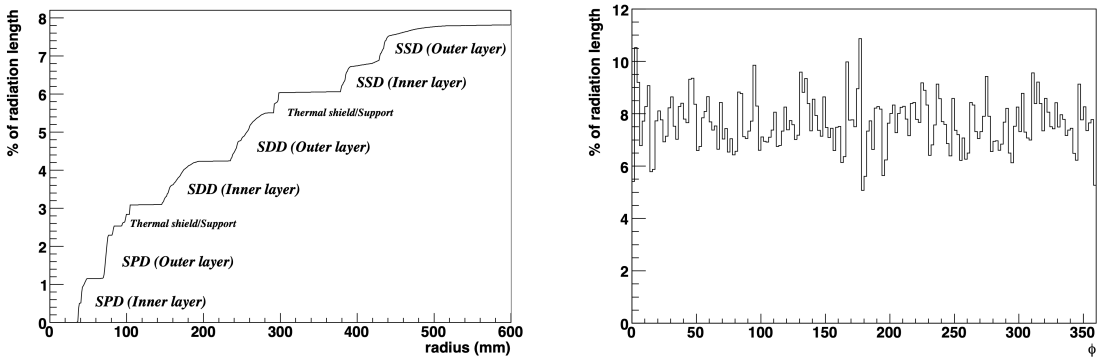

Figure 3.5: Left: Integral of material thickness of the ITS as a function of radius. Right: The total material encountered by a perpendicular track crossing the ITS versus azimuthal angle. [108]

high electric field. Charged particles traversing the TPC volume ionize the gas, which produces electrons. They are accelerated in the electric field in the MWPC and further ionize gas atoms and cause electron avalanches. The induced current on the pad plane is read out and the precise position in the pad plane is measured. Together with an accurate measurement of the arrival time relative to the collision time of the beams, the z coordinate is calculated by the product of the drift time and drift velocity ($z = v_{\text{drift}} \times t_{\text{drift}}$). In this way, the complete trajectory in space of all charged particles traversing the TPC can be determined.

During the electron amplification ions are produced as well, which drift in the opposite direction with a small drift velocity. These ions accumulate in the gas volume and distort the electric field, which affects the drift path of electrons. In order to avoid this ion backflow, the gating grid is added to the MWPC. By changing the voltage supply to the gating grid, it can collect electrons from the TPC volume and ions from the readout chambers or, conversely, allow both to pass through. When TPC accepts a trigger, the gating grid opens for a certain time corresponding to electron drift time through the full TPC ~ 100 μs. Then the grid is closed for the time needed to collect all the ions produced during the gas amplification ~ 200 μs. (for Ar mixture gas.) This is an intrinsic dead time of the TPC, which limits the rate of a few kHz in Pb–Pb collisions.

The simultaneous measurement of the momentum p of a particle and its specific ionization loss $\mathrm{d}E/\mathrm{d}x$ in the TPC gas provides PID information. The mean energy loss $\mathrm{d}E/\mathrm{d}x$ per unit path length can be described by the Bethe-Bloch formula:

$$\left\langle \frac{dE}{dx} \right\rangle = \frac{4\pi N e^4}{m_e c^2} \frac{Z^2}{\beta^2} \left(\ln \frac{2 m_e c^2 \beta^2 \gamma^2}{I} - \beta^2 - \frac{\delta(\beta)}{2} \right) \tag{3.2}$$

where $m_e c^2$ is the rest energy of the electron, Z denotes the charge of the projectile, N the number density of electrons in the traversed matter, e the elementary charge, β and

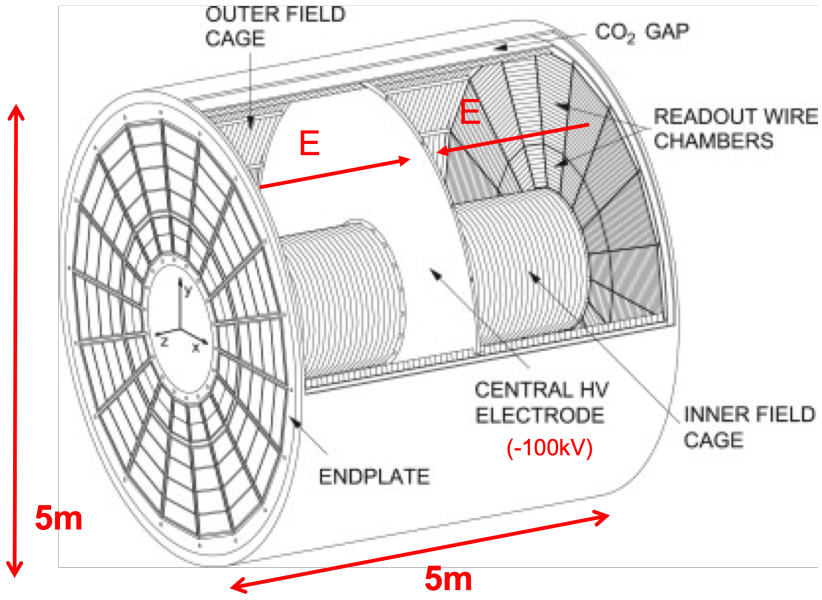

Figure 3.6: The schematic view of ALICE TPC field cage. The field cage is a hollow cylindrical structure with a diameter of 5 m and a length of 5 m. A voltage of -100 kV is applied to the central electrode. The red arrows indicate the direction of the electric field E.

γ are velocity of the projectile $\beta = v/c$ and Lorentz factor $1/\sqrt{1-\beta^2}$, respectively, I is the mean excitation energy of the atom. Figure 3.8 shows an example of $\mathrm{d}E/\mathrm{d}x$ for the positive muons in copper over a wide range of muon's kinetic energy. Eq.3.6 is valid in the region $0.1 \lesssim \beta\gamma \lesssim 1000$ with an accuracy of a few percent. In this region, $\mathrm{d}E/\mathrm{d}x$ depends only on the particle's velocity β and not on the mass, therefore particles with the same momenta but different mass can be characterized by their $\mathrm{d}E/\mathrm{d}x$. In the analysis of experimental data, parameterization other than the Bethe-Bloch function is often used. In ALICE, the form proposed by the ALEPH experiment [112] is adopted:

$$f(\beta\gamma) = \frac{P_1}{\beta^{P_4}}\left(P_2 - \beta^{P_4} - \ln\left(P_3 + \frac{1}{(\beta\gamma)^{P_5}}\right)\right), \tag{3.3}$$

where P_{1-5} are parameters determined by the fit to measured data.

Figure 3.9 shows $\mathrm{d}E/\mathrm{d}x$ in the TPC measured in pp collisions at $\sqrt{s} = 13$ TeV as a function of the particle momentum. It is clearly seen electrons and pions are nicely separated over the wide momentum range. However, at 0.5 GeV/c and 1 GeV/c, as the electron band crosses those of kaon and proton, electrons are inevitably contaminated. Therefore, to suppress hadron contamination, complementary PID information from the TOF detector is used in this thesis. The key quantity for particle identification is the resolution $\sigma_{dE/dx}$ of the $\mathrm{d}E/\mathrm{d}x$ measurement. It depends on the number of TPC track points measured with cosmic tracks, which is about 5.2% in pp collisions [105].

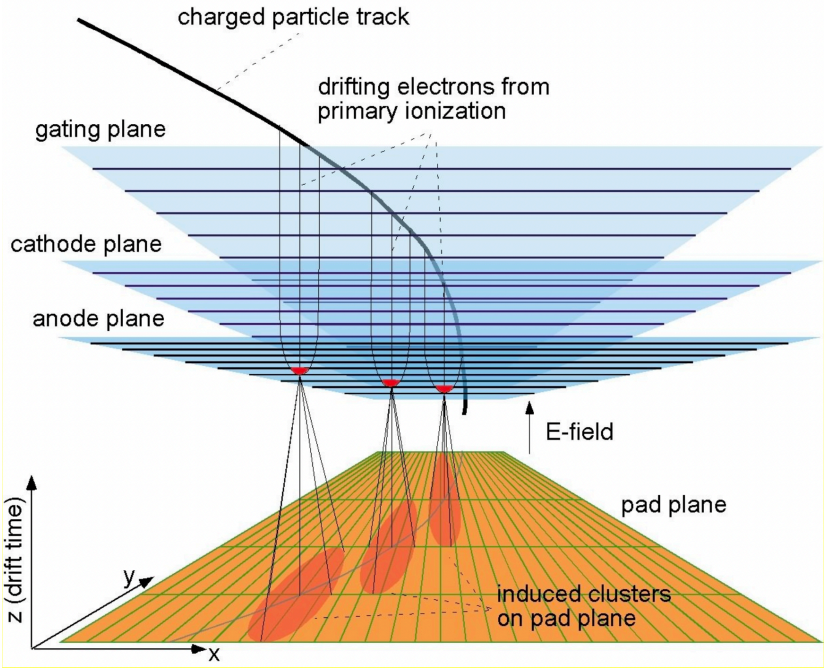

Figure 3.7: ALICE TPC working principle

3.2.3 Transition Radiation Detector

The role of Transition Radiation Detector (TRD) [113] is to provide tracking, electron identification, and triggering. The TRD is placed outside the TPC, from 2.9 m to 3.7 m from the beam axis, which covers the full azimuth and pseudorapidity range $|\eta| < 0.84$ (Fig. 3.10). The TRD consists of 522 chambers and each chamber comprises a foam/fibre radiator followed by a Xe-CO_2-filled MWPC preceded by a drift region of 3 cm.

The working principle of the TRD is based on the transition radiation (TR) occurring when a charged particle crosses the boundary between two media with different dielectric constants. For highly relativistic particles ($\gamma \gtrsim 1000$), the emitted photon is in the X-ray range and absorbed in high-Z gas. The ejected electrons are detected by multiwire proportional chambers (MWPC). Electrons can be distinguished from other charged particles by measuring a characteristic signal of TR photon.

Fig. 3.11 shows a schematic cross-section of a chamber and its radiator. The local coordinate system is similar to the global coordinate system, rotated such that the x-axis is perpendicular to the chamber. Six layers of chambers are installed to enhance the pion rejection powers.

The eID performance is expressed in terms of the electron efficiency and the corresponding pion efficiency. The electron identification performance is overall better than the design value. At 90% electron efficiency, a pion rejection factor of about 70

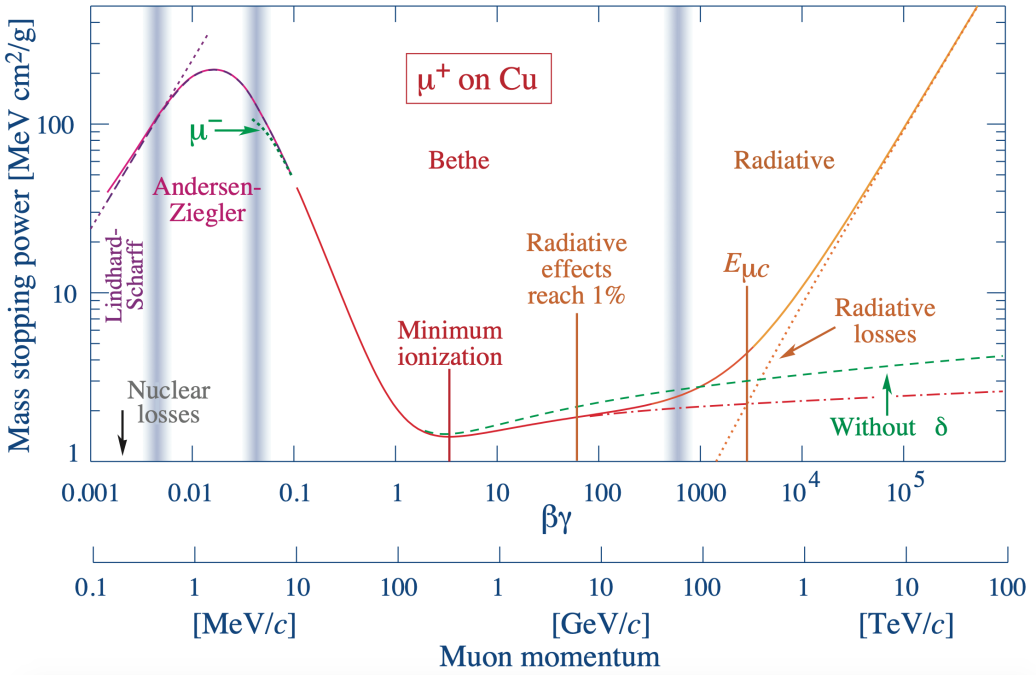

Figure 3.8: Ionization energy loss for positive muon in copper as function of $\beta\gamma = p/Mc$ [5].

is achieved at a momentum of 1 GeV/c for simple identification algorithms [114].

In this analysis, the TRD is not actually used for electron identification but contributes to the track reconstruction. As described in Sec. 3.3, the TRD improves the overall momentum resolution by providing additional space charge points at large radii.

3.2.4 Time-of-Flight Detector

Particle identification in the ALICE central barrel is complemented by the Time-of-Flight (TOF) detector [115]. It is a large area array of Multi-gap Resistive Plate Chambers (MRPC) [116], which is positioned at 370−399 cm from the beam axis and covering the full azimuth and the pseudorapidity range $|\eta| < 0.9$. The chamber is operated with a high and uniform electric field over the full sensitive gaseous volume. The main characteristic is traversing particles ionized immediately and starting to gas avalanche, which leads to quick time response. A schematic layout of one supermodule inside the ALICE spectrometer in Fig. 3.12. The time-of-flight is measured as the difference between the particle arrival time and the event collision time, which is provided by the T0 detector, as will be described in the following Sec. 3.2.5. The time resolution of the detector $\sim$ 40 ps for pp collisions. A combinatorial algorithm based on a χ^2 minimization between all the possible mass hypotheses is used in this case [117]. The

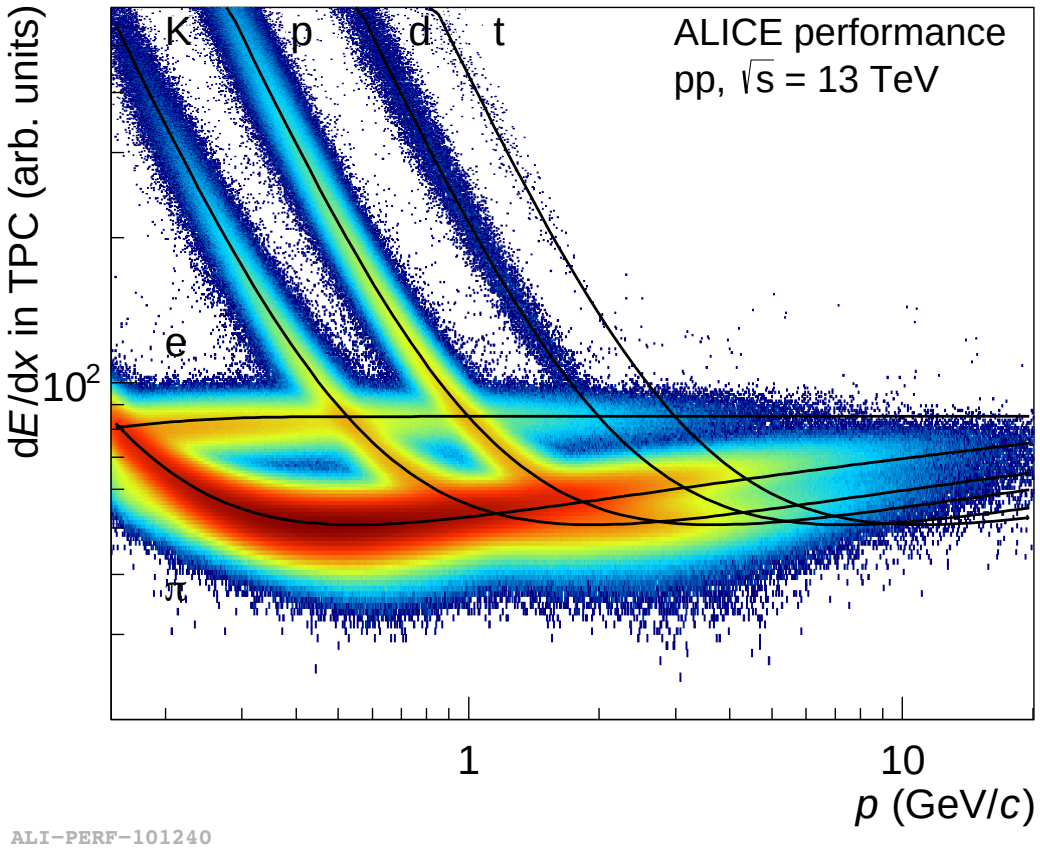

Figure 3.9: Specific energy loss $\mathrm{d}E/\mathrm{d}x$ in the TPC as a function of particle momentum in pp collisions at $\sqrt{s} = 13$ TeV. The lines show the parameterizations of the expected mean energy loss.

time-of-flight t_{TOF} can be related to particle mass through velocity β:

$$\beta = \frac{1}{t_{\mathrm{TOF}} c}, \tag{3.4}$$

$$m = \frac{p}{\beta\gamma} = \frac{p}{c}\sqrt{\frac{c^2 t_{\mathrm{TOF}}^2}{l^2} - 1}, \tag{3.5}$$

where p is particle momentum, l is track length. Due to the curvature of the trajectory in the magnetic field, tracks with $p_{\mathrm{T}} < 0.3$ GeV/c do not reach the TOF detector. For $p_{\mathrm{T}} > 0.3$ GeV/c, the detector can provide a K/π separation up to 3 GeV/c and a K/p separation up to 5 GeV/c with 3σ. Figure 3.13 shows the resulting $\beta = v/c$ of charged particle in pp collisions at $\sqrt{s} = 13$ TeV.

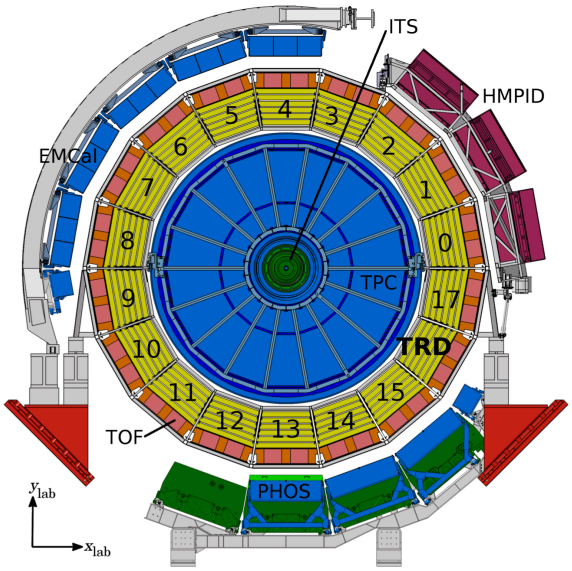

Figure 3.10: Schematic cross-section of the ALICE detector perpendicular to the LHC beam direction

3.2.5 T0 Detector

The T0 [118] detector consists of two arrays of Cherenkov counters with a quartz radiator and photomultiplier tube, which is used to measure collision time with high precision. The time resolution is 25 ps, and the collision time is used as the reference time for the TOF detector. T0 is also used for the determination of the primary vertex, and positioned at opposite sides of the interaction point (IP) at $4.61 < \eta < 4.92$ (T0A) and $-3.28 < \eta < -2.97$ (T0C), respectively (Fig. 3.14).

3.2.6 V0 Detector

The V0 detector [119] is made up of two arrays of 32 scintillators as shown in Fig. 3.15, installed on both sides of the ALICE IP and located at small angles, covering forward (V0A $2.8 < \eta < 5.1$) and backward (V0C $-3.7 < \eta < -1.7$) pseudorapidity regions. The V0A detector is located 340 cm from the interaction point on the side opposite to the muon spectrometer, whereas V0C is fixed to the front face of the hadronic absorber, 90 cm from the interaction point. The material consists of BC4041 scintillating material (2.5 and 2.0 cm in thickness for V0A and V0C, respectively) with 1 mm in diameter Wave-Length Shifting (WLS) fibers. The light is guided to the photo-multiplier system. The PMTs are fixed on the V0A disk holder in groups of 4 units and connected directly to the WLS fibers. They are installed on the absorber in groups of 8 units for the V0C and connected to counters through optical fibers 3.22 m long. The V0 detector has several functions. First, it provides the minimum-bias trigger for inelastic pp

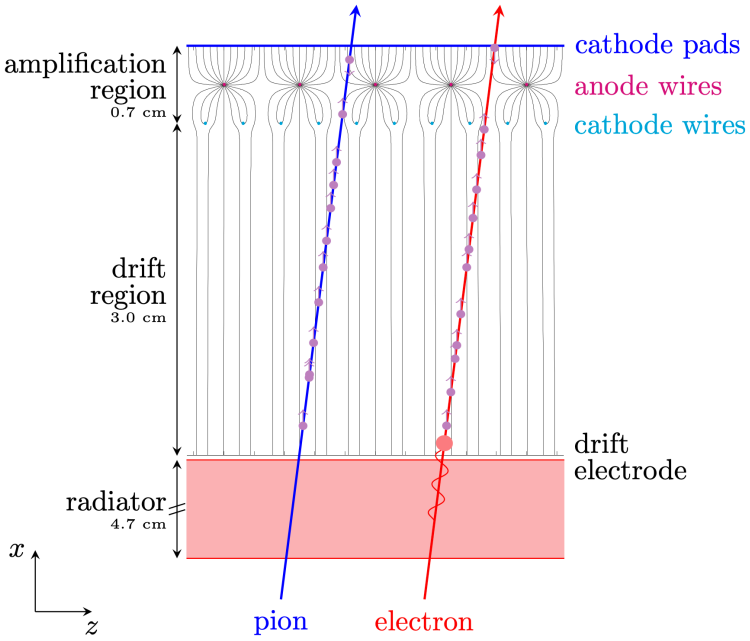

Figure 3.11: Schematic cross-section of a TRD chamber in the x-z plane (perpendicular to the wires) with tracks of a pion and an electron to illustrate the ionization energy deposition and the TR contribution. The large energy deposition due to the TR photon absorption is indicated by the large red circle in the drift region.

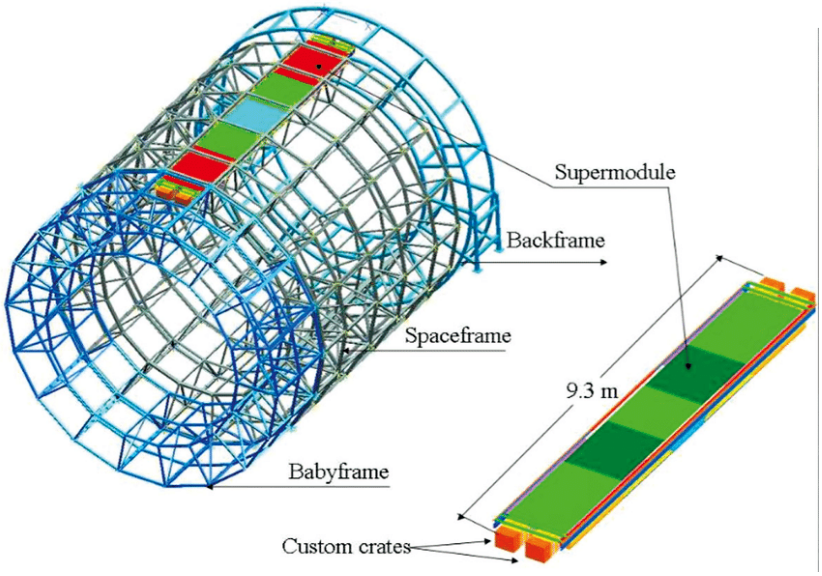

Figure 3.12: Schematic view of super module of Time-Of-Flight (TOF) detector.

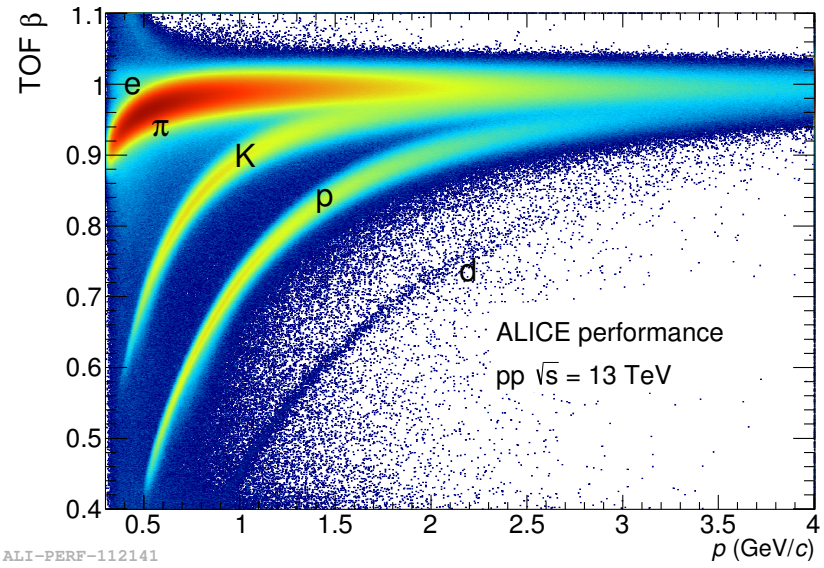

Figure 3.13: TOF β as a function of particle momentum in pp collisions at $\sqrt{s}$ = 13 TeV.

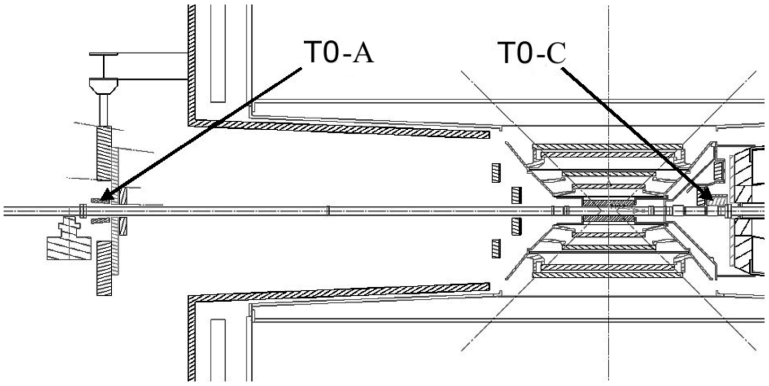

Figure 3.14: The layout of T0 detector arrays inside ALICE [108].

collisions to ALICE detectors, which aims to acquire inelastic events with as little bias as possible. This trigger requires a coincident signal on both sides of the V0 detector ("V0AND" trigger logic). This requirement reduces a substantial amount of background events such as interactions of the beam with residual gas inside the beam pipe or with mechanical structures of the beam line. As the number of measured particles on the V0 arrays and the number of primary emitted particles are proportional to each other, the V0 serves as an indicator of the centrality of the collision via the multiplicity measured in V0 in the event. The V0 can provide multiplicity triggers by requiring a coincident signal on both V0 sides, and a total measured V0 multiplicity

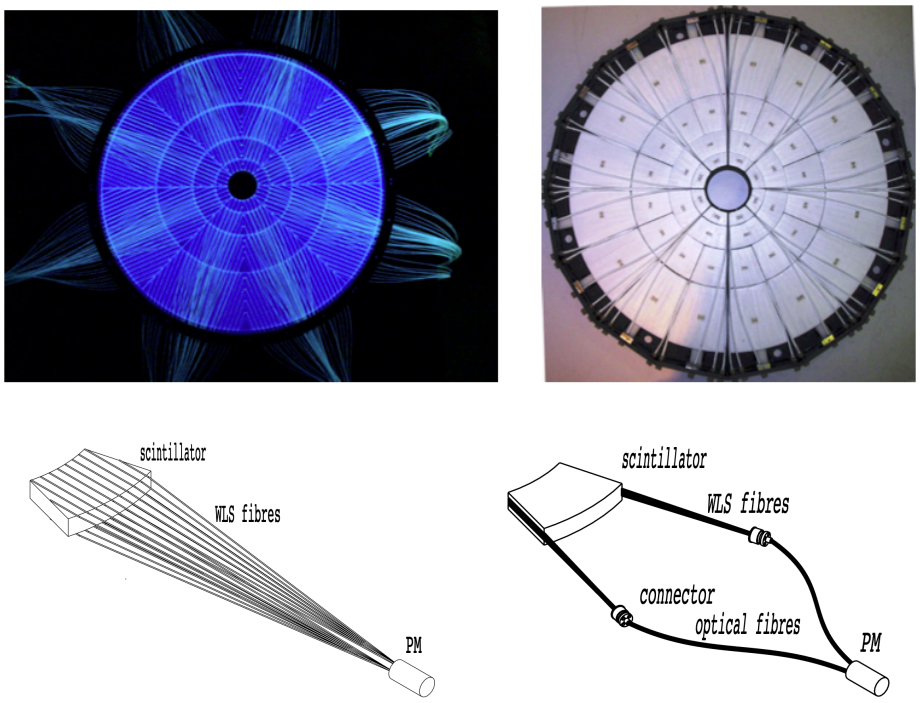

Figure 3.15: Top: Front view of V0A (left) and V0C (right) arrays. Bottom: Schematic design of the V0A (left) and V0C (right) detection elements [108].

(V0M) above a certain threshold. Finally, the V0 detector, as well as the T0 detector, provide luminosity in pp collisions with a good precision of about 10% [120].

3.3 Tracking and Vertexing

This section describes track finding in the ALICE central barrel. The step begins with clusterization, in which the detector data such as signal amplitudes, signal times etc. and their associated errors are converted into "clusters". The clusterization is performed independently for each detector. The next step is to determine the preliminary interaction vertex using the two innermost layers (SPD) of the ITS. The vertex is defined as the space point where the maximum number of lines defined by pairs of clusters among two SPD layers, called tracklets, converge at a point.

Subsequently, track finding and fitting are performed in three stages, following an inward-outward-inward scheme [105, 121]. The track reconstruction is based on the Kalman Filter approach [122, 123]. As illustrated in Fig. 3.16, the first step of track finding is the track seeding in the outermost pad rows of the TPC (1st path). The seed is propagated towards the primary vertex through the TPC volume and the ITS layers. Then a second propagation step is performed in the outward direction from

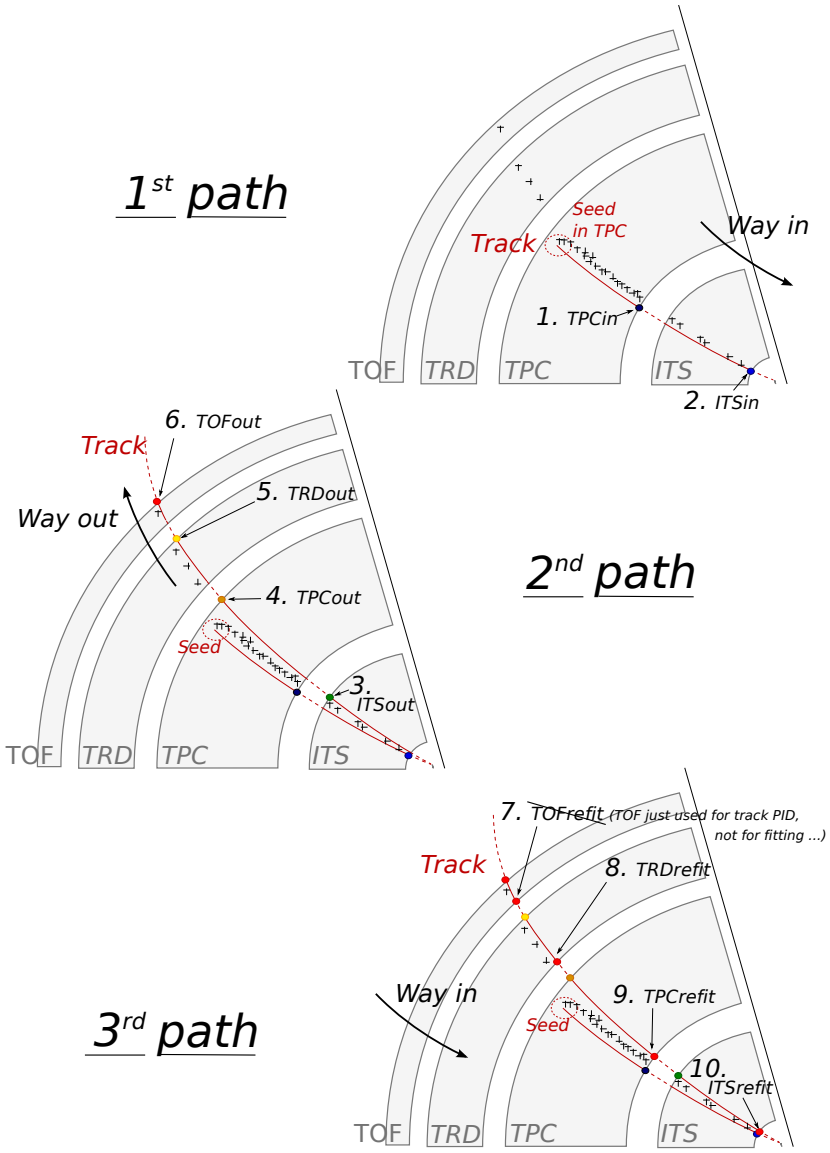

Figure 3.16: Principles of tracking for an ALICE event, showing the three successive paths allowing to build a track and refine its parameters [124].

the innermost ITS layer to the outer detectors such as TRD and TOF (2nd path). Finally, the primary tracks are refitted back to the primary vertex or as close to the vertex as possible in the case of secondary tracks (3rd path). The improvement in p_{T} resolution after applying a vertex constraint and including the TRD in the track fitting is shown in the left and right panels of Figure 3.17, respectively. The vertex constraint significantly improves the resolution of TPC standalone tracks, while it has no effect on ITS-TPC tracks (green and blue square overlap). Including TRD in the tracking improves the resolution by about 40% at high p_{T} for pp collisions recorded at both low

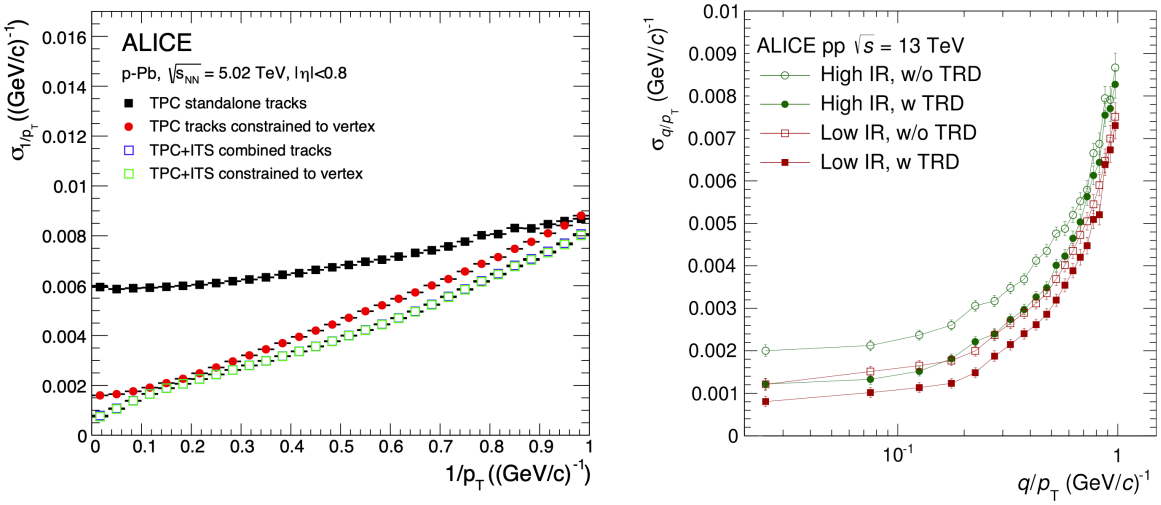

Figure 3.17: Left: the p_{T} resolution in p-Pb collisions for standalone TPC and ITS-TPC matched tracks with and without constraint to the vertex. Right: Improvement of the q/p_{T} (inverse transverse momentum scaled with particle charged) resolution in data in pp collisions when TRD information is included in the tracking for various running scenarios. The labels low and high IR indicate interaction rates (IR) of 12 and 230 kHz, respectively. The left and right fugres are taken from [105] and [114].

and high interaction rates.

Once track is reconstructed, the bending radius r of the track is used to determine its transverse momentum as follows:

$$p_{\mathrm{T}}\ [\mathrm{GeV}] = 0.3qrB\ [\mathrm{T}\cdot\mathrm{m}], \tag{3.6}$$

where q is the particle charge and B is the magnetic field.

3.4 Data Taking

This section summarises ALICE data taking. The detail can be found in Refs. [105, 108]. The ALICE experiment has operated in several different running modes with significantly different characteristics.

The principal design requirement is determined by the Pb–Pb collisions which are characterized by a relatively low interaction rate and relatively short running time (one month per year) but with a huge event size produced by the large number of charged particles traversing the detectors. In proton-proton (pp) or proton-nucleus (p–Pb) running modes, the interaction rates are much higher (up to hundreds of kHz), whereas the event size is smaller and the running time is several (one) months per year in pp (p–Pb).

3.4.1 Trigger System

The trigger decision is generated by the Central Trigger Processor (CTP) [125] based on detector signals and information about the LHC bunch-filling scheme. The CTP evaluates trigger inputs from the trigger detectors every machine clock cycle ($\sim$ 25 ns). The Level 0 trigger (L0) decision is made $\sim$ 0.9 μs after the collision using V0, T0, EMCal, PHOS, and MTR. Information about the LHC bunch-filling scheme was used by CTP to suppress the background. The bunch crossing mask (BCMask) provided the information as to whether there are bunches coming from both A-side and C-side, or one of them, or neither, at a resolution of 25 ns. The beam-gas interaction background was studied by triggering bunches without a collision partner and subtracted from the physics data taken with the requirement of the presence of both bunches.

The events accepted at L0 are further evaluated by the Level 1 (L1) trigger algorithm in the CTP. The L1 trigger decision is made 260 LHC clock cycles ($\sim$ 6.5 μs) after L0. The latency is caused by the computation time (TRD and EMCal) and propagation times (ZDC, 113 m from IP2). The L0 and L1 decisions, delivered to the detectors with a latency of about 900 ns, trigger the buffering of the event data in the detector front-end electronics.

The Level 2 (L2) decision, taken after about 88 μs corresponding to the drift time of the TPC, triggers the sending of the event data to DAQ and, in parallel, to the High Level Trigger system (HLT). During Run 2, depending on the specific running scenarios (e.g. when taking downscaled minimum bias events in parallel with rare triggers), L2 was used to reject events with multiple collisions from different bunch crossings pile up in the TPC (past-future protection). The events with L2 were subsequently filtered in the HLT.

3.4.2 The High Level Trigger

The role of the HLT is to reconstruct the charged-particle tracks by processing data from all available ALICE detectors and to reduce the data volume that is stored per-

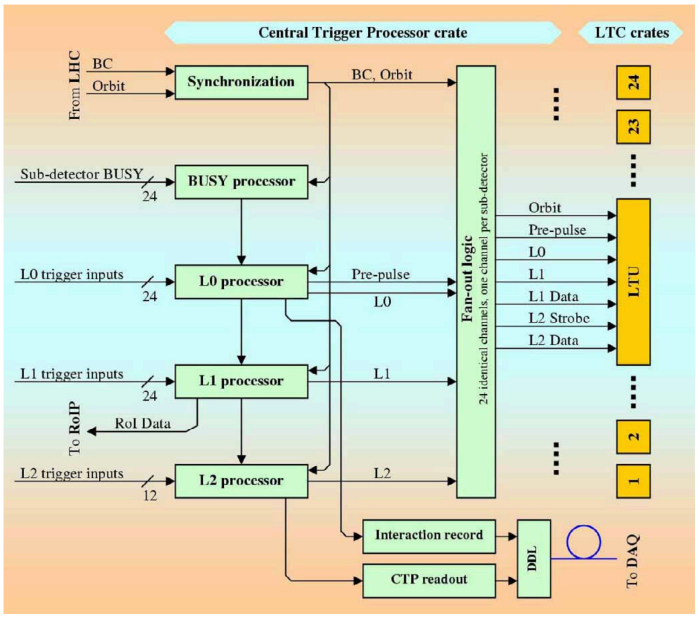

Figure 3.18: Block diagram of the Central Trigger Processor [126].

manently to a reasonable size and to fit in the allocated tape space. The entire HLT operation is based on full real-time event reconstruction.

After the LHC Run 1, there was an important upgrade of the TPC readout electronics, employing a new version of the Readout Control Unit (RCU2) [127] which uses the updated optical link speed of 3.125 Gbps instead of the previous readout rate of 2.125 Gbps. The upgrades, along with an improved TPC readout scheme, doubled the theoretical maximum TPC readout data rate to 48 GB/s, thus allowing ALICE to record twice as many events. In addition, the HLT was updated to be able to cope with the increased data rate of Run 2.

Since the TPC produces most of data volume ($\sim$ 91% for Pb–Pb and $\sim$ 95% for pp), event reconstruction is the most computationally intensive task for the HLT. Therefore the HLT is mainly designed to process TPC data. In Run 2, cluster-finder and track reconstruction algorithms are implemented in FPGA and GPU in the HLT which allows us to reduce the data size in real time [128]. These performance can be found in Fig. 3.19. The left of Fig. 3.19 shows processing time of the newly implemented FPGA-based algorithm (blue), which significantly reduced processing time compared to the offline cluster finding (red). The right of Fig. 3.19 shows the overall speedup achieved by the HLT GPU tracking which is computed as the ratio of the processing time of offline (CPU) tracking and the single-core processing time. Overall, the HLT tracking algorithm executed on the CPU is 15-20 times faster than the offline tracking algorithm used in Run 1.

The online data compression techniques developed and used in the ALICE HLT have more than quadrupled the amount of data that can be stored for offline event

processing.

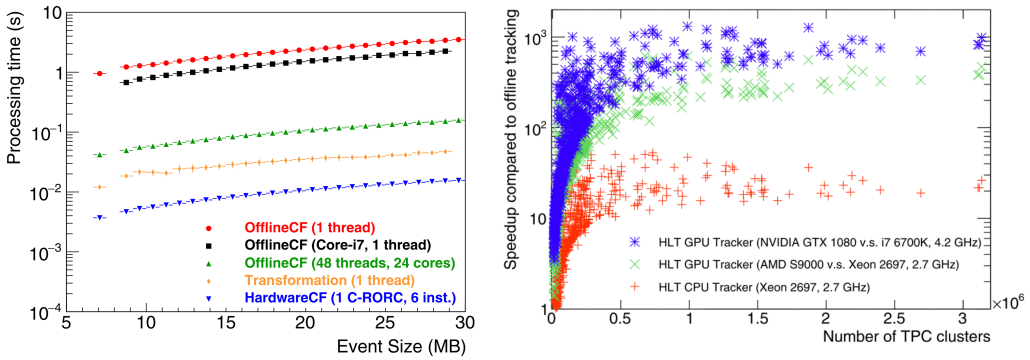

Figure 3.19: Left: Processing time of the hardware cluster finder and the offline cluster finder. Right: Speedup of HLT tracking algorithm executed on GPUs and CPUs compared to the offline tracker normalized to a single core and corrected for the serial processing part that the CPU contributes to GPU tracking as a function of the input data size expressed in terms of the number of TPC clusters. Figures are taken from Ref. [128].

3.4.3 Run Condition in Run 2

Table. 3.3 shows running condition during Run 2. The typical rate for pp and Pb–Pb data-taking in Run 2 is hundreds of kHz and 8 kHz, respectively. Corresponding data size per event is a few megabytes for pp collision and several gigabytes for Pb–Pb collision. The ALICE data volume is dominated by the event size of the TPC, which is scaled with the charged-particle multiplicity, including pileup tracks from other interactions within the TPC drift time window of $\sim$ 100 μs. The maximum TPC event size observed in central Pb–Pb collisions, reaches 70 MB. Figure 3.20 shows integrated luminosity for various triggers in pp collisions at $\sqrt{s} = 13$ TeV during LHC Run 2 (2015-2018), where some of the triggers relevant to this analysis will be explained in Chapter 4.

Table 3.3: Running conditions in pp, p–Pb and Pb–Pb collisions during Run 2 [129].

	pp	p–Pb	Pb–Pb
Luminosity ($\mathrm{cm^{-2}\ s^{-1}}$)	$< \times\ 10^{31}$	(1-2)$\times\ 10^{26}$	10^{25-27}
σ_{INEL} (mb)	$\sim$ 70	2500	8000
Rate (Hz)	$1 \times\ 10^{6}$	(2-4)$\times\ 10^{5}$	10^{2-4}

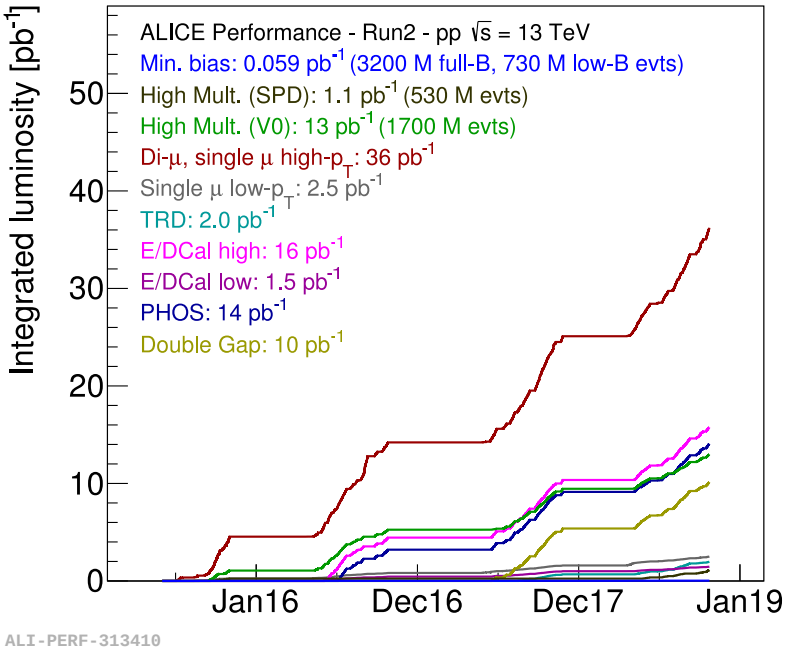

Figure 3.20: Integrated luminosity for various triggers in pp collisions at $\sqrt{s} = 13$ TeV during LHC Run 2 (2015-2018).

Chapter 4

Analysis

This chapter describes the details of the dielectron and direct-photon analysis. The analysis begins with the event selection (Sec. 4.1), the primary track selection (Sec. 4.4), and the electron identification (Sec. 4.5), followed by the pair analysis (Sec. 4.6). Obtained raw dielectron spectra are corrected for the pair reconstruction efficiency using the MC simulation (Sec. 4.7). In Sec. 4.8, dielectron yield from known hadronic decays is estimated using MC simulation to compare the corrected dielectron signal. Obtained dielectron cross section as a function of invariant mass m_{ee} and pair transverse momentum $p_{\mathrm{T,ee}}$ are reported in Sec. 4.11. Afterward, the direct photon fraction is extracted from the invariant mass spectra and the direct photon spectrum is constructed by using the decay photon spectrum as described in Sec. 4.12.

4.1 Datasets and Event Selection

The data used for the analysis were collected in 2016–2018 during LHC proton-proton run at $\sqrt{s} = 13$ TeV with a nominal magnetic field of $B = 0.5$ T in the ALICE central barrel. Figure 4.1, 4.2 and 4.3, show interaction rate, number of colliding bunches (μ) at LHC point 2 (IP2), and average number of inelastic collisions per bunch crossing as a function of time (run number) with respective data-taking year. A run is the time from the start to the end of the data acquisition. Vertical dashed lines indicate a change of polarity, and a duration to have the same polarity settings of the magnet is called "period". The experimental data consists of a chunk of periods. The interaction rate in pp collisions steadily increases every year, from 120 kHz to 260 kHz. The average number of interactions per bunch crossing (μ) varies from 0.01 to 0.06.

4.1.1 Event Classification

The events are characterized by charged-particle multiplicity and classified based on the correlation between a total charge in the V0 detectors (V0M amplitude) and the total number of charged-particle multiplicity at mid-rapidity. The reason why we use V0M amplitude which is determined at forward (backward) rapidity is to avoid

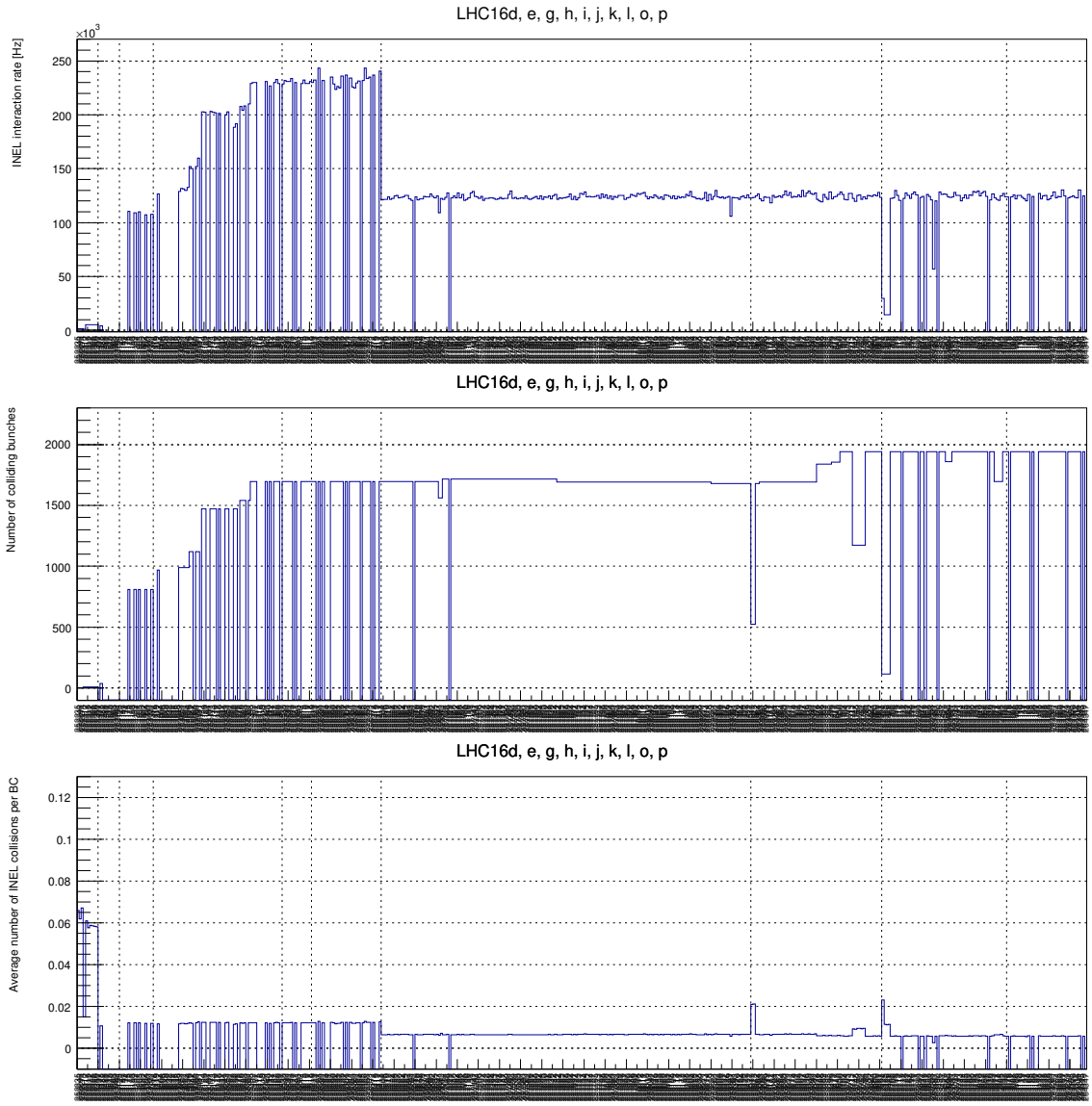

Figure 4.1: Interaction rate (top), number of colliding bunches at LHC point 2 (middle), and average number of inelastic collisions per bunch crossing (bottom). Period LHC16d, e, g, h, i, j, k, l, o, p (separated by dashed line) are shown. Information is taken from aliqaevs and if the run has no information, values are set -999.

auto-correlation bias [130, 131]. Figure 4.4 shows the correlation between minimum-bias and high-multiplicity triggered events. The charged-particle multiplicity linearly scales with V0 amplitude for both event classes. The V0 amplitude is divided into multiplicity classes and expressed in percentile (V0M percentile) with respect to whole V0M amplitude, where low values indicate collisions with larger multiplicity.

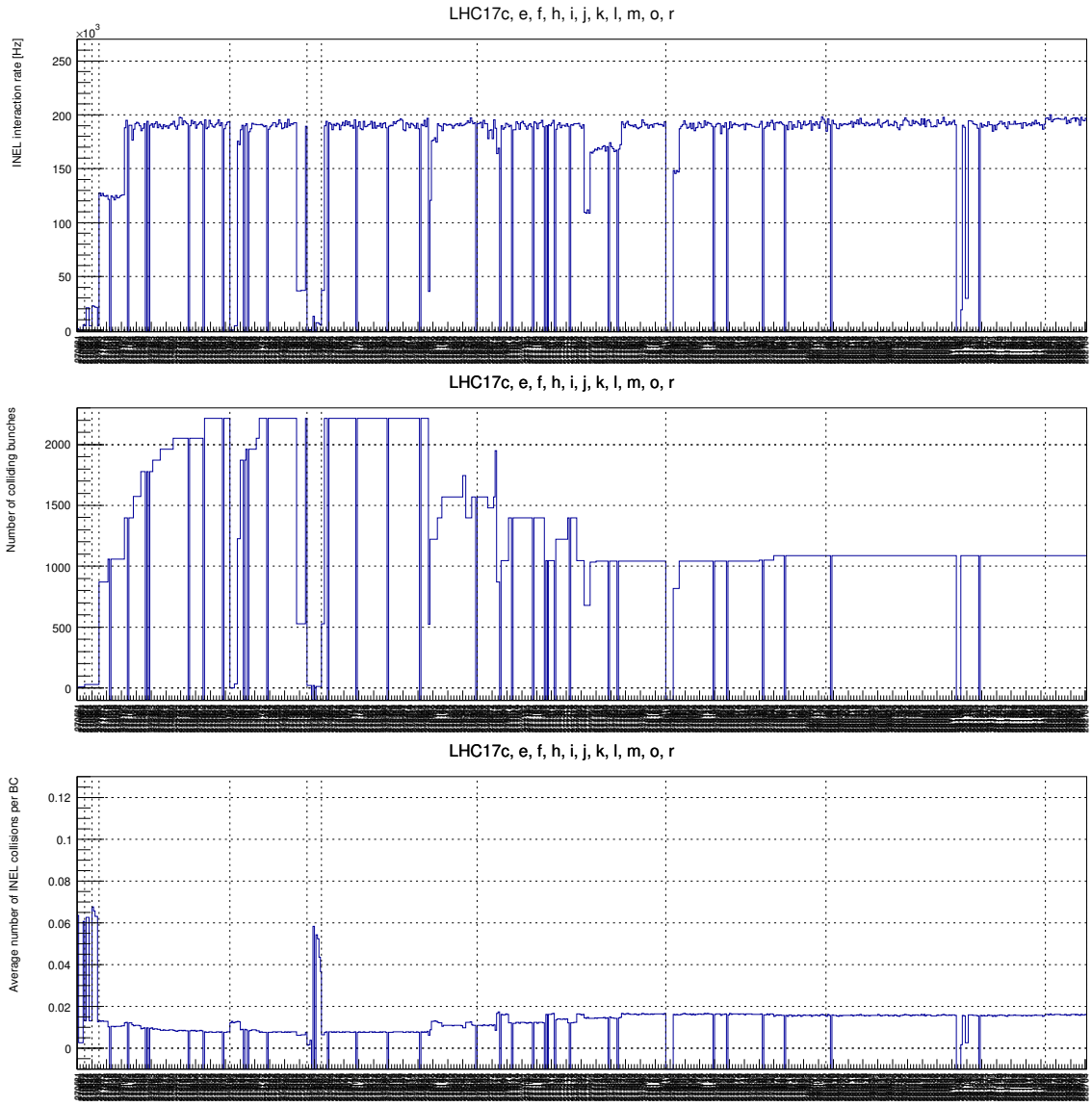

Figure 4.2: Interaction rate (top), number of colliding bunches at LHC point 2 (middle), and average number of inelastic collisions per bunch crossing (bottom). Period LHC17c, e, f, h, i, j, k, l, m, o, r (separated by dashed line) are shown. Information is taken from aliqaevs and if the run has no information, values are set -999.

4.1.2 Trigger Conditions

The data sample is selected by using minimum-bias (MB) trigger and high-multiplicity (HM) triggers for the analysis of inelastic and high-multiplicity pp events. Both triggers require a coincident signal in both V0A and V0C scintillators.

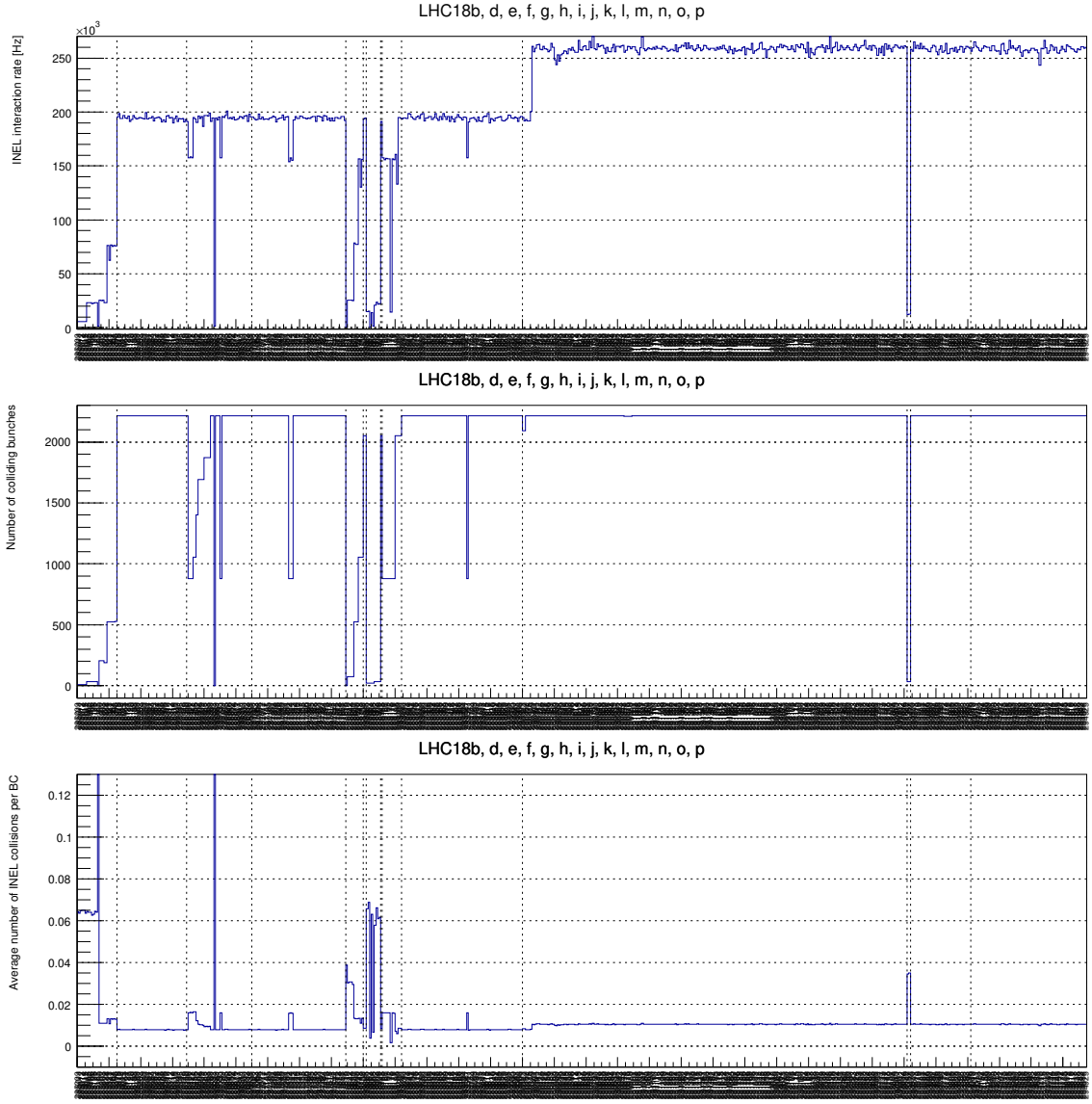

Figure 4.3: Interaction rate (top), number of colliding bunches at LHC point 2 (middle), and average number of inelastic collisions per bunch crossing (bottom). Period LHC18b, d, e, f, g, h, i, j, k, l, m, n, o, p (separated by dashed line) are shown. Information is taken from aliqaevs and if the run has no information, values are set -999.

4.1.3 High-Multiplicity Trigger Selection

The HM trigger is used to enhance the sample of events with high multiplicities, which additionally requires V0M amplitude to exceed a certain threshold. Since V0 photomultipliers show a continuous aging effect, the HM trigger threshold needs to be adjusted several times during data taking to keep the trigger selection factor constant as shown

in the top of Fig. 4.5. As a result of these adjustments, the HM trigger threshold over mean V0 multiplicity is almost flat and kept ~ 5 for the 2016 sample as shown in the bottom of Fig. 4.5. The 2017 and 2018 samples are also adjusted as well. The stability of high-multiplicity trigger can be checked by the actual triggered event. Figure 4.6 shows the run-by-run trend of ratio HM over MB triggered event for 2016-2018 samples. Overall, most of the run the HM/MB ratio is constant and stable during data taking. However, the HM/MB ratios from runs shaded in blue show significantly lower compared to other runs. This is due to the adjustments of the downscaling factor of the trigger, which usually occurs at the beginning of the year or period. Such runs are removed from the analysis because the trigger performance is not stable.

With runs that guaranteed the stability of the triggers, we select the 0.1% of events with the highest V0M amplitude as shown in the left of Fig. 4.7. The corresponding percentile distribution is shown on the right of Fig. 4.7 and found to be flat. For the 2016 sample, as the V0 multiplicity percentile is non-flat, the sample is not used in this analysis.

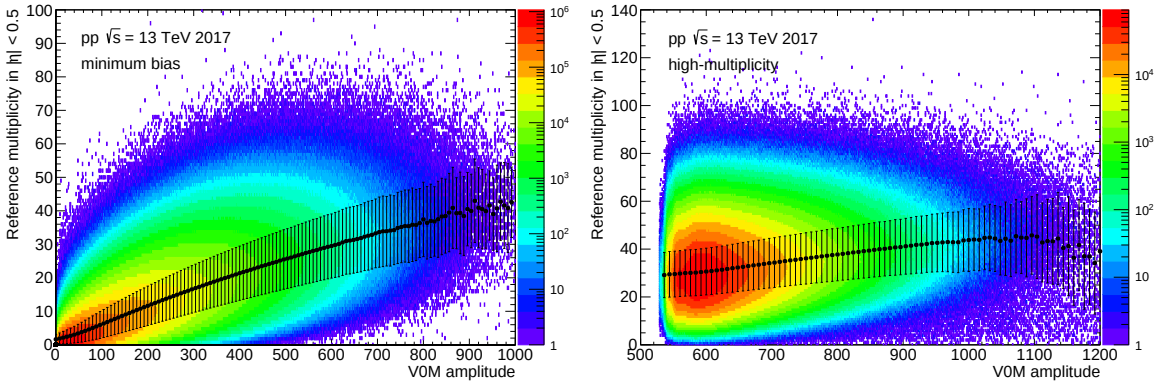

Figure 4.4: Correlation between V0M amplitude and reference multiplicity at mid-rapidity in minimum-bias (left) and high-multiplicity (right) events. Black points show mean values of reference multiplicity for each V0M amplitude value, and the error bars correspond to the RMS of the distribution.

4.1.4 Event Selection

Physical collision events are selected as follows.

Machine Induced Background Rejection

Background events such as beam-gas interactions are rejected by using information from the V0 detectors placed at forward and backward rapidities [105]. The arrival time of the V0 signal is exploited to discriminate collision events from background events caused by the LHC Beam 1 or Beam 2. Fig. 4.8, shows the correlation between

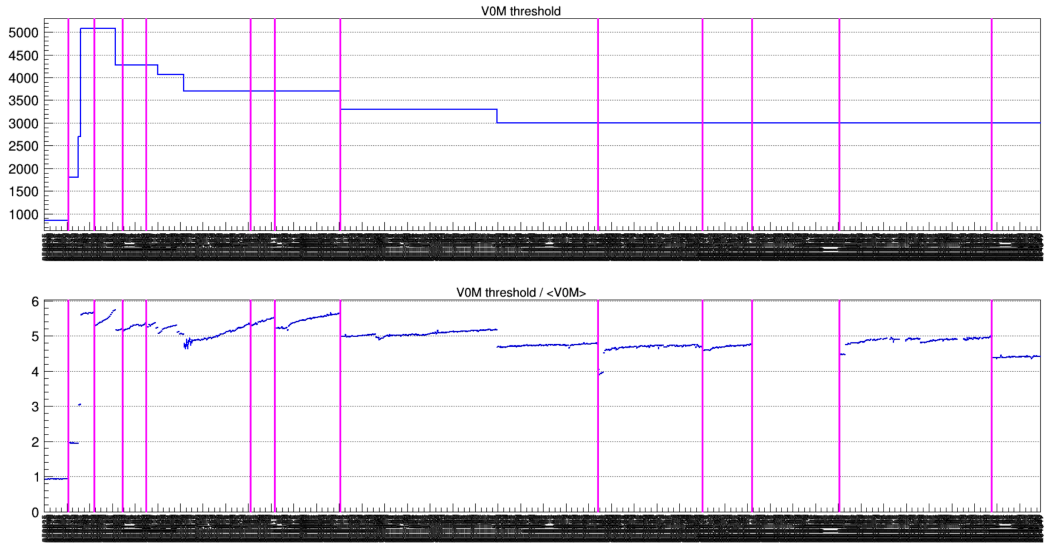

Figure 4.5: Example of V0 high-multiplicity trigger threshold (top) and the ratio V0 high-multiplicity threshold over mean V0 multiplicity (bottom) as a function of run number during 2016 pp data taking. All 2016 data are shown including some periods which are not used for the analysis. Figure was taken from [132].

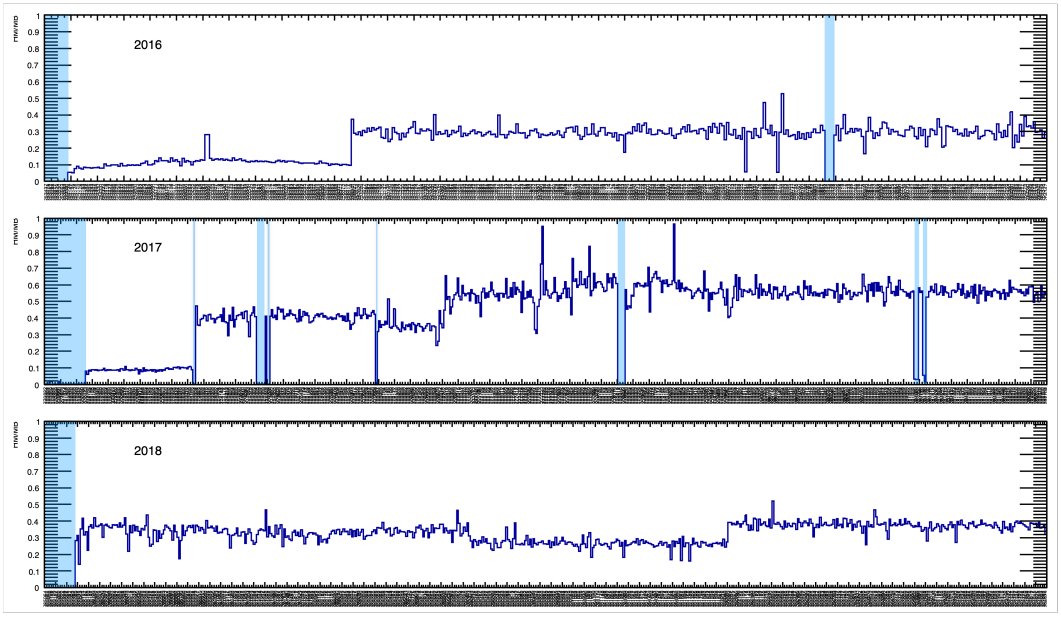

Figure 4.6: Number of event ratio, HM over MB vs run for respective data taking year. From top to bottom 2016 (not used in HM analysis), 2017, and 2018 datasets are shown.

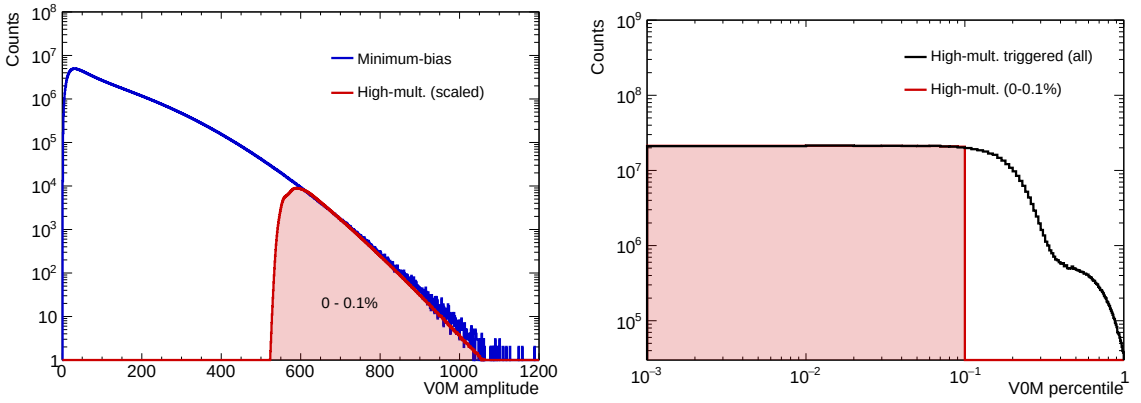

Figure 4.7: Left: V0M amplitude distributions in minimum-bias (red) and high-multiplicity events (blue). The red shaded area represents 0-0.1% of V0M multiplicity class in pp collisions at $\sqrt{s}$ = 13 TeV. Right: V0M percentile distribution in high-multiplicity events (0-0.1% is selected).

the sum $t_{\mathrm{V0A}} + t_{\mathrm{V0C}}$ and difference $t_{\mathrm{V0A}} - t_{\mathrm{V0C}}$, where t_{V0A} and t_{V0C} are arrival time measured by the two V0 detectors. The main peak from beam-beam collision in the nominal interaction point is $t_{\mathrm{V0A}} - t_{\mathrm{V0C}} = 8.3$ ns, which is well separated from the Beam 1-induced and Beam 2-induced background interactions at $t_{\mathrm{V0A}} - t_{\mathrm{V0C}}$ = -14.3 ns and $t_{\mathrm{V0A}} - t_{\mathrm{V0C}} = 14.3$ ns, respectively. These background events can be rejected using the V0 time gate in the trigger. Residual backgrounds can be further removed using the number of SPD clusters which will be described in the following. Since background particles usually cross the pixel layers in a direction parallel to the beam axis, they tend to leave a larger number of hits on SPD layers and give a smaller number of SPD tracklets pointing to the vertex. As a result, background particles appear as outliers for the main diagonal correlation from physical events. Figure 4.9 shows the correlation in all triggered events (left) and after applying rejection of beam-gas event via online trigger selection (right). All events above the red line are removed to reject residual beam-gas and pile-up events in minimum-bias (top row) and high-multiplicity (bottom row) events, respectively.

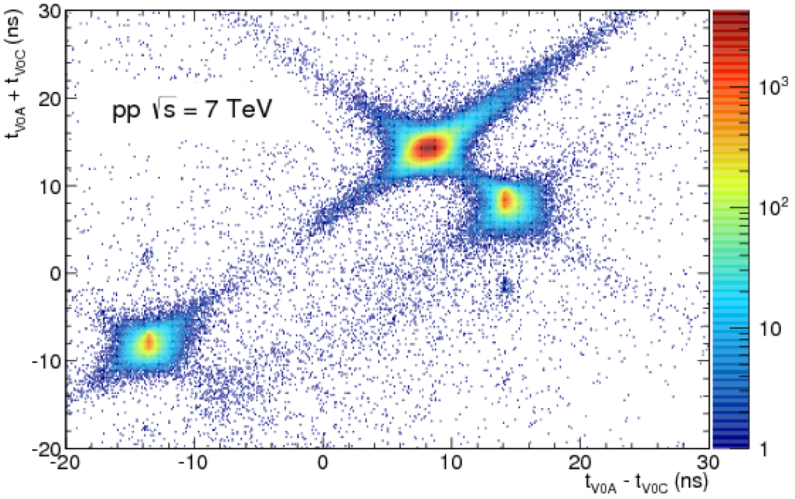

Figure 4.8: Correlation between the sum and difference of signal times in V0A and V0C detectors. Three classes of event beam–beam interactions at (8.3 ns, 14.3 ns), background from beam 1 at (-14.3 ns, -8.3 ns), and background from beam 2 at (14.3 ns, 8.3 ns) can be clearly distinguished. Figure taken from Ref. [105].

Pileup Rejection

Due to the high interaction rate and the high μ value, additional pp collisions (pileup) can be recorded within TPC readout time ($\sim$ 100 μsec). The pileup collision has two different distinctive natures: "In-bunch pileup", where two (or more) collisions occur in the same-bunch crossing, and "Out-of-bunch pileup", where two (or more) collisions occur before and after the collision of interest. These should be removed as they affect the number of reconstructed tracks per event. The in-bunch pileup can be rejected if multiple candidates of interaction vertices are reconstructed. The event from the out-of-bunch pileup event can be removed either at the event selection level as same as the in-bunch pileup or at the track selection level, i.e., requiring matching to fast detectors: ITS or TOF, or pointing to the main vertex via DCA_z.

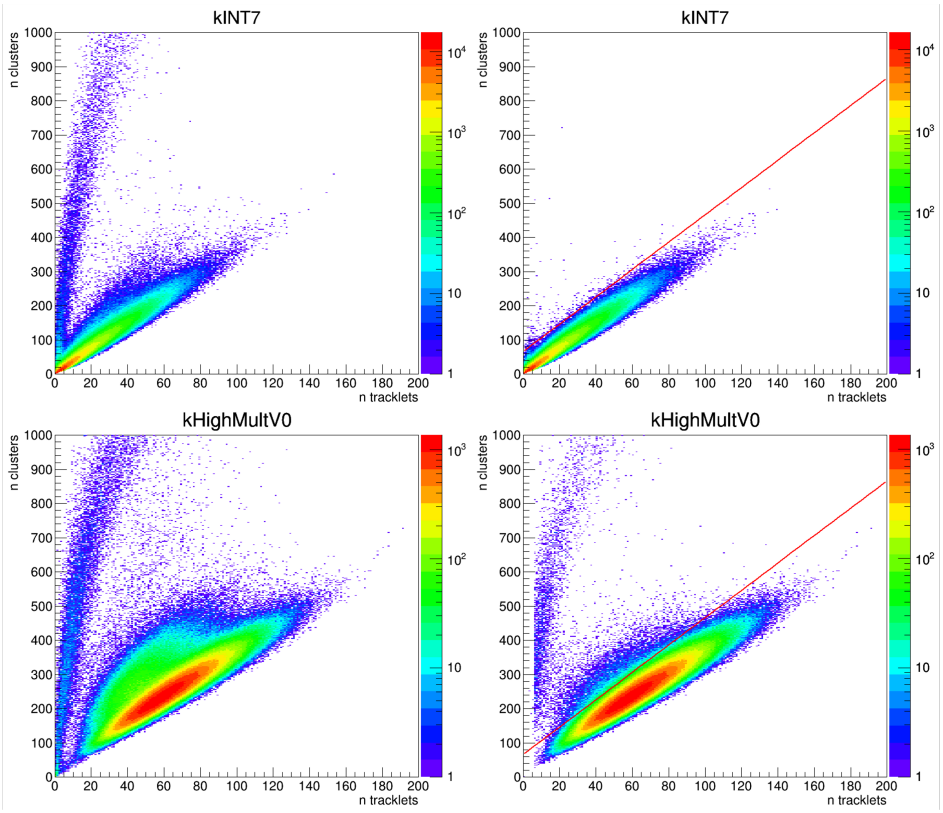

Figure 4.9: Correlation between the number of SPD tracklets and the number of SPD clusters in all triggered events (left) and events after the clean-up by the online trigger based on the V0 time gate [133]. The top and bottom rows show minimum-bias and high-multiplicity triggered events. The red line indicates the cut based on the SPD clusters and the tracklets correlation.

In addition, the vertex position is restricted with $|z_{\mathrm{vtx}}| < 10$ cm along the beam axis (Fig.4.10), and the event is required to have at least one contributing track to

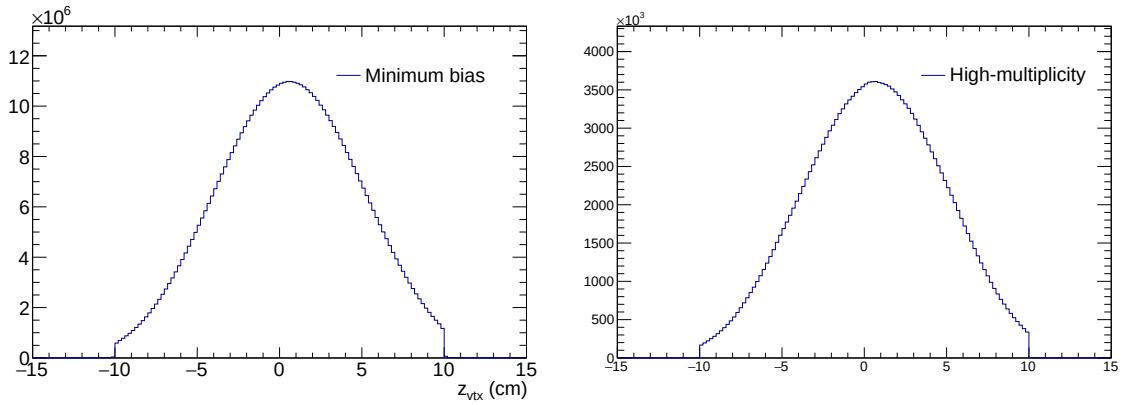

Figure 4.10: Z vertex distribution in minimum-bias events (left) and high-multiplicity events (right).

the vertex. After these event selections, in total 1.73×10^9 minimum-bias and 3.38×10^8 high-multiplicity pp events are selected for the analysis. The breakdown by year is shown in Table 4.1.

Table 4.1: The number of events after physics selection and event selection criteria in minimum-bias and high-multiplicity triggered events.

Year	Min.bias	High-multiplicity
2016	415×10^6	-
2017	604×10^6	195×10^6
2018	710×10^6	143×10^6
Total	1730×10^6	338×10^6

Integrated Luminosity

The trigger condition described in Sec. 4.1.2 is denoted "V0AND", i.e., trigger fulfills V0A *and* V0C condition. The integrated luminosity of the analyzed minimum-bias data sample is calculated as:

$$\mathcal{L}_{\rm int}^{\rm MB} = \frac{N_{\rm V0AND}}{\sigma_{\rm V0AND}^{pp}}, \tag{4.1}$$

where $N_{\rm V0AND}$ is the number of analyzed "V0AND" events, $\sigma_{\rm V0AND}^{pp}$ is visible cross section[1] observed under "V0AND" trigger condition, which is measured in a van der Meer (vdM) scan [134]. The $N_{\rm V0AND}$ is calculated as the number of minimum-bias events after passing the event selection criteria mentioned above ($N_{\rm evt} = 1.73{\times}10^9$), corrected for the vertex reconstruction efficiency $\epsilon_{\rm evt}^{\rm vtx}$:

$$N_{\rm V0AND} = N_{\rm evt}/\epsilon_{\rm evt}^{\rm vtx}. \tag{4.2}$$

While the efficiency to reconstruct the collision vertex is basically 100% when two electrons are present in the event, this is not the case for overall V0AND-triggered events. The study was performed in the previous study and found to be $\epsilon_{\rm evt}^{\rm vtx} = 97.0 \pm 0.5\%$ [132]. The vdM scan was performed every data-taking year [135] and the following values are obtained:

$$\sigma_{\rm V0AND}^{2016} = 58.44 \pm 1.9\,{\rm mb} \tag{4.3}$$
$$\sigma_{\rm V0AND}^{2017} = 58.10 \pm 2.7\,{\rm mb} \tag{4.4}$$
$$\sigma_{\rm V0AND}^{2018} = 57.52 \pm 2.1\,{\rm mb} \tag{4.5}$$

The integrated luminosities are calculated for each year, and total integrated luminosity was $\mathcal{L}_{\rm int}^{\rm MB} = 30.7 \pm 0.7\ {\rm nb}^{-1}$. For the high-multiplicity triggered events ($N_{\rm evt} = 3.38{\times}10^8$), the vertex reconstruction efficiency is 100% with negligible uncertainties. Offline information from the V0 detector is used to select 0.1% of $\sigma_{\rm V0AND}^{pp}$ cross section, which result in an integrated luminosity of $\mathcal{L}_{\rm int}^{\rm HM} = 5.8 \pm 0.2\ {\rm pb}^{-1}$. The source of global uncertainty is thought to have originated from luminosity uncertainty, namely trigger inefficiency. This inefficiency is estimated by independent π^0 analysis, which gives 2%, but does not enter the dielctron or direct-photon cross section. The high-multiplicity trigger, efficiency is high enough so that uncertainty is not assigned.

4.2 Monte Carlo Simulation

In order to understand the detector response of the electrons and calculation of electron reconstruction efficiency, Monte Carlo (MC) simulated data are used. The MC data is produced on a run-by-run basis, to reproduce the same detector configuration extracted from the Offline Conditions DataBase (OCDB). The OCDB stores all detailed

[1] Visible cross section is given by $\sigma_{\rm vis} = \epsilon \cdot \sigma_{\rm INEL}$, where ϵ is detector efficiency.

information of detectors, i.e., geometry, calibration, and specific aspects such as active ITS areas, dead pixels, voltage settings, noisy channels, etc. Proton-proton events are generated with PYTHIA event generator with "Monash 2013" tune [55, 136]. The PYTHIA program is widely used for the generation of high-energy-physics 'events', i.e., sets of particles produced in high-energy collisions. It contains theory and models for a number of physics aspects, including hard and soft interactions, parton distributions, initial- and final-state parton showers, multiparton interactions (MPI), fragmentation, and decay. The generated particles are propagated through the ALICE detector using GEANT3 package [137], which provides particle energy loss and deposition given detector geometry and material properties.

4.3 Quality Assurance

A basic quality assurance (QA) of track matching and calibration is performed for all detectors by the ALICE Quality Assurance group in a centralized way. The results of checks are recorded in the Run Condition Table (RCT) together with quality flags which indicates run is usable or not. Based on the RCT, only runs flagged as good for ITS, TPC, TRD, TOF, and V0 are selected. Since the scope of centralized QA is rather global, even if the RCT flag is good, depending on the analysis, one needs to check specific observables if they do not show significant deviation with respect to the real data.

For the analysis-specific QA, the total number of electron and positron candidates (electrons) per event is checked run-by-run, to see the stability of the dataset. To this purpose, the electron candidates are selected by applying loose PID cuts. According to the trending plot, the mean and RMS of all entries are determined. A run is excluded if its point is out of 3σ. Figure 4.11 shows a trend of electrons per event in minimum-bias events for different years. The blue solid line and the dashed lines indicate mean and RMS, respectively. All runs are accepted in this QA. In addition, trends in minimum-bias events are compared with MC-simulated data to see if the MC reproduces the trend of the experimental data. Figure 4.12, shows the ratio of the trend of electron candidates between the data and the MC in minimum-bias events. Since the absolute value of each run is slightly different between the data and the MC, the ratio is not necessarily consistent with unity. However, overall, the trend is flat and stable from 2016 to 2018 data samples.

A similar check has been done in high-multiplicity triggered events (Fig. 4.13) and the same run selection criterium is applied. As for the high-multiplicity events, dedicated MC simulations do not exist. Therefore we employed the same MC simulation as minimum-bias event analysis. By choosing exactly the same run numbers as high-multiplicity samples, we make a ratio between minimum-bias and high-multiplicity events, of each normalized to the same MC simulation. As shown in Fig. 4.14, the trend of double ratio are found to be quite stable.

More detailed QA was performed to see if the basic variables of the dielectron

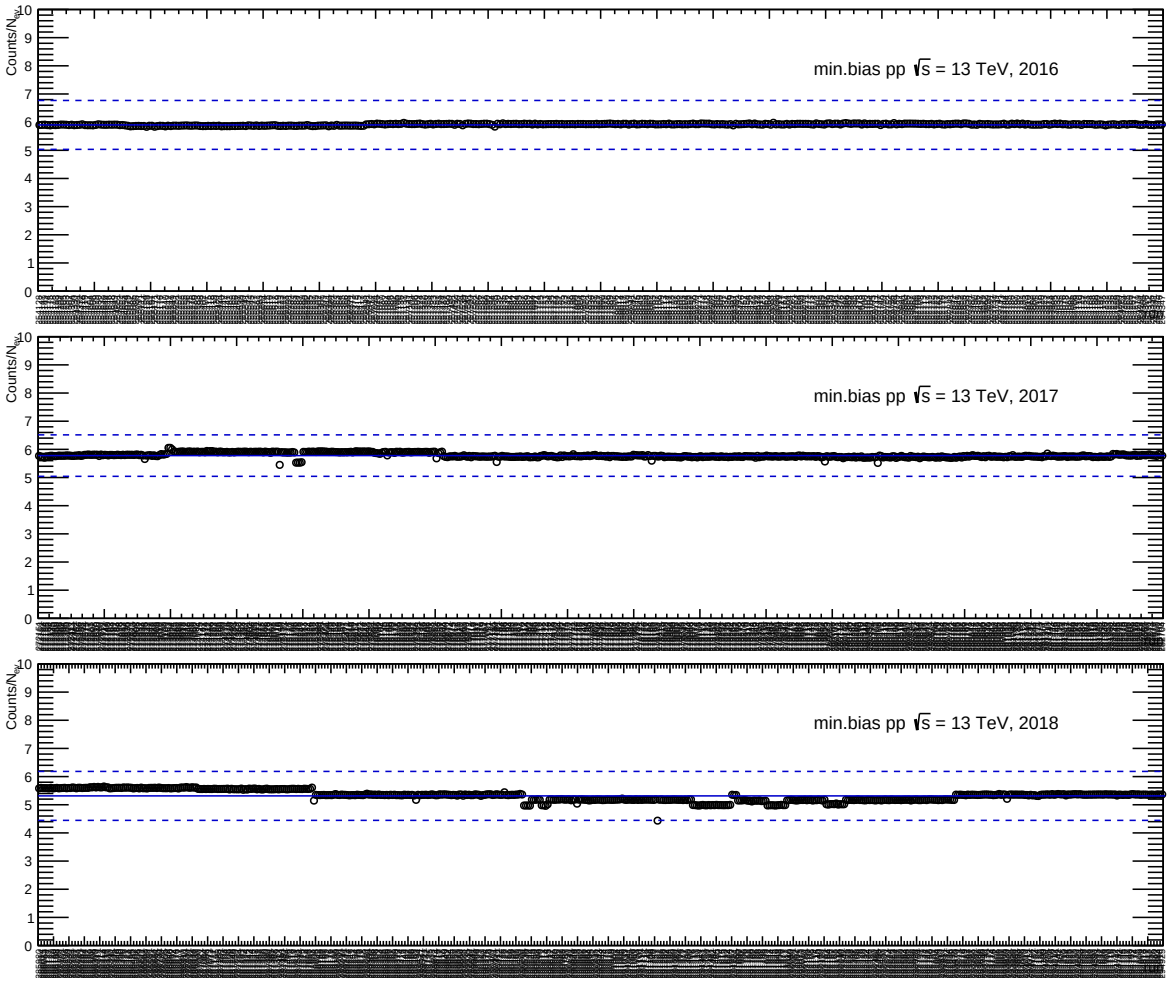

Figure 4.11: Number of sum of electron and positron candidates per event as a function of time (run numbers) in minimum bias events. The blue dashed lines stands for 3σ away from the mean value of the number of candidates. All runs are accepted in this QA.

analysis were properly reproduced in experimental data and MC simulation. We compared the distributions such as the position of z-vertex, charged-particle multiplicity, track variables such as the number of clusters in the TPC and the ITS, η, ϕ and p_{T} distribution and so on. All these results are in good agreement between the and the MC.

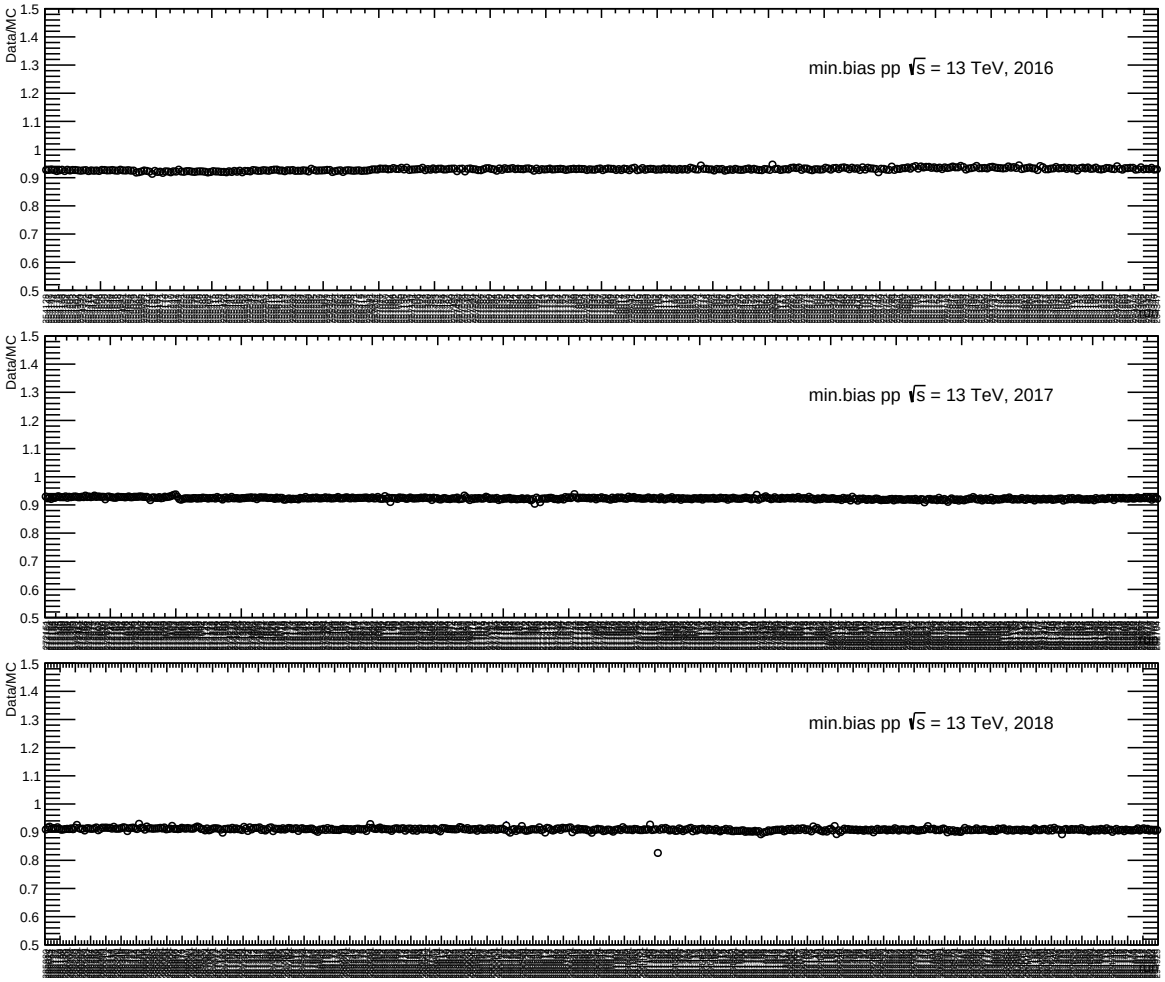

Figure 4.12: Ratio between the data and the MC simulation of the trend of the number of electron candidates in minimum bias events.

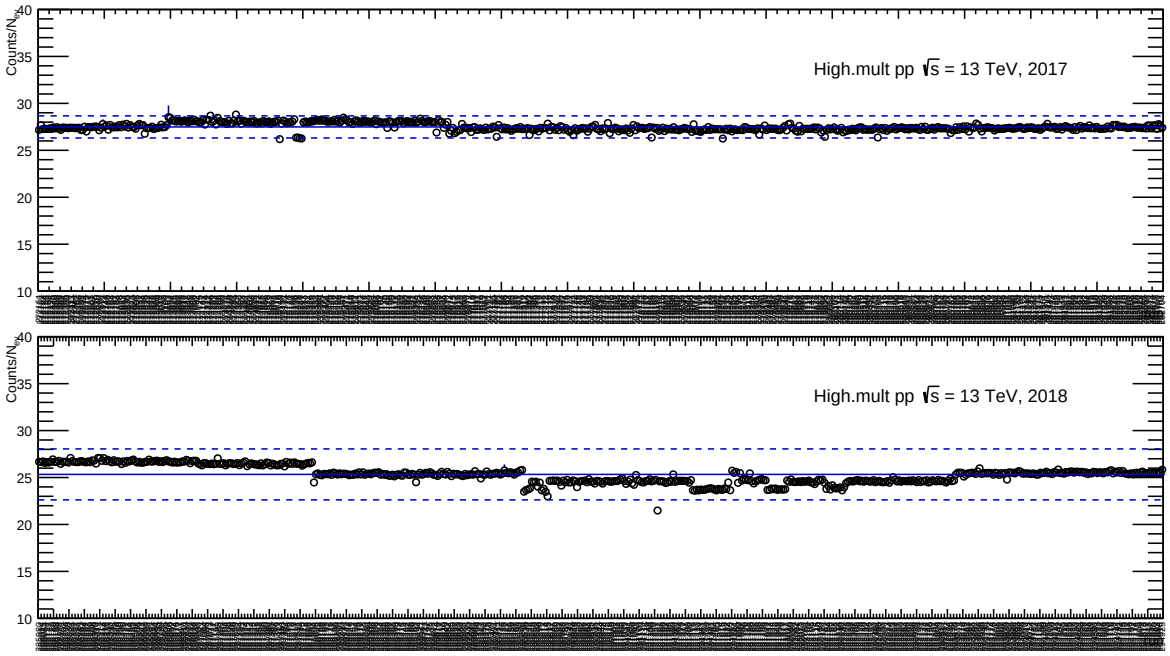

Figure 4.13: Number of sum of electron and positron candidates per event as a function of time (run numbers) in high-multiplicity events. The blue dashed lines stands for 3σ away from the mean value of the number of candidates. Only a run from 2018 was excluded.

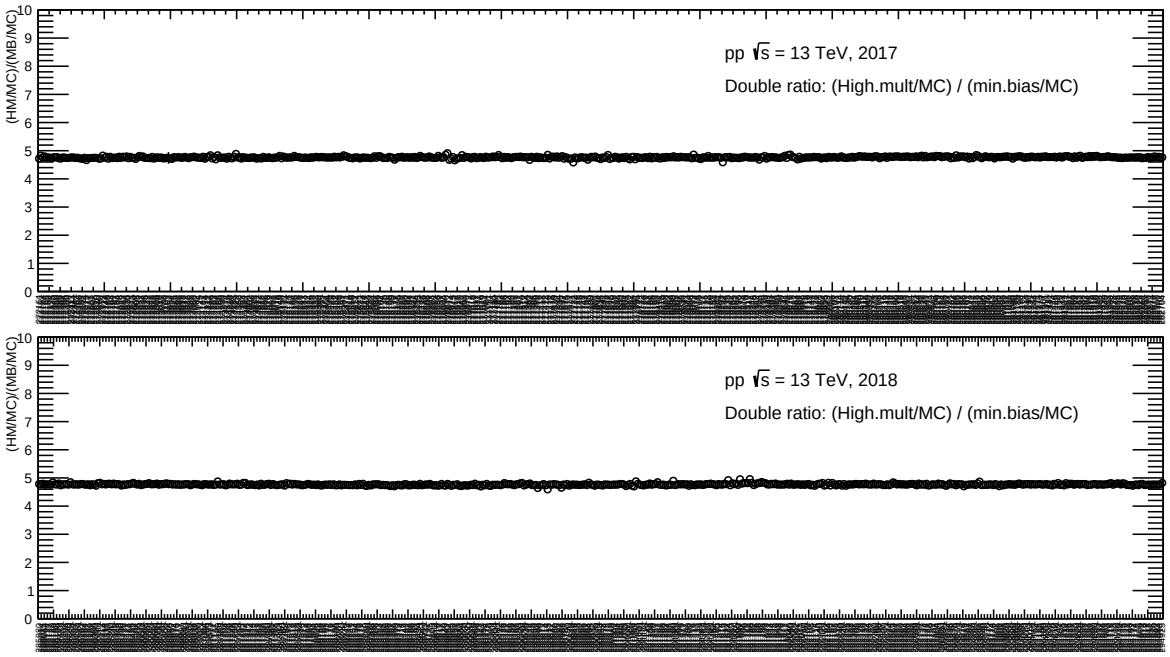

Figure 4.14: Ratio of high-multiplicity over minimum-bias triggered events of the number of electron candidates. Each dataset is normalised to the same MC simulation.

4.4 Primary Track Selection

The main requirement of the track selection is to select well-reconstructed tracks that originated from the primary interaction vertex and to eliminate secondary tracks from real photon conversions and weak decays of strange hadrons. Several TPC track properties defined in Ref. [138] are used to ensure the track quality. Table 4.2 summarises the track selection criteria that have been applied in this analysis. Below, the main variables used in this analysis are listed with a short description and selection criteria.

Table 4.2: Primary track selection for the analysis. The selection criteria are common for MB- and HM-triggered data analysis.

Track Variable	Requirement
Number of TPC clusters	≥ 80
Number of TPC crossed rows	$\geq$100
Ratio of TPC crossed rows / findable clusters	> 0.8
χ^2 per TPC cluster	< 4
TPC refit	required
Number of ITS clusters	≥ 3
χ^2 per ITS cluster	< 4.5
ITS refit	required
p_{T}	> 0.2 GeV/c
$\lvert\eta\rvert$	< 0.8
Hit in the first SPD layer	required
Allowed number of shared ITS clusters	0
Reject kink daughters	required
DCA$_{xy}$	< 1.0 cm
DCA$_z$	< 3.0 cm
Cut on DCA$_{xy}$ and DCA$_z$ independently	yes

A charged particle passes through the TPC, it induces a signal on a given pad-row. If a charge in a search window of 5 pads in the wire direction and 5 bins in the time direction, exceeds a certain threshold and fulfills certain quality criteria, it is called "cluster". The maximum number of clusters per track is set to 159, corresponding to the number of pad rows in a specific TPC sector. All reconstructed tracks need to have at least 80 clusters in the TPC. A p_{T}-resolution relevant quantity of a track is the effectively sampled track length of a particle in the TPC. The number of effective TPC clusters is called the number of crossed rows, which is roughly proportional to the track length. The minimum number of crossed rows equal to 100 is required for

all reconstructed tracks. The number of findable clusters is defined as the number of geometrically possible clusters that can be assigned to a track. Dead zones due to chamber boundaries or the limited η-acceptance are taken into account. A minimum ratio of crossed rows over findable clusters of 80% is required. Track reconstruction in the TPC gives χ^2 per cluster for the quality of the fitting procedure. A maximum number of χ^2 per cluster equal to 4 is required.

Similar quality cuts are applied to the ITS. A maximum of six layers of hits (number of clusters) are assigned per track, and at least 3 clusters are required. As well as the TPC, the quality of the ITS track can be controlled by the χ^2 per cluster, which is required to a maximum of 4.5. In addition, a successful refit is required by the Kalman filter, which is applied for both TPC and ITS tracks.

Afterward, charged particle tracks with $|\eta| < 0.8$ and a minimum transverse momentum $p_{\mathrm{T}} > 0.2$ GeV/c are selected. In this kinematic range, reconstruction efficiency is reasonably high and far from acceptance edge effects. Below $p_{\mathrm{T}} = 0.2$ GeV/c, particles are not well-defined as they are deflected by the magnetic field.

Tracks from real photon conversions in the detector material are rejected by imposing a hit on the first SPD layer. The cut can remove conversions from occurring in the detector material beyond this layer though there is some inefficiency due to the inactive area of the SPD as shown in Fig. 4.15. To suppress the remaining background from real photon conversion on a single-track basis, the ITS cluster of candidates is checked if each track shares clusters with others. If tracks with sharing clusters are found, they are likely to originate from a photon as they have a small opening angle. Such tracks can be removed from the requirement of no shared ITS clusters.

Additionally, tracks can be reconstructed by the weak decays of $K^{\pm} \to \mu^{\pm}\nu$. Such a particle is called "kink" and produces a neutral particle which cannot be directly reconstructed in the ITS and TPC, whereas a charged particle carries away some part of mother particle energy and is bent in the magnetic field in the same direction with a smaller radius. Tracks that exhibit such kink topology are rejected from the analysis as well. The contribution from secondary tracks is reduced by restricting the distance of the closest approach (DCA) to the primary vertex. The cut on DCA in the transverse plane and in the longitudinal direction, are applied $\mathrm{DCA_{xy}} < 1.0$ cm and $\mathrm{DCA_{z}} < 3.0$ cm, respectively. These cuts are optimized to keep dielectron pairs from the decays of semileptonic open charm and beauty mesons, which have decay lengths of the order of hundred micrometers ($c\tau \sim 150$ μm for D and $c\tau \sim 470$ μm for B mesons). The same track selection criteria are adopted for the analysis of minimum-bias and high-multiplicity data analysis.

4.5 Electron Identification

The identification of electrons is performed via specific energy loss $\mathrm{d}E/\mathrm{d}x$ in the TPC and information on the time-of-flight of the TOF detector. The detector PID response is expressed in terms of deviations between measured and expected values for a given

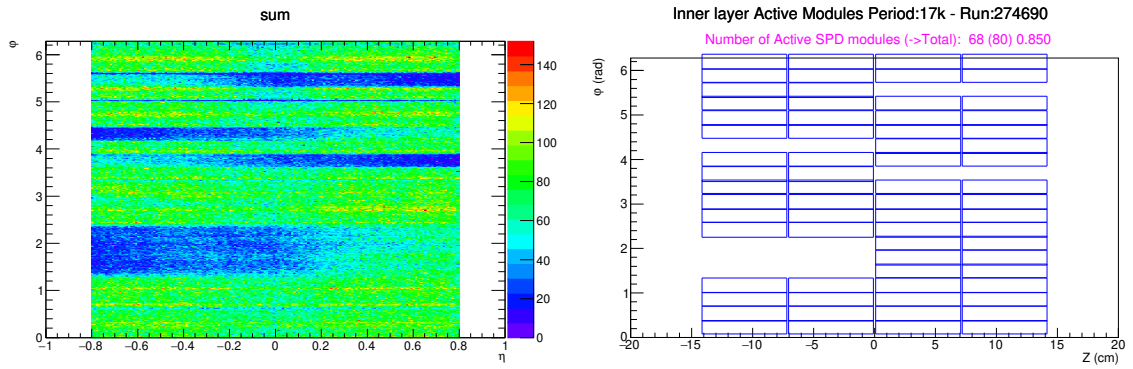

Figure 4.15: η - ϕ distribution of primary tracks in data (left) and corresponding active area of SPD 1st layer (right) taken from certain period of 2017 data.

species hypothesis and particle momentum, normalized by detector d$E/$dx resolution (σ). For example, the TPC PID information for the electron hypothesis is given in units of TPC nσ defined as follows:

$$n(\sigma_{\mathrm{e}}) = \frac{\langle d\mathrm{E}/dx\rangle^{\text{measured}} - \langle d\mathrm{E}/dx\rangle^{\text{expected for e}}}{\sigma_{\mathrm{e}}}, \tag{4.6}$$

where $\langle d\mathrm{E}/dx\rangle^{\text{expected for e}}$ denotes expected Bethe Bloch parametrization, called "spline", corrected for the low momentum effect. Applying cut on nσ band around 0 gives most likely electron candidates.

4.5.1 TPC and TOF Post-calibration

Due to the imperfectness of PID calibration of TPC and TOF detectors, nσ distribution for data shows some deviation and does not follow a single Gaussian in terms of $\mu \neq 0$, $\sigma \neq 1$. This is corrected manually by applying the recalibration procedure described below. First, the nσ distribution is projected in different momentum and pseudorapidity intervals and fitted with a single Gaussian. The initial fitting range is set to $\pm$ 5σ, and by using the obtained new mean and width, Gaussian fitting is repeated in $\pm$ 1.5σ-2σ around its mean. Figure 4.16 shows an example fit to nσ distribution. The width σ and the mean μ values are extracted for each momentum and η interval. Fig. 4.17 shows obtained two-dimensional correction maps for nσ_{TPC} created in data taking all periods in 2017. The correction maps were produced for every period and compared with each other. Since they were found to be similar for different periods, data samples are merged and a single map is produced year-by-year using all good runs. Correction of nσ_{e} is performed track-by-track according to following transformation:

$$\mathrm{n}\sigma_{\mathrm{e}} \rightarrow \frac{\mathrm{n}\sigma_{\mathrm{e}} - \mathrm{mean}}{\mathrm{width}}. \tag{4.7}$$

One can see that mean (width) is close to zero (unity) after the re-calibration (Fig. 4.18) It is worth to mention that in 2018 datasets the splines are only available for limited

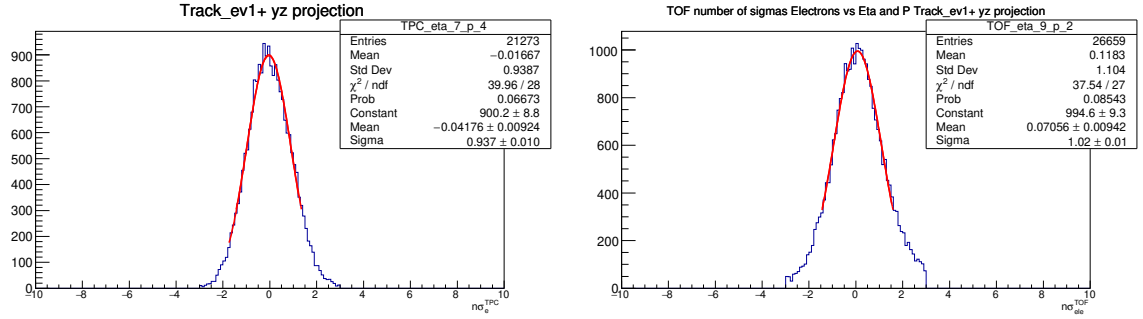

Figure 4.16: nσ distribution of TPC in the range $-0.3 < \eta < -0.2$ and $0.5 < p < 0.6$ GeV/c and TOF in the range $0.0 < \eta < 0.1$ and $0.5 < p < 0.6$ GeV/c fitted with a Gaussian.

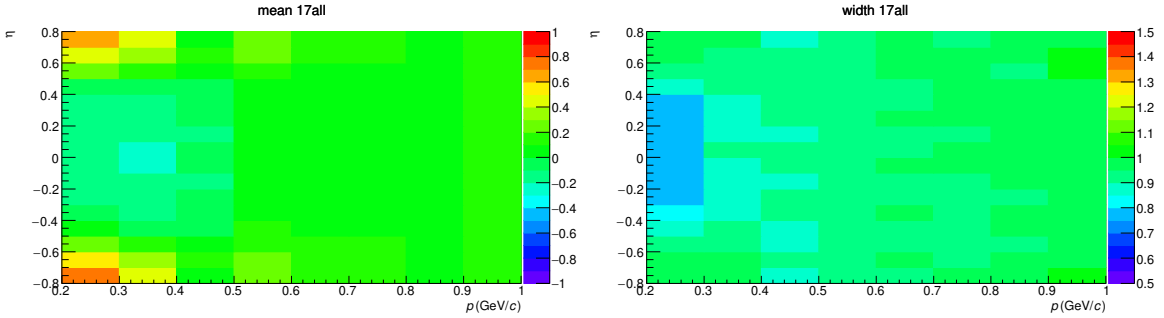

Figure 4.17: Mean of $n\sigma^{TPC}$ as a function of track momentum p versus pseudorapidity η from all 2017 periods.

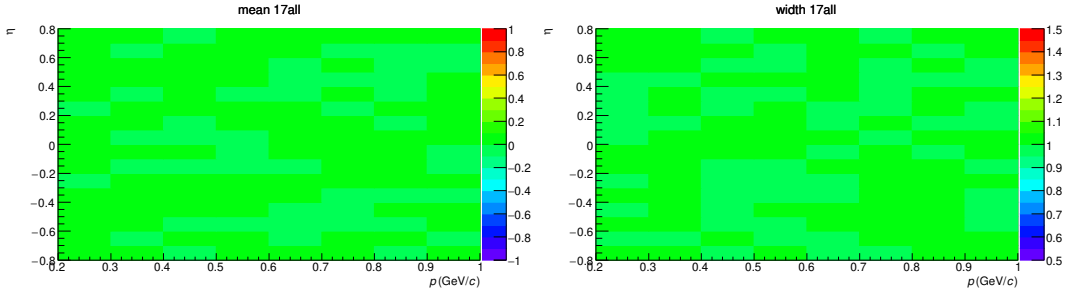

Figure 4.18: Mean (left) and width (right) of TPC nσ_e as a function of track momentum p and pseudorapidity η obtained using 2017 periods after re-calibration.

periods (Fig. 4.19 top), and the splines show a significant difference with respect to the rest periods (Fig. 4.19 bottom). Therefore, each was recalibrated separately. Similar procedure is performed for nσ TOF. All other period-wise correction maps are summarised in Appendix B. As they do not show significant differences, maps created in

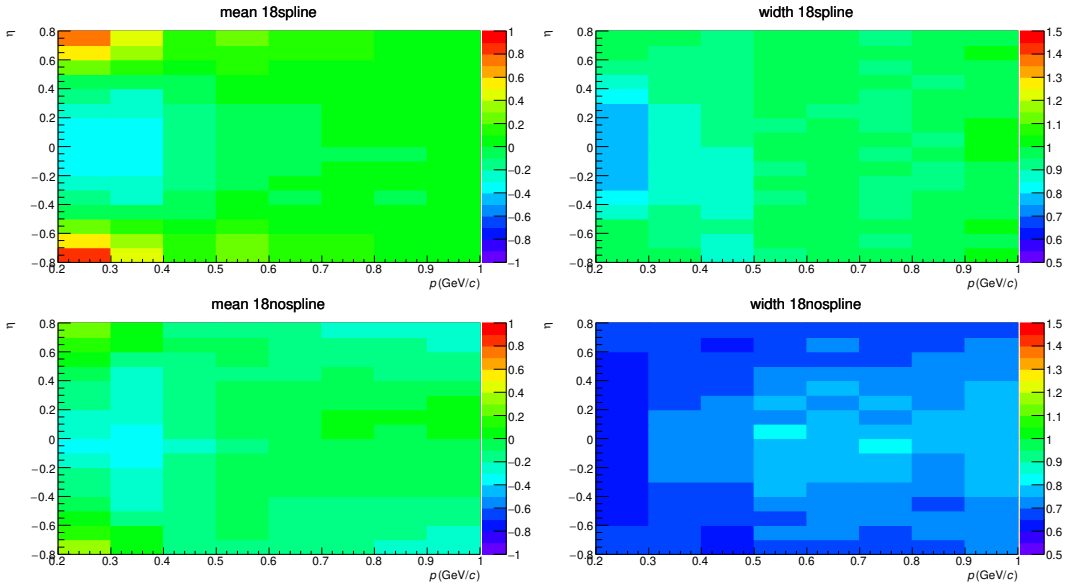

Figure 4.19: Mean (left) and width (right) of $n\sigma^{TPC}$ as a function of track momentum p versus pseudorapidity η obtained using a period from '18spline' (Top) and from '18 without spline' (Bottom).

MB-triggered events are adapted to the HM-triggered data analysis.

PID response in MC simulations is also studied. For the TPC, there is an option to make nσ distribution to follow a unit Gaussian, which is implemented in the ALICE analysis framework. Therefore, the re-calibration procedure is not applied to the MC simulated $n\sigma^{TPC}$. On the other hand, the mean and width of TOF nσ distribution show non-uniformity, it is corrected as well as real data.

4.5.2 Cut Settings of Electron Identification

Electron candidates need to be selected with cuts to minimize the fraction of hadrons in the electron samples while maintaining high electron identification efficiency. In principle, electrons can be identified using both TPC and TOF information. However, as the matching efficiency between the TPC and the TOF is low, the TPC standalone PID selection is also considered. This analysis adopted the PID strategy which was investigated in the previous study [132]. According to Ref. [132], electrons are chosen by combining two independent PID schemas. The first PID scheme is named "TPCTOFreq" which selects electrons based on both TPC and TOF signals, while the second scheme is named "TPCHadRej" which requires pure TPC-based hadron rejection. Both settings are summarised in Table 4.3 and two subsamples are combined with logical OR. Corresponding PID histograms can be found in Fig. 4.20.

Table 4.3: PID selection of electrons for the analysis. Electron candidate is accepted if either of the two PID requirements is fulfilled.

Cut setting	Detector	Particle	nσ cut	p range [GeV/c]
TPCTOFreq	TPC	electron (accept)	[-3, 3]	[0.2,∞]
	TPC	pion (reject)	[-∞, 4]	[0.2,∞]
	TOF	electron (accept)	[-3, 3]	[0.4,∞]
TPCHadRej	TPC	electron (accept)	[-3, 3]	[0.2,∞]
	TPC	pion (reject)	[-∞, 4]	[0.2,∞]
	TPC	Kaon (reject)	[-4, 4]	[0.2,∞]
	TPC	Proton (reject)	[-4, 4]	[0.2,∞]

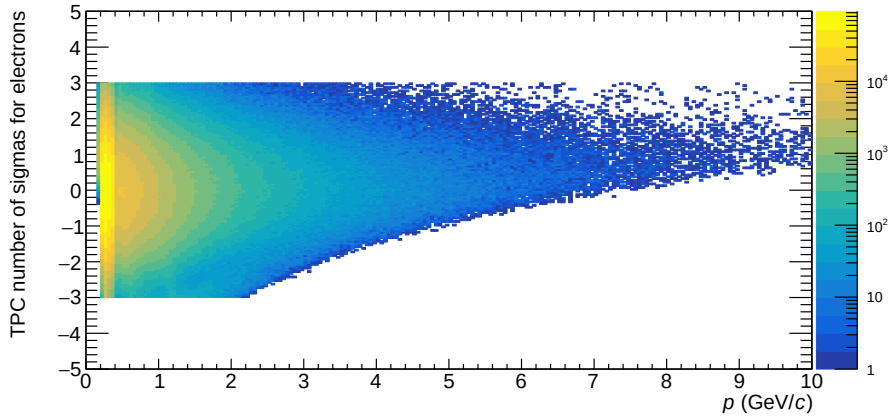

(a)

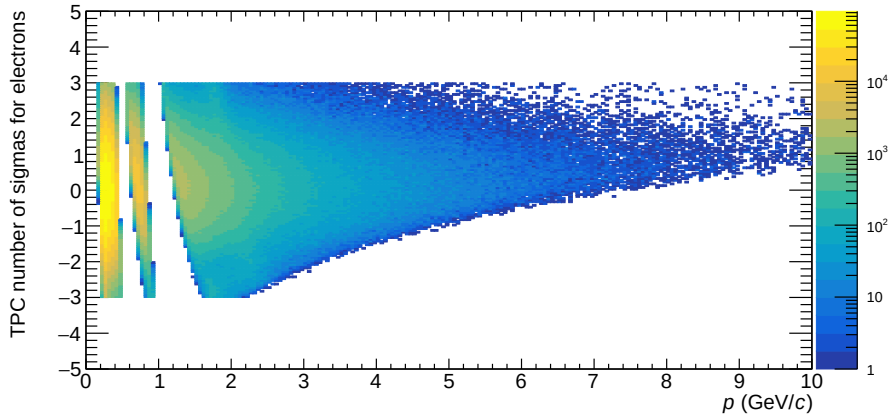

(b)

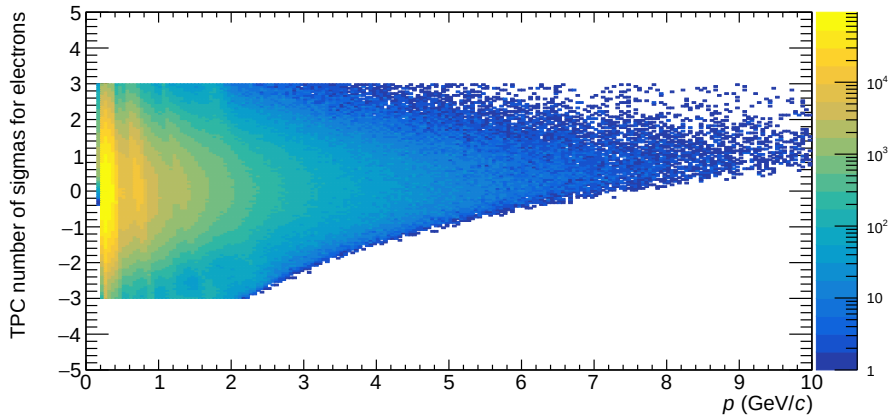

(c)

Figure 4.20: (From top to bottom) PID histograms for the respective cut setting: (a) "TPCTOFreq", (b)"TPCHadRej" and (c) combined sample, after the post calibration.

The PID performance such as electron purity as a function of transverse momentum was evaluated in a single track and pair level in Ref. [132]. The purity of a single track in the data was well reproduced by the MC. At the single track level, the purity was found to be 98% at 0.5 GeV/c and 94% at 1 GeV/c, which leads to negligible impact on pair analysis.

4.6 Pair Analysis

Electron and positron candidates in an event are combined into pairs. By using single track kinematic information, the invariant mass $m_{\rm ee}$ and transverse momentum $p_{\rm T,ee}$ of the pair are calculated as:

$$m_{\rm ee}^2 = (p_+ + p_-)^2 = (E_+ + E_-)^2 - (\vec{p}_+ + \vec{p}_-)^2, \tag{4.8}$$

$$p_{\rm T,ee}^2 = (\vec{p}_{x,+} + \vec{p}_{x,-})^2 + (\vec{p}_{y,+} + \vec{p}_{y,-})^2, \tag{4.9}$$

where $p_\pm$ is 4-momentum, $E_\pm$ is calculated as $E_\pm = \sqrt{\vec{p}_\pm^2 + m_e^2}$, $m_e = 511$ keV/c^2 and $\vec{p}$ denotes 3-momentum.

Electron pairs consist of correlated pairs from signals and uncorrelated combinatorial pairs. Former are defined as pairs originating from $\rm e^+e^-$ from a vector meson decays or semileptonic decay of $c\bar{c}$ and $b\bar{b}$. These are what we would like to measure, but in reality, the origin of electrons and positrons is unknown. Most of the unlike-sign pairs N_{+-} are dominated by a random combination of electrons and positrons. These pairs are uncorrelated and called combinatorial backgrounds. Besides, even if the pairs have the same mother, there are correlated backgrounds that come from real photon conversion in the detector material. To extract the signal, these backgrounds need to be subtracted. The combinatorial background B is subtracted and conversion backgrounds are further rejected by pair cuts. The background is estimated via the geometric mean of like-sign pairs $\sqrt{N_{++}N_{--}}$ within the same event:

$$B = 2\sqrt{N_{++}N_{--}}. \tag{4.10}$$

This background could contain correlated like-sign pairs such as $\pi^0 \to \rm e^+e^-\gamma \to e^+e^-e^+e^-$. B is corrected for the different detector acceptance of unlike-sign and like-sign pairs by the following factor:

$$R = \frac{N_{+-,\rm MIX}}{2\sqrt{N_{++,\rm MIX} \cdot N_{--,\rm MIX}}} \tag{4.11}$$

where, $N_{+-,\rm MIX}$, and $N_{\pm\pm,\rm MIX}$ denote unlike-sign pairs and like-sign pairs calculated with mixed event techniques, respectively. Thus, the physical signal is obtained as

$$S = N_{+-} - R \cdot B, \tag{4.12}$$

The invariant mass distribution of unlike-sign, like-sign and signal pairs in $0 < p_{\rm T,ee} < 6$ GeV/c for respective data-taking year and corresponding R-factor are shown below (Fig. 4.21 and 4.22).

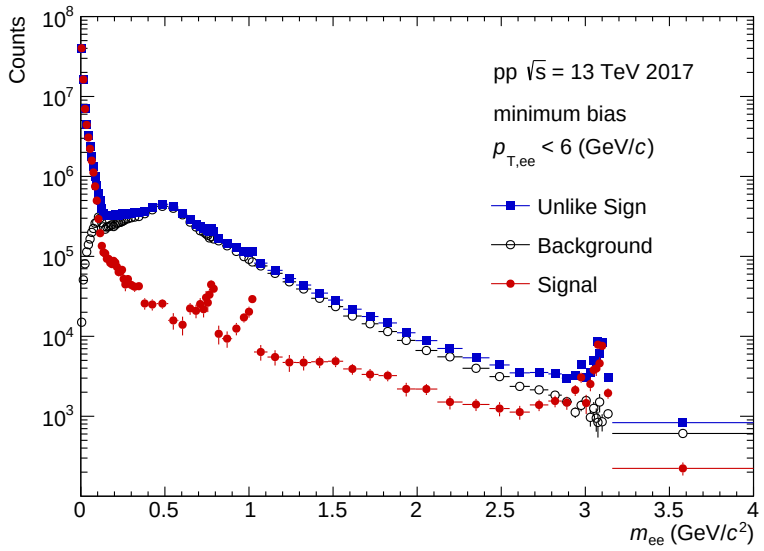

Figure 4.21: Dielectron invariant mass distribution of unlike-sign pairs (blue square), like-sign pairs with acceptance correction (black open circle), and signal pairs (red full circle).

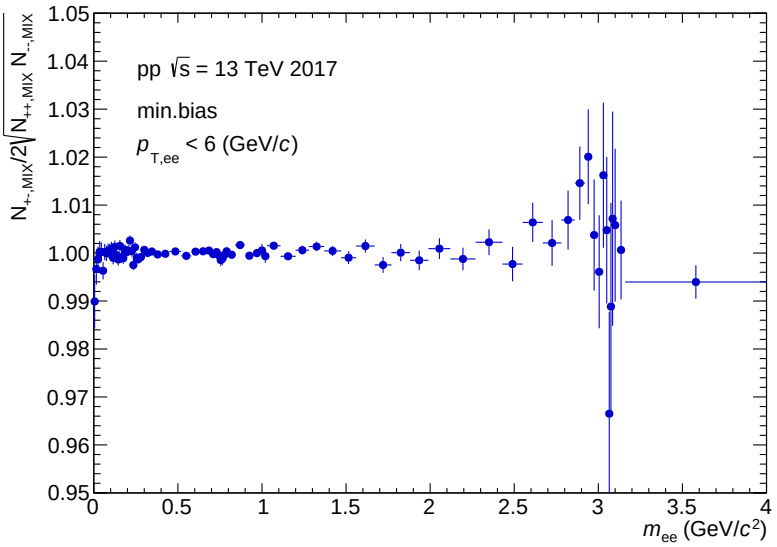

Figure 4.22: R-factor in the range $0 < p_{\mathrm{T,ee}} < 6$ GeV/c.

4.6.1 Conversion Rejection

As described in Sec. 4.4, e^+e^- pairs originating from real photon conversions are rejected at the single track level by requiring a hit on the first SPD layer and zero ITS shared cluster with other tracks. The latter requirement improves the signal-to-background ratio of dielectron pairs as shown in Fig. 4.23.

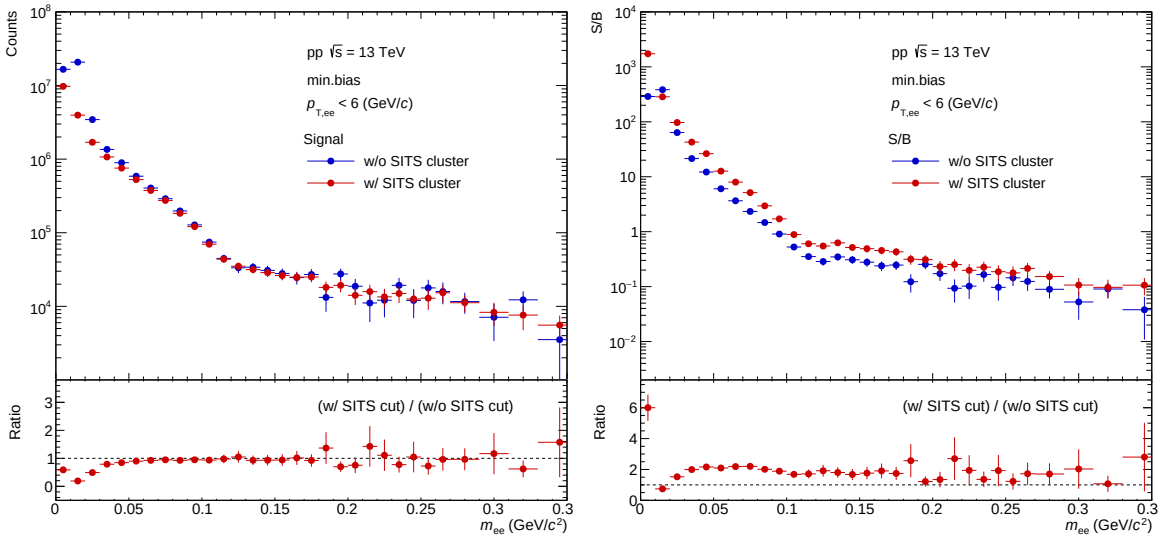

Figure 4.23: Comparison of raw signal (left) and signal to background ratio (right) in MB-triggered events showing the effect of no shared ITS clusters requirement.

However, since the inactive area of the SPD increases as time passes, additional conversion rejection is necessary. This can be done by exploiting the pair properties of decay products, i.e., the correlation between the opening angle cut and invariant mass. As photons do not have physical mass, the pair travels in the same direction as the photon, resulting in their opening angle being very small. These particles are bent only in the azimuthal direction with respect to the direction of the magnetic field. The orientation of the e^+e^- pair plane with respect to the $\hat{z}$ direction, i.e., the magnetic field, the angle φ_v is calculated as

$$\vec{u} = \frac{\vec{p}_+ + \vec{p}_-}{|\vec{p}_+ + \vec{p}_-|}, \tag{4.13}$$

$$\vec{v} = \vec{p}_+ \times \vec{p}_-, \tag{4.14}$$

$$\vec{w} = \vec{u} \times \vec{v}, \tag{4.15}$$

$$\vec{u}_a = \frac{\vec{u} \times \hat{z}}{|\vec{u} \times \hat{z}|}, \tag{4.16}$$

$$\varphi_v = \arccos\left(\frac{\vec{w} \cdot \vec{u}_a}{|\vec{w}||\vec{u}_a|}\right), \tag{4.17}$$

where $\vec{p}_-$ ($\vec{p}_+$) is the 3-dimensional momentum vector of electron (positrons). The typical φ_v distribution of the conversion pair and from other sources are simulated with MC as shown in Fig. 4.24. Due to the small opening angle, conversion pairs give clear peaks at $\varphi_v = \pi$, while ones from other sources give a flat distribution. In addition, as the ALICE tracking algorithm assumes the particle arises from the primary vertex, pairs from off-vertex decay acquire fake invariant mass. With these characteristic φ_v and m_{ee} distributions, conversion signals can be visualized by using MC simulation as shown in Fig. 4.25. The red arrows indicated peaks around 10 MeV/c^2 (a), 15 MeV/c^2 (b), 27 MeV/c^2 (c), and 42 MeV/c^2 (d) are from conversions that occurred in the beam pipe and the ITS materials. In this mass region, another source of e^+e^- pair is from π^0 Dalitz decays ($m_{ee} < 40$ MeV/c^2), conversions are separated from such pairs by making use of a cut on the orientation of e^+e^- pairs. Pairs whose φ_v is larger than > 2 and

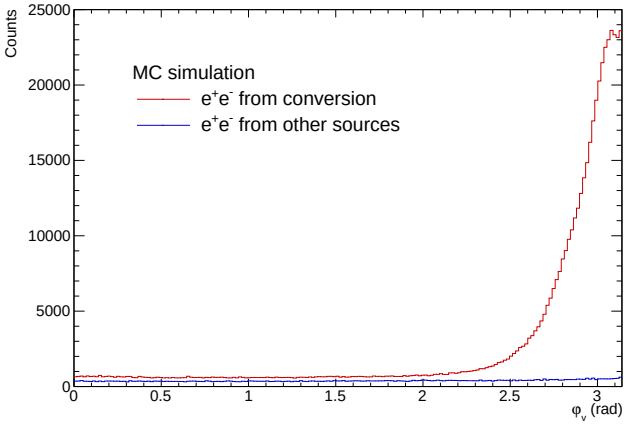

Figure 4.24: MC simulated φ_v distribution of e^+e^- from conversions (red) and from other sources (blue).

below 100 MeV/c^2 are rejected in this analysis. Rejection is applied for the unlike-sign and like-sign pairs in the same and mixed events and is consistently applied to the analysis of HM-triggered data. Fig.4.26 shows raw signal and signal-to-background ratio before and after φ_v rejection. The resulting unlike-sign pairs, combinatorial background and R-factor with applied φ_v rejection are shown in MB- and HM-triggered events in Fig. 4.27 and 4.28, respectively. Corresponding signal-to-background and the statistical significance for the dielectron signal are shown as well (Fig. 4.29 and 4.30). The statistical significance is defined as $S/\sqrt{S+2B}$, where factor 2 accounts for the subtraction of background using like-sign pairs [139]The signal-to-background ratio around $m_{ee} \sim 0.5$ GeV/c^2, where combinatorial background contribution is the largest, is 0.04 and 0.02 for MB- and HM-triggered events, respectively. Although the signal-to-background ratio is worse for HM events than for MB events by factor ~ 2, and the number of HM-triggered events is 5 times smaller than one from MB-triggered events, statistical significance is comparable due to the larger electron multiplicity.

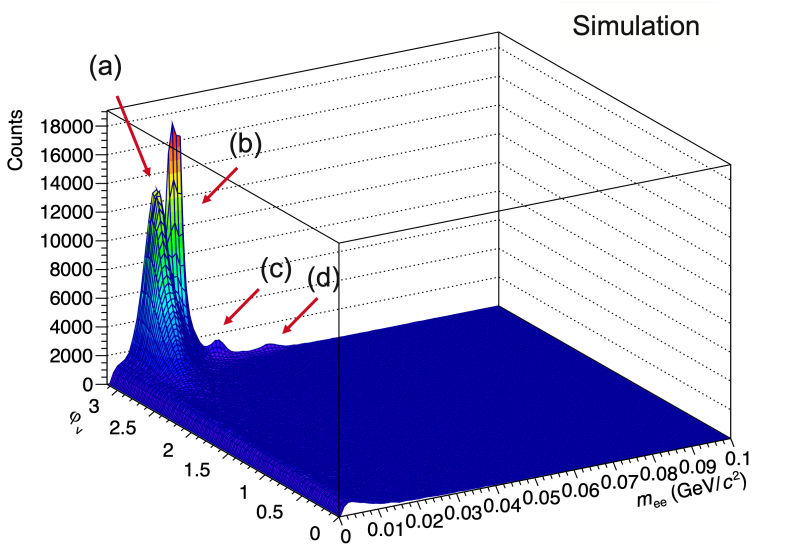

Figure 4.25: MC simulated φ_v versus m_{ee} distributions of all dielectron signals. The conversion peaks (a)–(d) are indicated by red arrows. A φ_v-flat bank structure appeared below 40 MeV/c^2 is due to e^+e^- from Dalitz decays of π^0.

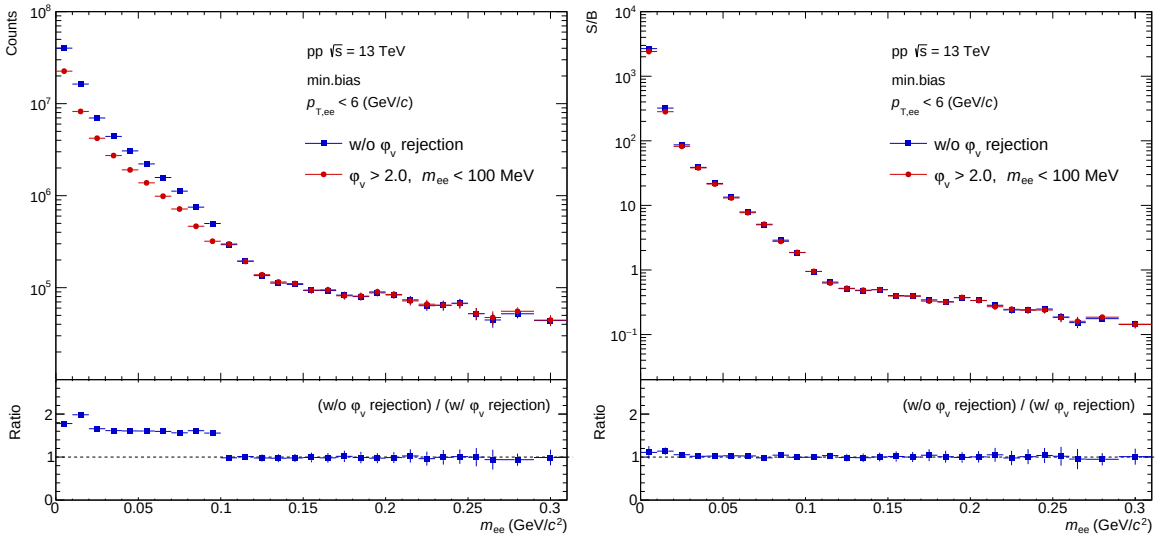

Figure 4.26: The comparison of raw signal (left) and signal-to-background ratio (right) in MB-triggered events showing the effect of φ_v rejection.

Finally, raw dielectron yields in MB-triggered events in the range $m_{ee} < 4$ GeV/c^2 are shown in Fig. 4.31 and 4.32. The spectra are normalized to the number of analyzed events and the real-photon conversion rejection is applied to the spectra. In any slice

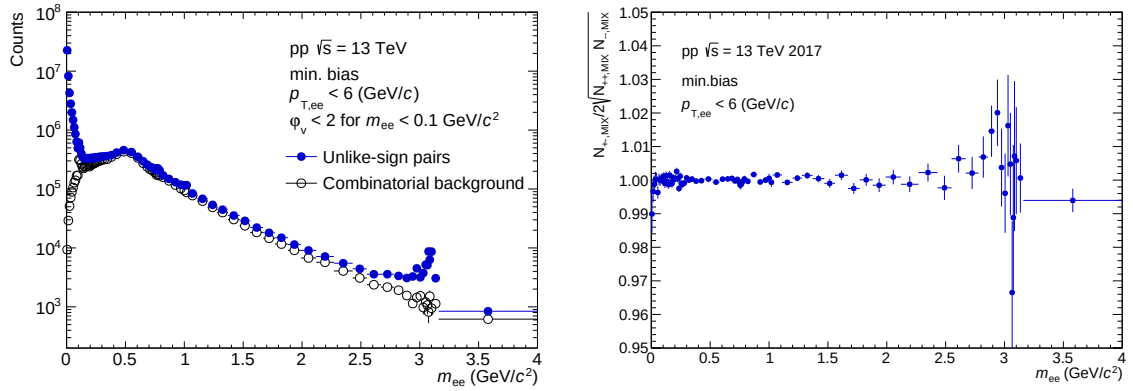

Figure 4.27: Left: Unlike-sign pairs N_{+-}, combinatorial background B. Right: R-factor in minimum-bias events (p_{T}-integrated case)

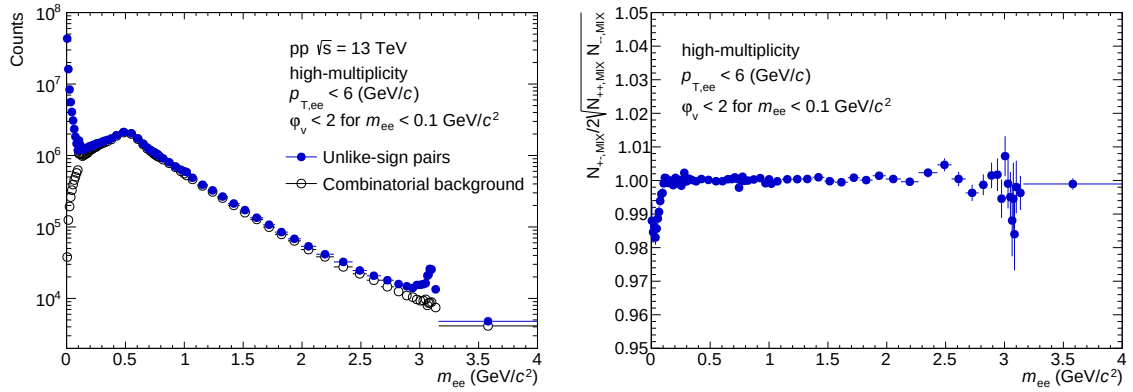

Figure 4.28: Left: Unlike-sign pairs N_{+-}, combinatorial background B. Right: R-factor in high-multiplicity events (p_{T}-integrated case).

of $p_{\mathrm{T,ee}}$ intervals, ρ, ϕ, and J/ψ peaks are visible. Raw yields in HM-triggered data are shown in Fig. 4.33 and 4.34.

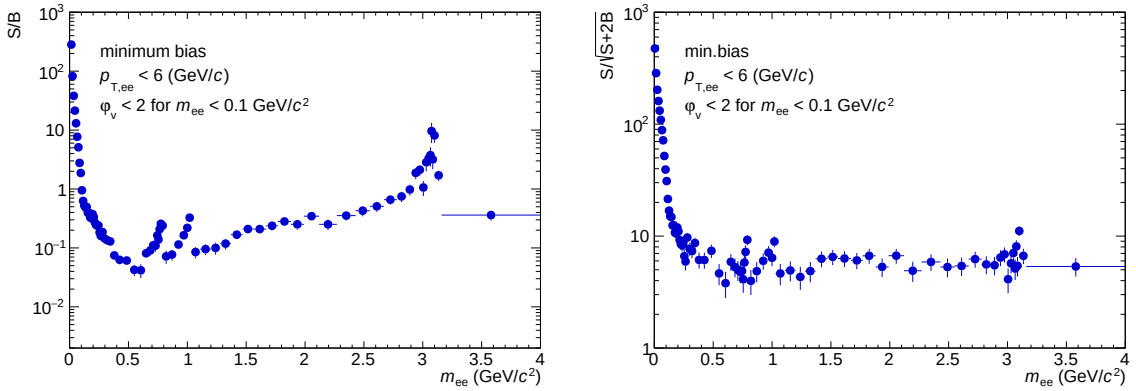

Figure 4.29: Signal-to-background ratio (left) and statistical significance (right) of di-electron signal in minimum-bias events.

.

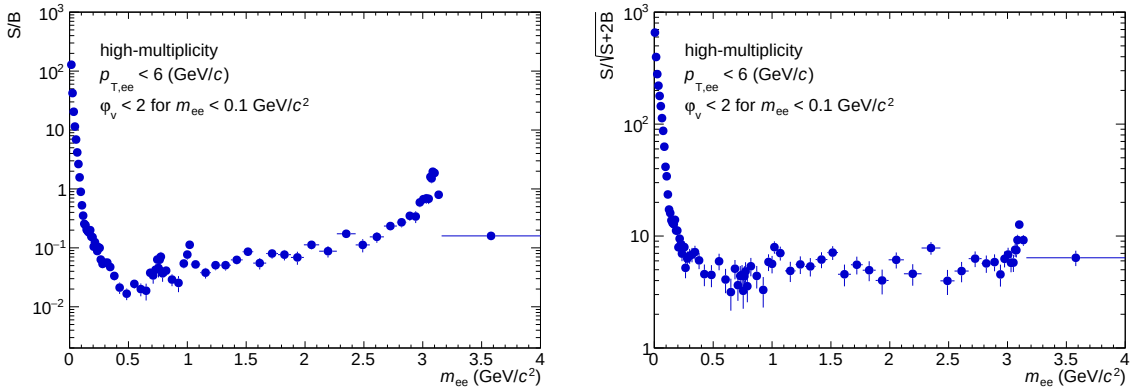

Figure 4.30: Signal-to-background ratio (left) and statistical significance (right) of di-electron signal in high-multiplicity events.

4.7 Efficiency Correction

The raw dielectron signal needs to be corrected for the reconstruction efficiency. To this purpose, a detailed detector simulation using the Monte Carlo method is employed. Proton-proton collisions are generated with the event generator PYTHIA8 [55] with "Monash 2013" [56] (so-called tune) for light hadron decays and "Perugia 2011" [140] tune of PYTHIA6.4 [136] for heavy-flavour decays. A choice of different PYTHIA versions is motivated by the fact that Monash 2013 tune reproduces many of the relevant light hadron multiplicities. It used MB-, Drell-Yan, and underlying-event data from the LHC to constrain the initial state radiation and multi-parton-interaction (MPI) parameters, combined with data from SPS and the Tevatron to constrain the energy scaling. Perugia 2011 tune of PYTHIA6.4 uses the same value of λ_{QCD} for all shower

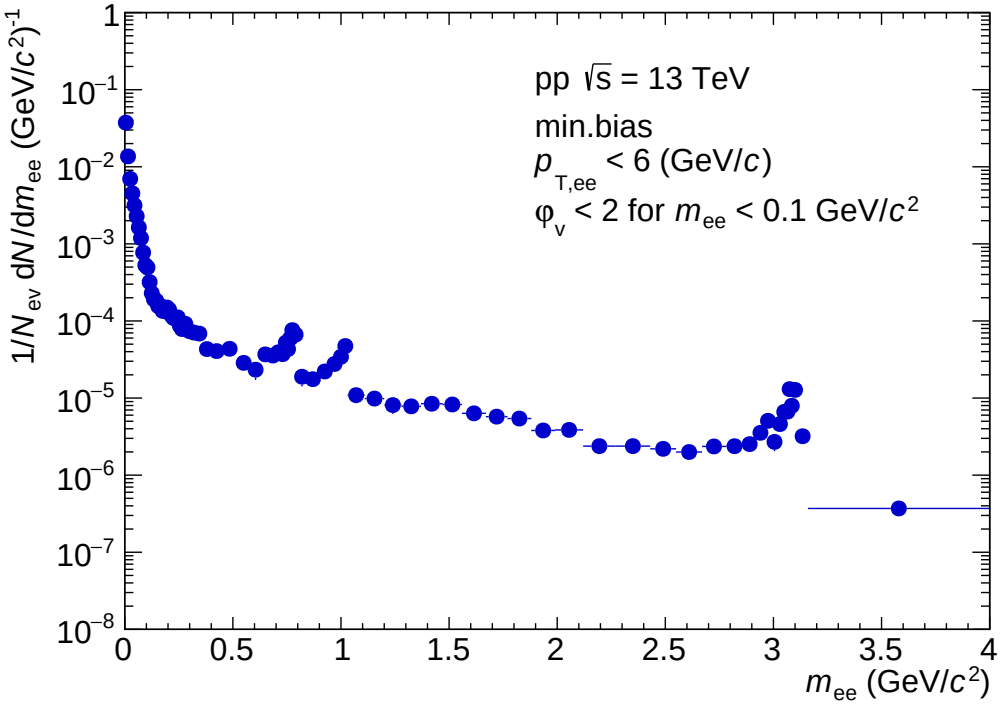

Figure 4.31: Raw dielectron signal normalized to the number of analyzed minimum-bias events. Rejection of conversion electrons is applied as described in the text.

activity (initial-state and final-state radiation) to simplify matching applications and was constrained by results from LEP, SPS and Tevatron experiments as well as by early data from LHC for minimum-bias and underlying event activities in pp collisions at $\sqrt{s}$ = 0.9 and 7 TeV. As a result, it describes reasonably well the transverse momentum spectra of heavy-flavor hadrons. The generated particles are propagated through the ALICE detector using the GEANT3 package [137], which provides particle energy loss in a given detector geometry and material properties. Afterward, the signal reconstruction efficiency is studied as a function of m_{ee} and $p_{T,ee}$ for the respective e^+e^- sources: resonance and Dalitz decays of light-flavor mesons, correlated semileptonic decays of charm and beauty hadrons, and J/ψ decays. The total signal reconstruction efficiency is obtained as a weighted average of these efficiencies, where the weights are determined from the expected relative contributions to the yield.

4.7.1 Detector Response Matrices

High-energy electrons emit radiation and lose energy when they are accelerated by the electromagnetic fields of nuclei or by an external magnetic field while traversing in the ALICE detector. The reconstructed momentum of electrons is also affected by the finite detector resolution.

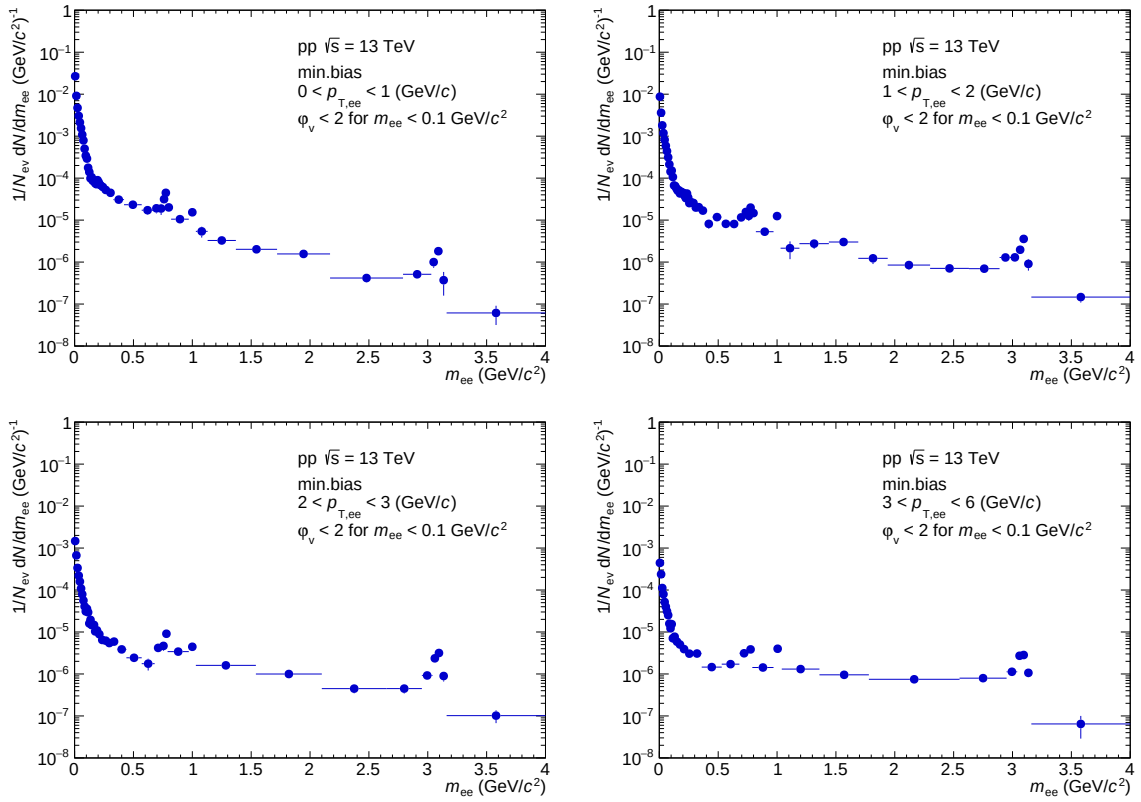

Figure 4.32: Raw dielectron signal normalized to the number of analyzed minimum-bias events. Rejection of conversion electrons is applied as described in the text.

These effects can be seen in Fig. 4.35, where the difference between generated $p_{\mathrm{T}}^{\mathrm{gen}}$ and reconstructed $p_{\mathrm{T}}^{\mathrm{rec}}$ momentum for electrons with generated transverse momentum in the range $0.5 < p_{\mathrm{T}}^{\mathrm{gen}} < 0.6$ GeV/c. The width of the distribution $\Delta p_{\mathrm{T}}/p_{\mathrm{T}} = (p_{\mathrm{T}}^{\mathrm{gen}} - p_{\mathrm{T}}^{\mathrm{rec}})/p_{\mathrm{T}}^{\mathrm{gen}}$ around zero is due to the finite detector resolution, and the tail in $\Delta p_{\mathrm{T}} > 0$ is due to the radiative energy loss of electrons.

Since invariant mass spectra shown in Sec. 4.6 use reconstructed momentum, efficiency should be evaluated as a function of reconstructed momentum instead of generated momentum. One-dimensional unfolding is applied to the generated MC electrons, as described in [141]. The smearing was performed based on the two-dimensional histograms which contain the difference between generated and reconstructed variables as a function of generated one (Fig. 4.36). The resolution map is produced using the same track selection criteria as the main analysis but without p_{T} cut to apply to smear for generated low momentum tracks. Electrons are selected in the range $|\mathrm{n}\sigma^{\mathrm{TPC}}| < 5$. The (c) and (d) of Fig. 4.36 show $\Delta\phi_{\mathrm{T}}$ of electron and positron, respectively, and their responses are flipped due to opposite polarity.

For a given $p_{\mathrm{T}}^{\mathrm{gen}}$, η^{gen} and ϕ^{gen} range, the detector response matrices projected and three smeared numbers (Δp_{T}, $\Delta\eta$ and $\Delta\phi$) are extracted based on the projected

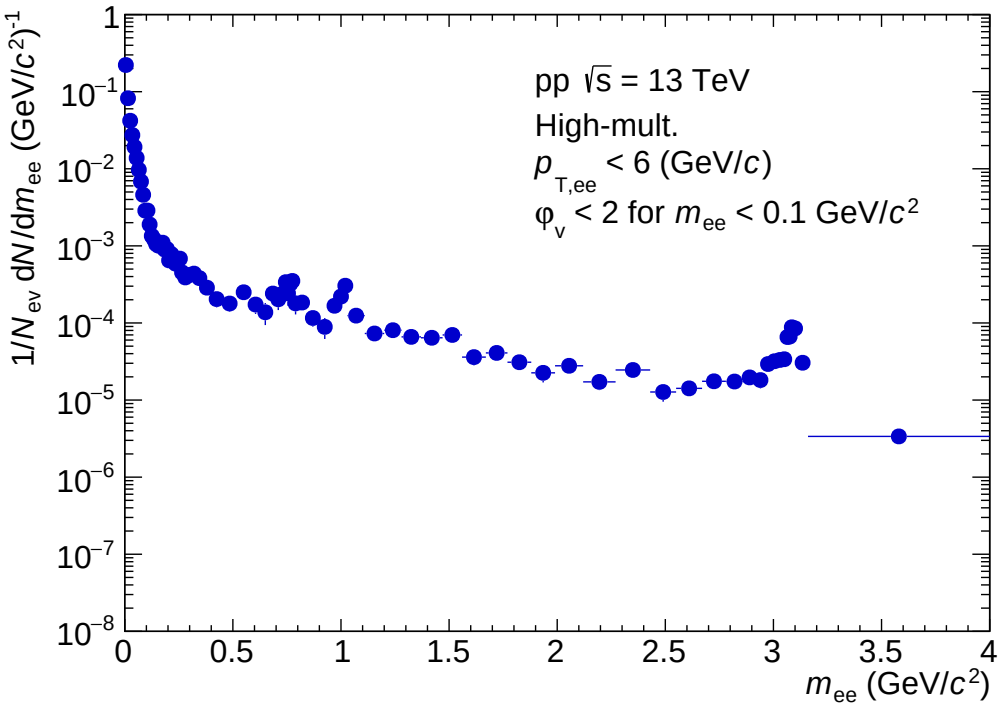

Figure 4.33: Raw dielectron signal normalized to the number of analyzed high-multiplicity events. Rejection of conversion electrons is applied as described in the text.

distributions. Then the generated momentum vector of an electron is transformed into the corresponding measurable momentum

$$x_{\mathrm{meas}} = x_{\mathrm{gen}} + \Delta(x_{\mathrm{gen}}), \tag{4.18}$$

where $x_{\mathrm{meas}} = p_{\mathrm{T}}$, η and ϕ. The transformation is performed before acceptance cuts. Since detector response is different year by year due to different TPC gas composition, maps are produced for each data-taking year.The smearing effect on generated pairs from same-mother resonance and Dalitz decays and J/ψ can be seen in the left and the right of Fig. 4.37, respectively.

4.7.2 Single Electron Efficiency

The single electron efficiency is defined as a function of $x = p_{\mathrm{T}}$, η and ϕ,

$$\epsilon(x) = \frac{(\frac{\mathrm{d}N}{\mathrm{d}x})_{\mathrm{rec}}}{(\frac{\mathrm{d}N}{\mathrm{d}x})_{\mathrm{meas}}}, \tag{4.19}$$

where $(\frac{\mathrm{d}N}{\mathrm{d}x})_{\mathrm{meas}}$ is generated electrons which is applied smearing procedure and $(\frac{\mathrm{d}N}{\mathrm{d}x})_{\mathrm{rec}}$ stands for the reconstructed electrons, respectively.

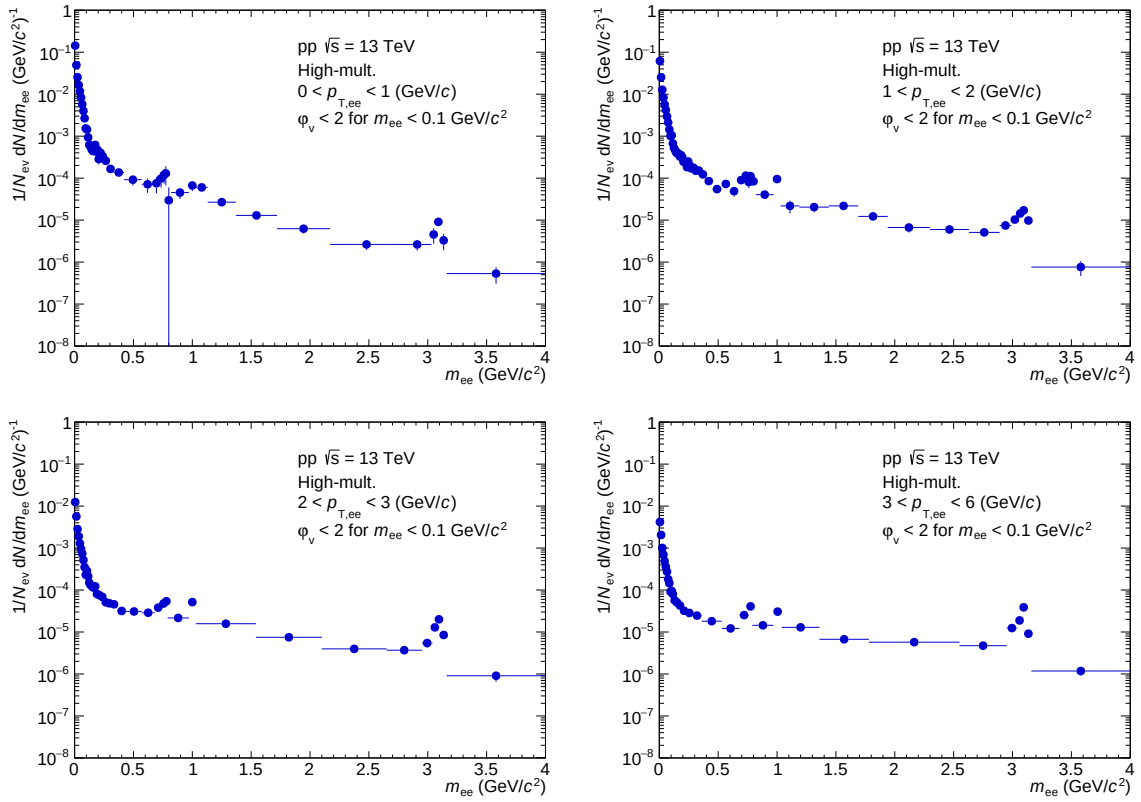

Figure 4.34: Raw dielectron signal normalised to the number of analysed high-multiplicity events. Rejection of conversion electrons is applied as described in the text.

The efficiency is calculated using primary electrons, i.e., not from secondary or conversions. The left of Fig. 4.38 shows generated, smeared, and reconstructed electrons as a function of p_{T}. The numerator and denominator of the efficiency are within acceptance and passed the same track selection and PID requirements as described in Sections 4.4 and 4.5. Corresponding single-track reconstruction efficiency for electrons and positrons as a function of p_{T} is shown in the right of Fig. 4.38. Significant drops of efficiency around 0.5 GeV/c and 1 GeV/c, reflect rejection of hadron contamination from kaons and protons, respectively.

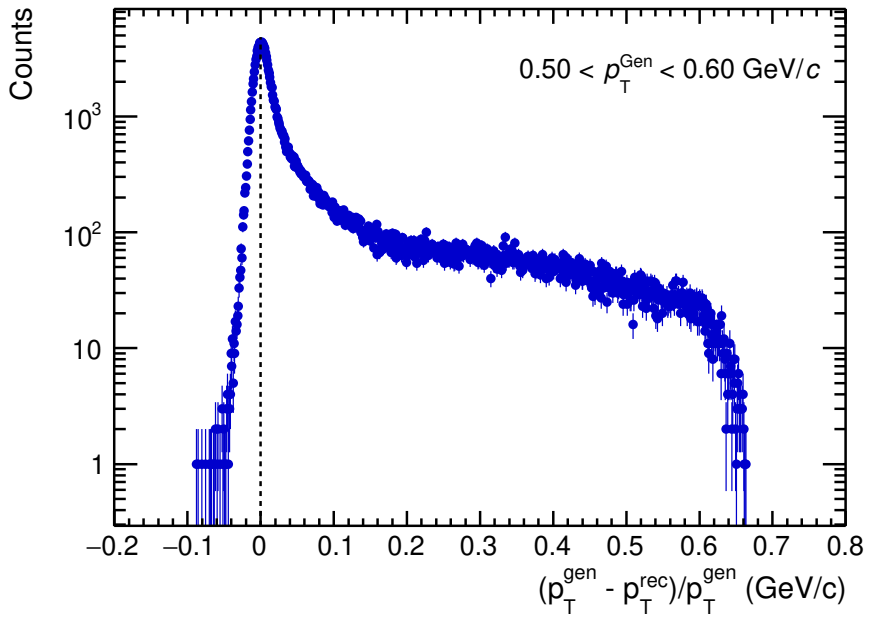

Figure 4.35: Transverse momentum resolution in $0.50 < p_{\mathrm{T}}^{\mathrm{gen}} < 0.60$ GeV/c^2.

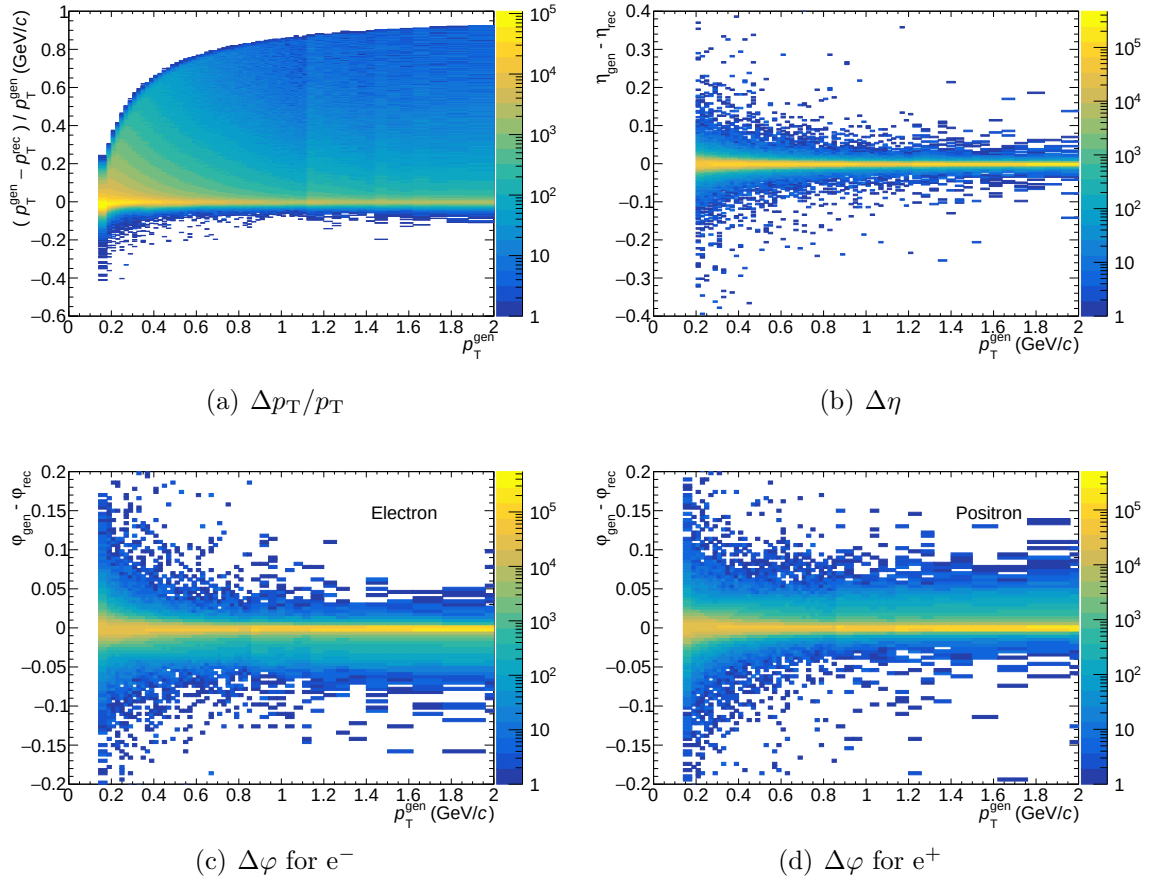

(a) $\Delta p_T/p_T$ (b) $\Delta\eta$

(c) $\Delta\varphi$ for e^- (d) $\Delta\varphi$ for e^+

Figure 4.36: Detector response matrices for generated electrons and positrons.

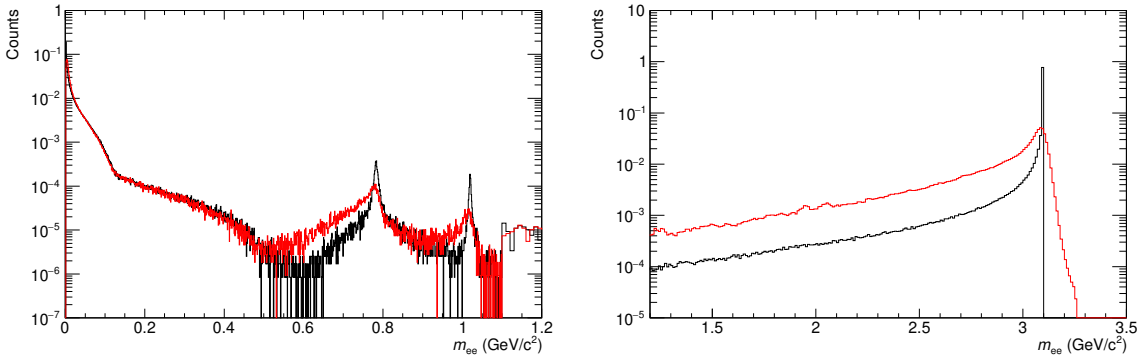

Figure 4.37: Before (black) and after (red) smearing applied to the generated electron pairs. Left: generated pairs from same-mother resonance and Dalitz decays. Right: generated pairs from J/ψ. Both generated spectrum and smeared spectrum are applied p_T cut ($p_T > 200$ MeV/c).

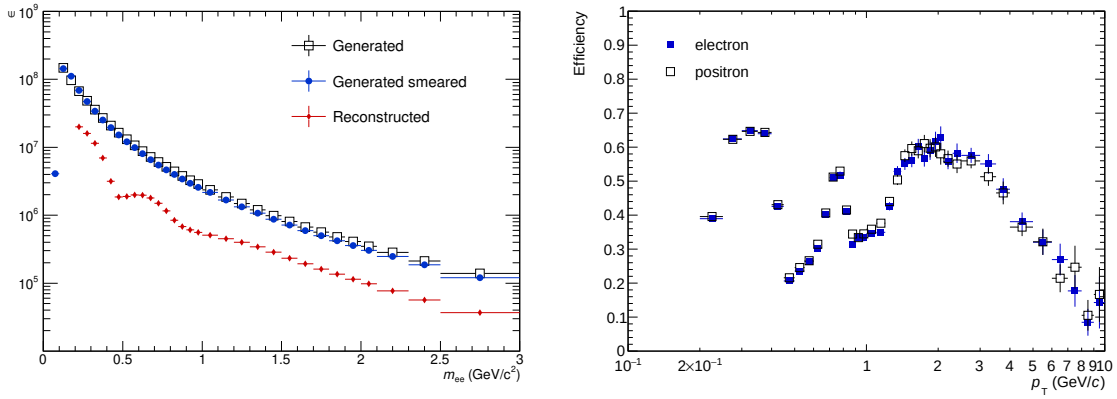

(a) $p_{\mathrm{T,e}}$ (b) $p_{\mathrm{T,e}}$

Figure 4.38: Left: The $p_{\mathrm{T,e}}$ distribution of electrons. Generated, smeared and reconstructed electrons are shown. Right: Single electron and positron efficiency as a function of $p_{\mathrm{T,e}}$.

Table 4.4: Possible combination of electron pairs from open heavy-flavor hadron decays.

Process	Effective BR
(i) $pp \to c\bar{c} \to \mathrm{e^+e^-}$	$\mathrm{BR}(c \to \mathrm{e}) = 7.5^{+0.59}_{-0.65}\%$
(ii) $pp \to b\bar{b} \to \mathrm{e^+e^-}$	$\mathrm{BR}(b \to \mathrm{e}) = 10.2\%$
(iii) $pp \to b\bar{b} \to c + \mathrm{e} + b \to \mathrm{e^+e^-} + b$	$\mathrm{BR}(b \to c \to \mathrm{e}) = 8.1^{+0.69}_{-0.94}\%$
(iv) $pp \to b\bar{b} \to c + \mathrm{e} + \bar{c} + \mathrm{e}$	$\mathrm{BR}(b \to c\bar{c}) = 5.6\pm\ 0.73\%$
(v) $pp \to b\bar{b} \to c + \mathrm{e} + b \to c + \mathrm{e} + \mathrm{e}$ (like − sign)	

4.7.3 Pair Efficiency

The pair reconstruction efficiency is defined as the ratio between reconstructed pairs and generated pairs after the smearing procedure is applied. The definition is given as a function of invariant mass and pair transverse momentum:

$$\epsilon(m_{\mathrm{ee}}, p_{\mathrm{T,ee}}) = \frac{(\frac{\mathrm{d}^2 N^{\mathrm{ee}}}{\mathrm{d}m_{\mathrm{ee}}\mathrm{d}p_{\mathrm{T,ee}}})_{\mathrm{rec}}}{(\frac{\mathrm{d}N^{\mathrm{ee}}}{\mathrm{d}m_{\mathrm{ee}}})_{\mathrm{meas}}}, \tag{4.20}$$

where $(\frac{dN^{\mathrm{ee}}}{dm_{\mathrm{ee}}})_{\mathrm{rec}}$ is the number of reconstructed electrons, $(\frac{dN^{\mathrm{ee}}}{dm_{\mathrm{ee}}})_{\mathrm{meas}}$ is one from generated and smeared electrons for each leg. For the calculation of the pair reconstruction efficiency, only correlated pairs are considered, which include pairs from the same mothers, i.e., light-flavour and J/ψ meson decays or from the decays of semi-leptonic decays of charmed and bottom hadrons. The correlated light-flavor pairs are simulated by PYTHIA8 with Monash 2013 tune. The J/ψ signal is generated by PYTHIA6.4 with the Perugia 2011 tune. This MC production takes into account two body decay ($J/\psi \to \mathrm{e^+e^-}$) and radiative decay ($J/\psi \to \mathrm{e^+e^-}\gamma$). These are simulated using PHOTOS [142], which includes the radiative component of the J/ψ decay.

The calculation of dielectron efficiency from open heavy-flavour hadron decays is studied in the previous studies [132, 143]. We consider the heavy-flavor dielectrons derived from the combinations as summarised in Table 4.4. To this purpose, a heavy-flavor enriched MC simulation is used to increase statistics. In this MC simulation, dielectrons from different heavy-flavor sources are generated in each event with the following probabilities:

1 $c\bar{c} \to \mathrm{e^+e^-} + X$ (8%): a charm quark-antiquark pair is generated per event, and charmed hadrons (D mesons or Λ_{c} baryons) are forced decay semileptonically, with a constraint on both produced electrons to be within $|y_{\mathrm{e}}| < 1.2$.

2 $b\bar{b} \to \mathrm{e^+e^-} + X$ (8%): a beauty quark-antiquark pair is generated per event, and beauty hadrons (B mesons or Λ_{b} baryons) are forced decay semileptonically, with a constraint on both produced electrons to be within $|y_{\mathrm{e}}| < 1.2$.

3 $b\bar{b} \rightarrow \mathrm{e} + X$ (66%): a beauty quark-antiquark pair is generated per event, and at least one electron in an event originating from open-heavy flavor decay should be produced in $|y_{\mathrm{e}}| < 1.2$. Neither beauty nor charmed hadrons (if present) are forced to decay semileptonically, also no rapidity constraint is applied for any other electrons produced in an event.

For the study of (i) $c\bar{c} \rightarrow \mathrm{e}^{+}\mathrm{e}^{-}$ pair efficiency, only events containing exactly one charmed hadron and one charmed anti-hadron are selected, and no beauty quark hadron should be present in the generated event. In this way, the pairing of correlated electrons and positrons from charmed hadrons becomes straightforward, and only unlike-sign pairs from charmed hadrons are produced. These unlike-sign pairs are used for the calculation of $c\bar{c} \rightarrow \mathrm{e}^{+}\mathrm{e}^{-}$ pair efficiency. For the study of pair efficiency from open beauty decays, a similar way as open charme hadrons is adopted for the process of (ii) $b\bar{b} \rightarrow \mathrm{e}^{+}\mathrm{e}^{-}$. As for (iii) - (v), it is complicated due to the significant probability of $B^0 \leftrightarrow \bar{B}^0$ oscillations which create unlike-sign and like-sign dielectron pairs at various rates. For these studies, the process of dielectron production 3. is used. To simplify the pairing procedure, only events containing exactly one beauty hadron and one beauty anti-hadron are selected requiring no charm quarks present in the event and no oscillation of B mesons (B meson oscillation veto). The latter is implemented in MC simulations as "wrong-sign" decays, i.e., decays like $B \rightarrow \mathrm{e}^{-}$ or $\bar{B} \rightarrow \mathrm{e}^{+}$, which can be easily tagged. For consistency with the experimental data analysis, like-sign contributions originating from decays like $B \rightarrow \mathrm{e}^{-}$ and $\bar{B} \rightarrow D \rightarrow \mathrm{e}^{+}$ are subtracted both from generated and reconstructed unlike-sign pairs.

The electrons from real photon conversion are not taken into account in the correlated light-flavor pairs. These pairs are rejected in the experimental data via φ_v rejection (Section 4.6.1), which might reject even good signal pairs. To compensate for this effect, the same selection criteria were applied to the MC simulation. The φ_v rejection applied efficiency for the respective sources are shown in Fig. 4.39.

The final signal efficiency is given by the combined form:

$$\epsilon_{\mathrm{total}} = \epsilon_{\mathrm{LF}} \frac{\mathrm{d}N^{ee}_{\mathrm{LF}}}{\mathrm{d}N^{ee}} + \epsilon_{J/\psi} \frac{\mathrm{d}N^{ee}_{J/\psi}}{\mathrm{d}N^{ee}} + \epsilon_{c\bar{c}} \frac{\mathrm{d}N^{ee}_{c\bar{c}}}{\mathrm{d}N^{ee}} + \epsilon_{b\bar{b}} \frac{\mathrm{d}N^{ee}_{b\bar{b}}}{\mathrm{d}N^{ee}} \tag{4.21}$$

where, $\mathrm{d}N^{ee}_{\mathrm{LF}}/\mathrm{d}N^{ee}$, $\mathrm{d}N^{ee}_{J/\psi}/\mathrm{d}N^{ee}$, $\mathrm{d}N^{ee}_{c\bar{c}}/\mathrm{d}N^{ee}$ and $\mathrm{d}N_{b\bar{b}^{ee}}/\mathrm{d}N^{ee}$ are relative fraction of $\mathrm{e}^{+}\mathrm{e}^{-}$ pairs from light-flavor, J/ψ, open charm and open beauty hadrons, respectively. The relative fraction is calculated based on the hadronic cocktail simulations which will be described in Sec.4.8. The resulting total pair efficiency is shown in Fig. 4.40 and 4.41. Afterward, the raw signal is corrected for the obtained total efficiency. Corrected signals are shown in Fig. 4.42 and 4.43 for MB events, and Fig. 4.44 and 4.45 for HM events, respectively.

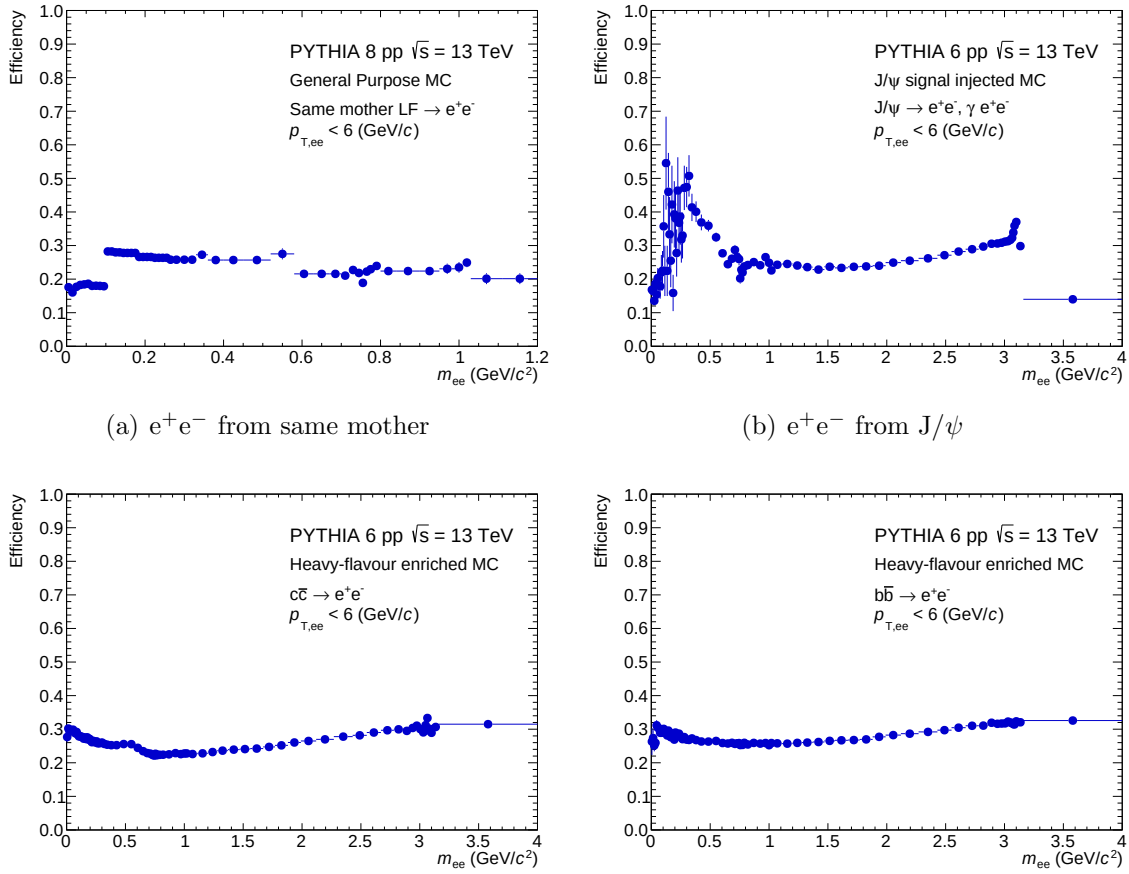

(a) e^+e^- from same mother

(b) e^+e^- from J/ψ

(c) e^+e^- from open-charm hadron

(d) e^+e^- from open-beauty hadron

Figure 4.39: Pair efficiency for respective e^+e^- sources

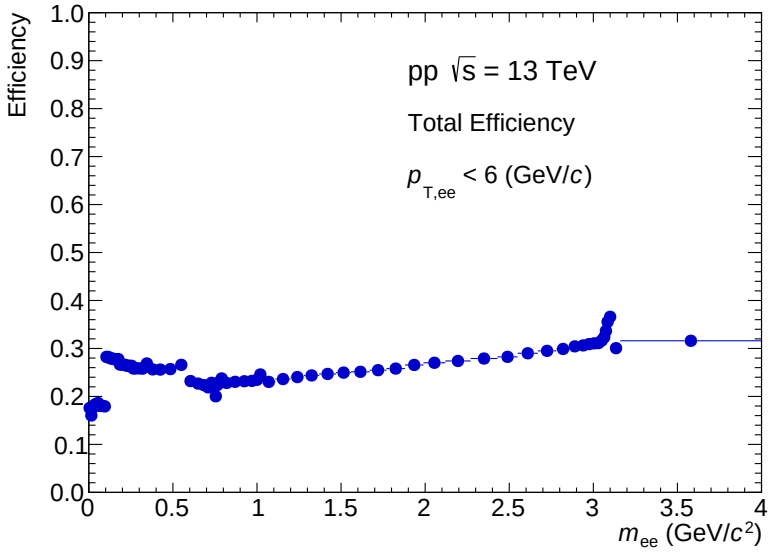

Figure 4.40: Total efficiency

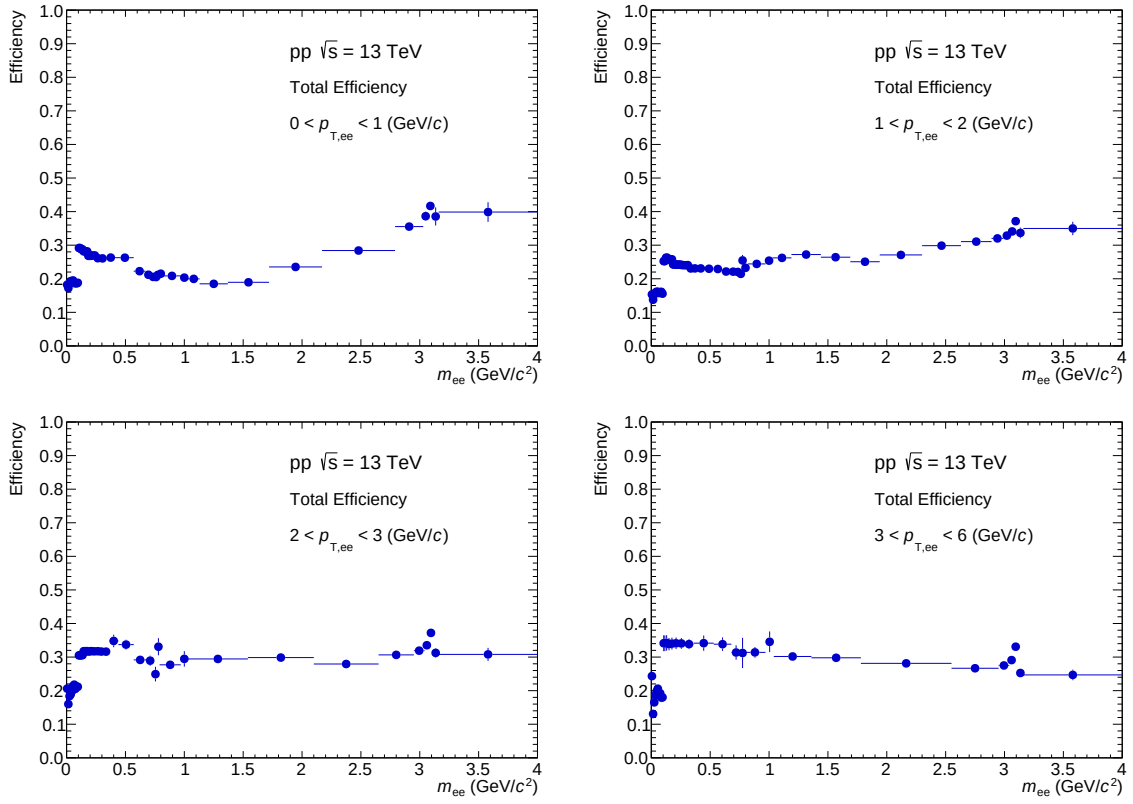

Figure 4.41: Total efficiencies in respective $p_{\mathrm{T,ee}}$ slices.

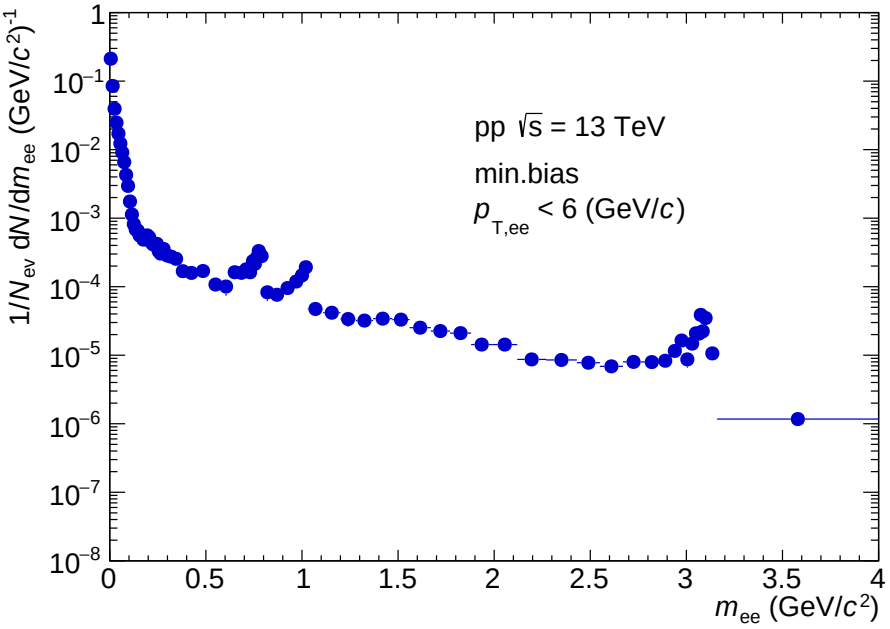

Figure 4.42: Efficiency corrected signal in minimum-bias events for $p_{\mathrm{T,ee}} < 6$ GeV/c.

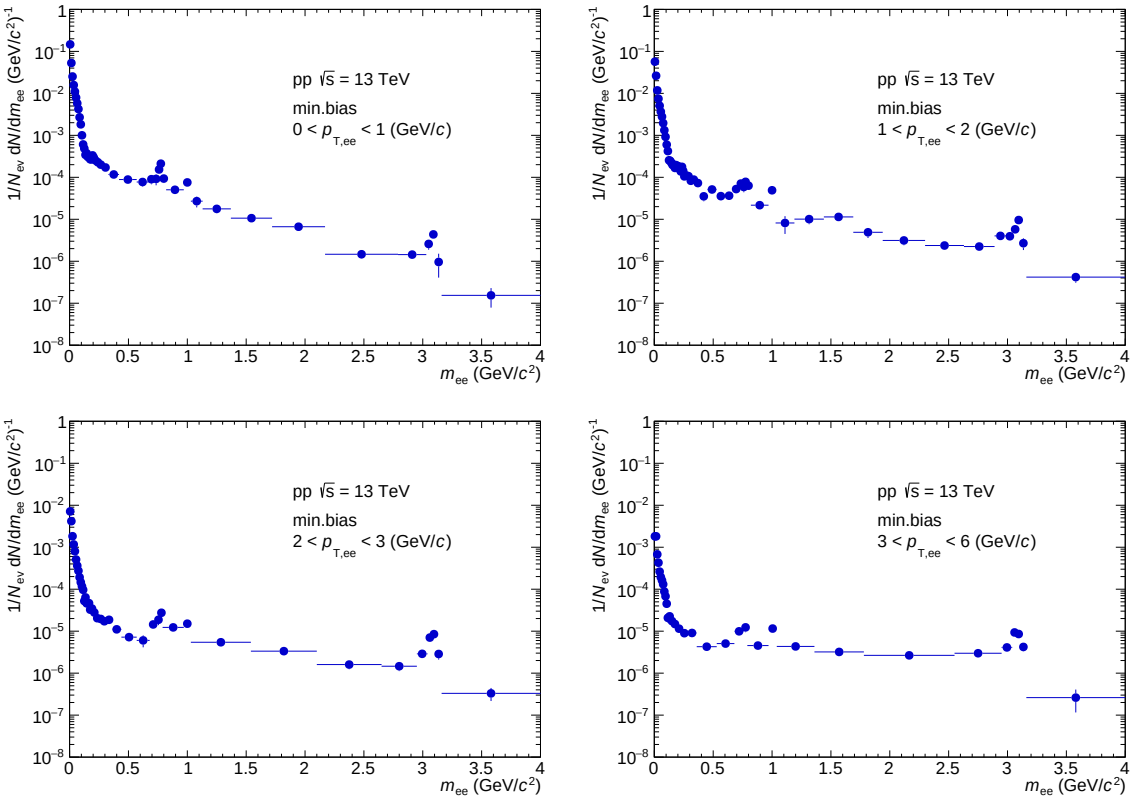

Figure 4.43: Efficiency corrected signal in minimum-bias events for different $p_{\mathrm{T,ee}}$ intervals.

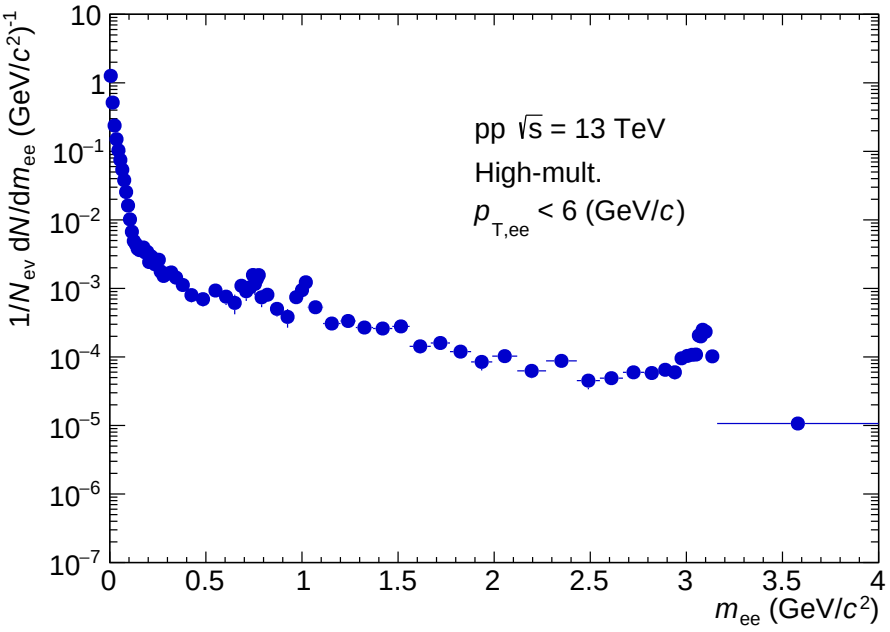

Figure 4.44: Efficiency corrected signal in high-multiplicity events for $p_{\mathrm{T,ee}} < 6$ GeV/c.

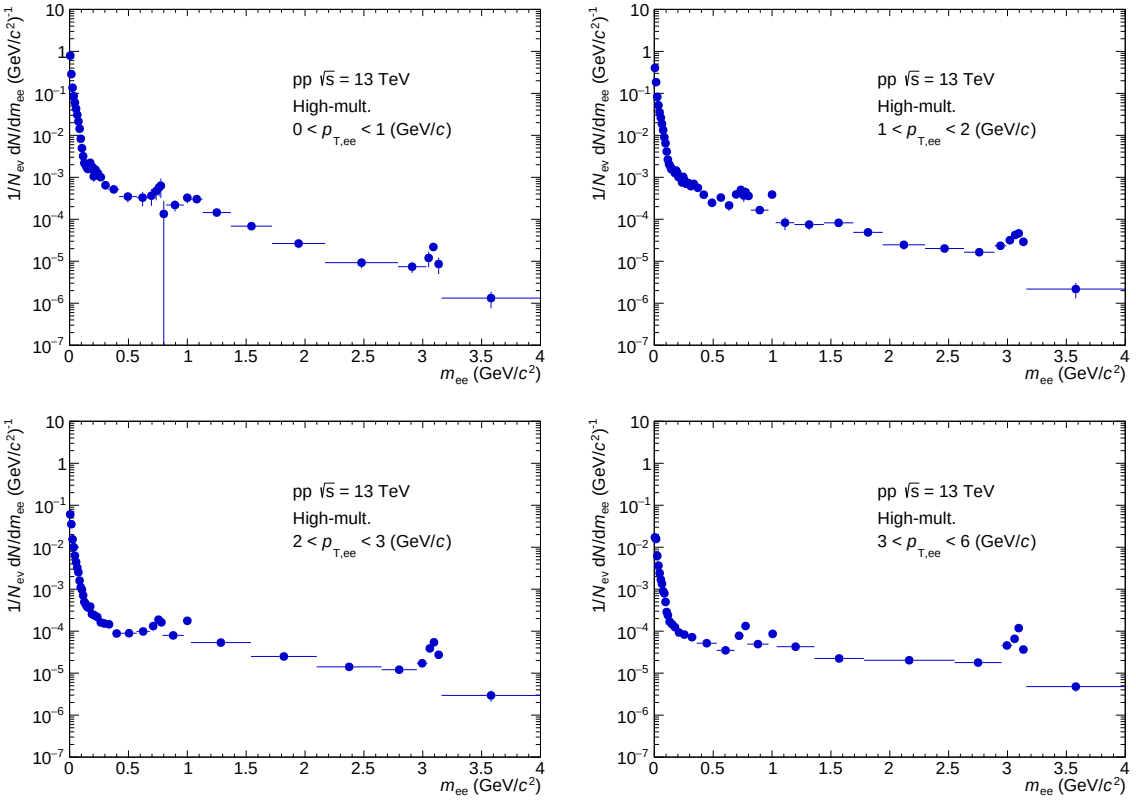

Figure 4.45: Efficiency corrected signal in high-multiplicity events for different $p_{\mathrm{T,ee}}$ intervals.

4.8 Hadronic Cokctail

The dielectron spectrum is compared with the expected dielectron yield from known hadron decays, i.e., the hadronic cocktail. This section describes the hadronic cocktail simulations of light-flavor and heavy-flavor meson decays (π^0, η, η', ρ, ω, ϕ, J/ψ), and open heavy-flavor decays. The detailed procedure is described in [144]. Cocktail calculations for the high-multiplicity pp collisions are discussed as well.

4.8.1 Light-Flavour Hadrons and J/ψ

The Dalitz decays of light neutral mesons (π^0, η, η') and the dielectron decays of vector mesons (ρ, ω, ϕ) are considered. For J/ψ meson, two body decay (J/$\psi \rightarrow e^+e^-$) and radiative decay (J/$\psi \rightarrow e^+e^-\gamma$) are taken into account. Table 4.5 summarises the simulated particles, decay modes, and corresponding branching ratios and sources for the inputs.

All mesons are assumed to be unpolarised, with flat rapidity distribution at mid-rapidity. The mass distribution of dielectron Dalitz decays follows the Kroll-Wada expression in Eq. 2.8 [97], with electromagnetic form factors measured by the NA60 experiment [145, 146]. The 2-body decays of ω and ϕ mesons are generated using Gounaris-Sakurai expression to describe their mass shape [147]. The ρ line shape has been studied in detail by the NA60 experiment [145] who confirmed the need for Boltzmann term beyond the standard description [148] and provided a precise measurement.

These are simulated with phenomenological event generator EXODUS developed by PHENIX collaboration [149]. EXODUS can simulate the phase-space distribution of all relevant sources of electrons electron pairs and the decay of these sources. The input particle spectrum is converted to have uniform quantity $(1/N_{\rm ev})(\mathrm{d}^2N/\mathrm{d}p_{\rm T}\mathrm{d}y)$ $(\mathrm{GeV}/c)^{-1}$, where $N_{\rm ev}$ is supposed to consider MB-triggered events. In case the spectrum is normalized to inelastic events, additional correction is applied by multiplying $\sigma_{\rm V0AND}/\sigma_{\rm INEL}\sim 0.75$ [150]. to the number of MB-triggered events. Each particle spectrum is parameterized in the following way.

Parameterizations of π^0, ϕ, and J/ψ meson are obtained by a fit to measured spectra. The π^0 [54], is parametrised using two-component model (TCM) function [151, 152] below

$$\frac{1}{N_{\rm ev}}\frac{d^2N}{dp_{\rm T}dy} = A_e \exp\frac{-(\sqrt{p_{\rm T}^2+M^2}-M)}{T_e} + \frac{A}{(1+\frac{p_{\rm T}^2}{T^2n})^{-n}} \times p_{\rm T} \tag{4.22}$$

where M equals to the produced hadron mass, ($m_{\pi^0} = 0.135$ GeV/c^2), A_e, T_e, A, T, n are free parameters. Figure. 4.46 shows the TCM fit to π^0 in minimum-bias (left) and high-multiplicity (right) events.

Table 4.5: Summary of light-flavour hadron and J/ψ meson decays contributing to dielectron spectrum. Branching ratios are taken from [5]. (∗) ... common m_{T} scaling factors are used for MB and 0-0.1% multiplicity class.

Particle	Mass (MeV/c^2)	Decay mode (BR)	Input or Estimation Method
π^0	134.9768 ± 0.0005	$e^+e^-\ \gamma$ (1.174 ± 0.035) %	π^0 in MB and 0-0.1% mult. class [54]
η	547.862 ± 0.017	$e^+e^-\ \gamma$ (6.9 ± 0.4) $\times 10^{-3}$	η in MB and 0-0.1% mult. class [54]
ρ^0	775.26 ± 0.25	e^+e^- (4.72 ± 0.05) $\times 10^{-5}$	m_{T} scaling, $S_{\rho^0} = 0.87$ [153] (∗)
ω	782.65 ± 0.12	$\pi^0\ e^+e^-$ (7.7 ± 0.6) $\times 10^{-4}$ e^+e^- (7.36 ± 0.15) $\times 10^{-5}$	m_{T} scaling, $S_\omega = 0.572$ [154] (∗)
η'	957.78 ± 0.06	$\gamma\ e^+e^-$ (4.91 ± 0.27) $\times 10^{-4}$ $\omega\ e^+e^-$ (2.0 ± 0.4) $\times 10^{-4}$	m_{T} scaling, $S_{\eta'} = 0.40$ [136] (∗)
ϕ	1019.461 ± 0.016	$\pi^0\ e^+e^-$ (1.33 $\pm^{+0.07}_{-0.10}$) $\times 10^{-5}$ $\eta\ e^+e^-$ (1.08 ± 0.04) $\times 10^{-4}$ e^+e^- (2.973 ± 0.034) $\times 10^{-4}$	ϕ in MB [155] p_{T} dependent multiplicity scaling is applied to ϕ in 1% mult. class [156] to adjust 0-0.1% mult. class
J/ψ	3096.900 ± 0.006	e^+e^- (5.971 ± 0.032)% $e^+e^-\ \gamma$ (8.8 ± 1.4) $\times 10^{-3}$	J/ψ in MB [157]. p_{T} dependent multiplicity scaling is applied to MB J/ψ according to [43])

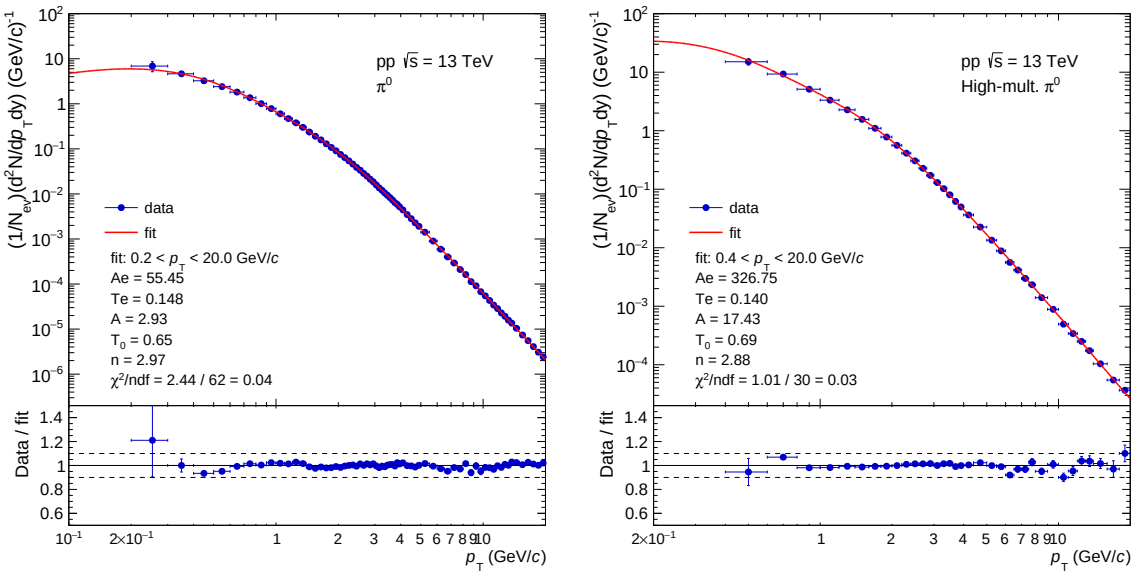

Figure 4.46: TCM fit to neutral pion [54]. The minimum-bias π^0 (left) is measured at transverse momenta p_{T} in the range $0.2 < p_{\mathrm{T}} < 200$ GeV/c and fitting is performed at $0.2 < p_{\mathrm{T}} < 20$ GeV/c. The high-multiplicity π^0 (right) is measured at transverse momenta p_{T} in the range $0.4 < p_{\mathrm{T}} < 50$ GeV/c and fitting is performed at $0.4 < p_{\mathrm{T}} < 20$ GeV/c.

Following the approach outlined in [158], η/π^0 ratio is parameterised as a function of p_{T} using empirical function [159]

$$\eta/\pi^0(p_{\mathrm{T}}) = \frac{A + N \cdot B(1 + (\frac{p_{\mathrm{T}}}{p_0})^2)^{-n}}{1 + B \cdot (1 + (\frac{p_{\mathrm{T}}}{p_0})^2)^{-n}}, \tag{4.23}$$

where A, N, B, p_0, n are free parameters. Fig. 4.47) shows the empirical fit to η/π^0 measured in MB- (left) and HM-triggered (right) events, respectively. Then, the p_{T} differential yield of η is extracted by multiplying π^0 yield and (η/π^0) ratio. As the π^0 and η spectra have correlated systematic uncertainty when we make a ratio between them, systematic uncertainty on η/π^0 ratio is partially canceled out. Therefore for the systematic uncertainty of of η contribution, η/π^0 ratio is shifted by $\pm$ 1σ. Comparison between constructed η and η p_{T} distributions, in MB and HM events are shown in Figure 4.48 (left) and (right), respectively.

Other particles such as η', ρ, and ω mesons are generated assuming m_{T} scaling [160], replacing p_{T} with $\sqrt{m^2 - m_{\mathrm{T}}^2 + (p_\pi/c)^2}$. For the m_{T} scaling, particle yields are normalised at high p_{T} relative to the π^0 yield as follows: 0.40 $\pm$ 0.8 for η' (predicted by PYTHIA6), 0.87 $\pm$ 1.7 for ρ [153], and 0.57 $\pm$ 0.11 for ω [154]. For the systematic uncertainty, the factor varied $\pm$ 20%. The same m_{T} scaling factors are adopted for the high-multiplicity η', ρ, and ω mesons.

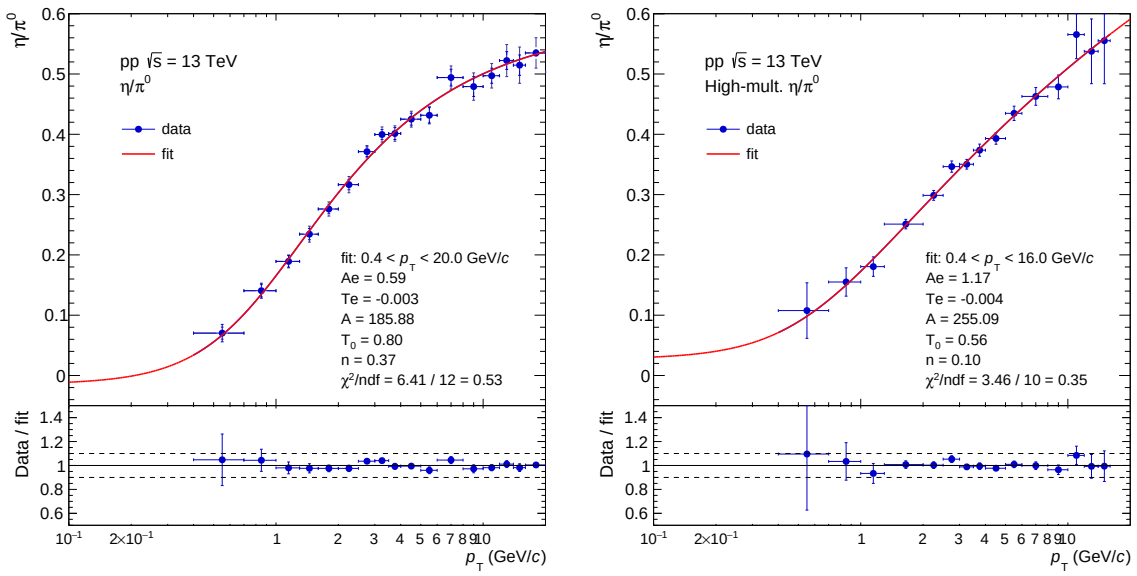

Figure 4.47: Emprirical fit to η/π^0 ratio [54]. The minimum-bias η/π^0 (left) is measured at transverse momentum p_{T} in the range $0.4 < p_{\mathrm{T}} < 50$ GeV/c and fitting is performed at $0.4 < p_{\mathrm{T}} < 20$ GeV/c. The high-multiplicity η/π^0 (right) is measured at transverse momentum p_{T} in the range $0.4 < p_{\mathrm{T}} < 16$ GeV/c and fitting is performed at the same p_{T} range.

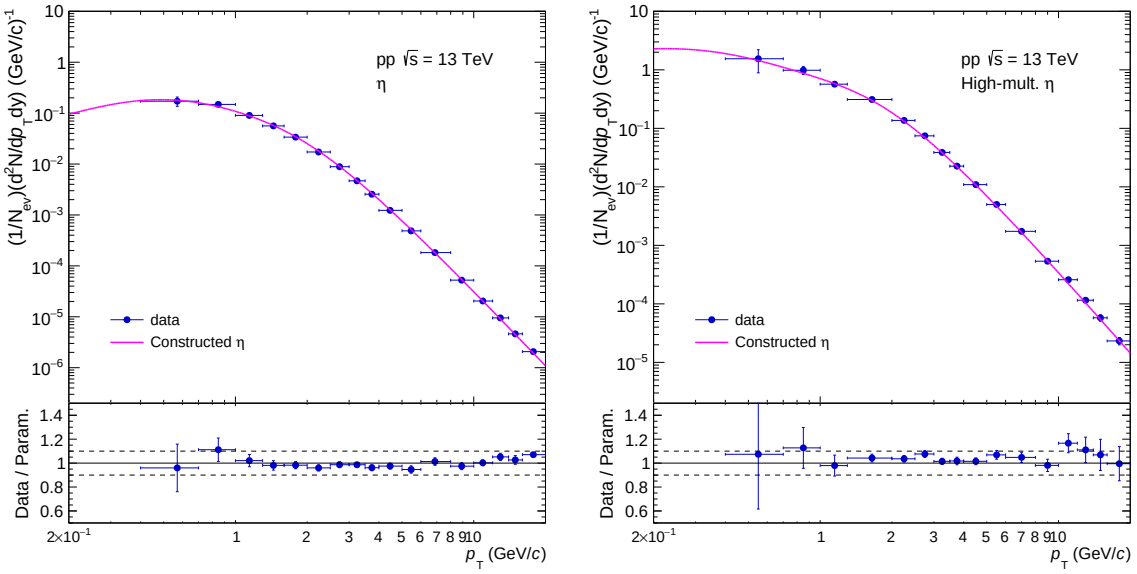

Figure 4.48: Comparison between measured η and constructed η ($= \pi^0 \times \eta/\pi^0$) parameterization for minimum-bias and high-multiplicity cocktails.

For the ϕ meson [155], fitting was performed using the Modified Hagedorn [161]

$$\frac{1}{N_{\rm ev}}\frac{{\rm d}^2N}{{\rm d}p_{\rm T}{\rm d}y} = p_{\rm T} \times A \times (e^{(ap_{\rm T}+bp_{\rm T}^2)} + \frac{p_{\rm T}}{p_0})^{-n}, \tag{4.24}$$

where A, a, b, p_0, n are free parameters. As the ϕ spectrum is measured using data sample collected in 2015, corresponding visible cross section $\sigma^{2015}_{\rm V0AND} = 57.8 \pm 2.9$ mb [162] is used to normalize the number of minimum-bias events. For the systematic uncertainty, the fitting parameter A is scaled by $\pm$ 10%.

For the high-multiplicity ϕ cocktail, the input spectrum is taken from [156], where the definition of multiplicity class is different from this analysis. The $p_{\rm T}$ distribution for multiplicity class I ($\langle {\rm d}N_{\rm ch}/{\rm d}\eta\rangle = 25.75 \pm 0.40$) used in the ϕ analysis [156] is close to our multiplicity class ($= 31.34 \pm 0.52$). Assuming ϕ yield linearly increases with multiplicity, the ϕ spectrum for high multiplicity is obtained by scaling with respect to the class I spectrum. The scaling factor is calculated as

$$\begin{aligned}\frac{\langle {\rm d}N/{\rm d}\eta\rangle_{0-0.1\%}}{\langle {\rm d}N/{\rm d}\eta\rangle_{\rm MultClassI}} &= (31.34 \pm 0.52)/(25.75 \pm 0.40) \\ &= 1.22 \pm 0.03.\end{aligned} \tag{4.25}$$

Fitting examples of ϕ meson are shown in Fig. 4.49.

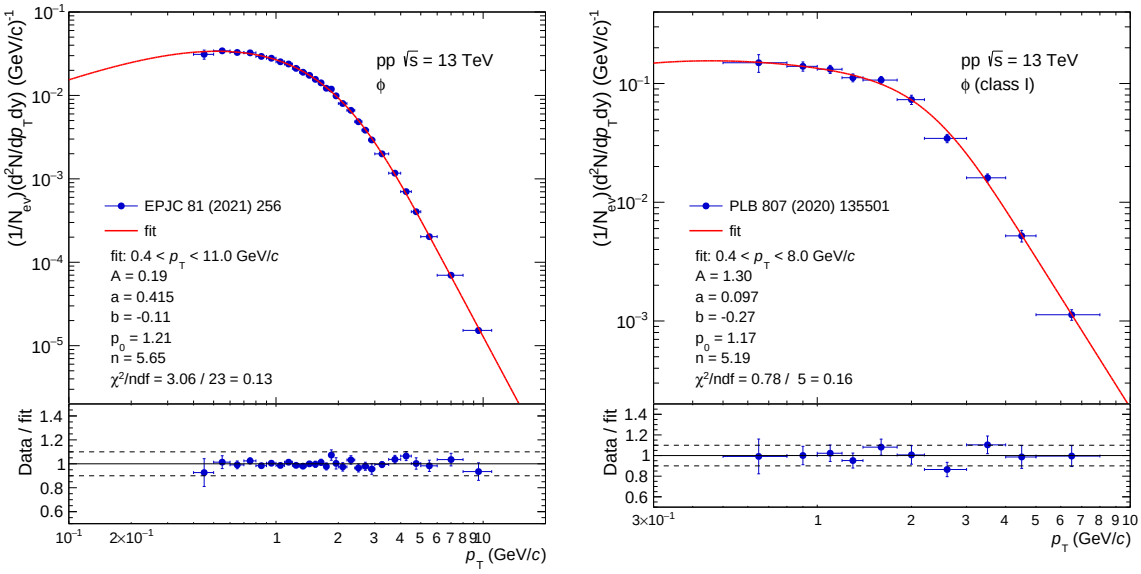

Figure 4.49: Modified Hagedorn fit to ϕ meson in minimum-bias and high-multiplicity cocktails. The minimum-bias ϕ (left) is measured at transverse momentum $p_{\rm T}$ in the range $0.4 < p_{\rm T} < 11$ GeV/c and the high-multiplicity η/π^0 (right) is measured at transverse momentum $p_{\rm T}$ in the range $0.4 < p_{\rm T} < 8$ GeV/c. Both fits are performed at the same measured $p_{\rm T}$ range.

Finally, J/ψ [157] is parameterised by using the power law function (Fig. 4.50)

$$f(p_{\mathrm{T}}) = C \times \frac{p_{\mathrm{T}}}{\{1 + (p_{\mathrm{T}}/p_0)^2\}^n}, \tag{4.26}$$

where C, p_0, n are free parameters. It is known that J/ψ yield increases faster than linearity with respect to charge particle multiplicity [43]. The relative enhancement of J/ψ production is shown in the left of Fig. 4.51 as a function of $\mathrm{d}N_{\mathrm{ch}}/\mathrm{d}\eta/\langle \mathrm{d}N_{\mathrm{ch}}/\mathrm{d}\eta(\mathrm{INEL} > 0)\rangle$ at mid-rapidity $|\eta| < 1$. The closest value of relative charged-particle multiplicity between high-multiplicity events and minimum-bias events is ≈ 4.5 and corresponding scaling factors are 7 for $0 < p_{\mathrm{T}} < 4$ GeV/c, 11 for $4 < p_{\mathrm{T}} < 10$ GeV/c at $\mathrm{d}N_{\mathrm{ch}}/\mathrm{d}\eta/\langle \mathrm{d}N_{\mathrm{ch}}/\mathrm{d}\eta(\mathrm{INEL} > 0)\rangle = 4.33$, respectively. For the systematic uncertainty estimation, the factors were varied by $\pm$ 10%.

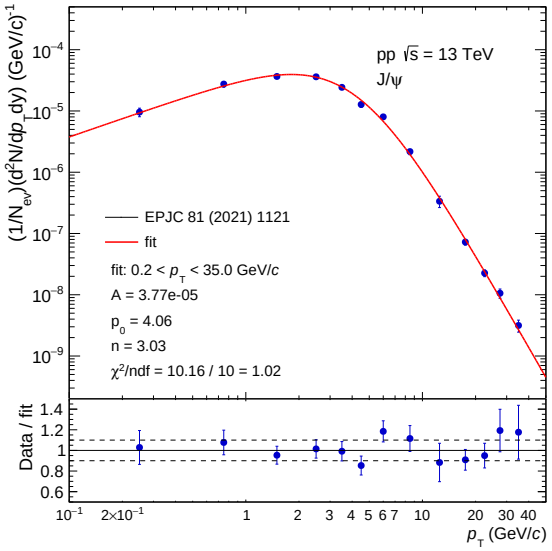

Figure 4.50: Power law fit to J/ψ in minimum-bias events.

Particles are generated based on the parameterizations and acceptance cuts ($|\eta| < 0.8$) are applied to both legs, to be consistent with real data analysis. Generated tracks are smeared using resolution maps prepared year-by-year as described in Sec.4.7.1. Afterward, the cocktail is normalized to the integrated luminosity

$$\mathcal{L}_{\mathrm{int}} = \frac{N_{\mathrm{gen}}}{\sigma_{\mathrm{V0AND}}}, \tag{4.27}$$

where N_{gen} denotes the number of generated events, σ_{V0AND} is the visible cross section reported in Sec. 4.1.4. As the final cocktail needs to be normalized to the number of inelastic pp events, the cocktail yields are divided by $\sigma^{\mathrm{YEAR}}_{\mathrm{V0AND}}/\sigma_{\mathrm{INEL}}$, where σ_{INEL} is total inelastic scattering cross section $\sigma_{\mathrm{INEL}} = 79.5 \pm 1.8$ mb measured by TOTEM experiment [163]. Afterward, the obtained cocktail is combined via weighted average, where the weights are given by the corresponding number of events [5].

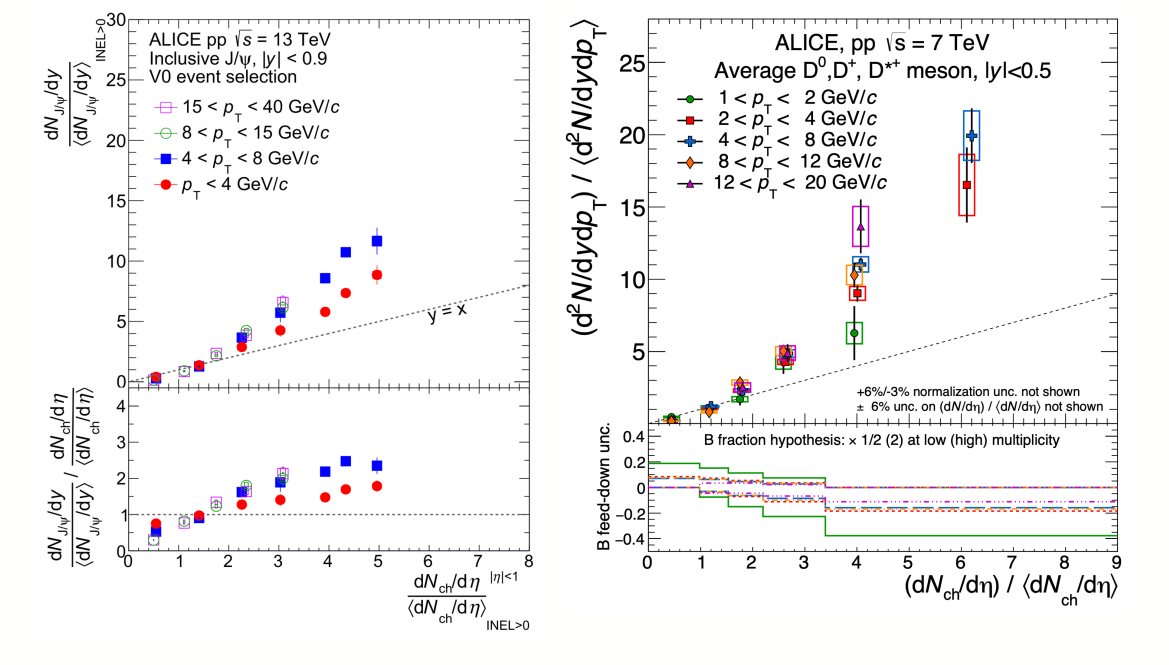

Figure 4.51: Left: normalized inclusive J/ψ yield at mid-rapidity as a function of charged-particle multiplicity in pp collisions at $\sqrt{s}$= 13 TeV [43]. Right: average of D^0, D^+ and D^{*+} relative yields as a function of the relative charged-particle multiplicity at central rapidity [44].

4.8.2 Open Charm and Open Beauty Hadrons

Electron pairs originate from correlated semileptonic decays of $c\bar{c}$ and $b\bar{b}$ are simulated with the leading order (LO) event generator PYTHIA6 with Perugia 2011 tune [136,140]. The PYTHIA6 utilizes LO-pQCD matrix elements for $2 \rightarrow 2$ processes together with a leading-logarithmic p_{T}-ordered parton shower and an underlying-event simulation including multi-parton interactions. The fragmentation and hadronization of the charm and beauty quarks are based on the Lund string model. The Perugia 2011 tune considered the first LHC data, mainly from multiplicity and underlying-event related measurements. In this tune, the parton distribution functions are parametrized with the CTEQ5L functions [164]. The $c\bar{c}$ and $b\bar{b}$ pairs are produced one or event for each in full phase space. The charm is forced to decay semileptonically, while the decay of the beauty is not. They are normalised to the integrated luminosity of pythia events $\mathcal{L}_{\mathrm{int}}$ as follows:

$$\mathcal{L}_{\mathrm{int}} = \frac{(N_{\mathrm{q}} + N_{\mathrm{qbar}})_{y<|1|}/2}{2\mathrm{d}\sigma_{\mathrm{qqbar}}/\mathrm{dy}}, \tag{4.28}$$

where N_{q} (N_{qbar}) is the number of generated quarks (anti quarks), $\mathrm{d}\sigma_{\mathrm{qqbar}}/\mathrm{d}y$ indicates cross section at mid-rapidity. For the $c\bar{c}$ contribution, the branching ratio (BR) of c $\rightarrow$

e needs to be squared as they are forced to decay. The $c\bar{c}$ and $b\bar{b}$ cross sections are

- $\mathrm{d}\sigma_{\mathrm{c\bar{c}}}/\mathrm{d}y|_{y=0} = 1689 \pm 124\ (\mathrm{stat.}) \pm 152\ (\mathrm{syst.})\ ^{+299}_{-296}\ (\mathrm{BR})\ \mu\mathrm{b}$
- $\mathrm{d}\sigma_{\mathrm{b\bar{b}}}/\mathrm{d}y|_{y=0} = 82 \pm 7\ (\mathrm{stat.}) \pm 5\ (\mathrm{syst.}) \pm 5\ (\mathrm{BR})\ \mu\mathrm{b}$

These cross sections are obtained by the re-extraction based on the updated BR($c \to e$) $= 7.3^{+0.61}_{-0.84}\%$ (Fig. 4.63). The re-extraction procedure can be found in Sec. 4.10. Dielectrons from open charm decays in high-multiplicity events are simulated by following the same procedure as J/ψ cocktail. As shown in the right of Fig. 4.51, multiplicity dependence of D meson production with $p_{\mathrm{T}} > 1$ GeV/c at $\sqrt{s} = 7$ TeV is studied [44]. The enhancement factor for each p_{T} interval is taken from the closest value of relative charged-particle multiplicity of our measurement ≈ 4. Afterward, the enhancement factor as a function of p_{T} (Fig. 4.52) is used and open charm contribution in minimum-bias events is scaled according to the factors. Due to the absence of the data below $p_{\mathrm{T}} = 1$ GeV/c indicated in the dashed line, the same enhancement factor in $1 < p_{\mathrm{T}} < 2$ GeV/c is assumed. Here red and blue lines show the upper and lower limits, determined according to the measured values in [44]. The study also reported no significant difference between the production of D mesons and J/ψ from beauty hadron decays. Therefore, the same weights are applied to the open beauty contribution.

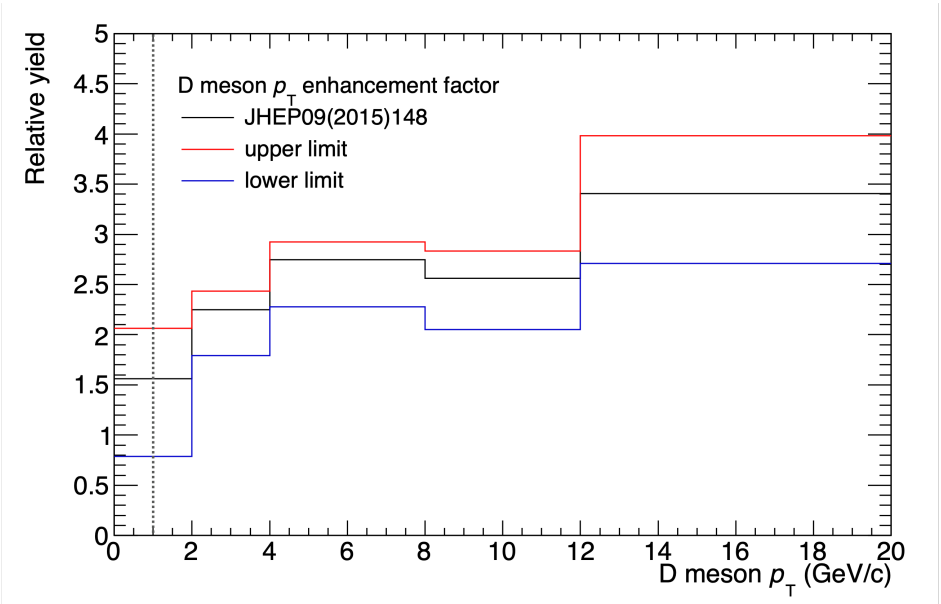

Figure 4.52: D meson enhancement factor as a function of p_{T} for the high-multiplicity heavy-flavour cocktail. Upper (red) and lower (blue) limits are taken to estimate systematic uncertainty.

4.8.3 Systematic Uncertainty

Possible sources of systematic uncertainties for the hadronic cocktail are evaluated as follows:

- Branching ratio (BR)
- Resolution
- Uncertainties of the input spectrum
- m_{T} scaling factor
- Uncertainties of multiplicity dependence of charm and beauty production

The BR-derived systematic uncertainty takes into account the uncertainty of all BRs in all decay modes listed in Table. 4.5. Uncertainties derived from resolution are taken from those evaluated in the previous studies [132]. The uncertainty of the input particle spectrum (π^0, η, ϕ and J/ψ) also contributes to the uncertainty of the cocktail. Each spectrum shifted $\pm1\sigma$ according to the systematic uncertainty and repeated fitting procedure. The uncertainty on the m_{T} scaling factor is relevant for ρ, ω and η' meson only, and those scaling factors vary 20%. For the HM heavy-flavor cocktail, uncertainty on the multiplicity scaling factor is varied according to the upper and lower limit of the enhancement factor shown in Fig. 4.52.

A cocktail is generated by varying each item one by one and the total cocktail is compared to the standard one. The relative uncertainties at minimum-bias and high-multiplicity analysis are shown in Fig.4.53 and 4.54, respectively. Since the m_{T} scaling factor used in the minimum-bias cocktail is commonly used for the high-multiplicity cocktail, the same uncertainty was assigned to the high-multiplicity cocktail. The maximum deviation to the standard is taken as a systematic uncertainty. Each source is added in quadrature. The uncertainty of resolution is taken from a published study [51].

Table 4.6: Summary of systematic uncertainty of minimum-bias and high-multiplicity cocktail.

Source	Uncertainty
Branching ratio (BR)	4%
Resolution	8%
Parameterization	5-10%
Heavy-flavor	8%
m_{T} scaling factor	12% ($\rho/\omega/\eta'$)
Multiplicity scaling (HM only)	$\sim$ 30%

Figure 4.55 and 4.56 show obtained dielectron mass spectra of hadronic cocktails with acceptance cuts and smearing.

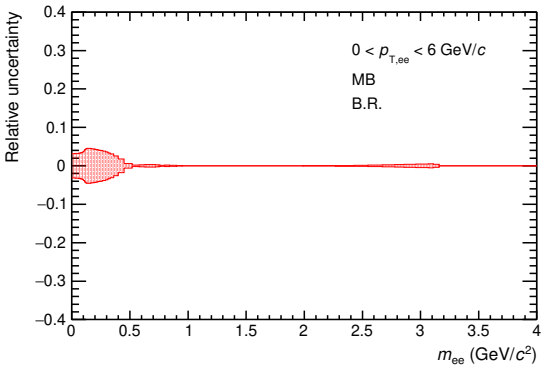

(a) BR

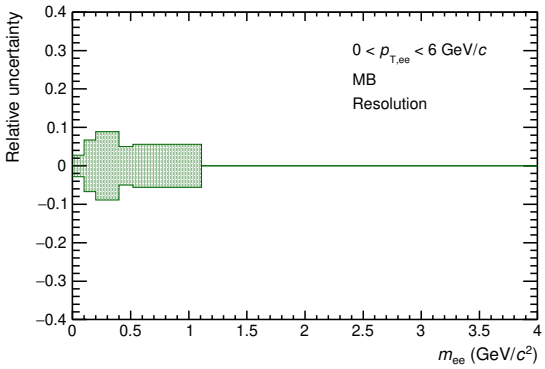

(b) Resolution

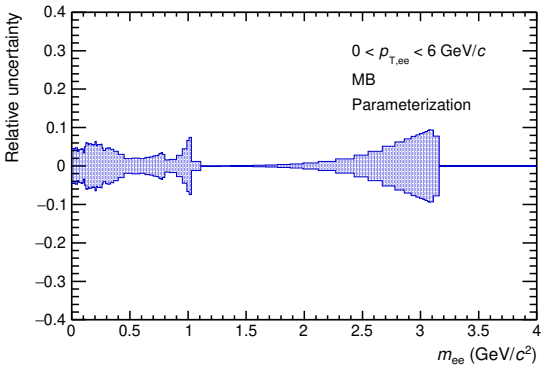

(c) Parameterization of input spectra

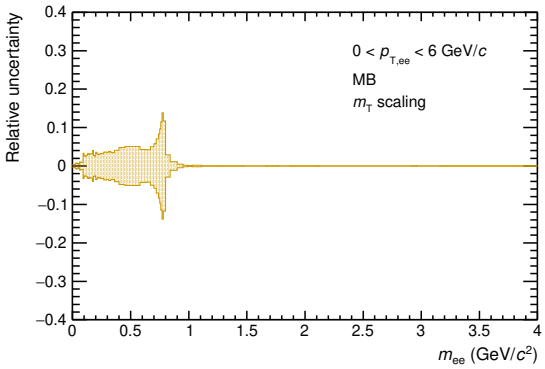

(d) m_{T} scaling

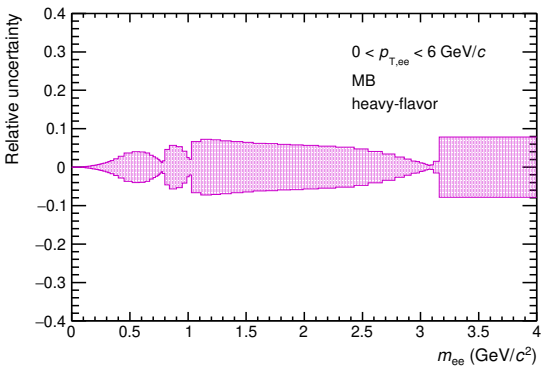

(e) Heavy-flavor

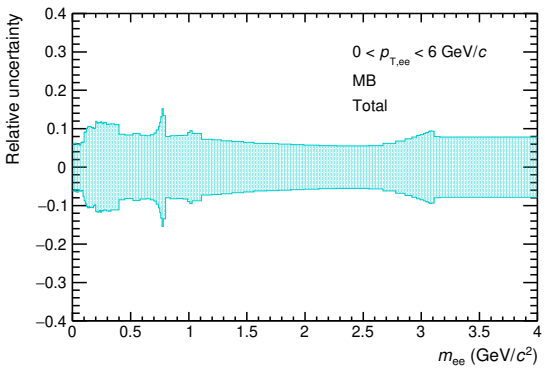

(f) Total

Figure 4.53: Systematic uncertainty of minimum-bias cocktail for each contribution (a)-(e). Characteristic mass dependence (or peaks) corresponds to the mass region of the particle considered. (f) shows total cocktail uncertainty obtained by the quadratic sum of each contribution.

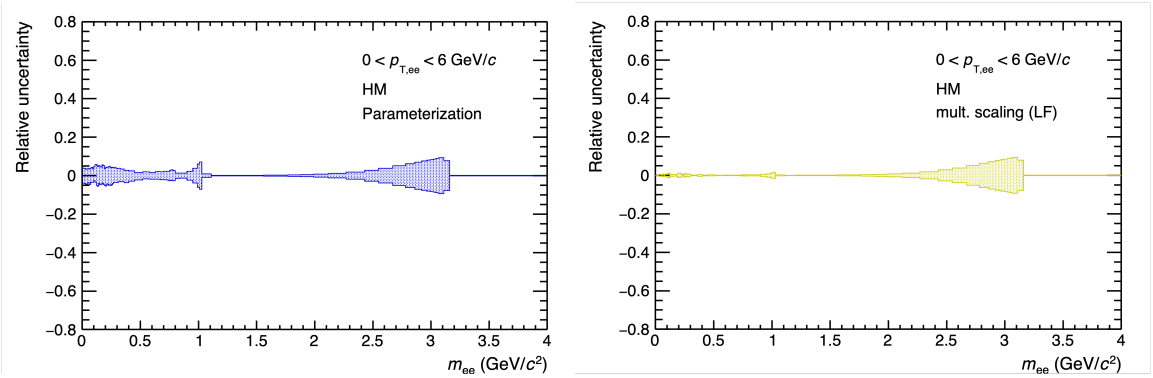

(a) Parameterization of input spectra

(b) Light-flavor Mult. scaling

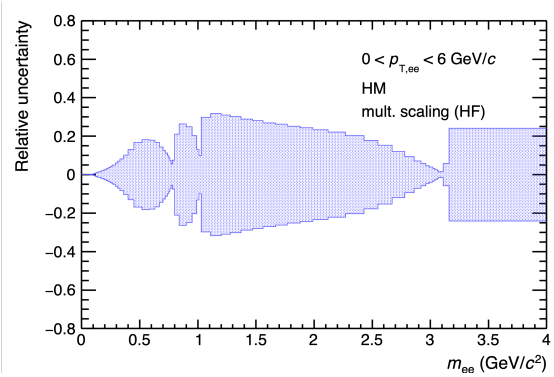

(c) Heavy-flavor Mult. scaling

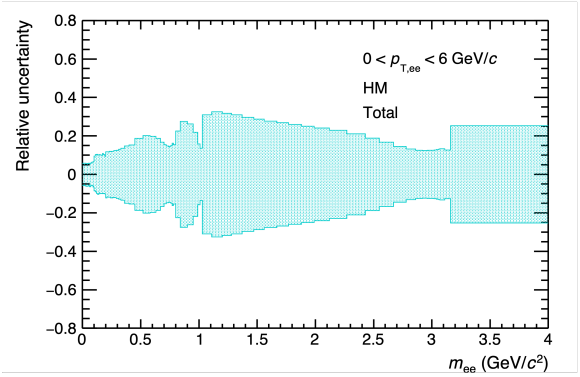

(d) Total

Figure 4.54: Systematic uncertainty of high-multiplicty cocktail for respective sources and total.

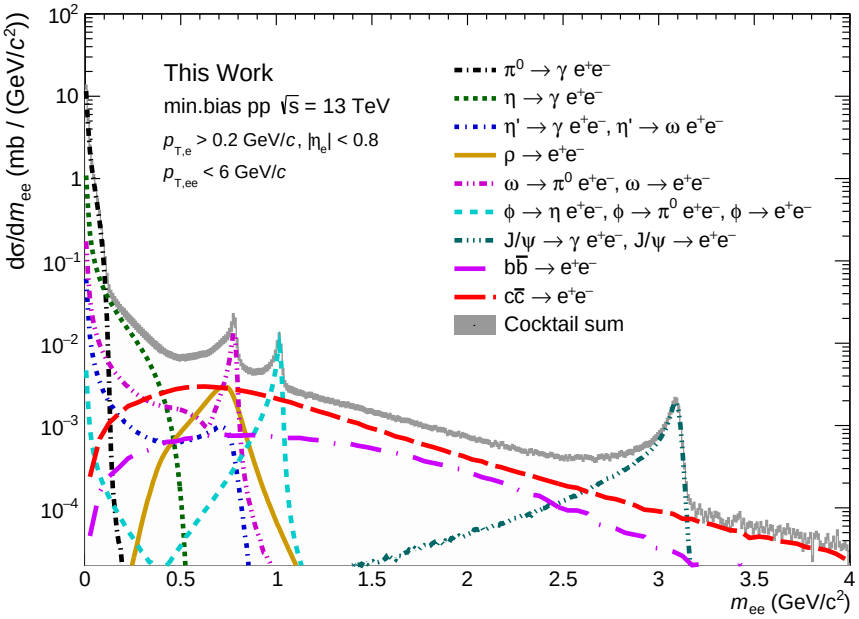

Figure 4.55: Dielectron mass spectra of the hadronic cocktail in pp collisions at $\sqrt{s} = 13$ TeV. The grey band is the sum of all contributions with total systematic uncertainty.

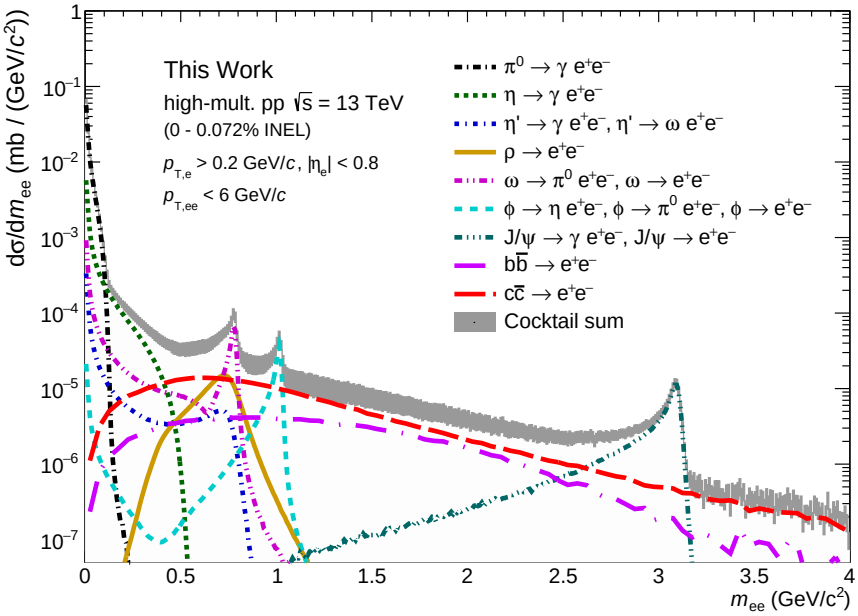

Figure 4.56: Dielectron mass spectra of the hadronic cocktail in high-multiplicity pp collisions at $\sqrt{s} = 13$ TeV. The grey band is the sum of all contributions with total systematic uncertainty.

4.9 Systematic Uncertainty for the Data Analysis

Systematic uncertainties are summarized in this section. Results from minimum bias and high-multiplicity analysis are reported in parallel.

4.9.1 Tracking and PID

The stability of the track and PID selection criteria are a source of systematic uncertainties, which are estimated via cut variations. Variables are changed at the same time, by picking a tighter, standard, or looser value randomly, and extracted corrected signals are compared to the one from a standard selection. The variations are shown in Table 4.7. Those cut settings vary the pairing efficiency by 10%. The RMS of the relative difference with respect to the standard is assigned as systematic uncertainty. To avoid statistical fluctuation, the check is performed using coarse $m_{\rm ee}$ and $p_{\rm T,ee}$ binning:

- $m_{\rm ee}$ binning: 0, 0.04, 0.08, 0.14, 0.35, 1.03, 2.80, 3.10, 4.00,
- $p_{\rm T,ee}$ binning: 0, 0.2, 0.4, 0.6, 0.8, 1.0, 2.0, 3.0, 4.0, 5.0, 6.0, 10.0.

The resulting systematic uncertainties for tracking and PID are 1-4.5% and 1-8% for minimum-bias and high-multiplicity analysis, respectively.

Table 4.7: Tracking and PID selection settings. Texts written in bold are standard.

Requirements	Variations
Max. χ^2 per ITS cluster	3.5, **4.5**, 5.5
Min. number of ITS clusters	2, **3**, 4
Min. number of TPC crossed rows	**100**, 120, 130
Min. number ratio of $N^{\rm TPC\ crossed\ rows}$ / $N^{\rm findable\ clusters}$	0.7, **0.8**, 0.9
Max. fraction of shared TPC clusters	**0.4**, 0.6, 0.8
Max. χ^2 per TPC cluster	3, **4**, 5
TOF electron identification	$\lvert {\rm n}\sigma^{\rm TOF}_{\rm ele}\rvert < 2$, **3**
TPC electron identification	$\lvert {\rm n}\sigma^{\rm TPC}_{\rm ele}\rvert < 2.5$, **3**, 3.5
TPC pion rejection	${\rm n}\sigma^{\rm TPC}_{\rm pion} < 3$, 3.5, **4**
TPC kaon rejection	$\lvert {\rm n}\sigma^{\rm TPC}_{\rm kaon}\rvert <$ **4**, 0.5 shift to upper direction, 0.5 shift to lower direction
TPC proton rejection	$\lvert {\rm n}\sigma^{\rm TPC}_{\rm proton}\rvert <$ **4**, 0.5 shift to upper direction, 0.5 shift to lower direction

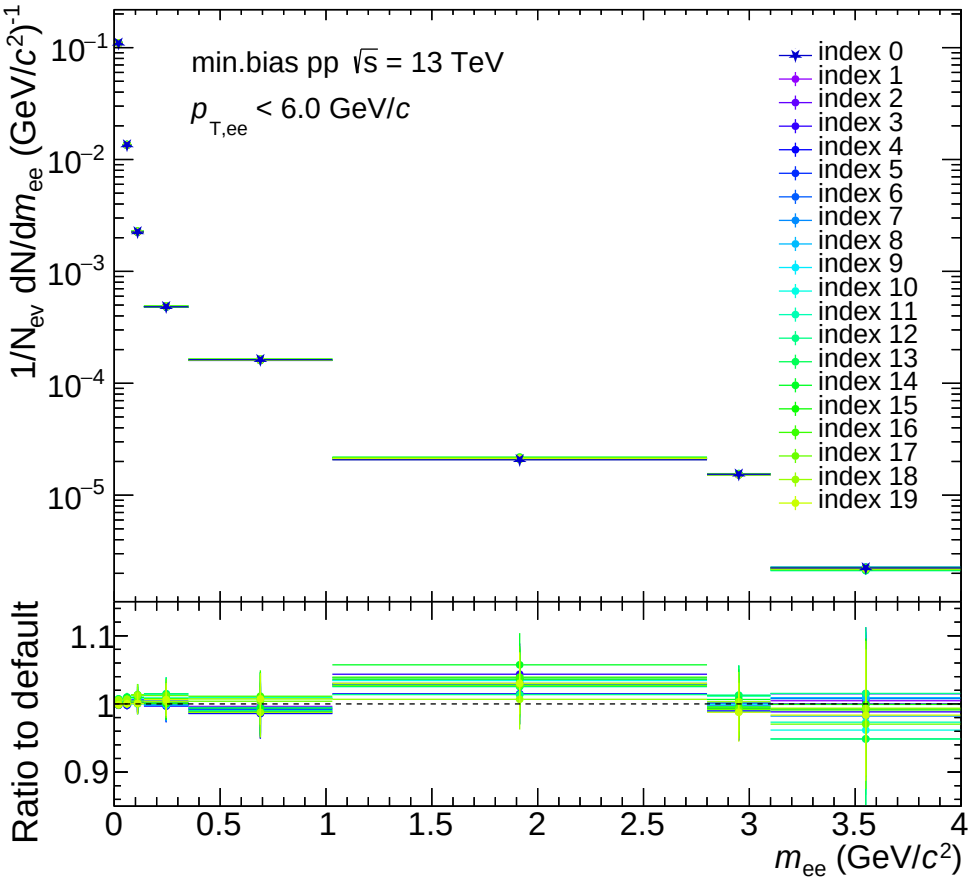

Figure 4.57: Efficiency corrected signal for different track and PID cut variations in minimum-bias events. Index 0 corresponds to the default cut setting and other variations (index i with i = 1-19) are randomly selected track and PID selections listed in Table 4.7

4.9.2 Tracking

ITS-TPC Track Matching

ITS-TPC track matching efficiency is defined as the ratio of tracks reconstructed with clusters in the TPC and the ITS over the total number of TPC tracks. The systematic uncertainty on the efficiency arises from discrepancies in efficiency between data and MC. The uncertainty of the single track efficiency is calculated centrally by the Data Processing Group in ALICE. The p_{T}-dependent uncertainties are evaluated in respective data-taking years (2016, 2017, and 2018). A maximum uncertainty of 3% is taken from the 2018 dataset, which is the largest of the three years, which leads to 6% on the pair level.

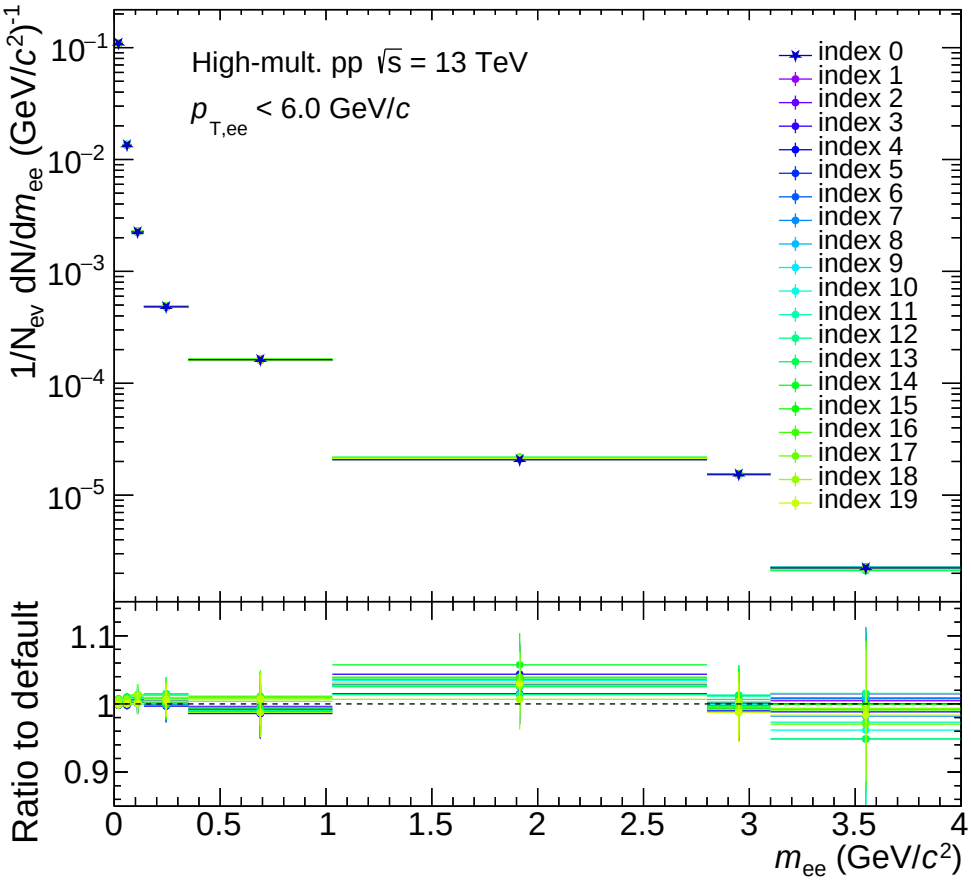

Figure 4.58: Efficiency corrected signal for different track and PID cut variations in HM-triggered events. Index 0 corresponds to the default cut setting and other variations (index i with i = 1–19) are randomly selected track and PID selections listed in Table 4.7

A Hit on The First SPD Layer

A hit on the SPD first layer is required to suppress electrons from photon conversion at the detector material. Unlike other track cuts investigated in the cut variations, this requirement significantly suppresses conversions and change efficiency, therefore we estimate it independently. Charged pions are selected in the TPC with $|\mathrm{n}\sigma^{\mathrm{TPC}}_{\mathrm{pion}}| < 2$, requiring tighter DCA selections ($\mathrm{DCA}_{xy} < 0.1$ (cm) and $\mathrm{DCA}_{z} < 0.1$ (cm)) to suppress secondary pion. The ratio of the number of $\pi^{\pm}$ with a hit in the first SPD layer over the number of $\pi^{\pm}$ with a hit in any of two SPD layers are calculated in data and MC and then, their relative difference is taken as a systematic uncertainty. As shown in Fig.4.59, the results were found to be at most 1% for a single track level for both minimum-bias and high-multiplicity events.

No Shared ITS Cluster

The requirement of no shared ITS cluster is also studied, and the efficiency is defined as the ratio of the number of electron candidates with and without no shared ITS cluster requirement. As a result, it was found that the Monte Carlo simulation reproduces experimental data well in minimum-bias events (Fig.4.60), whereas one from high-multiplicity events is slightly worse. Uncertainty from the requirement of a hit in the first SPD layer, and no shared ITS cluster are added in quadrature, and 2% (minimum-bias) and 3% (high-multiplicity) uncertainties are assigned to the the pair.

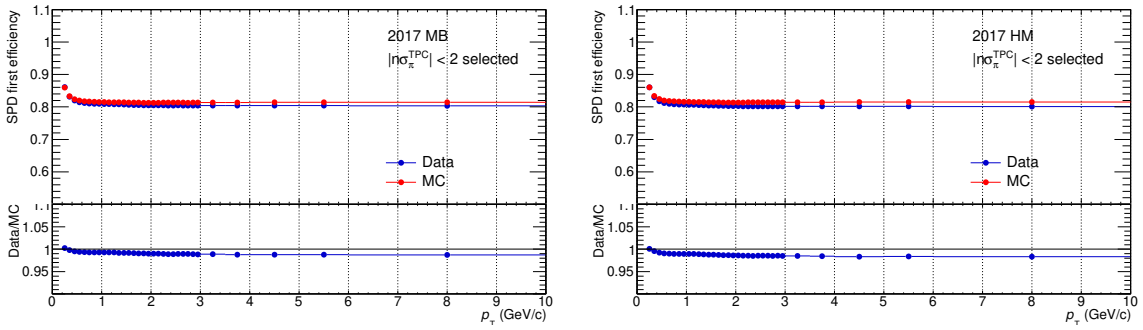

Figure 4.59: Comparison of the efficiency of with and without hit on the first SPD layer requirement in data and MC in minimum-bias (left) and high-multiplicity (right) events, respectively.

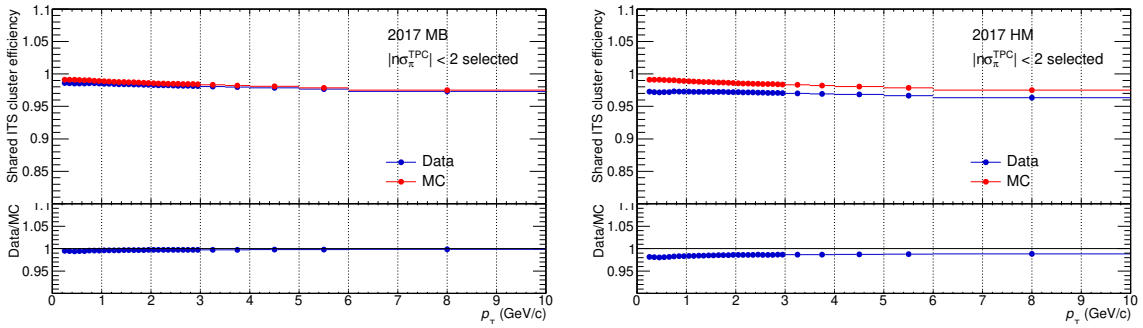

Figure 4.60: Comparison of the efficiency of with and without no shared ITS cluster requirement in data and MC in minimum-bias (left) and high-multiplicity (right) events, respectively.

4.9.3 φ_v rejection

The systematic uncertainty of ϕ_v rejection is estimated as varying maximum φ_v rejection window. $\pi/2$, 2 (standard), 2.3 rad are tested. In total, 0.9 - 2.2% (0.5 - 5.3%) is assigned below 100 MeV/c^2 in minimum bias (high-multiplicity) analysis.

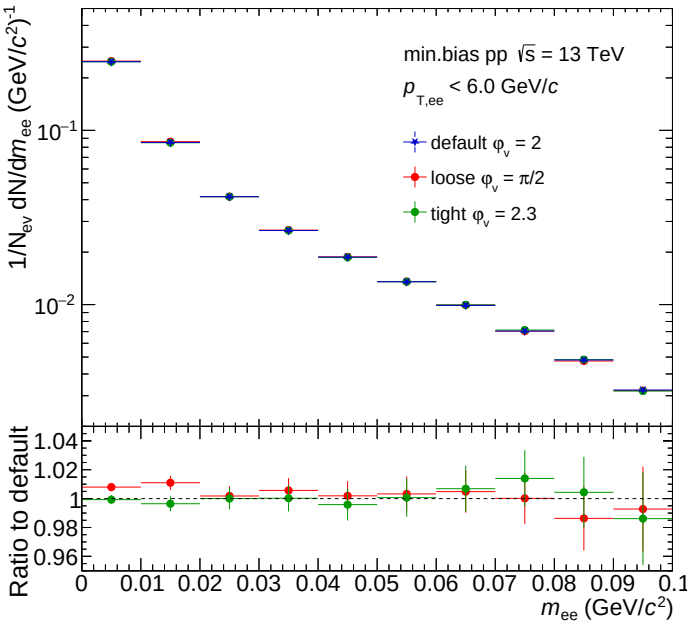

Figure 4.61: Efficiency corrected signal in the range $p_{\mathrm{T,ee}} < 6$ GeV/c for differnt φ_v rejection cut in minimum-bias events.

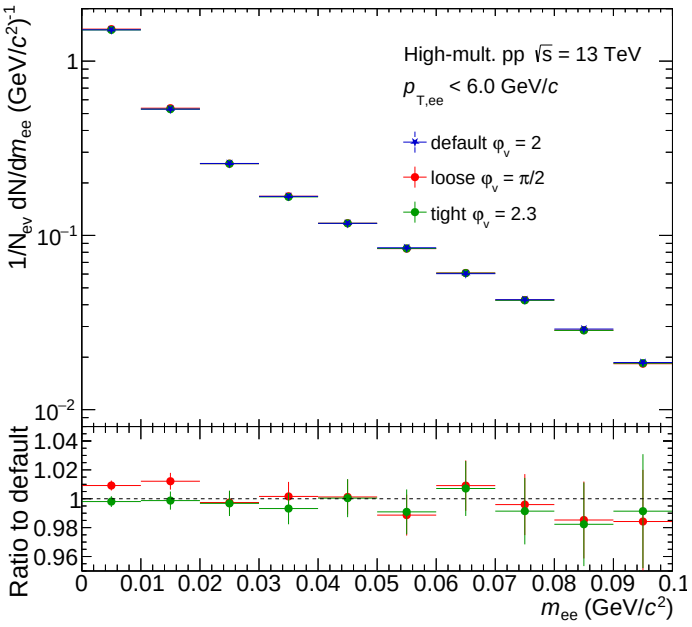

Figure 4.62: Efficiency corrected signal in the range $p_{\mathrm{T,ee}} < 6$ GeV/c for differnt φ_v rejection cut in high-multiplicity events.

4.9.4 Total Systematic Uncertainty

The summary of each contribution for minimum bias and high-multiplicity analysis are listed in the Table 4.8. The total systematic uncertainties are obtained by adding individual contributions in quadrature.

Table 4.8: Summary of total systematic uncertainty of minimum bias and high-multiplicity data analysis

Source	MB	HM
ITS-TPC track matching	6%	6%
Tracking + PID (mass dep.)	1-4.5%	1-8%
Shared ITS cluster & hit on first SPD cluster	2%	3%
φ_v cut ($m_{\mathrm{ee}} < 0.100$ GeV/c^2)	0.9-2.2%	0.5-5.3%

4.10 Charm and Beauty Production Cross Sections

The charm and beauty cross sections are extracted from the dielectron mass spectrum in the IMR ($1.03 < m_{\rm ee} < 2.86$ GeV/c^2), where the dominant contribution is electrons from open heavy-flavour hadron decays. The detailed study performed in the previous study [132, 143] and results were reported in [51] as follows.

- $\mathrm{d}\sigma_{\rm c\bar{c}}/\mathrm{d}y|_{y=0} = 974 \pm 138$ (stat.) ± 140 (syst.) ± 214 (BR) μb
- $\mathrm{d}\sigma_{\rm b\bar{b}}/\mathrm{d}y|_{y=0} = 79 \pm 14$ (stat.) ± 11 (syst.) ± 5 (BR) μb

At that time, the branching fraction of charm-hadron decays to electron BR($c \rightarrow e$) was $9.6 \pm 0.4\%$. In this thesis, we re-extracted charm and beauty cross sections i.e., $\sigma_{\rm c\bar{c}}$ and $\sigma_{\rm b\bar{b}}$ at mid-rapidity with 4 times larger statistics compared to the previous study. In addition, with updated BR($c \rightarrow e$), This re-evaluation will lead to the reduction of systematic uncertainty of hadronic cocktail from heavy-flavour hadron decays. In addition, recently ALICE reported measurement of the charm fragmentation function in pp collisions at $\sqrt{s} = 5.02$ TeV [165]. According to this result the effective BR($c \rightarrow e$) was evaluated to $7.3^{+0.61}_{-0.84}\%$ [166].

Measured dielectron cross section in the intermediated mass region ($1.03 < m_{\rm ee} < 2.86$ GeV/c^2) below $p_{\rm T,ee} = 6$ GeV/c are selected and projected over two-dimensional invariant mass $m_{\rm ee}$ and pair transverse momentum $p_{\rm T,ee}$ distributions. A simultaneous fit to the mass and pair transverse momentum is performed with the least square method by using the following function

$$f(m_{\rm ee}, p_{\rm T,ee}) = S_{\rm LF} N_{\rm LF} + S_{\rm J/\psi} N_{\rm J/\psi} + S_{\rm c\bar{c}} N_{\rm c\bar{c}} + S_{\rm b\bar{b}} N_{\rm b\bar{b}}, \tag{4.29}$$

where, N_i with $i =$ LF, J/ψ, $c\bar{c}$, $b\bar{b}$ stand for the dielectron contribution from light-flavour and J/ψ, charm and beauty hadron decays, and S_i with $i =$ LF, J/ψ, $c\bar{c}$, $b\bar{b}$ are corresponding free parameters. Each contribution is normalised to the MC template from the hadronic cocktail simulation described in Sec. 4.8. The S_i of light-flavour and J/ψ contribution is fixed to 1, while $S_{\rm c\bar{c}}$ and $S_{\rm b\bar{b}}$ are kept free. $N_{\rm c\bar{c}}$ and $N_{\rm b\bar{b}}$ are normalised to the integrated luminosity $\mathcal{L}_{\rm int}$:

$$\mathcal{L}_{\rm int} = \frac{(N_{\rm q} + N_{\rm \bar{q}})_{y<|1|}/2}{2\mathrm{d}\sigma_{\rm q\bar{q}}/\mathrm{dy}}, \tag{4.30}$$

where $N_{\rm q}$ ($N_{\rm \bar{q}}$) is the number of generated quarks (antiquarks), $\mathrm{d}\sigma_{\rm q\bar{q}}/\mathrm{d}y$ indicates the cross section at mid-rapidity. The two fit parameters are the scaling factors with respect to the reference charm and beauty cross sections

$$\mathrm{d}\sigma_{\rm c\bar{c}}/\mathrm{d}y|_{y=0} = S_{\rm c\bar{c}} \times \mathrm{d}\sigma_{\rm c\bar{c}}/\mathrm{d}y|^{\rm ref}_{y=0} \tag{4.31}$$

$$\mathrm{d}\sigma_{\rm b\bar{b}}/\mathrm{d}y|_{y=0} = S_{\rm b\bar{b}} \times \mathrm{d}\sigma_{\rm b\bar{b}}/\mathrm{d}y|^{\rm ref}_{y=0}, \tag{4.32}$$

where $\mathrm{d}\sigma_{\rm c\bar{c}}/\mathrm{d}y|^{\rm ref}_{y=0}$ and $\mathrm{d}\sigma_{\rm b\bar{b}}/\mathrm{d}y|^{\rm ref}_{y=0}$ are normalised to the published values mentioned above. For each combination of scaling scaling factors $S_{\rm c\bar{c}}$ and $S_{\rm b\bar{b}}$ the χ^2 value is

calculated as

$$\chi^2 = \sum_i^n \left(\frac{x_i - \mu_i}{\sqrt{(\sigma_{x_i}^{stat})^2 + (\sigma_{\mu_i}^{stat})^2}} \right)^2. \tag{4.33}$$

The values of the data points and MC simulations in bin i are given by x_i and μ_i, and $\sigma_{x_i}^{stat}$ and $\sigma_{\mu_i}^{stat}$ are their statistical uncertainties. The result of the fit is determined by the minimum of the χ^2 value. Figure.4.63 shows the scan of the χ^2 value within parameter space. The magenta and cyan dashed lines show statistical uncertainty of $S_{\mathrm{c\bar{c}}}$ and $S_{\mathrm{b\bar{b}}}$, respectively. The point where the two lines intersect gives minimum χ^2. The obtained scaling factors are

$$S_{\mathrm{c\bar{c}}} = 1.735 \pm 0.13 \text{ (stat.)},$$
$$S_{\mathrm{b\bar{b}}} = 1.038 \pm 0.09 \text{ (stat.)}.$$

The fit quality is very good ($\chi^{2/\mathrm{ndf}} = 59.94/66$) and it was found that these factors are highly anti-correlated (-0.67), which was confirmed in the previous analysis. The systematic uncertainty is estimated as follows:

- Data points are shifted $\pm$ 1σ coherently in each $p_{\mathrm{T,ee}}$ slice assuming data points are correlated point by point.
- BR of charm and beauty are varied $\pm$ 1σ.

Then fitting is repeated and relative uncertainty with respect to default is considered as systematic uncertainty. In this way, extracted heavy-flavor cross sections are

- $\mathrm{d}\sigma_{\mathrm{c\bar{c}}}/\mathrm{d}y|_{y=0} = 1689 \pm 124 \text{ (stat.)} \pm 152 \text{ (syst.)} \, ^{+299}_{-296} \text{ (BR) } \mu\mathrm{b}$
- $\mathrm{d}\sigma_{\mathrm{b\bar{b}}}/\mathrm{d}y|_{y=0} = 82 \pm 7 \text{ (stat.)} \pm 5 \text{ (syst.)} \pm 5 \text{ (BR) } \mu\mathrm{b}$.

Compared to the previous study [51], the statistical and systematic uncertainty of these cross sections are reduced by half. With this update of BR, the central value of the charm and beauty cross sections in pp collisions at $\sqrt{s} = 5.02$ TeV [167] and at $\sqrt{s} = 7$ TeV [144] are also changed accordingly. All these values are monotonically increased. Furthermore, the obtained charm production cross section was found to be consistent with fixed order plus next-to-leading logarithms (FONLL) calculations [168].

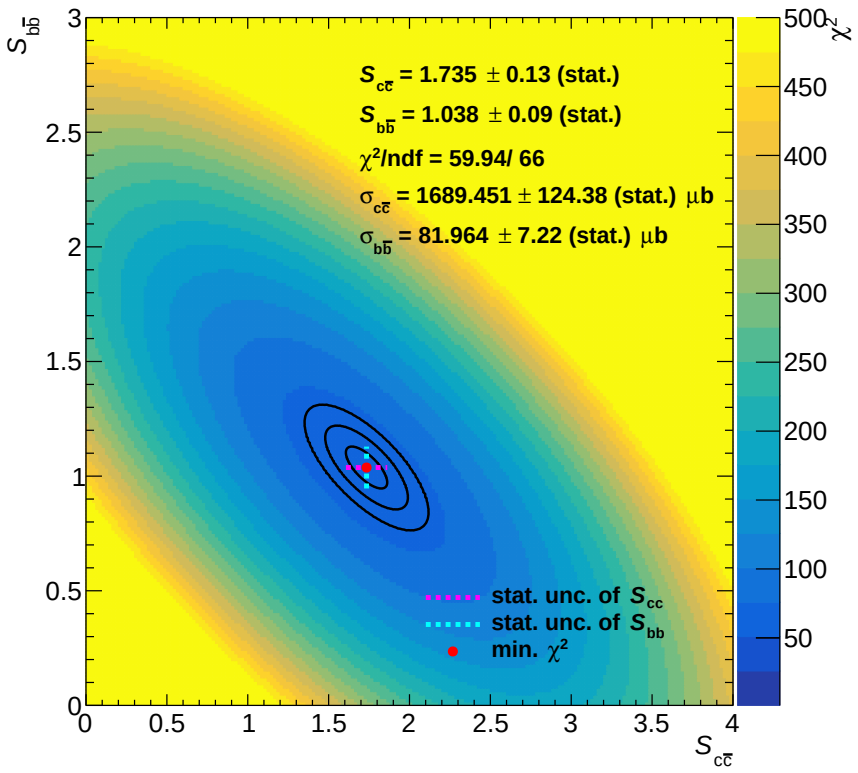

Figure 4.63: Scan of χ^2-value within parameter space. The minimum χ^2 of this map is shown in the red point, where the red and green dotted lines are crossed. Black lines show the error ellipse of the two parameters corresponding to 1σ, 2σ, 3σ contours with respect to the minimum χ^2, from inside out.

4.11 Dielectron Cross Section

The dielectron mass $m_{\rm ee}$ and transverse momentum $p_{\rm T,ee}$ spectra are presented. The differential dielectron cross section is given by

$$\frac{\mathrm{d}^2\sigma_{\rm ee}}{\mathrm{d}m_{\rm ee}\mathrm{d}p_{\rm T,ee}} = \frac{1}{\mathcal{L}_{\rm int}} \frac{S\left(m_{\rm ee}, p_{\rm T,ee}\right)}{\Delta m_{\rm ee} \varepsilon_{\rm ee}^{\rm trig} \varepsilon_{\rm ee}^{\rm vtx} \varepsilon_{\rm ee}^{\rm rec}\left(m_{\rm ee}, p_{\rm T,ee}\right)} \tag{4.34}$$

where

- $S(m_{\rm ee}, p_{\rm T,ee})$ is measured dielectron signal extracted in Sec. 4.6,
- $\mathcal{L}_{\rm int}$ is integrated luminosity reported in Sec. 4.1,
- $\Delta m_{\rm ee}$ and $\Delta p_{\rm T,ee}$ is the bin width in GeV,
- $\varepsilon_{\rm ee}^{\rm trig} = 0.99 \pm 0.01$ is taken from the previous study [132],
- $\varepsilon_{\rm ee}^{\rm vtx} = 1$ is vertex efficiency described in Sec. 4.1.4
- $\varepsilon_{\rm ee}^{\rm rec}(m_{\rm ee}, p_{\rm T,ee})$ is the pair reconstruction efficiency studied in Sec. 4.7,

The results are shown as either $\mathrm{d}\sigma/\mathrm{d}m_{\rm ee}$ or $\mathrm{d}\sigma/\mathrm{d}p_{\rm T,ee}$ presented in the ALICE central barrel acceptance $|\eta| < 0.8$ and $p_{\rm T,e} > 0.2$ GeV/c. The choice of mass binning in each $p_{\rm T,ee}$ bin was defined to be consistent with previous study [132]. The dielectron invariant mass spectrum integrated over $p_{\rm T,e} < 6$ GeV/c^2 is shown in Fig. 4.64. The experimental data is compared with the expected contribution of dielectrons from known hadron decays. Thanks to the measured input spectra (π^0, η, ϕ and J/ψ), and re-extracted heavy-flavor cross sections at IMR, the data and the hadronic cocktail are in good agreement within uncertainties over the whole mass range. This can be verified by looking at the dielectron $p_{\rm T,ee}$ spectrum in different $m_{\rm ee}$ intervals as shown in Fig. 4.65. Figure 4.66 shows mass spectra in the respective $p_{\rm T,ee}$ intervals. The $p_{\rm T,ee}$ spectra are well described by the hadronic cocktail for all $m_{\rm ee}$ slices.

Similar studies are performed for the high-multiplicity data analysis as a function of invariant mass (Fig. 4.67). The high-multiplicity π^0 spectrum was measured above $p_{\rm T} = 0.4$ GeV/c (right of Fig. 4.46), while one from minimum-bias starts at $p_{\rm T} = 0.2$ GeV/c (left of Fig. 4.46). Due to this limited $p_{\rm T}$ range, the constraint on the π^0 parameterization is not enough and the resulting π^0 cocktail tends to overestimate data, although being compatible with data within uncertainties. This overestimation is propagated to the cocktail contributions from decays of η and other $m_{\rm T}$-scaled particles such as ω meson as they are related to the π^0 cocktail. This can be visible in Fig. 4.68 and 4.69 (top left). Note that the impact on the direct-photon analysis is limited because overestimation appears below 1 GeV/c. Above $p_{\rm T,ee} = 1$ GeV/c, where we extract photon yield, it is verified that the data and the cocktail are consistent. Note that the largest source of the uncertainty of the hadronic cocktail comes from $p_{\rm T}$-dependent multiplicity scaling factor of heavy-flavor hadrons. The high-multiplicity

data and the cocktail are consistent with uncertainty. One can see that the hadronic cocktail describes the data for all $p_{\mathrm{T,ee}}$ slices over the whole investigated mass range is under control. Enlarged figures of the low-mass region above $p_{\mathrm{T,ee}} > 1$ GeV/c can be found in Appendix. C.

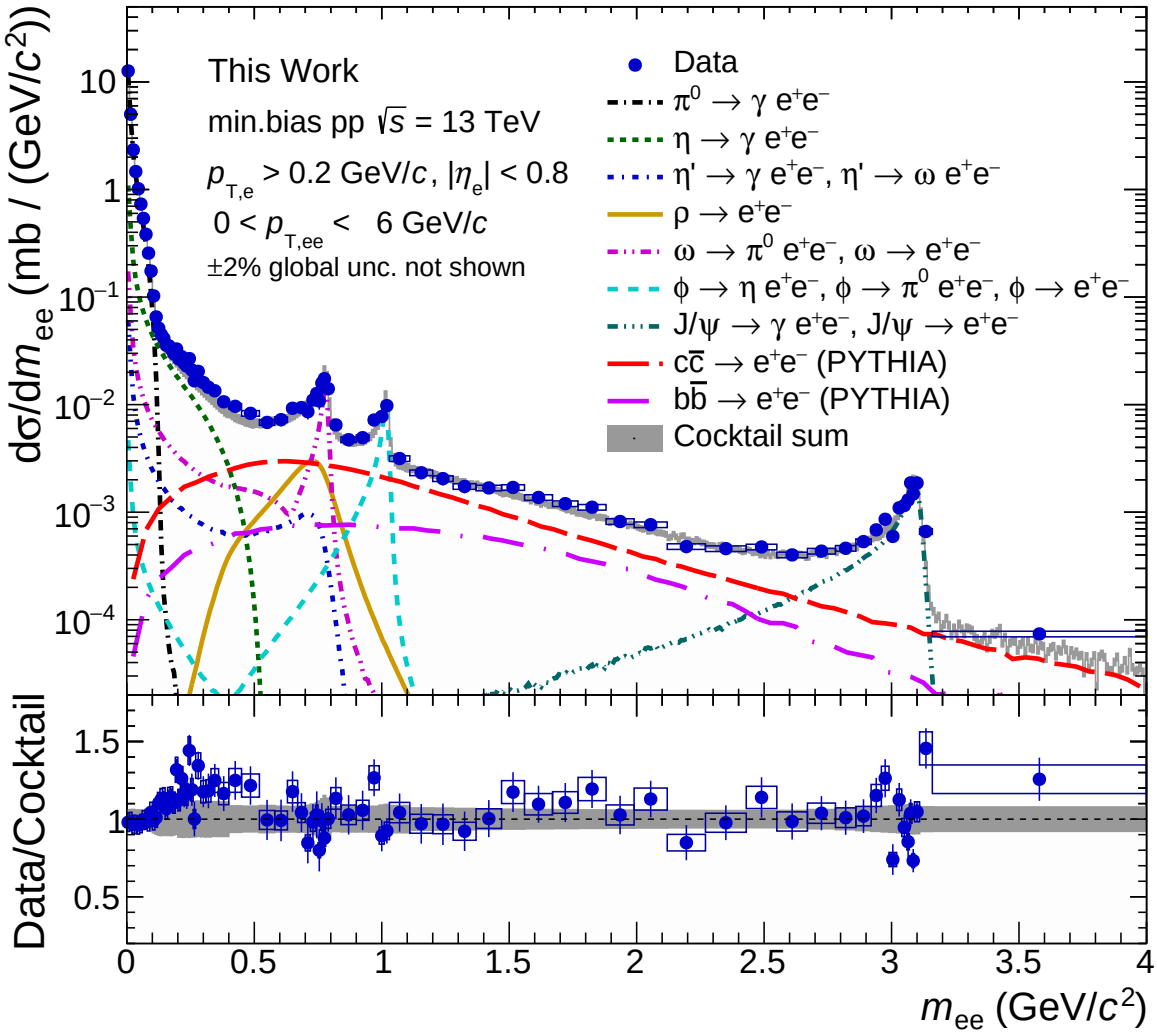

Figure 4.64: The dielectron cross section in inelastic pp collisions at $\sqrt{s} = 13$ TeV as a function of invariant mass in the range $p_{\mathrm{T,ee}} < 6$ GeV/c. The global scale uncertainty on the pp luminosity (2%) is not shown. Statistical and systematic uncertainties of the data are displayed as vertical bars and boxes. The expectation from the hadronic decay cocktail is shown as a band, together with individual sources.

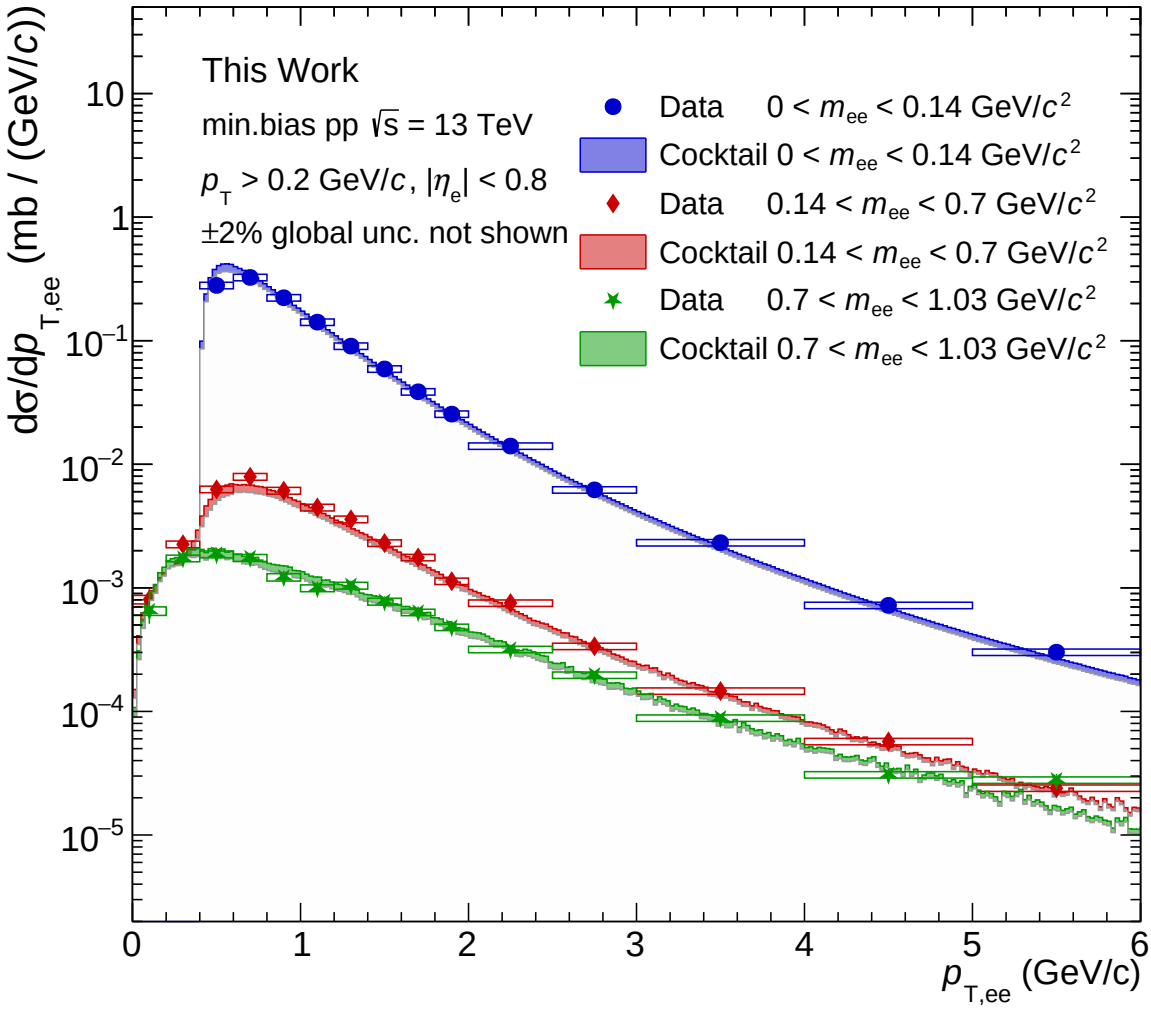

Figure 4.65: The dielectron cross section in inelastic pp collisions at $\sqrt{s} = 13$ TeV as a function of pair transverse momentum $p_{\mathrm{T,ee}}$. The global scale uncertainty on the pp luminosity (2%) is not shown. Statistical and systematic uncertainties of the data are displayed as vertical bars and boxes. Expectation from the hadronic decay cocktail is shown as a band.

4.12 Direct Photon Analysis

In the previous sections, we measured the dielectron continuum in minimum-bias and high-multiplicity events. In virtual photon analysis, a low invariant mass region is relevant for the extraction of direct-photon signals. Direct-photon fraction r is defined as

$$r = \frac{\gamma_{\mathrm{dir}}}{\gamma_{\mathrm{incl}}} = \frac{\gamma^*_{\mathrm{dir}}}{\gamma^*_{\mathrm{incl}}}\Big|_{m=0}, \tag{4.35}$$

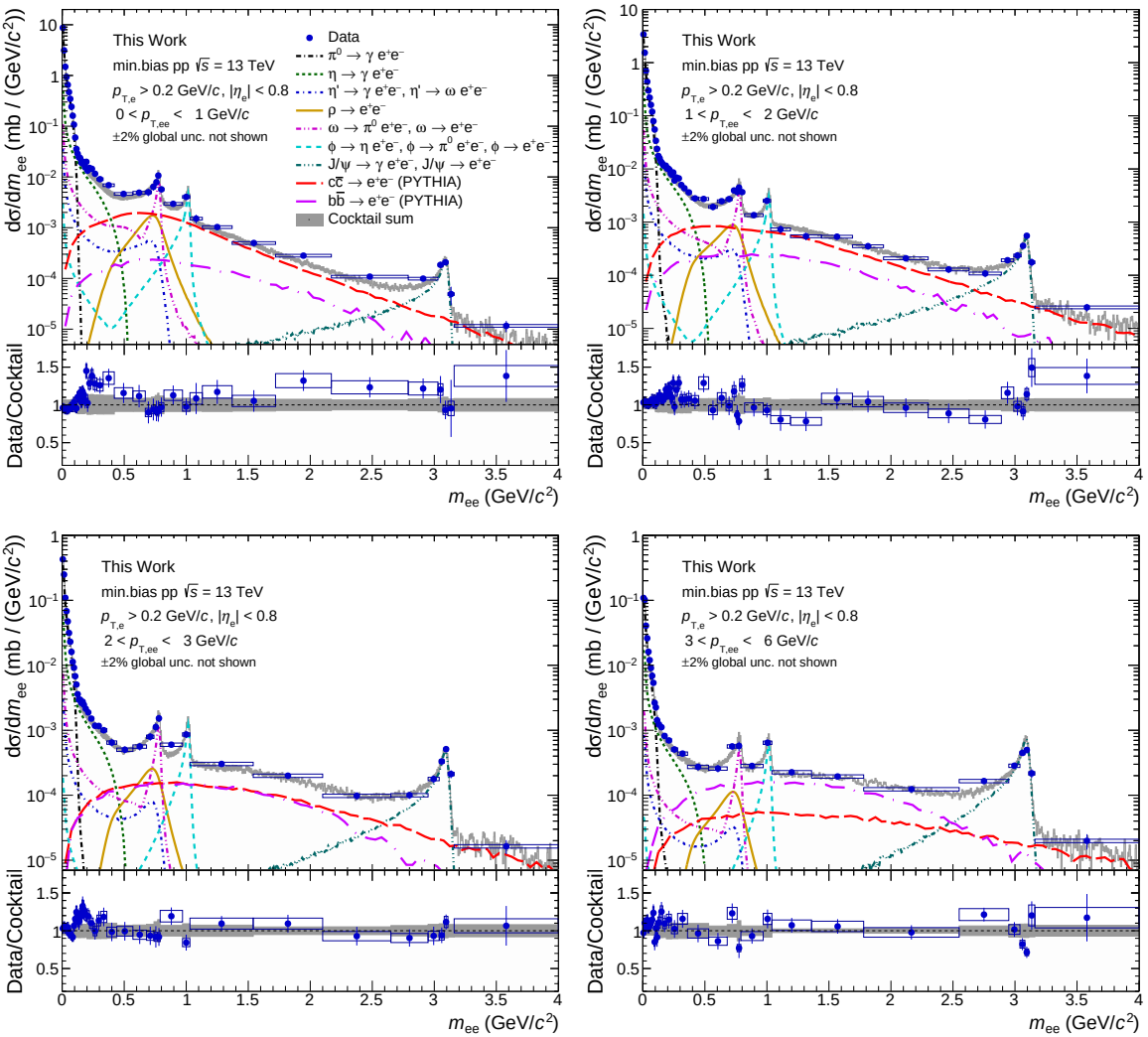

Figure 4.66: The dielectron cross section in inelastic pp collisions at $\sqrt{s} = 13$ TeV as a function of invariant mass in different $p_{\mathrm{T,ee}}$ bins: $0 < p_{\mathrm{T,ee}} < 1$ GeV/c (top left), $1 < p_{\mathrm{T,ee}} < 2$ GeV/c (top right), $2 < p_{\mathrm{T,ee}} < 3$ GeV/c (bottom left), and $3 < p_{\mathrm{T,ee}} < 6$ GeV/c (bottom right), respectively. The global scale uncertainty on the pp luminosity (2%) is not shown. The statistical and systematic uncertainties of the data are displayed as vertical bars and boxes. The expectation from the hadronic decay cocktail is shown as a band, and the data-to-cocktail ratio is presented below together with the cocktail uncertainty.

where γ_{incl} and γ_{decay} stands for inclusive and decay photon. With the direct-photon fraction r and relation $\gamma_{\mathrm{dir}} = \gamma_{\mathrm{incl}}$ - γ_{decay}, direct photon is calculated

$$\gamma_{\mathrm{dir}} = \frac{r}{1-r} \times \gamma_{\mathrm{decay}} \tag{4.36}$$

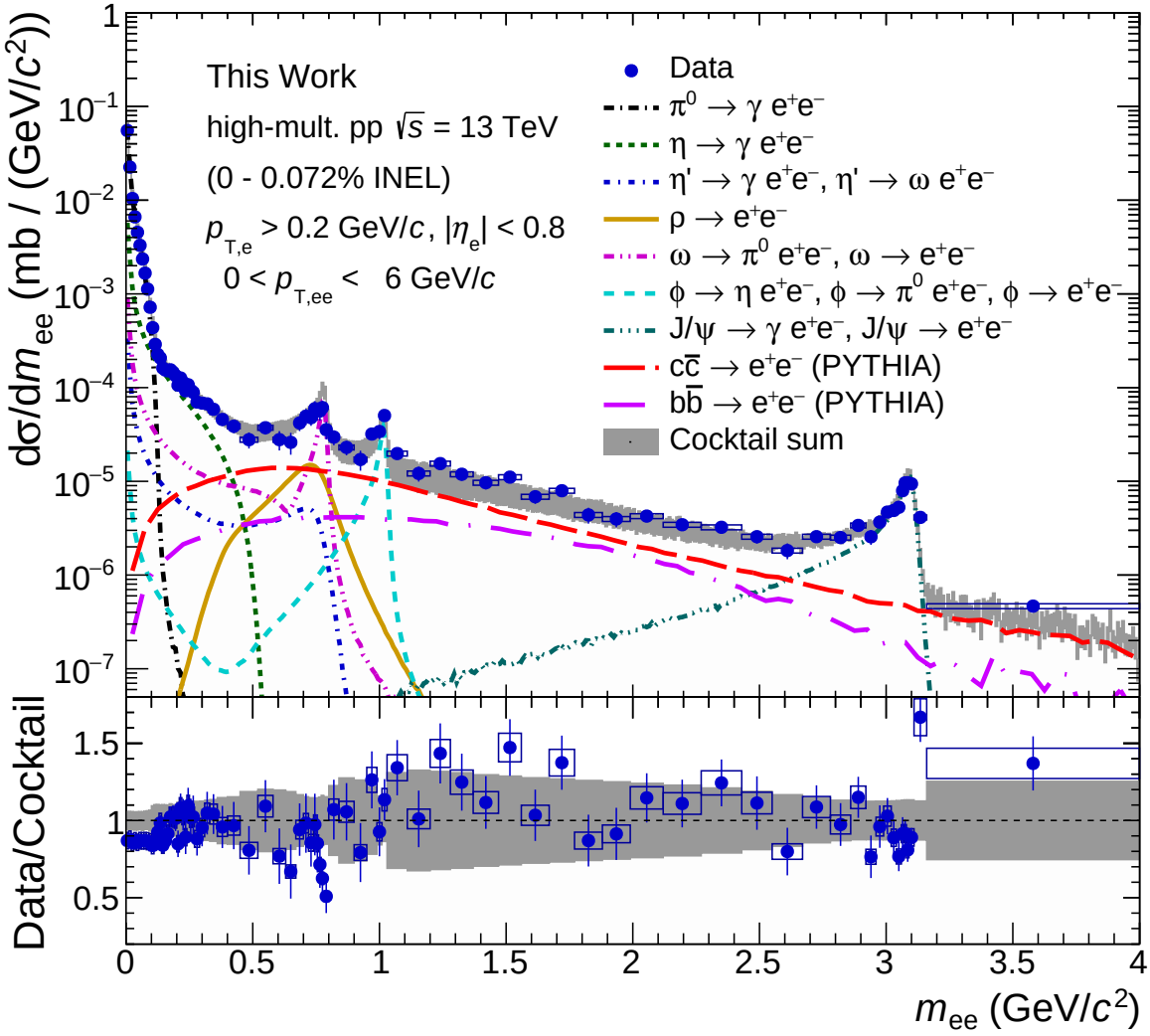

Figure 4.67: The dielectron invariant yield in high-multiplicity pp collision as a function of invariant mass in the range $p_{\mathrm{T,ee}} < 6$ GeV/c. Statistical and systematic uncertainties of the data are displayed as vertical bars and boxes, respectively. Expectation from the hadronic decay cocktail is shown as a band, together with individual sources.

4.12.1 Direct-Photon Signal Extraction

The r is extracted by a fit to the e^+e^- invariant mass distribution above π^0 mass with virtual photon contribution plus other contributions from hadron decay:

$$d\sigma/dm_{\mathrm{ee}} = r f_{\mathrm{dir}}(m_{\mathrm{ee}}) + (1-r) f_{\mathrm{LF}}(m_{\mathrm{ee}}) + f_{\mathrm{HF}}(m_{\mathrm{ee}}), \tag{4.37}$$

where $f_{\mathrm{LF}}(m_{\mathrm{ee}})$ and $f_{\mathrm{HF}}(m_{\mathrm{ee}})$ are contributions from light-flavour and heavy-flavour decays respectively, $f_{\mathrm{dir}}(m_{\mathrm{ee}})$ is the shape of direct photon contribution. The $f_{\mathrm{HF}}(m_{\mathrm{ee}})$

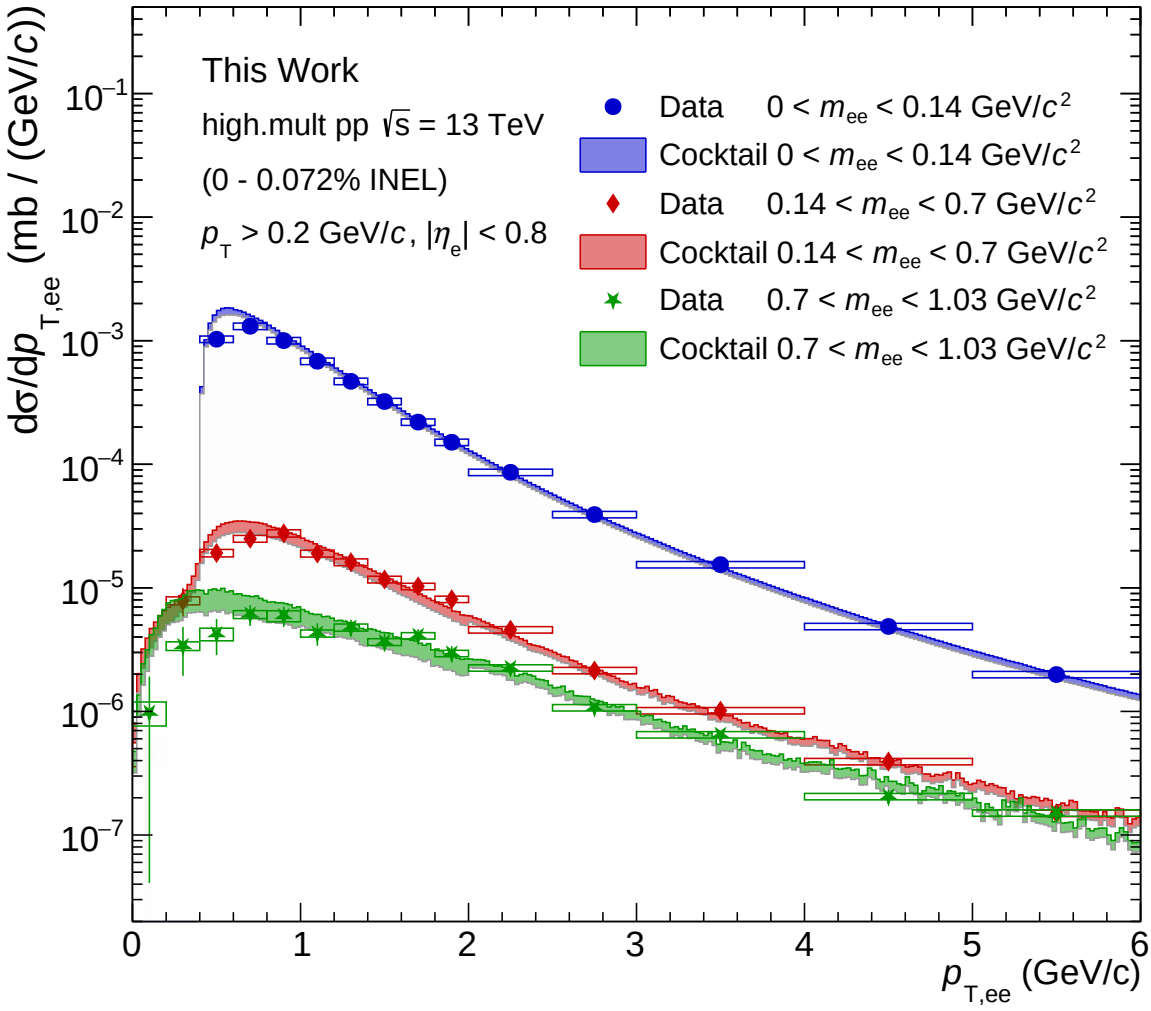

Figure 4.68: The dielectron cross section in high-multiplicity pp collision as a function of pair transverse momentum $p_{\mathrm{T,ee}}$. Statistical and systematic uncertainties of the data are displayed as vertical bars and boxes, respectively. Expectation from the hadronic decay cocktail is shown as a band.

is fixed to produce open charm and beauty cross sections at mid-rapidity, $f_{\mathrm{LF}}(m_{\mathrm{ee}})$ and $f_{\mathrm{dir}}(m_{\mathrm{ee}})$ are normalized independently to the data below 40 MeV/c^2, where $\mathrm{e^+e^-}$ from Dalitz decay and from direct photons have the same mass dependence. Note that thanks to the nice agreement with data and cocktail, in dielectron spectra, the normalization factor for $f_{\mathrm{LF}}(m_{\mathrm{ee}})$ is almost consistent with unity within 2% uncertainty. The direct photon fraction r is the only fit parameter, determined by the fitting to the data in $0.14 < m_{\mathrm{ee}} < 0.32$ GeV/c^2. Fig.4.70 and 4.71 show examples of r extraction in respective $p_{\mathrm{T,ee}}$ intervals for minimum-bias and high-multiplicity event analysis.

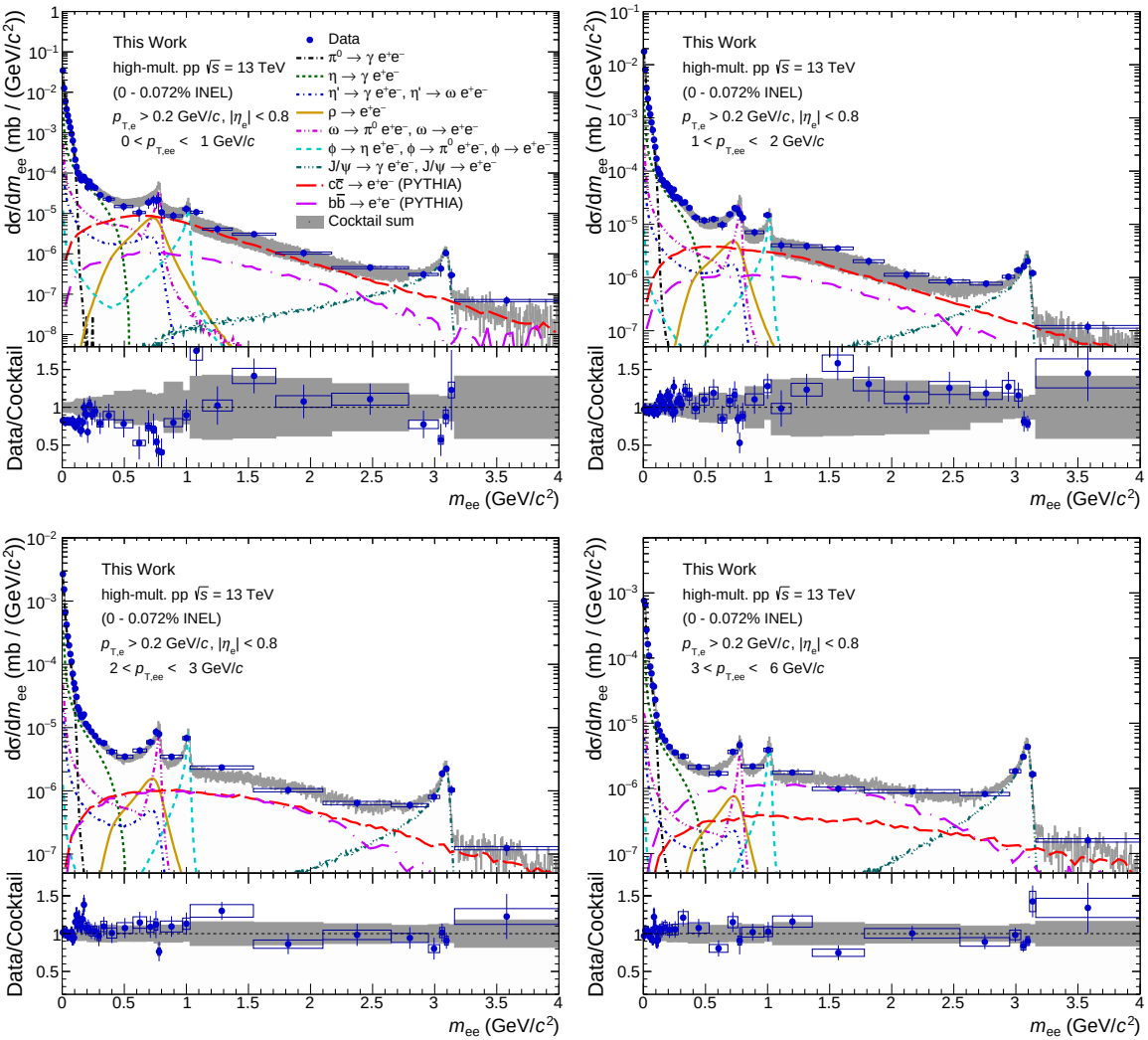

Figure 4.69: The invariant yield in high-multiplicity pp collisions at $\sqrt{s} = 13$ TeV as a function of invariant mass in different $p_{\mathrm{T,ee}}$ bins: $0 < p_{\mathrm{T,ee}} < 1$ GeV/c (top left), $1 < p_{\mathrm{T,ee}} < 2$ GeV/c (top right), $2 < p_{\mathrm{T,ee}} < 3$ GeV/c (bottom left), and $3 < p_{\mathrm{T,ee}} < 6$ GeV/c (bottom right), respectively. The statistical and systematic uncertainties of the data are displayed as vertical bars and boxes. The expectation from the hadronic decay cocktail is shown as a band, and the data-to-cocktail ratio is presented below together with the cocktail uncertainty.

4.12.2 Systematic Uncertainty of Direct Photon Extraction

Possible sources of systematic uncertainty on r, are as follows

1 Data points

2 Normalization range

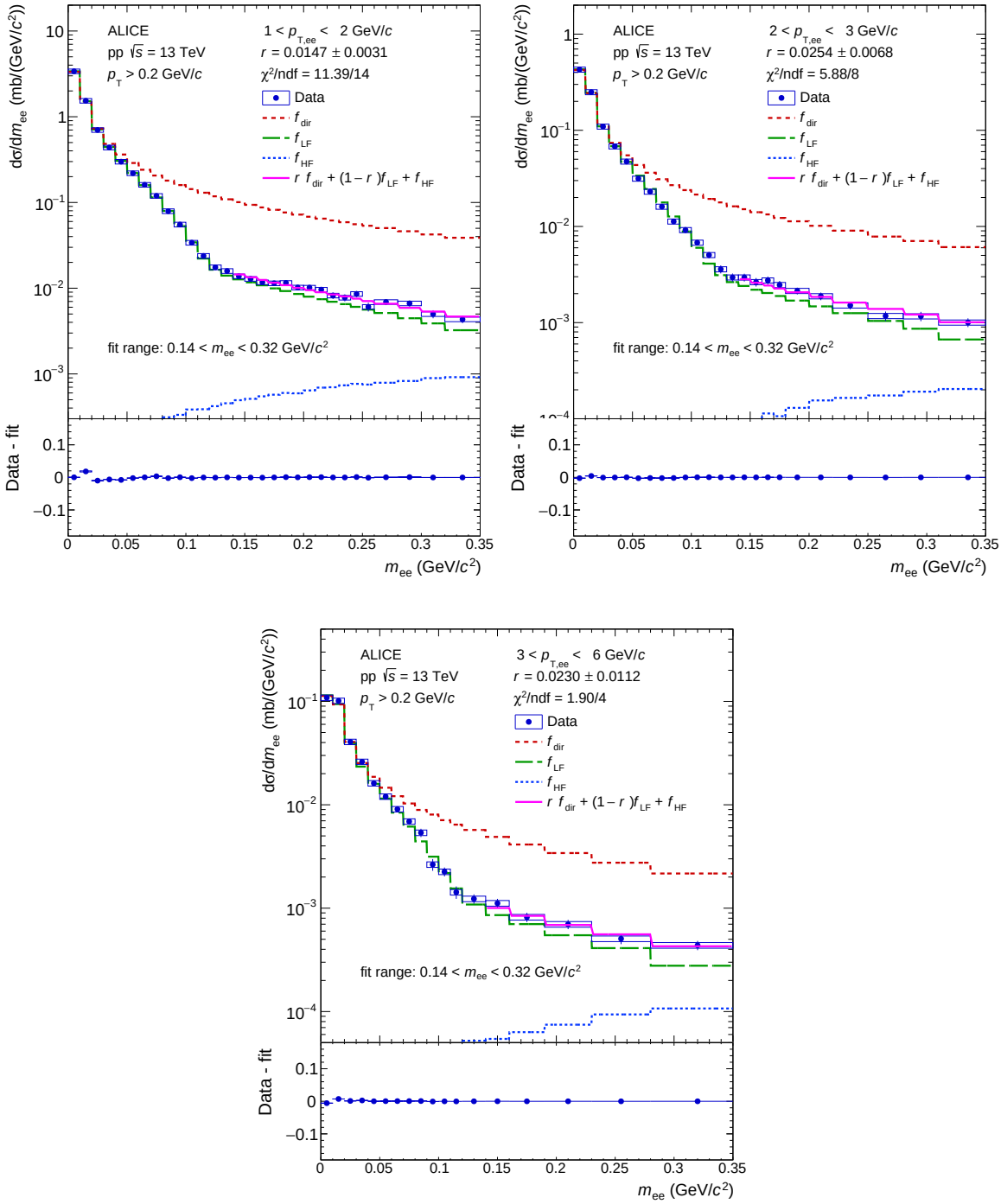

Figure 4.70: Top: Fit to the mass spectra in different $p_{\mathrm{T,ee}}$ intervals with a three-component function to extract photon fraction r in minimum-bias event analysis. Bottom: Residual distribution after the fitted function is subtracted by the data.

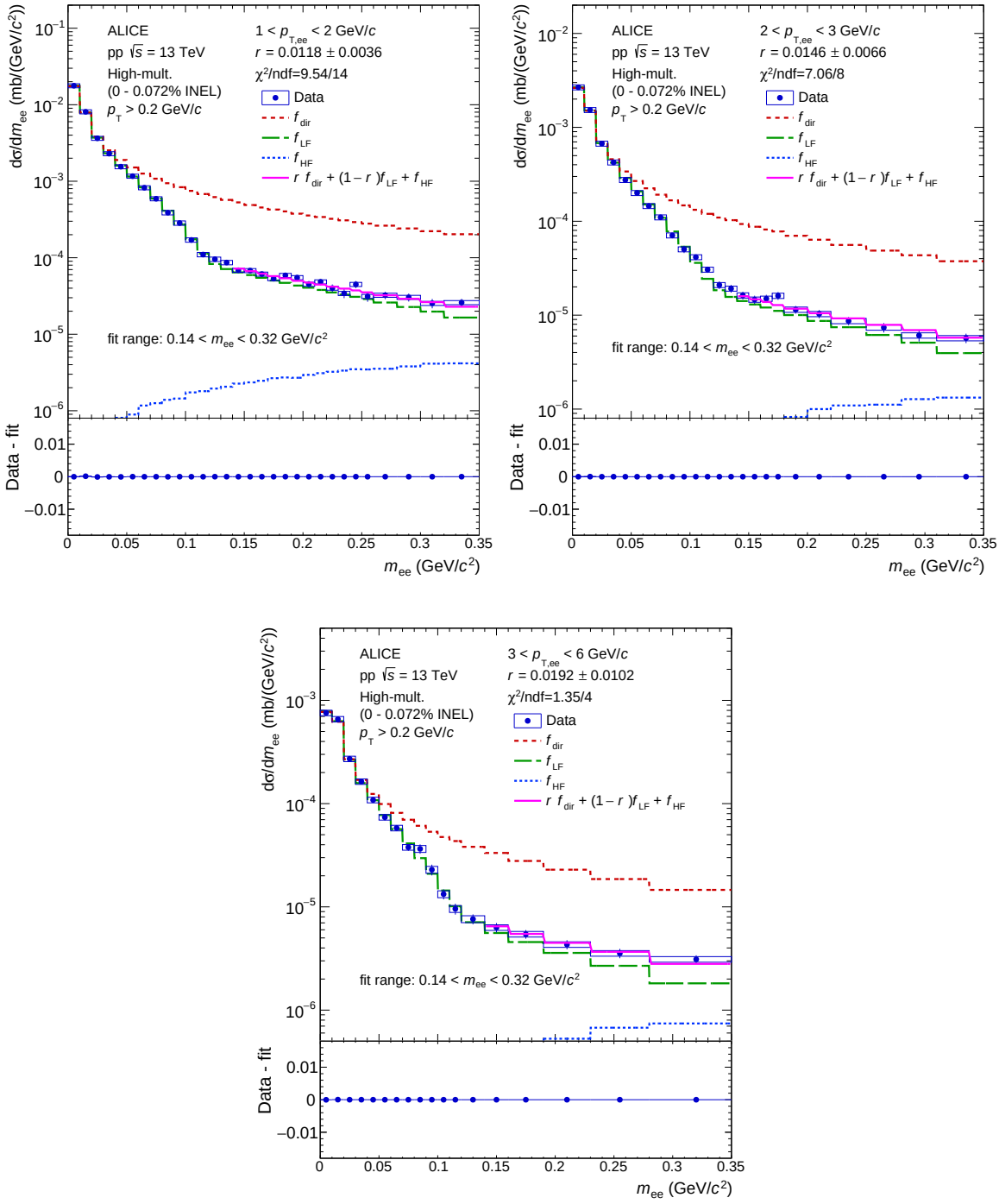

Figure 4.71: Top: Fit to the mass spectra in different $p_{\mathrm{T,ee}}$ intervals with a three-component function to extract photon fraction r in high-multiplicity event analysis. Bottom: Residual distribution after the fitted function is subtracted by the data.

3 Fitting range

4 η cocktail (η/π^0 parameterization)

5 HF cocktail

6 Scaling factor for high-multiplicity HF cocktail.

Direct-photon signal extracted repeatedly varying each item. As for η cocktail, since η parameterization is built by the product of π^0 and η/π^0, where correlated uncertainty between η and π^0 are already cancel. Therefore, we consider uncertainty of η/π^0 ratio instead of varying π^0 and η independently. The way of uncertainty estimation is different from source by source, i.e., for data, fitting, and η cocktail, The maximum difference with respect to the standard one is determined for each variation, and the largest of them is taken as a systematic uncertainty. For the case of fitting range, the weighted standard deviation is adopted, while RMS is used for heavy-flavor cocktail and its scaling. In order to calculate significance, we classified these systematic uncertainties according to their nature: point-to-point uncorrelated (Type A) or point-to-point correlated (Type B), which will be necessary for the significance calculation. Most of the sources are found to be p_{T}-correlated uncertainties except the normalization range. Total systematic uncertainty is calculated by adding them in quadrature. Table4.9 shows a summary of tested variations together with a type of uncertainty for each contribution. Visualization of breakdown can be found in Fig.4.72 and 4.73. The dominant contribution below $p_{\mathrm{T}} = 3$ GeV/c is from η cocktail uncertainties for both event multiplicity classes, whereas uncertainty comes data is the largest above $p_{\mathrm{T}} = 3$ GeV/c.

Table 4.9: Summary of total systematic uncertainty of virtual photon fraction r in minimum bias analysis

Source	Variations	Type
Di-electron spectrum	data points shifted 1 σ up/down	B
Normalization range	[20,30,40] MeV/c^2	A
Fitting range	[120,130,140,150] $\times$ [280,320,340] MeV/c^2	B
Light-flavor cocktail (η/π^0)	η/π^0 cocktail shifted 1 σ up/down	B
Heavy-flavor cocktail	$c\bar{c}$ and $b\bar{b}$ cross sections shifted 1 σ up/down	B
Mult. scaling of HF cocktail	upper and lower limit of scaling factor	B

Figure 4.74 and 4.75, show extracted r as a function of p_{T} in the range $1 < p_{\mathrm{T}} < 6$ GeV/c. Results compared with the published result are shown in the grey arrow. One can see that they are consistent within uncertainty, and now systematic uncertainty is significantly reduced for both minimum-bias and high-multiplicity events, thanks to the improved statistics and better knowledge of the η cocktail uncertainty.

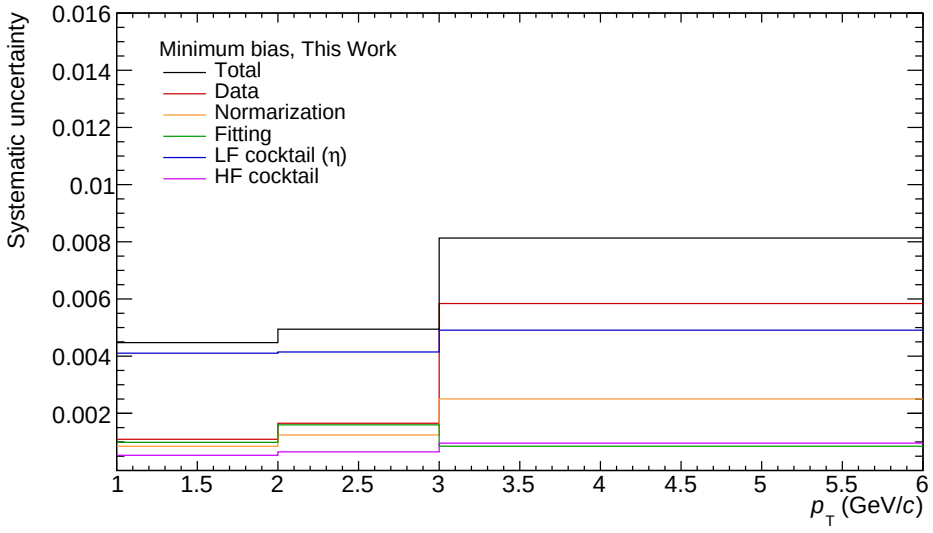

Figure 4.72: Summary of total systematic uncertainty of virtual photon fraction as a function of p_{T} in minimum-bias events.

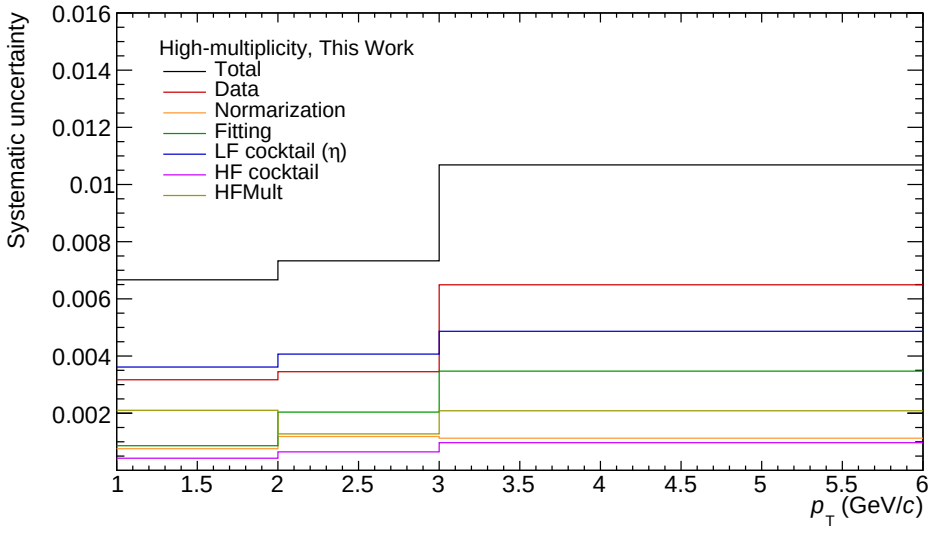

Figure 4.73: Summary of total systematic uncertainty of virtual photon fraction as a function of p_{T} in high-multiplicity events.

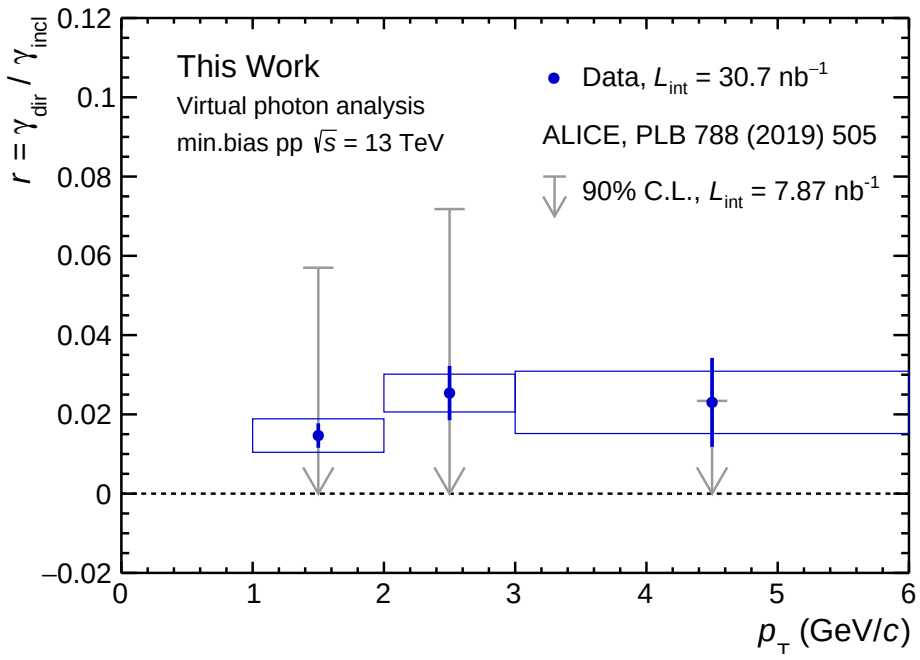

Figure 4.74: Virtual photon fraction r as a function of p_{T} in minimum-bias events.

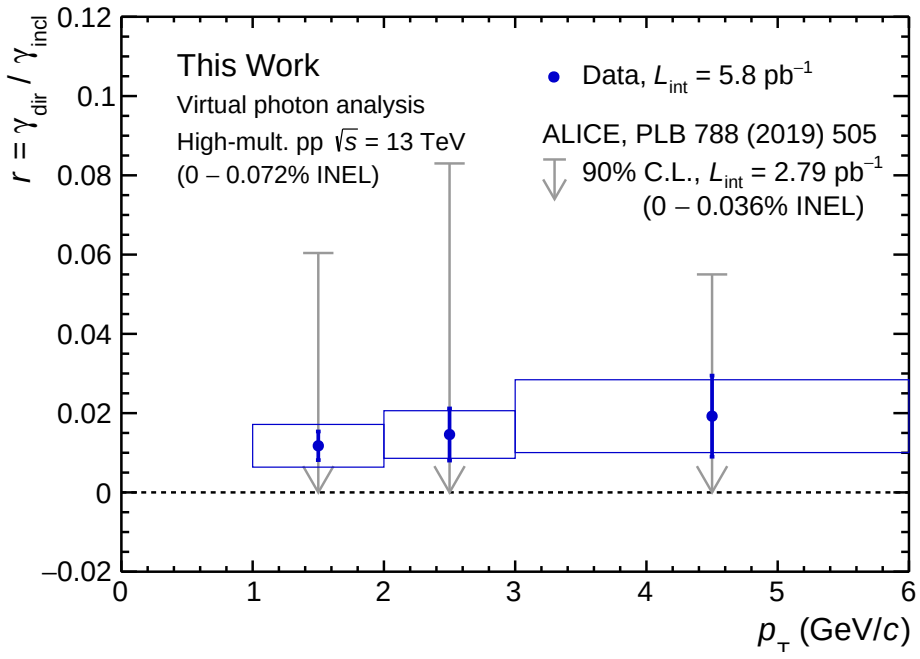

Figure 4.75: Virtual photon fraction r as a function of p_{T} in high-multiplicity events.

4.12.3 Significance of Direct Photon Signal

Pseudo-experiments under the null hypothesis assuming r is zero for all points were performed to calculate the significance of the direct-photon signal. The detailed procedure can be found in Ref. [25,169]. The model of the measurement of the direct-photon fraction r is based on the point-to-point uncorrelated (Type A) or point-to-point correlated (Type B) systematic uncertainties. It is assumed that the actual measurement can be described by certain values of nuisance parameter ε_B. Our limited knowledge of the actual values of the parameter is parameterized by Gaussian distributions with mean $\mu = 0$ and standard deviation $\sigma = 1$. ε_B is a deviation from a central value in units of the standard deviation. We now perform pseudo-experiments by randomly drawing ε_B from $N_{0,1}$. Suppose that r_0 is the true value of the photon fraction. The actual measurement in the p_{T} interval i will now fluctuate around $r_{\mathrm{mod,i}} = r_0 \cdot \varepsilon_B \sigma_{B,i,rel}$ as given by the statistical and type A systematic uncertainties added in quadrature. The uncertainties $\sigma_{B,i,rel}$ are the relative systematic type B uncertainty. A given pseudo data point in the p_{T} interval i is denoted by $r_{pd,i}$. The test statistic is defined by the following sum over pseudo-measurements in the different p_{T} intervals i: $t = \sum_{i=1}^{n_{\mathrm{data\ points}}}$ where $r_0 = 1$, $\sigma_{0,i} = r_{mod,i} \cdot \sigma_{i,stat+A,rel}$. The line indicates the value t_{data} of the test statistic for the real data. The p-values (number of pseudo-experiments with $t > t_{data}$ divided by the total number of pseudo-experiments) is indicated in the plot. The p-value is expressed in terms of the significance in units of the standard deviation of a Gaussian $(a \cdot \sigma)$ by solving $2\int_0^{\infty} N_{0,1}(x)dx = p$-value for a (two-tailed test). The resulting significance of the fraction r in the range $1 < p_{\mathrm{T}} < 6$ GeV/c, are about 3.2σ and 1.9σ for minimum-bias and high-multiplicity, respectively.

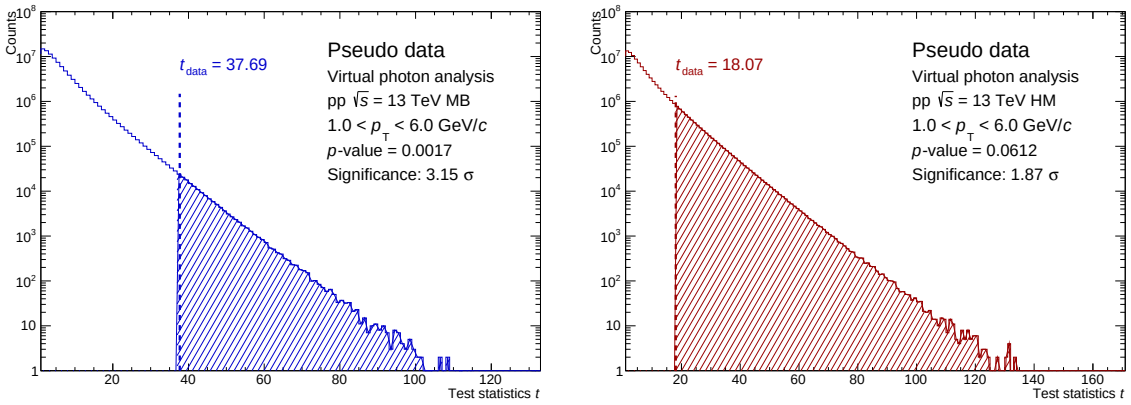

Figure 4.76: Distribution of the test statistic t for the direct-photon fraction r in different p_{T} slices. Pseudo-experiments performed under the null hypothesis H_0 : $r = 0$.

4.12.4 Decay Photon Simulation

In order to extract direct photon spectrum, decay photon is simulated. We take into account π^0, η, η', ρ, ω and ϕ mesons as the sources of decay photons. Parameterizations described in Section. 4.8, are also used in this simulation. All particles are generated in the kinematic region of $|y| < 1.0$ and $0 < p_{\mathrm{T}} < 50$ GeV/c in full azimuth, and decay into photons. Figure 4.77 and 4.78 show examples of generated mother particle distributions in minimum-bias events and high-multiplicity events. These particles are decayed into photons using PYTHIA6 decayer. The decay modes and corresponding branching ratios are summarized in Table 4.10.

Table 4.10: List of decay-photon sources and branching ratio [5].

Source	Decay mode	BR (%)
π^0	$\gamma\gamma$	98.8
	$e^+e^-\gamma$	1.17
η	$\gamma\gamma$	39.4
	$\pi^+\pi^-\gamma$	4.22
	$e^+e^-\gamma$	6.9×10^{-3}
η'	$\pi^0\gamma$	29.1
	$\omega\gamma$	2.62
	$\gamma\gamma$	2.21
ω	$\pi^0\gamma$	8.28
	$\eta\gamma$	4.6×10^{-4}
ρ^0	$\pi^+\pi^-\gamma$	9.9×10^{-3}
	$\pi^0\gamma$	6.0×10^{-3}
ϕ	$\eta\gamma$	1.3
	$\pi^0\gamma$	1.27×10^{-3}
	$\omega\gamma$	< 5 (C.L. = 84%)

Photons are selected in $|y| < 0.8$ to be consistent with dielectron analysis. Decay photon invariant yield as a function of p_{T} and relative contribution with respect to the total yield is shown in Fig. 4.79. The yield is dominated by π^0 in the full p_{T} range, and the second largest contribution comes from η meson. For the systematic uncertainty estimation, all parameterization shifted $\pm1\sigma$ and repeat cocktail generation. Relative uncertainty with respect to the standard one is taken as systematic uncertainty, which is about $\sim 4\%$. The high-multiplicity decay photon is also generated in the same way, and systematic uncertainty of $\sim 4\%$ is assigned.

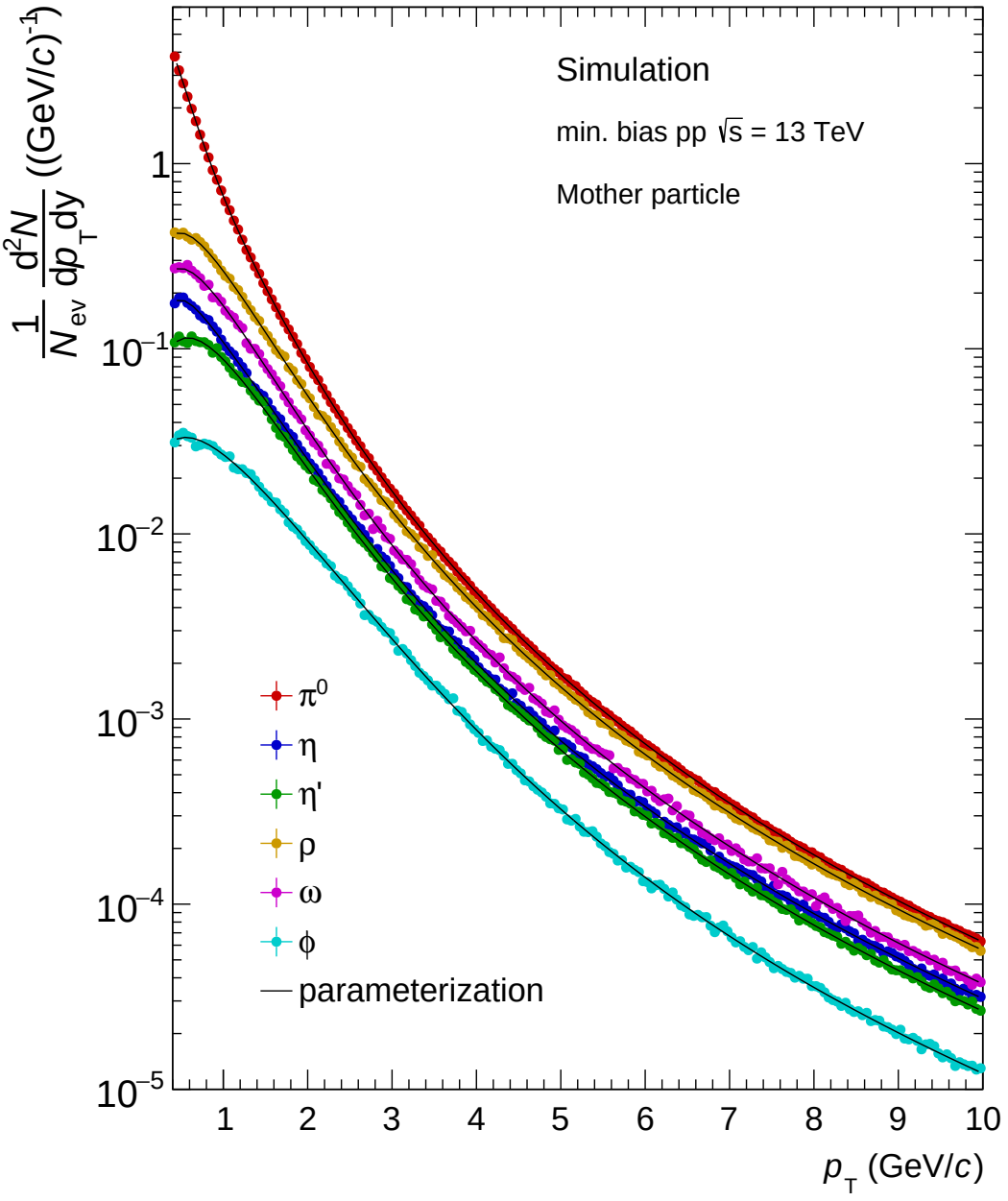

Figure 4.77: Generated mother particle as a function of p_{T} in minimum-bias event analysis. Corresponding parameterizations are overlaid.

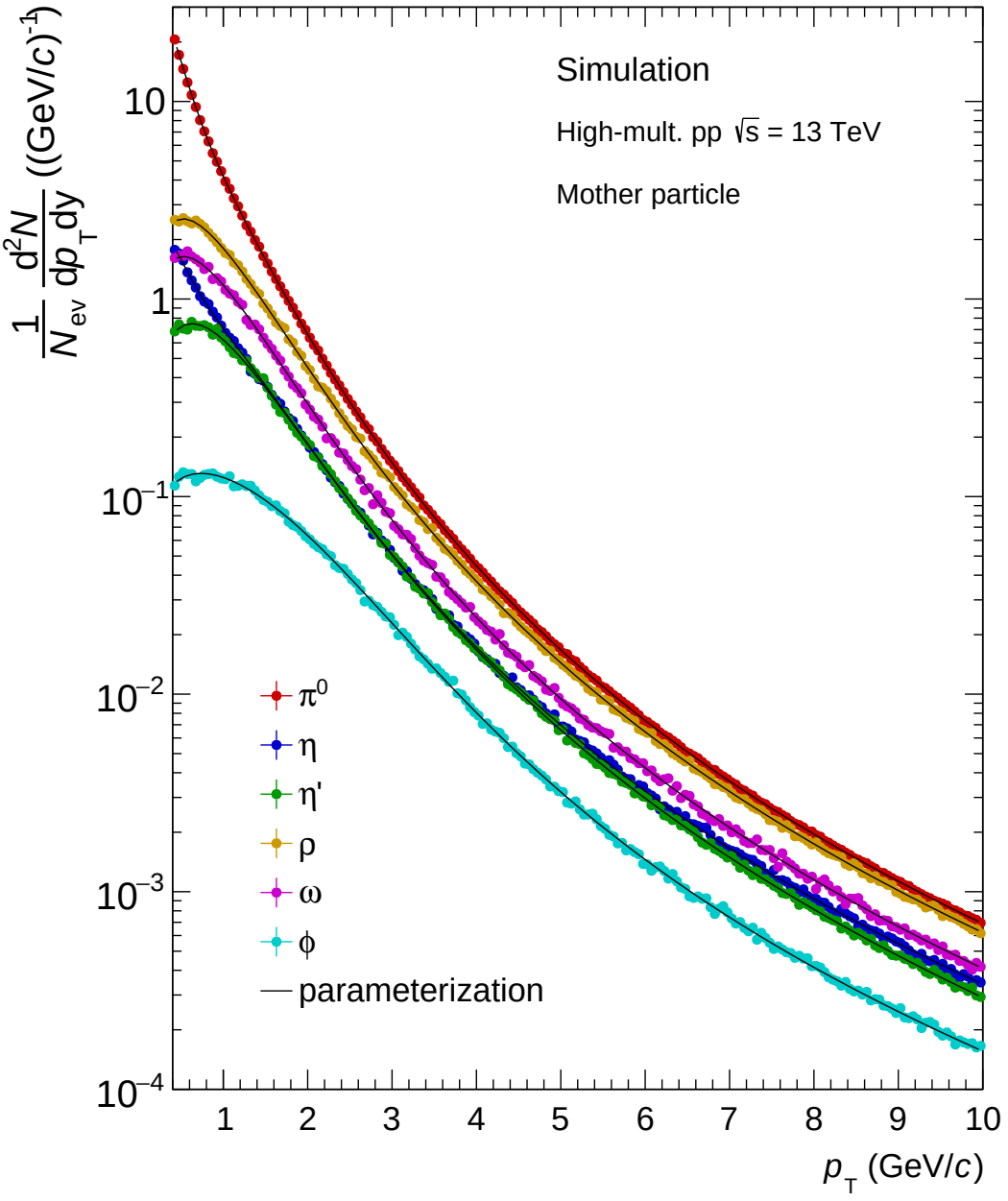

Figure 4.78: Generated mother particle as a function of p_{T} in high-multiplicity events. Corresponding parameterizations are overlaid.

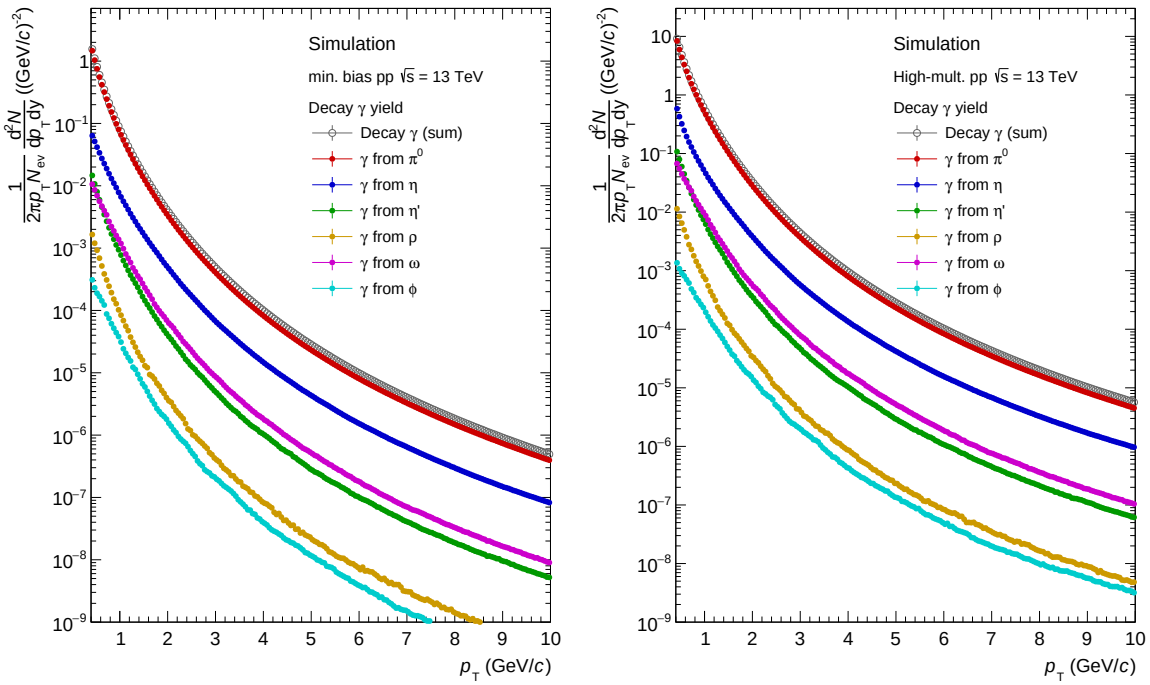

Figure 4.79: Decay photon yields as a function of p_{T} from respective photon sources in minimum-bias (left) and high-multiplicity (right) event analysis.

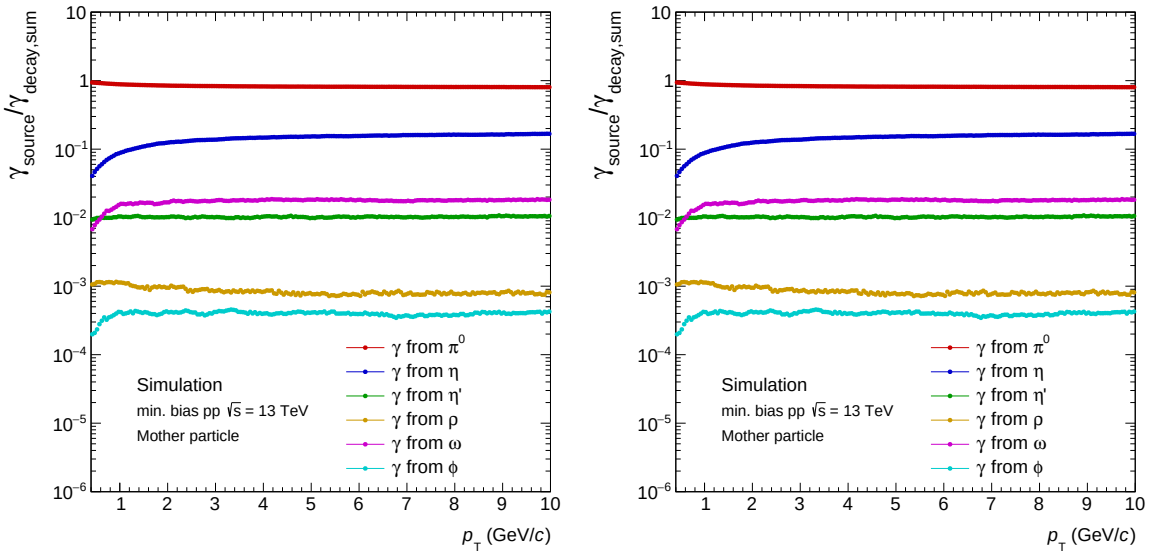

Figure 4.80: Relative fraction with respect to the total contribution in minimum-bias (left) and high-multiplicity (right) event analysis.

Chapter 5

Results and Discussions

5.1 Direct Photon Cross Section

Direct photon spectrum is constructed using the direct-photon fraction r and the decay photon cocktail obtained in the previous Chapter. Since an assumption that the mean p_{T} of the spectrum is the center of the bin is not correct for the steeply falling spectrum, it is necessary to shift the spectrum either in x- or y-directions according to the Lafferty-Wyatt method [170]. In this analysis, y-shifted was applied to make a ratio between results from two event multiplicity classes.

Figure 5.1 shows the direct photon invariant cross section at mid-rapidity $|\eta| < 0.8$ in the momentum range of $1 < p_{\mathrm{T}} < 6$ GeV/c. The results from minimum-bias data analysis are compared with prompt photon productions of two different NLO pQCD calculations from Vogelsang [53] and Shen [64] shown in a blue band and green line, respectively. These calculations employ CT10 [86–88] or CTEQ6.1M [89] proton PDFs and GRV [90] or BFG-II [91] fragmentation functions. The former is calculated in the range $2 < p_{\mathrm{T}} < 6$ GeV/c and the uncertainty band of the calculation is given by the simultaneous variation of the factorization, renormalization, and fragmentation scale values, μ ($0.5\ p_{\mathrm{T}} < \mu < 2\ p_{\mathrm{T}}$). The latter is calculated with $\mu = p_{\mathrm{T}}$, and extrapolated down to 0.5 GeV/c, where theoretical uncertainty is large. The questionable reliability of pQCD at low p_{T} further increases the uncertainty in this region of momentum. To constrain the scale dependence of the calculation, the factorization, renormalization, and fragmentation scales are taken to be proportional to the photon transverse momentum, and the proportionality constant is fixed using proton-proton measurements.

The experimental results on direct photon yield are also compared to the model which successfully describes collectivity in small collision systems with hydro-dynamical approach [64] and can predict thermal photon yield in high-multiplicity pp collisions. The model includes thermal contribution calculated based on the viscous hydrodynamical calculation with a lattice-QCD based equation of state, on top of the prompt photons.

Both prompt photon calculations from [53] and [64] are consistent with the data within uncertainty but tend to underestimate below $p_{\mathrm{T}} = 3$ GeV/c. The thermal contribution (orange dashed line), can be seen just below the prompt photons, and the

sum of these contributions (red dashed line) gives a slightly better description of the data. Looking at the theory over data ratio shown at the bottom, both prompt photon alone and total (prompt plus thermal) contribution are consistent within uncertainty with the data.

Direct photon spectrum in high-multiplicity events is calculated as in minimum-bias event analysis. As shown in Sec. 4.12, the extracted direct photon fraction r is similar to the one from the minimum-bias events. However, as reported in [54], the multiplicity dependent π^0 and η meson production leads to the multiplicity dependence of decay photon production. Taking into account the increased charged particle multiplicity and the decay photon yield in high-multiplicity events, the observed excess of direct photons implies a much higher total yield of direct photons in this event class. This can be seen in a comparison of the invariant yield between minimum-bias and high-multiplicity events as shown in Fig. 5.2. As shown in the bottom of Fig. 5.2, one can see that the high-multiplicity result gives a larger yield with respect to the one from minimum-bias. To compare the speed of increase with respect to minimum-bias events, we calculate the ratio of mean charged-particle multiplicity in high-multiplicity events and in minimum-bias events,

$$\langle \mathrm{d}N_{\mathrm{ch}}/\mathrm{d}\eta(\mathrm{HM})\rangle/\langle \mathrm{d}N_{\mathrm{ch}}/\mathrm{d}\eta(\mathrm{MB})\rangle = 4.43 \pm 0.10, \tag{5.1}$$

which gives a similar value to the bin-by-bin ratio. If anything, the results tend to be larger for all p_{T} bins. These bin-by-bin values can be found in Table 5.1.

Table 5.1: Bin-by-bin ratio of invariant yields between minimum-bias and high-multiplicity events.

p_{T} (GeV/c)	Ratio
$1 < p_{\mathrm{T}} < 2$	6.17 ± 2.30 (stat.) ± 3.37 (syst.)
$2 < p_{\mathrm{T}} < 3$	4.94 ± 2.59 (stat.) ± 2.27 (syst.)
$3 < p_{\mathrm{T}} < 6$	8.04 ± 5.80 (stat.) ± 4.74 (syst.)

Figure 5.3 shows the direct photon spectrum in the high-multiplicity event class at mid-rapidity $|\eta| < 0.8$, in the range $1 < p_{\mathrm{T}} < 6$ GeV/c. The result is compared with the theoretical predictions. As introduced in Sec. 1.3, multiple analyses reported multiplicity dependence of particle production in high-multiplicity pp collisions [42–44]. Similarly, direct-photon production could comply with some multiplicity dependence. However, as for high-multiplicity prompt photons, there is no theoretical prediction. From the private communication with W. Vogelsang and C. Shen, prompt photon calculations in high-multiplicity pp collisions seem to be challenging, if not impossible, in the context of ordinary pQCD calculations.

Therefore, the multiplicity dependence of prompt photons is estimated in several ways. One way to estimate is that the ratio of photon productions in high-multiplicity

events and inelastic events as we did in Eq. 5.1, which is taken to be the same as the ratio of charged particle productions in high-multiplicity events and inelastic events. The scaling factor is calculated as

$$\langle \mathrm{d}N_{\mathrm{ch}}/\mathrm{d}\eta(\mathrm{HM})\rangle/\langle \mathrm{d}N_{\mathrm{ch}}/\mathrm{d}\eta(\mathrm{INEL})\rangle = 5.90 \pm 0.22, \tag{5.2}$$

where $\langle \mathrm{d}N_{\mathrm{ch}}/\mathrm{d}\eta(\mathrm{HM})\rangle = 31.34 \pm 0.52$ and $\langle \mathrm{d}N_{\mathrm{ch}}/\mathrm{d}\eta(\mathrm{INEL})\rangle = 5.31 \pm 0.18$ are the charged-particle multiplicities in $|\eta_{\mathrm{ch}}| < 0.5$ measured in high-multiplicity and inelastic pp collisions, respectively [171].

Other ways were tested as follows:

1. The scaling factor extracted from measured neutral pion yields at sufficiently high p_{T} in the same pp event classes.

2. The scaling factor determined by using prompt-photon yield calculated in PYTHIA between two event multiplicity classes by making ratio of the p_{T} spectra at high p_{T}.

For each case, p-value was investigated to see if the data description is improved by the extracted factor. As a result, it was turned out that the best description of the HM results has been achieved by manually scaling pQCD calculations for pp collisions from Shen by a factor of $4.5 - 7.5$ and by adding on top the thermal-photon contribution calculated for HM events as described in Ref. [64]. These factor corresponds to $\sim 25\%$ uncertainty of the scaling factor determined in Eq. 5.2.

In Ref. [64], the thermal contribution is expected to depend on the charged-particle multiplicity. The data and theory comparison tells us that with the current precision, the data is consistent with both models, i.e., prompt photons from NLO pQCD calculation with multiplicity scaling alone (green) or the sum of the prompt and the thermal contributions within uncertainty. However, one could argue that the situation is the same as the minimum-bias event analysis and the QGP-like model gives a slightly better description than prompt photon alone. Moreover, it should be noted that the prompt photon without scaling can not account for the data at all, therefore a more sophisticated theoretical pQCD calculation as a function of charged-particle multiplicity is needed.

5.2 Direct Photon Yield as a Function of Multiplicity

Finally, p_{T}-integrated direct photon yields are studied as a function of charged-particle multiplicity in the range $1 < p_{\mathrm{T,ee}} < 3$ GeV/c. In this p_{T} range, one would expect that direct photons are dominated by thermal photons. Figure. 5.4 shows the data compared with the theoretical model by Shen. The point of the prompt photon in high-multiplicity events is scaled by 5.90 with respect to the one in minimum-bias events.

The data shows clear multiplicity dependence and is consistent with the theoretical prediction within uncertainty and supports the QGP-like model.

The result is also compared with other direct photon measurements at LHC energies. Figure 5.5 shows p_{T}-integrated direct photon yields from this study and measurements in Pb–Pb collisions at $\sqrt{s_{\mathrm{NN}}} = 2.76$ TeV. For the Pb–Pb data points, p_{T} spectra are integrated over $1 < p_{\mathrm{T}} < 5$ GeV/c. The statistical and systematic uncertainties are shown in the bar and box, respectively. Although the integration range is different, each point is dominated by the photon yield at the lowest p_{T} and can be discussed thermal-photon contribution. From the data, one would see a smooth evolution of direct photon production with event multiplicity. A smooth evolution of direct photon yields as a function of multiplicity was observed, which implies that particle multiplicity is one of the key quantities of direct photon production.

The Pb–Pb results are compared with a theoretical prediction by Gale [77] which includes photons from several sources such as prompt photons, pre-equilibrium photons, and thermal photons. The dashed orange and blue lines show the total contributions and prompt photons, respectively. The prompt photon is computed with next-to-leading-order pQCD using INCNLO [172], nCTEQ15-np PDF corrected for nuclear matter effects [173] and BFG2 [91] fragmentation function.

The Pb–Pb data points significantly above prompt photons and is consistent with the total photons. If we extend these theoretical lines towards the lower charged-particle multiplicity, the high-multiplicity data is better described by the total photons which includes thermal photons rather than the prompt photons alone. Taking into account this observation and consideration made in Fig. 5.4, the results support the similar conclusion in the previous section.

Of course, theoretical predictions for heavy-ion collisions may not be directly linked to pp collisions. Still, future theoretical work should provide us with a uniform framework that would be able to describe the direct photon yield across all collision systems as a function of multiplicity. This would help us to understand the possible onset of thermal radiation in small collision systems and the physics of pp collisions with a large number of produced particles.

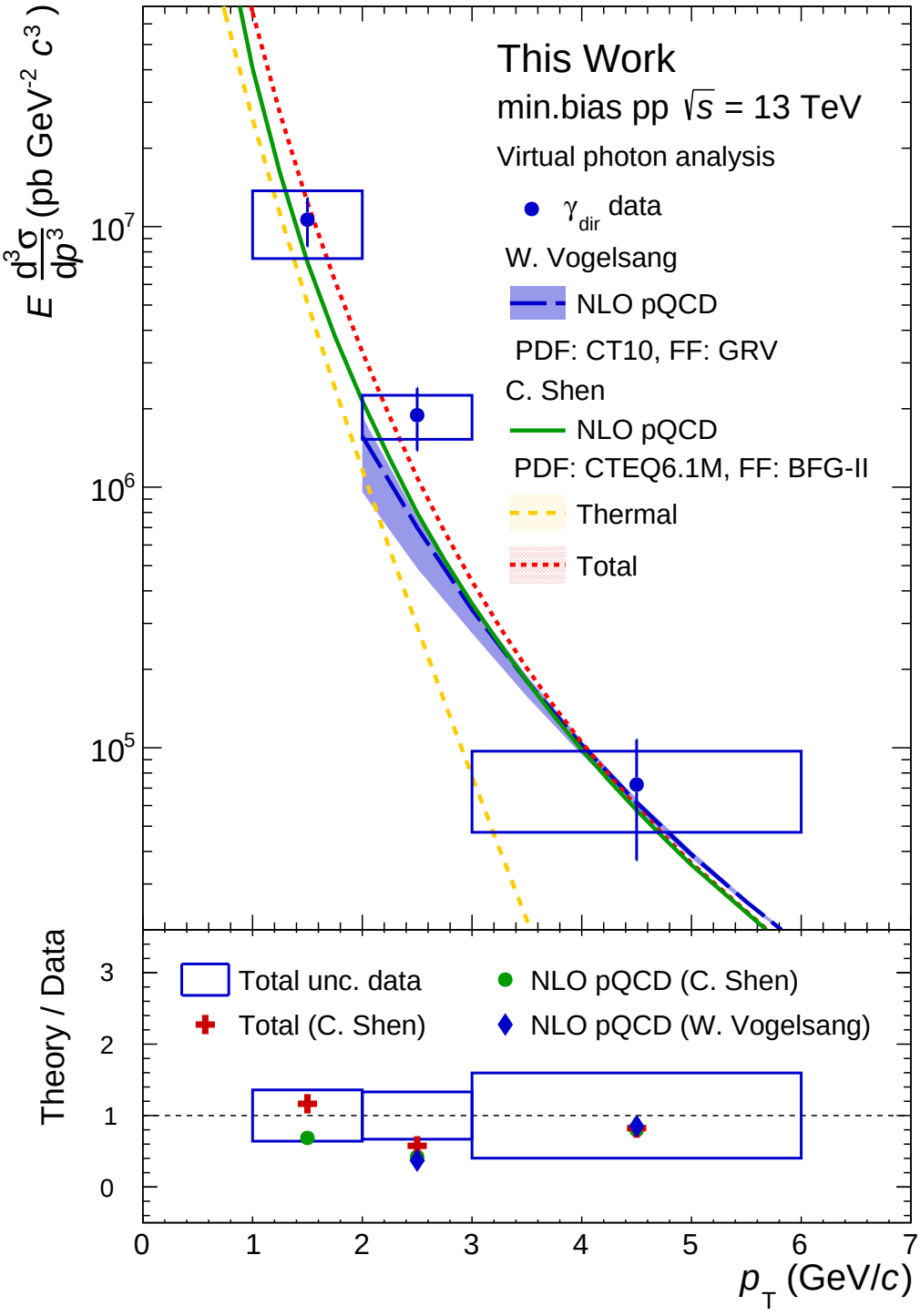

Figure 5.1: Direct photon yield $\gamma_{\rm dir}$ as a function of $p_{\rm t}$ in minimum-bias pp collisions. Statistical and systematic uncertainties of the data are displayed as vertical bars and boxes, respectively. The result is compared to theoretical calculations from [70] and [64].

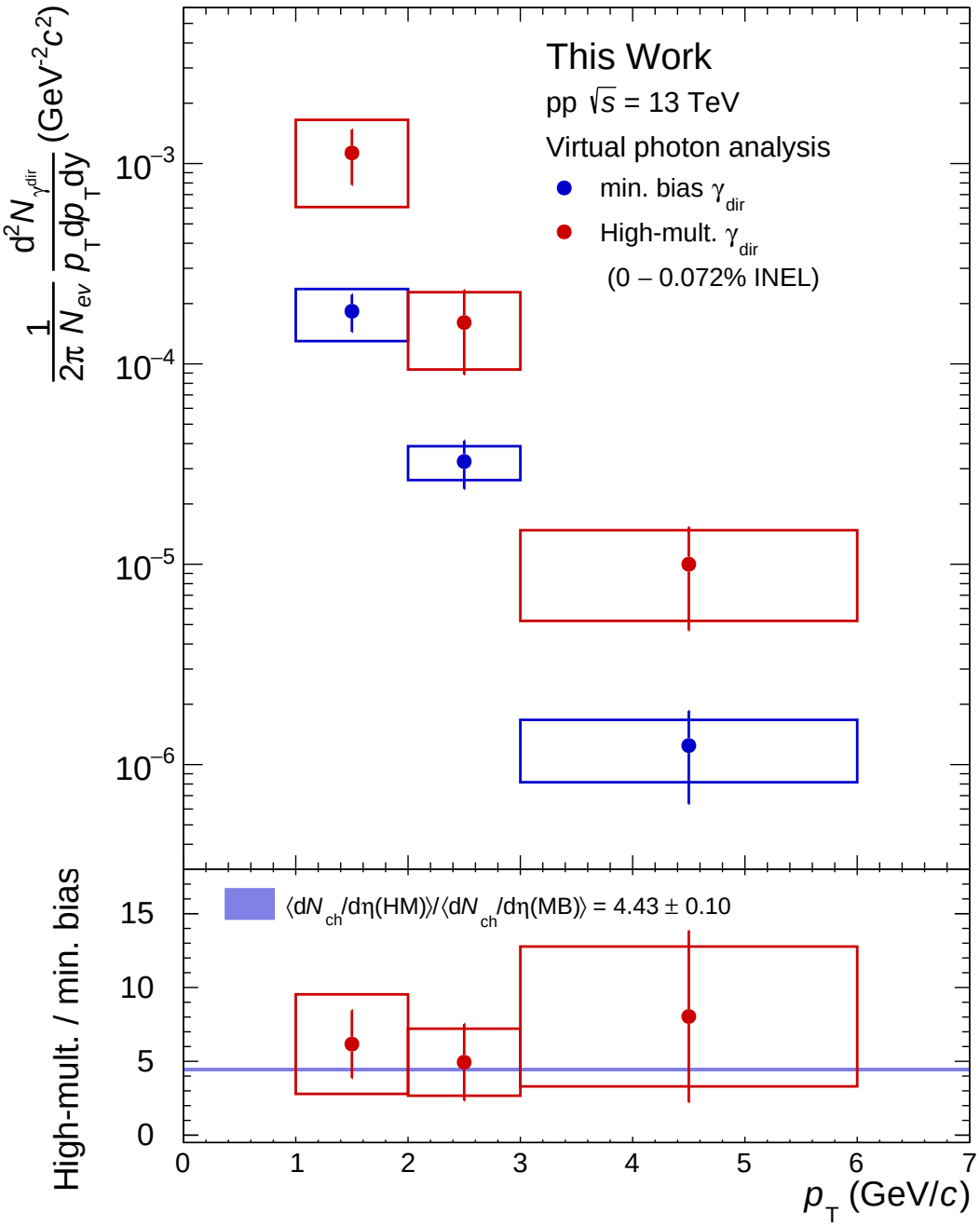

Figure 5.2: Multiplicity dependence of p_{T} differential direct photon yield γ_{dir}. The bottom panel shows the ratio of high-multiplicity over minimum photon yields. The data points are calculated assuming spectra are fully uncorrelated point-by-point. The blue band shown at the bottom indicates the ratio of mean charged-particle multiplicity at mid-rapidity in high-multiplicity over minimum-bias events.

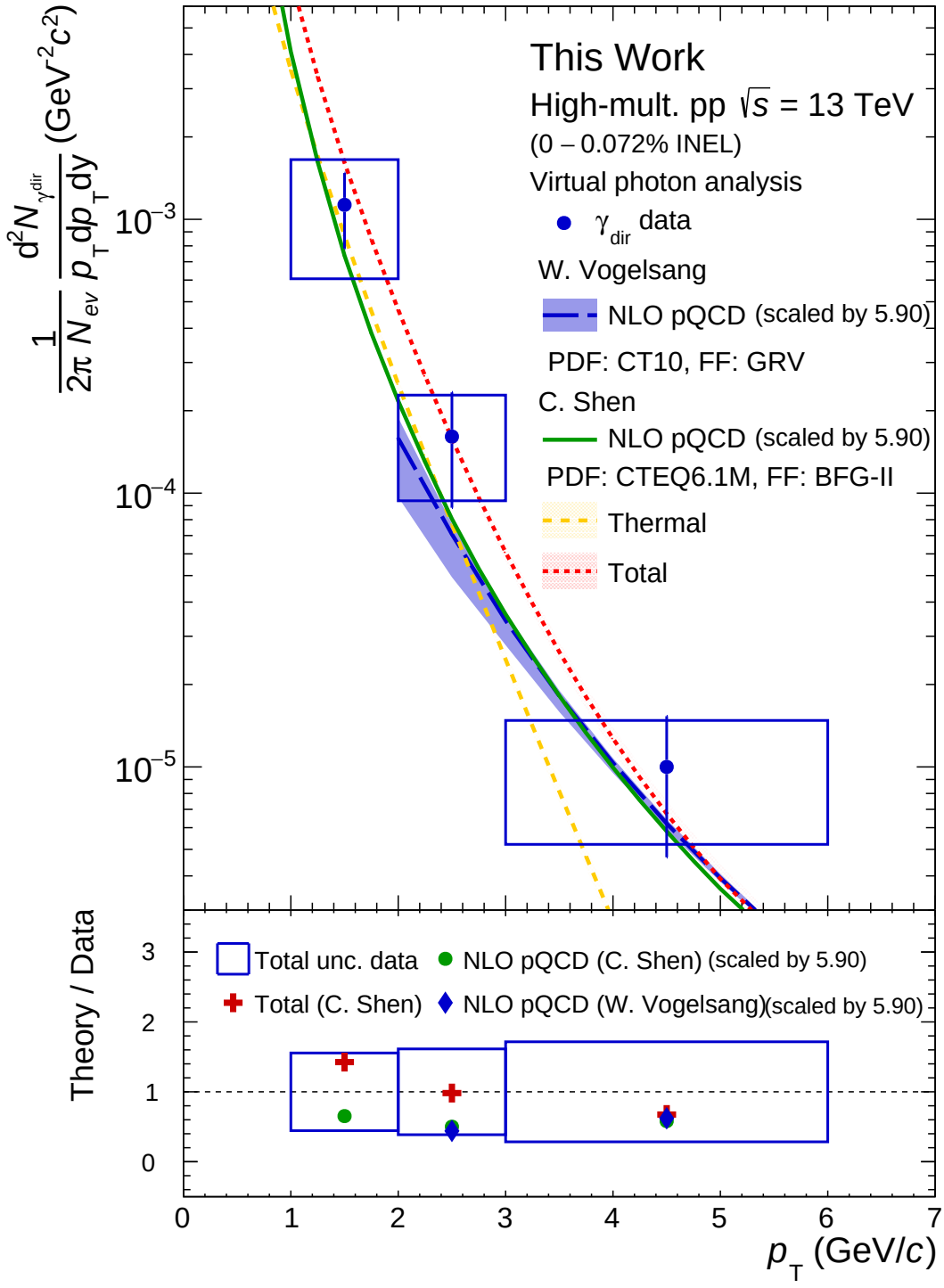

Figure 5.3: Direct photon yield γ_{dir} as a function of p_{t} in high-multiplicity pp collisions. Statistical and systematic uncertainties of the data are displayed as vertical bars and boxes, respectively. The result is compared to theoretical calculations from [70] and [64].

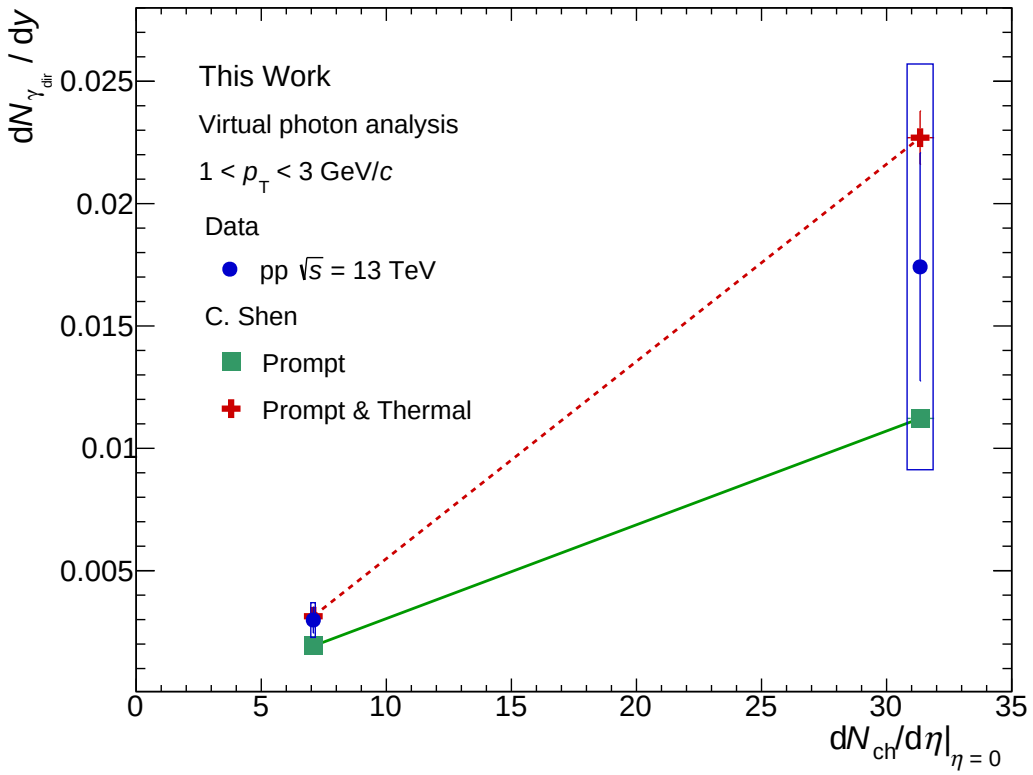

Figure 5.4: Integrated photon yield γ_{dir} as a function of charged particle multiplicity at mid-rapidity. Statistical and systematic uncertainties of the data are displayed as vertical bars and boxes, respectively. The result is compared to theoretical calculations from [70] and [64].

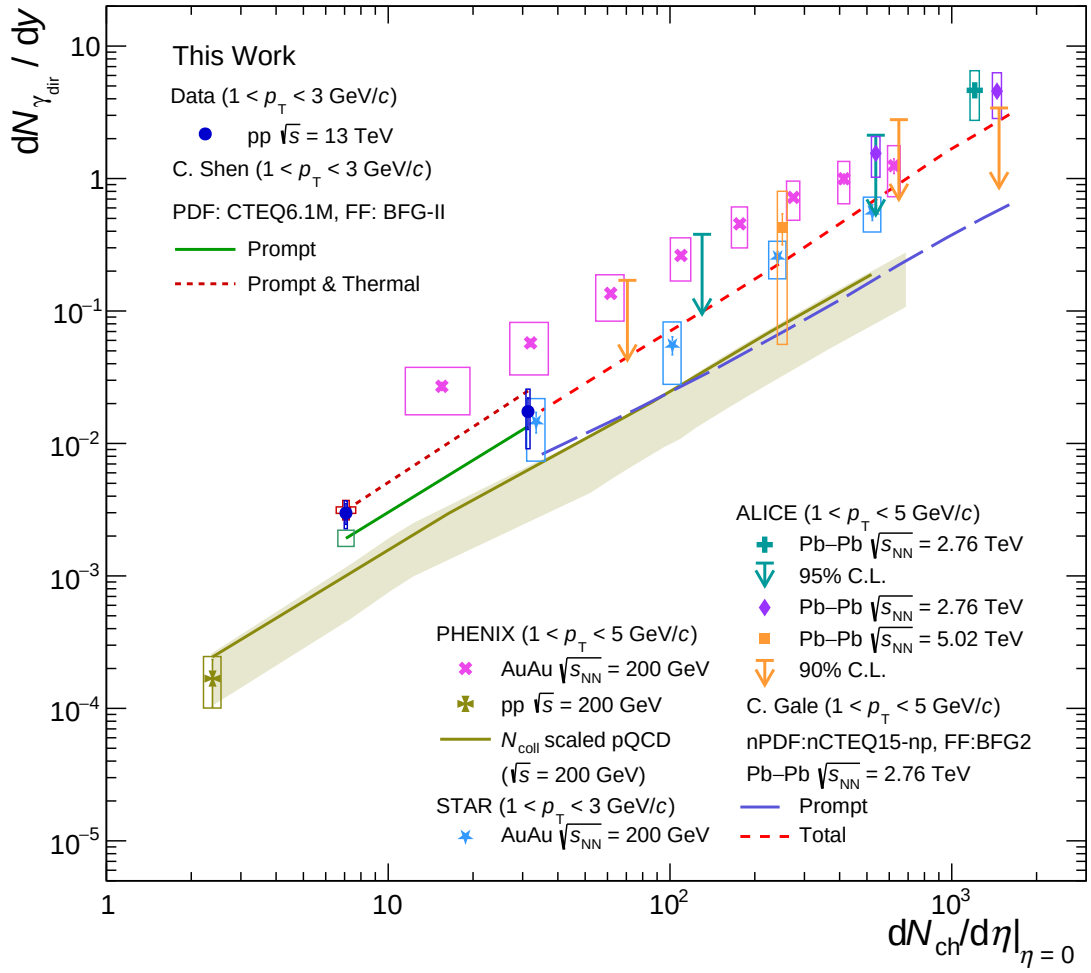

Figure 5.5: Compilation of integrated photon yield $\gamma_{\rm dir}$ as a function of charged particle multiplicity at mid-rapidity. The obtained results are compared with results from RHIC and LHC energies. The blue star and the magenta cross markers indicate results from Au–Au collisions at $\sqrt{s_{\rm NN}} = 200$ GeV by STAR [174] and PHENIX [49, 175] collaborations. The gold four-triangles marker and band show the result from pp collisions at $\sqrt{s} = 200$ GeV and $N_{\rm coll}$-based extrapolation of pQCD calculations [50], respectively. The LHC results are all taken from the ALICE collaboration. The data points in Pb–Pb collisions are taken from ALICE published result [25] (dark cyan cross) and preliminary results (violet diamond and orange square) measured at different collision energies [176], respectively. The Pb–Pb results at $\sqrt{s_{\rm NN}} = 2.76$ TeV are compared with the theoretical prediction by Gale [77]. The model includes prompt photons, pre-equilibrium photons, and thermal photons. The prompt photon is computed with next-to-leading-order pQCD using INCNLO [172], nCTEQ15-np PDF corrected for nuclear matter effects [173] and BFG2 [91] fragmentation function. Statistical and systematic uncertainties of the data are displayed as vertical bars and boxes, respectively.

Chapter 6

Conclusion and Outlook

This work presents the study of low transverse momentum direct photon production at mid-rapidity in proton-proton collisions for the first time at $\sqrt{s} = 13$ TeV. For the first time at the LHC energies, a significant yield of direct photons is observed at low transverse momentum in both inelastic and high-multiplicity classes. One of the purposes of this study is to search for thermal photon production in high-multiplicity pp collisions. Another motivation is to constrain pQCD at low p_{T} as the production of prompt photons is dominated by higher-order processes at LHC energies. Direct photon was measured via the internal conversion technique, which is expected to have a better signal-to-background ratio than the measurements of real direct photons with calorimeters or via the reconstruction of external conversions. In this technique, the different shape of the dielectron continuum is exploited to separate direct-photon signals and electrons from hadronic decays of Dalitz decays.

In the previous study [132], only upper limits were given for both event multiplicity classes due to the large systematic uncertainties. This analysis used about 4 times larger statistics with respect to the previous study. This study adopted the high precision π^0 and η measurements in the same event multiplicity classes, which were not available before. Also, based on the updated BR of $c \to e$ decay, $c\bar{c}$ and $b\bar{b}$ cross sections are re-extracted using simultaneous fit to two-dimensional m_{ee} versus $p_{\mathrm{T,ee}}$ distribution with a significantly better precision.

Dielectron production was reported in pp collisions at mid-rapidity $|\eta_{\mathrm{e}}| < 0.8$ in the kinematic range of $m_{\mathrm{ee}} < 4$ GeV/c^2 and $p_{\mathrm{T,ee}} > 0$ GeV/c in the minimum-bias and the high-multiplicity events. The results are compared with expected contributions from known hadron decays. As for the minimum-bias analysis, the data and the cocktail show nice agreement, and the validity of the cocktail was verified. As well as the minimum-bias analysis, in the high-multiplicity analysis, the data and cocktail are in good agreement above $p_{\mathrm{T}} = 1$ GeV/c, where we extract photon signal.

Direct photon signal was extracted from dielectron mass spectra at $m_{\mathrm{ee}} \ll p_{\mathrm{T,ee}}$, in the range $1 < p_{\mathrm{T}} < 6$ GeV/c with the significance of 3.2σ in minimum-bias pp collisions. Systematic uncertainties on direct photon fraction r were significantly reduced compared to the previously published study. Thanks to the precise measurements of π^0 and η in the same multiplicity class as studied in this work, it was also possible to

extract the direct photon excess in high-multiplicity pp collisions with the significance of 1.9σ. These results are the first measurement of low p_{T} direct photons in pp collisions at the LHC energies. With the direct-photon fraction r and cocktail simulation of decay photons, the direct photon p_{T} spectrum is constructed.

Direct photon spectrum in inelastic events was compared with theoretical predictions by Vogelsang [53] and Shen [64]. Prompt photons are calculated by the NLO pQCD calculation with different PDFs and FFs, i.e., CT10 or CTEQ6.1M proton PDFs and GRV or BFG-II fragmentation functions. The result was found to be consistent with both calculations within uncertainties, but the theory tends to underestimate the data down to 2 GeV/c. The model also includes thermal photons on top of the NLO pQCD calculation. The thermal contribution is calculated based on the model which describes collectivity in small systems with the hydro-dynamical approach. This QGP-like model gave a slightly better description at $p_{\mathrm{T}} < 3$ GeV/c, however, both models are consistent with the data within uncertainties.

As for the high-multiplicity event analysis, no reliable theoretical prediction of the prompt photon exists at the time of writing this thesis. Therefore, empirical scaling based on the measured charged particle multiplicities in between inelastic and high-multiplicity events was applied to the NLO pQCD calculations and compared with the high-multiplicity result. As a result, the data was found to be consistent with both standalone empirically scaled prompt photons and the sum of the thermal and prompt photons. Again it was found that the QGP-like model gives a slightly better description of the high-multiplicity data as well as minimum-bias data.

We also investigated p_{T}-integrated direct-photon yield as a function of charged-particle multiplicity. Since the photon yield is dominated by the low p_{T} point below $p_{\mathrm{T}} = 3$ GeV/c, photons that contribute to such regions should be sensitive to thermal-photon production. It was also found that the result showed clear multiplicity dependence, and the photon yield at high multiplicity increased by about factor 5 with respect to the one from the minimum-bias event. From the comparison between data and theoretical prediction, it was found that the data supports both a hydro-dynamical approach and a standalone prompt photon calculation.

Finally, the compilation of photon yields from LHC energies was presented. The p_{T}-integrated photon yields in the range $1 < p_{\mathrm{T}} < 5$ GeV/c were calculated from the direct-photon measurements in Pb–Pb collisions at $\sqrt{s}_{\mathrm{NN}} = 2.76$ TeV. A smooth evolution of direct photon yields as a function of multiplicity was observed, which implies that particle multiplicity is one of the key quantities of direct-photon production.

Theoretical prediction in heavy ion collisions was also discussed, which includes prompt, pre-equilibrium, and thermal photons. The Pb–Pb data points significantly above prompt photons and is consistent with the total photons. If we extend these theoretical lines towards the lower charged-particle multiplicity, the high-multiplicity data is better described by the total photons which includes thermal photons rather than the prompt photons alone. These observations support the statement made in the discussion about direct photon p_{T} spectra.

In summary, in this study, we measured low-p_{T} direct photon spectra with unprece-

dented precision for two different event multiplicity classes which are compatible with theoretical calculations. We observed clear multiplicity dependence of direct photon, which is compatible with an assumption of thermal photon presence in high-multiplicity pp collisions. A comparison with theoretical prediction has been made. With the current precision, we are not able to conclude which model can give a better description. However, for both direct photon p_{T} spectra and p_{T}-integrated photon yields, the QGP-like model consistently gives a better description of the results.

This study indicates the need for further theoretical efforts in particular for precise pQCD calculations in high-multiplicity pp collisions and more generally, for a uniform framework that would allow for a consistent description of direct photon production across various collisions systems. Future analysis of the experimental data collected during Run 3 and Run 4 periods of LHC operation, including more precise charm and beauty production as a function of multiplicity, will help to further reduce the experimental uncertainties and to pin down possible thermal contribution in pp collisions. These studies will form a crucial baseline for direct photon and dielectron measurement in heavy-ion collisions with Run 3 and Run 4 data.

Appendix A

Kinematic Variables

This appendix introduces useful variables used in this thesis. The z-axis is chosen as the beam going direction. The transverse momentum p_T and the transverse mass m_T are defined in terms of two momentum components of a particle:

$$p_T = \sqrt{p_x^2 + p_y^2}, \tag{A.1}$$

$$m_T = \sqrt{m^2 + p_T^2} = \sqrt{E^2 - p_z^2}, \tag{A.2}$$

where E, p_x, p_y, p_z and m are the energy, x, y, and z component of the momentum and the mass of the particle, respectively. The rapidity y of the particle is defined as

$$y \equiv \frac{1}{2}\ln\Big(\frac{E + p_z}{E - p_z}\Big). \tag{A.3}$$

The rapidity is transformed under the Lorentz boost in the z direction with the velocity β as follows

$$y \to y + \tanh^{-1}\beta, \tag{A.4}$$

The particle energy and z component of the momentum (p_z) can be written in terms of the rapidity (y) and transverse mass (m_{T}) as follows

$$E = m_{\mathrm{T}} \cosh\, y, \tag{A.5}$$

$$p_z = m_{\mathrm{T}} \sinh\, y. \tag{A.6}$$

The pseudorapidity η, can be expressed in terms of the angle, θ, between the particle momentum, $\vec{p}$, and z axis as follows

$$\eta = \frac{1}{2}\ln\Big(\frac{|\vec{p}| + p_z}{|\vec{p}| - p_z}\Big) = -\ln\Big(\tan\frac{\theta}{2}\Big), \tag{A.7}$$

Appendix B

TPC and TOF post-calibration

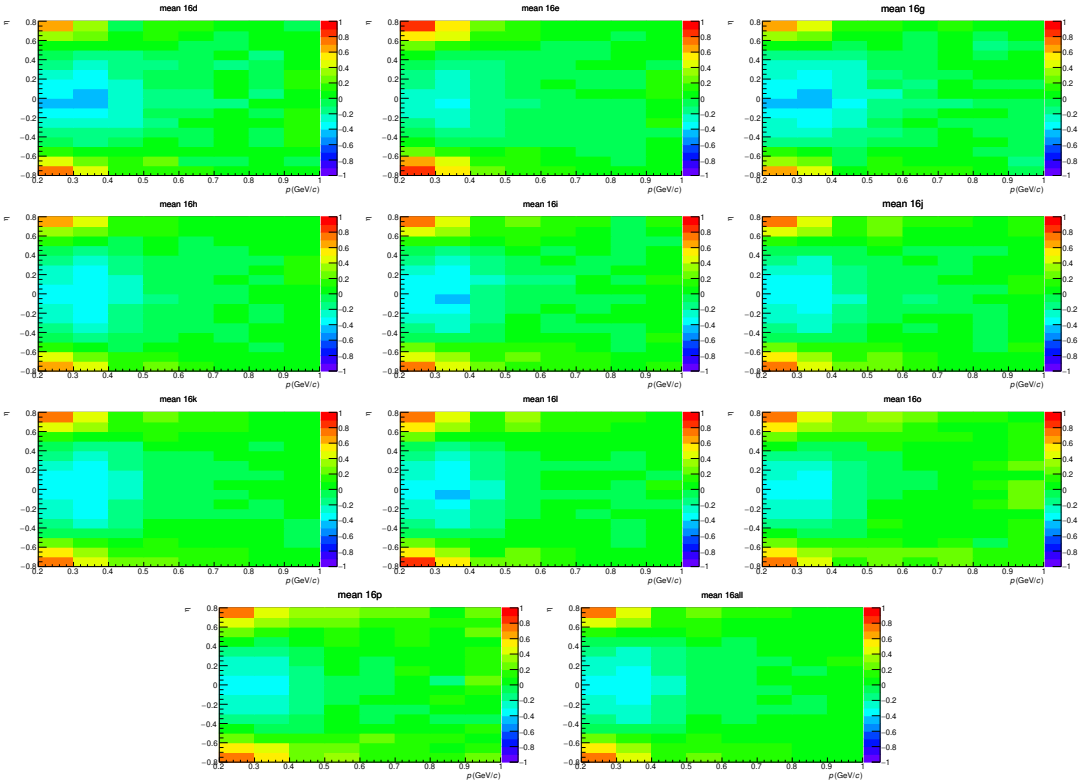

Figure B.1: mean of $n\sigma^{\mathrm{TPC}}$ as a function of track momentum p versus pseudorapidity η obtained using 2016 periods.

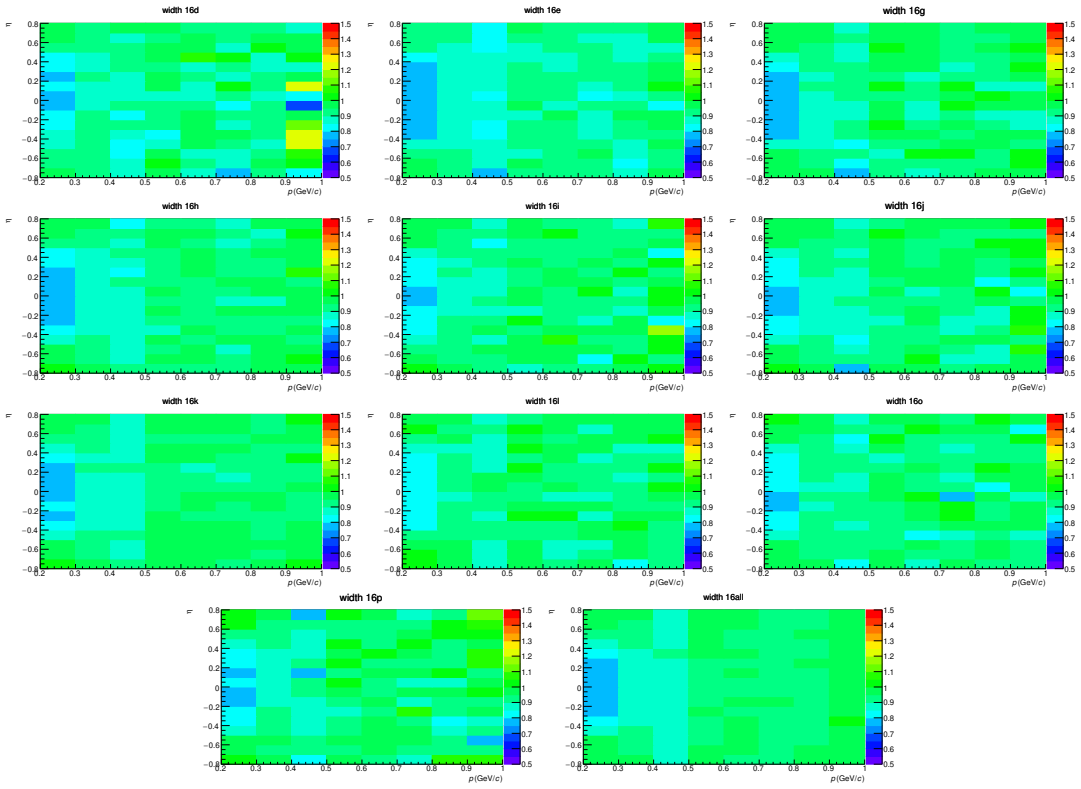

Figure B.2: width of $n\sigma^{\mathrm{TPC}}$ as a function of track momentum p versus pseudorapidity η obtained using 2016 periods.

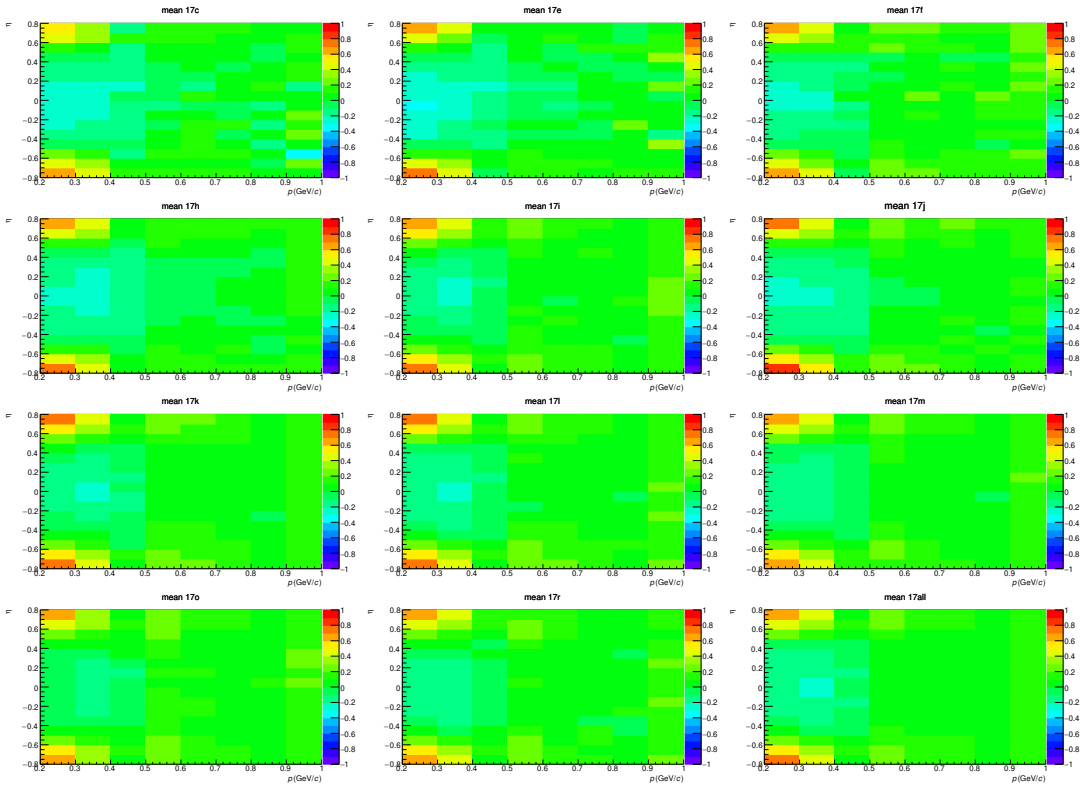

Figure B.3: mean of $n\sigma^{\mathrm{TPC}}$ as a function of track momentum p versus pseudorapidity η obtained using 2017 periods. Bottom right shows map created using all periods.

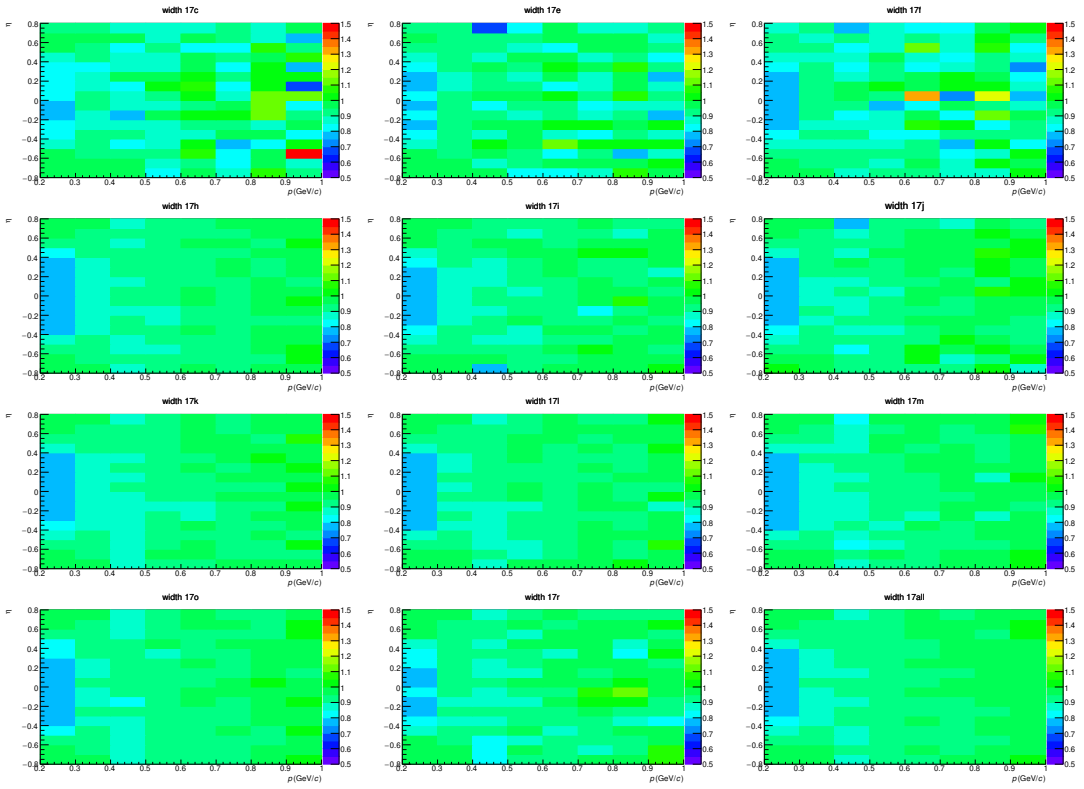

Figure B.4: width of $n\sigma^{\mathrm{TPC}}$ as a function of track momentum p versus pseudorapidity η obtained using 2017 periods. Bottom right shows map created using all periods.

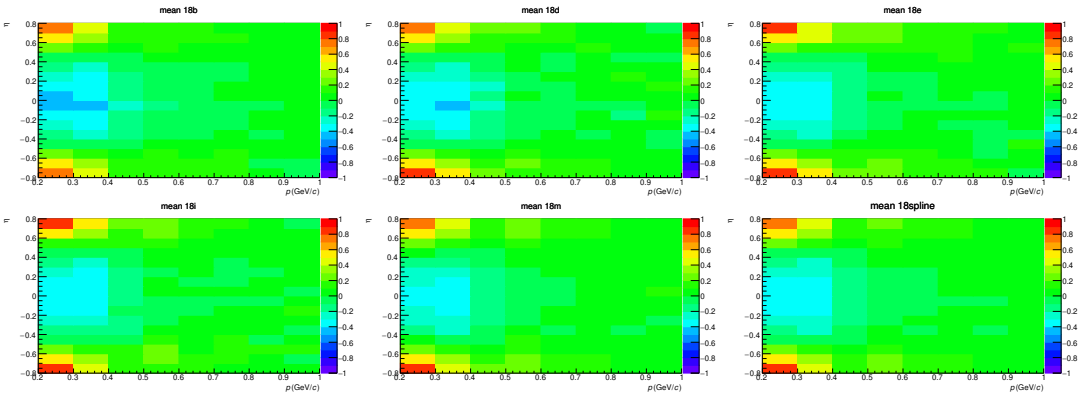

Figure B.5: mean of $n\sigma^{\mathrm{TPC}}$ as a function of track momentum p versus pseudorapidity η obtained using a period from '18spline'. Bottom right shows a map created using all periods.

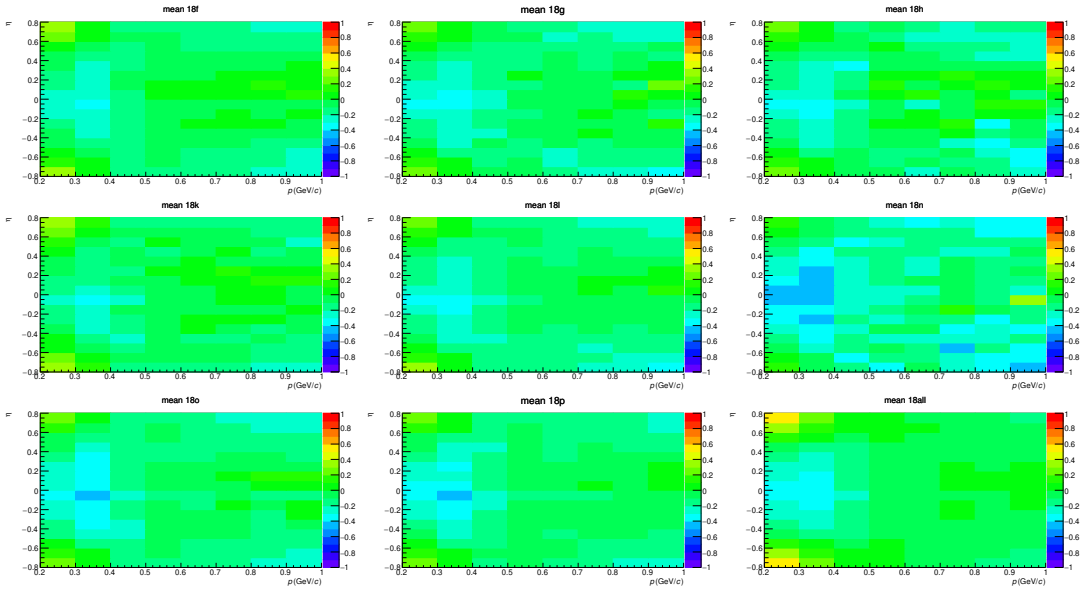

Figure B.6: mean of $n\sigma^{\mathrm{TPC}}$ as a function of track momentum p versus pseudorapidity η obtained using a period from '18nospline'. Bottom right shows map created using all periods.

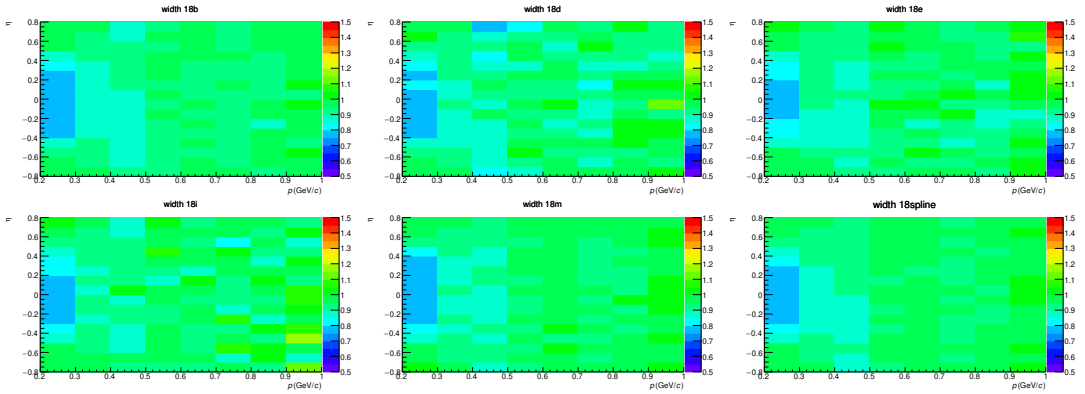

Figure B.7: width of $n\sigma^{\mathrm{TPC}}$ as a function of track momentum p versus pseudorapidity η obtained using a period from '18spline'. Bottom right shows map created using all periods.

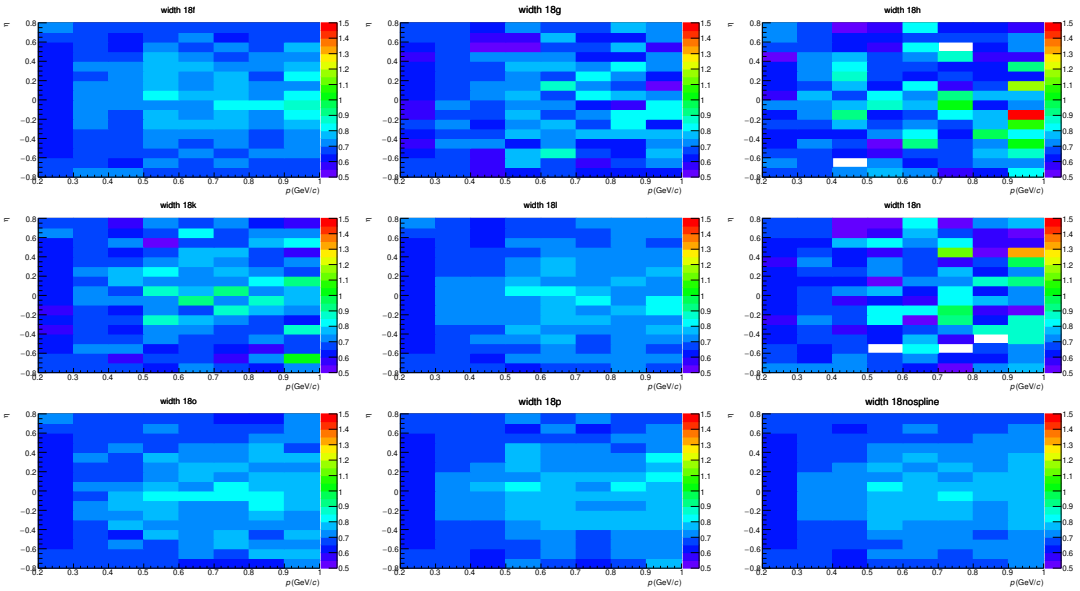

Figure B.8: width of $n\sigma^{\mathrm{TPC}}$ as a function of track momentum p versus pseudorapidity η obtained using a period from '18nospline'. Bottom right shows map created using all periods.

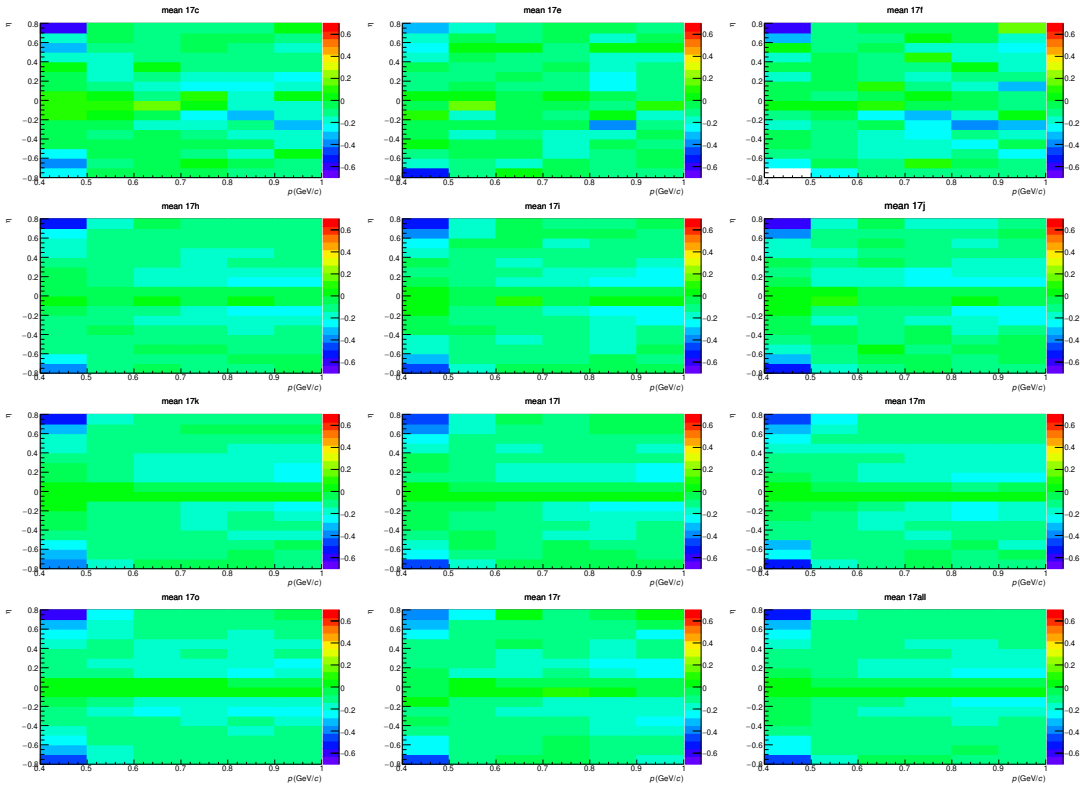

Figure B.9: mean of $n\sigma^{\mathrm{TOF}}$ as a function of track momentum obtained using 2017 periods. Bottom right shows map created using all periods.

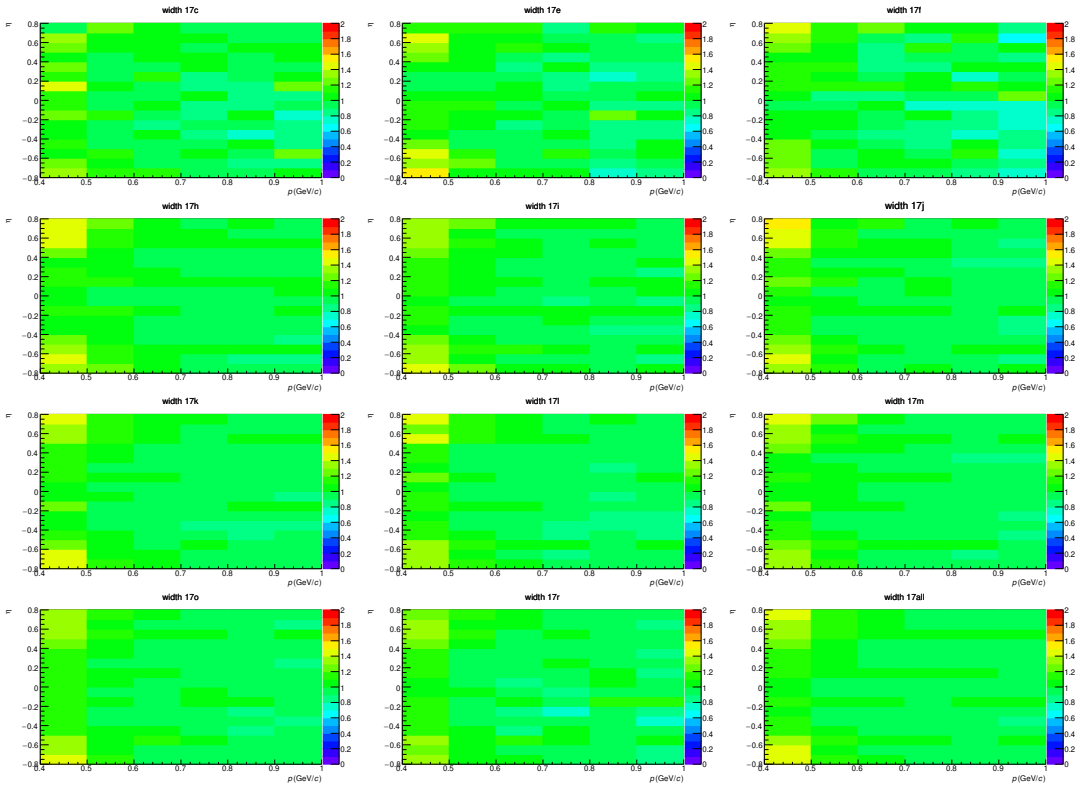

Figure B.10: width of $n\sigma^{\mathrm{TOF}}$ as a function of track momentum obtained using 2017 periods. Bottom right shows map created using all periods.

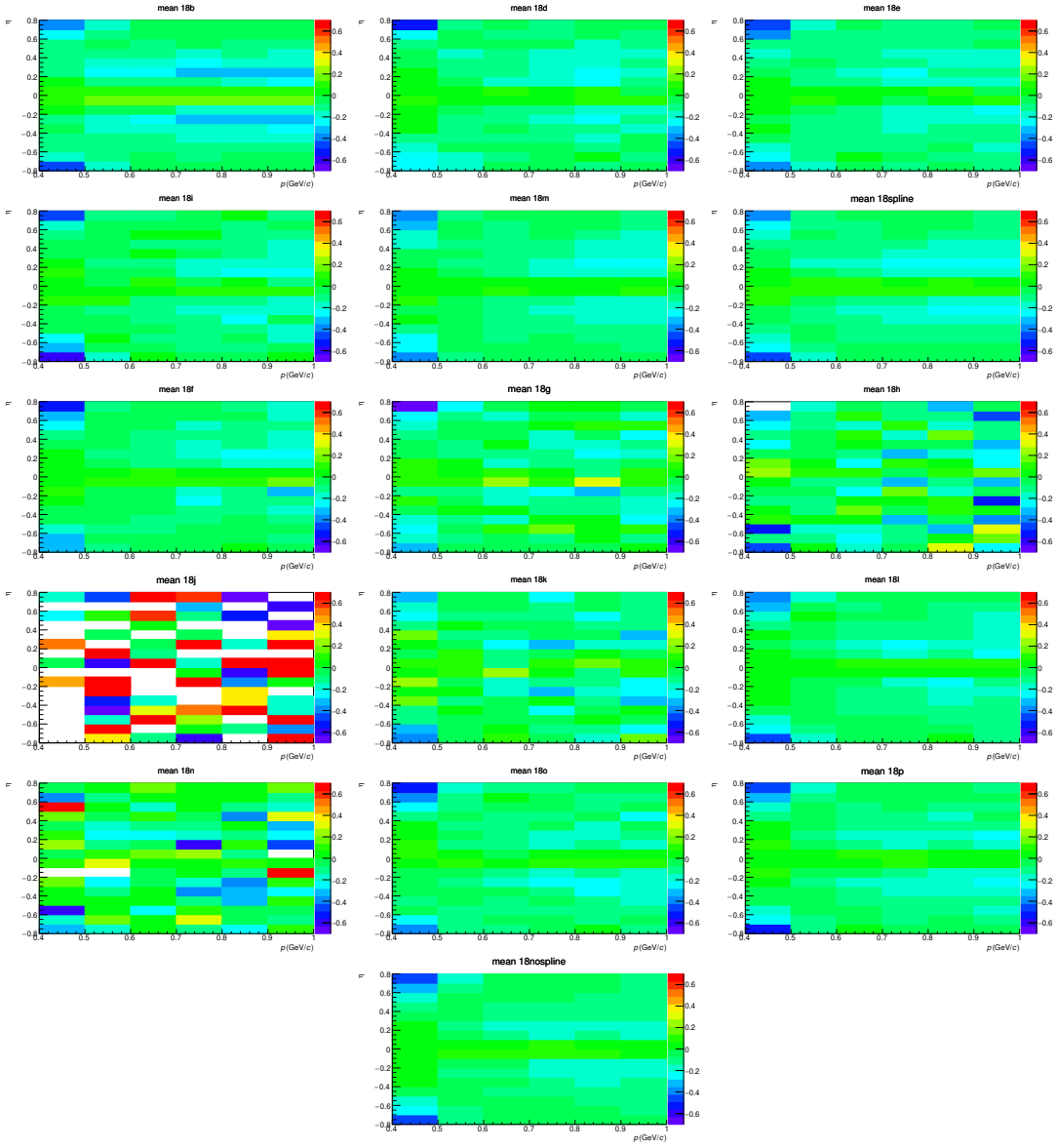

Figure B.11: mean of $n\sigma^{TOF}$ as a function of track momentum obtained using 2018 periods. Bottom right shows map created using all periods.

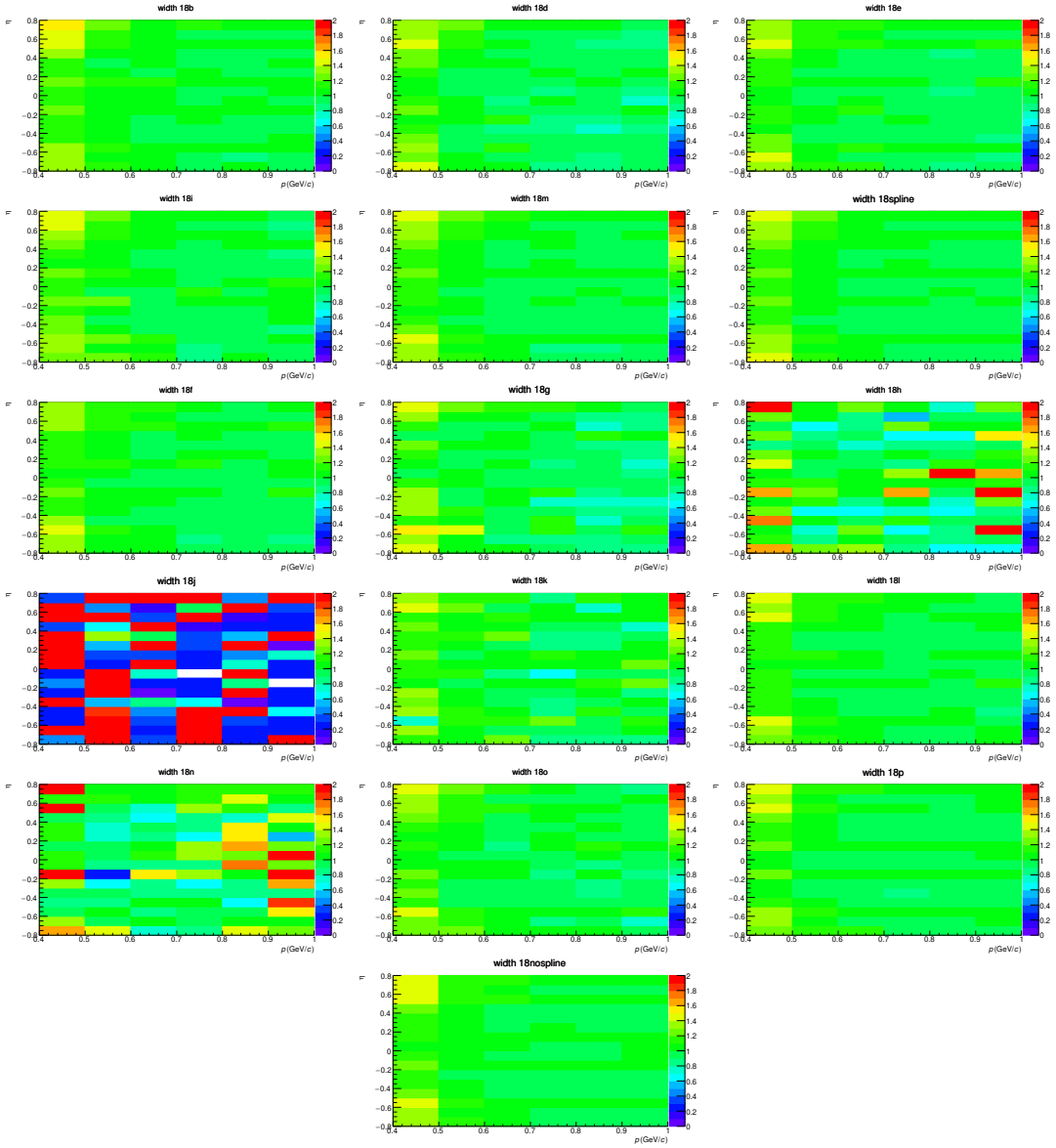

Figure B.12: width of $n\sigma^{\mathrm{TOF}}$ as a function of track momentum obtained using 2018 periods. Bottom right shows map created using all periods.

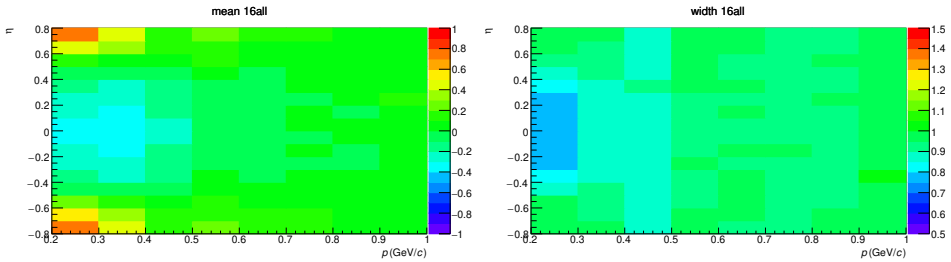

Figure B.13: Mean and width of TPC nσ_e as a function of p and η obtained using 2016 sample before re-calibration.

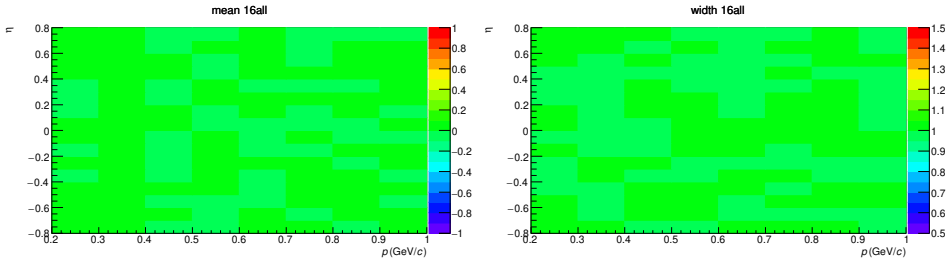

Figure B.14: Mean and width of TPC nσ_e as a function of p and η obtained using 2016 sample after re-calibration.

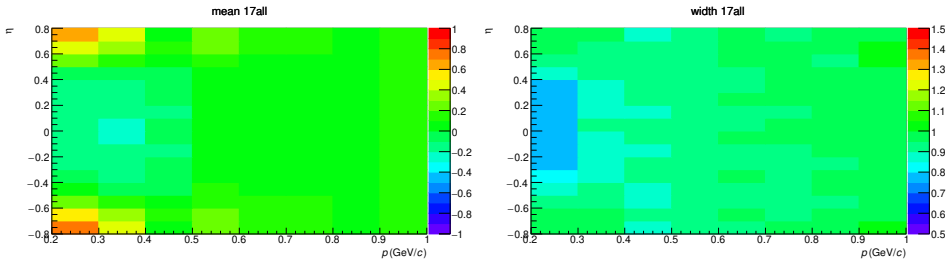

Figure B.15: Mean and width of TPC nσ_e as a function of p and η obtained using 2017 sample before re-calibration.

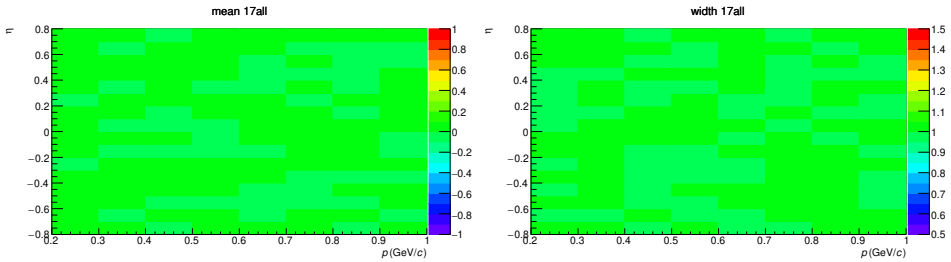

Figure B.16: Mean and width of TPC nσ_e as a function of p and η obtained using 2017 sample after re-calibration.

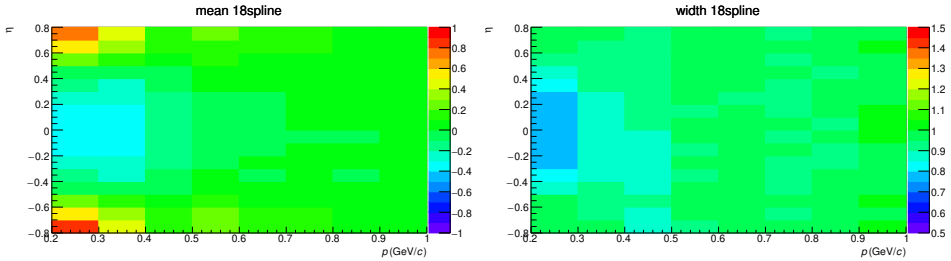

Figure B.17: Mean and width of TPC nσ_e as a function of p and η obtained using 2018 sample before re-calibration. The data sample consists of samples with TPC spline.

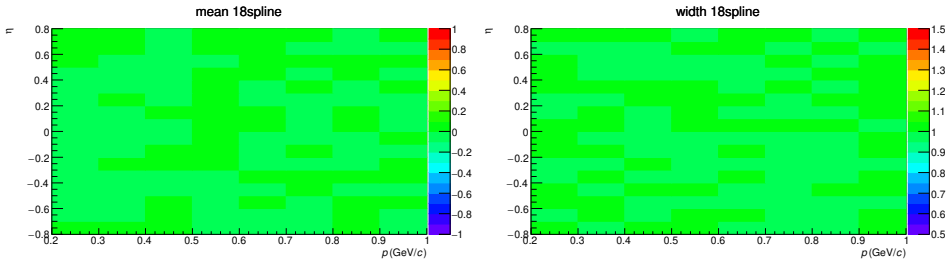

Figure B.18: Mean and width of TPC nσ_e as a function of p and η obtained using 2018 sample after re-calibration. The data sample consists of samples with TPC spline.

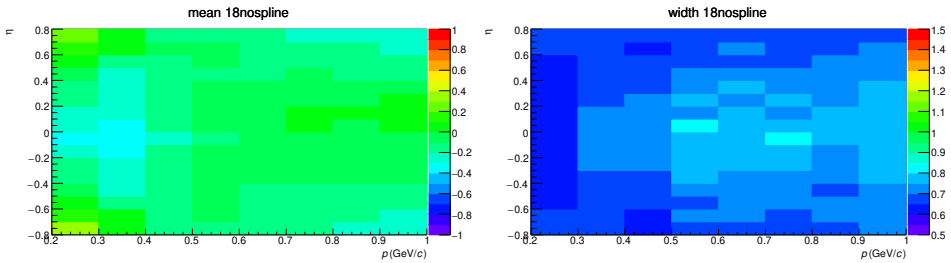

Figure B.19: Mean and width of TPC nσ_e as a function of p and η obtained using 2018 sample after re-calibration. The data sample consists of samples without TPC spline.

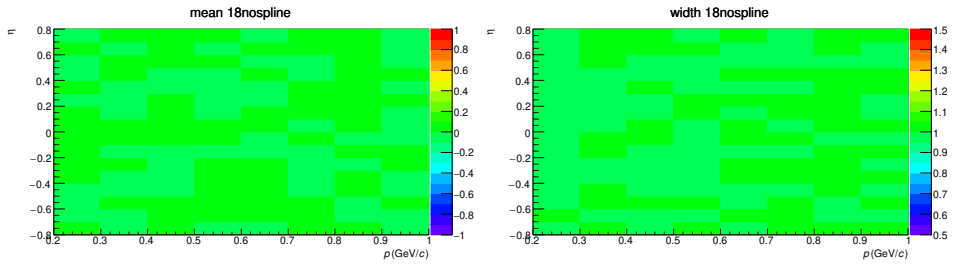

Figure B.20: Mean and width of TPC nσ_e as a function of p and η obtained using 2018 sample after re-calibration. The data sample consists of samples without TPC spline.

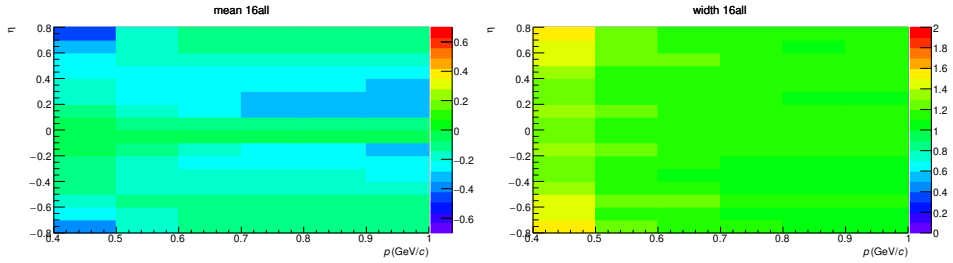

Figure B.21: Mean and width of TOF nσ_e as a function of p and η obtained using 2016 periods before re-calibration.

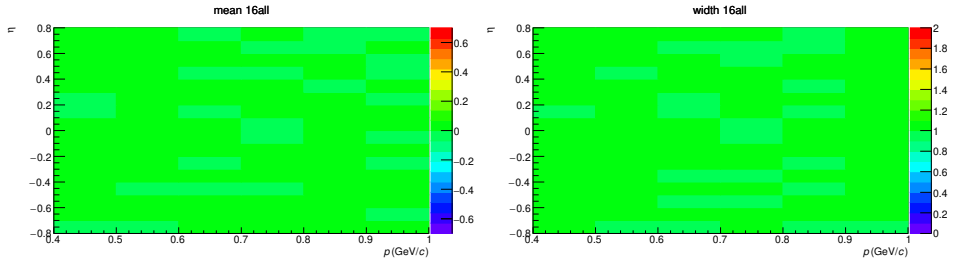

Figure B.22: Mean and width of TOF nσ_e as a function of p and η obtained using 2016 periods after re-calibration.

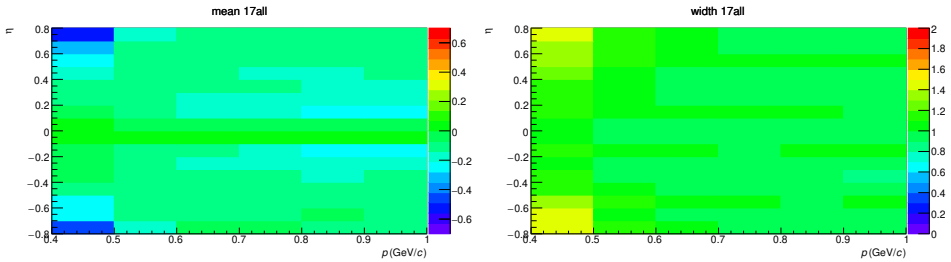

Figure B.23: Mean and width of TOF nσ_e as a function of p and η obtained using 2017 periods before re-calibration.

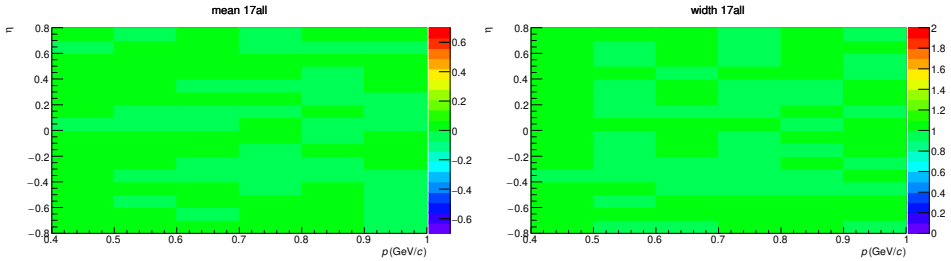

Figure B.24: Mean and width of TOF nσ_e as a function of p and η obtained using 2017 periods after re-calibration.

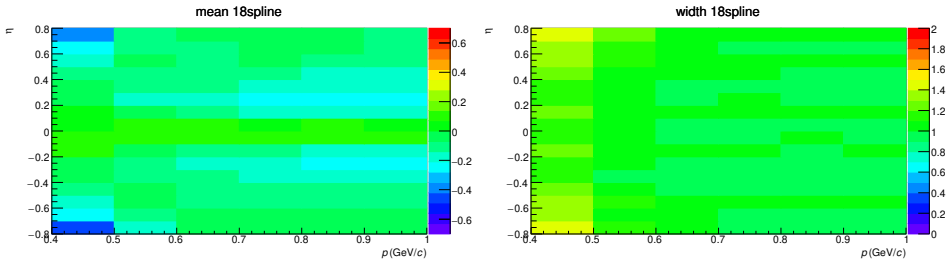

Figure B.25: Mean and width of TOF nσ_e as a function of p and η obtained using 2018 periods before re-calibration.

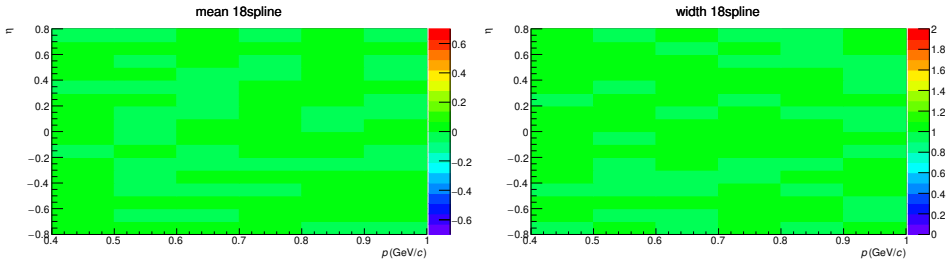

Figure B.26: Mean and width of TOF nσ_e as a function of p and η obtained using 2018 periods after re-calibration.

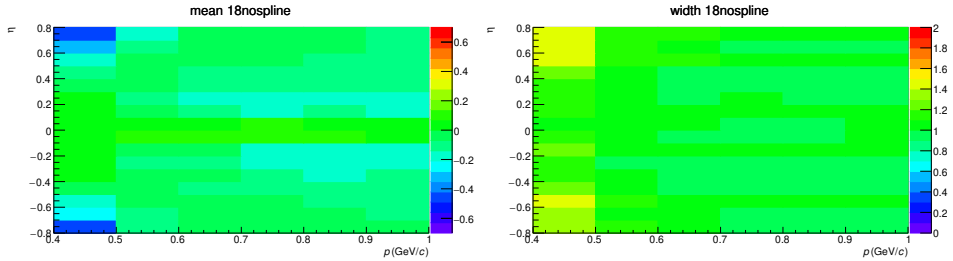

Figure B.27: Mean and width of TOF nσ_e as a function of p and η obtained using 2018 periods without TPC splines before re-calibration.

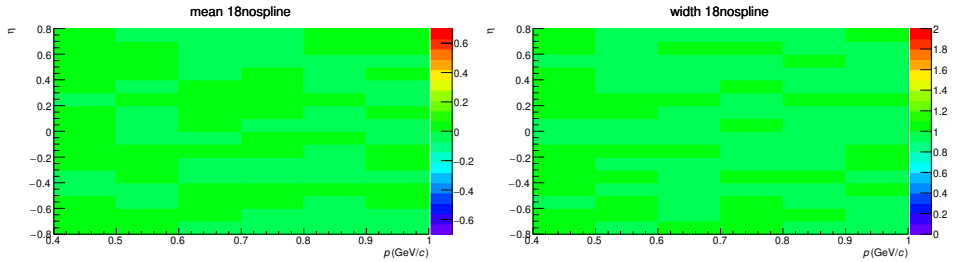

Figure B.28: Mean and width of TOF nσ_e as a function of p and η obtained using 2018 periods without TPC splines after re-calibration.

Appendix C

Dielectron mass spectra

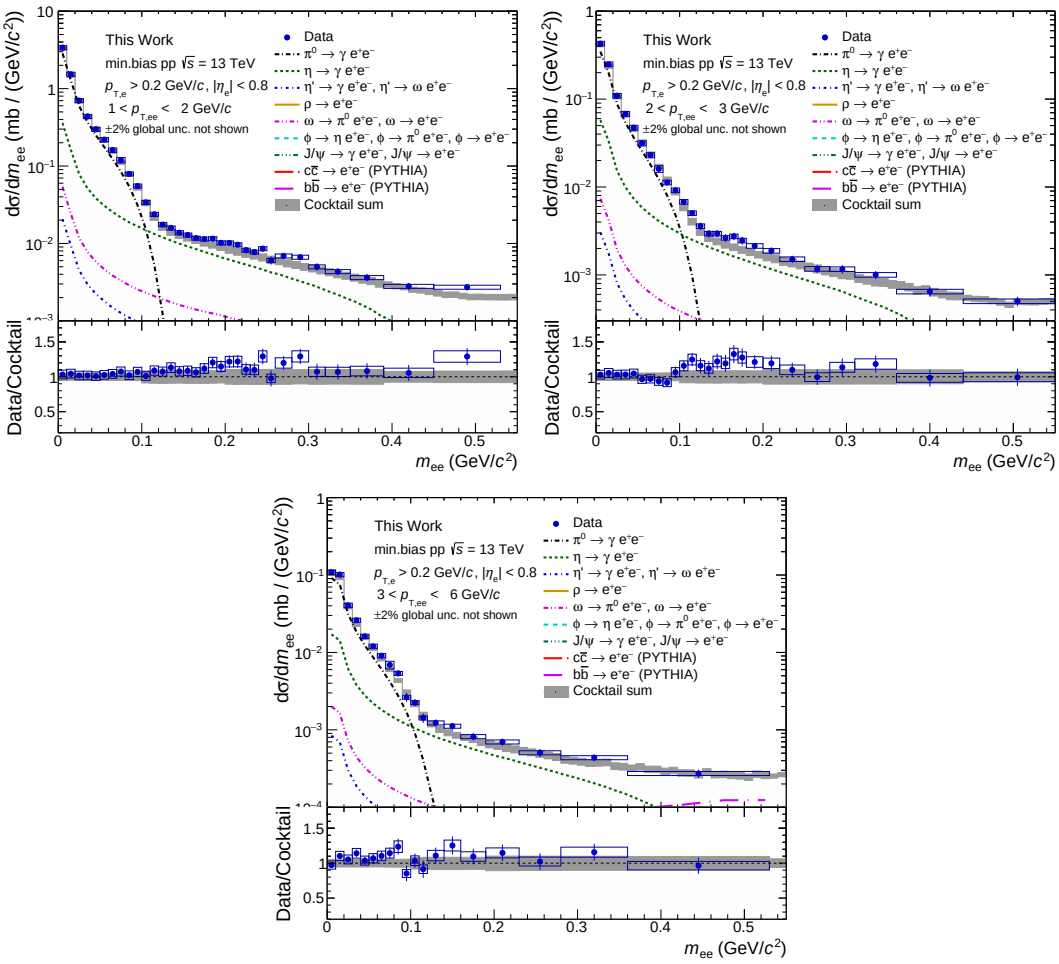

Figure C.1: The incariant mass spectra in minimum-bias pp collisions at $\sqrt{s} = 13$ TeV below 0.5 GeV/c^2.

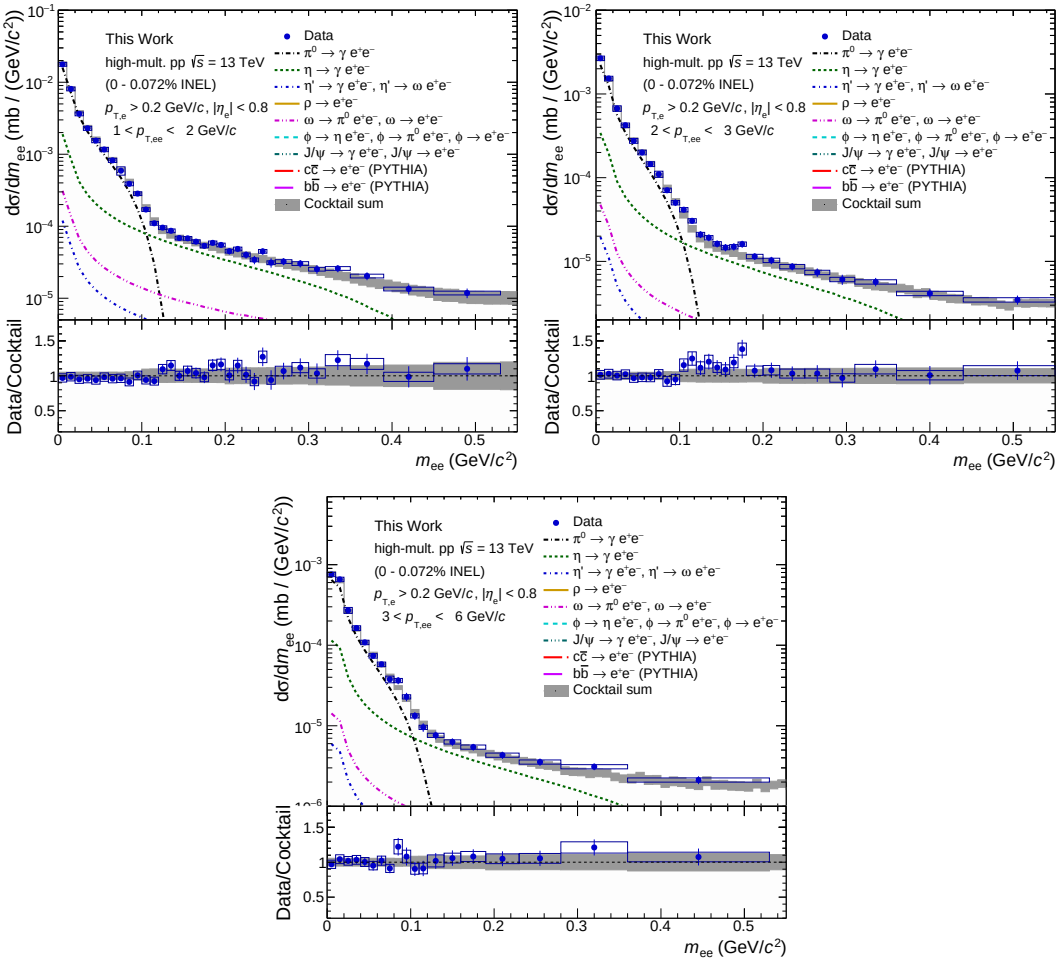

Figure C.2: The incariant mass spectra in high-multiplicty pp collisions at $\sqrt{s} = 13$ TeV below 0.5 GeV/c^2.

Appendix D

Test static t distributions for direct-photon fraction r

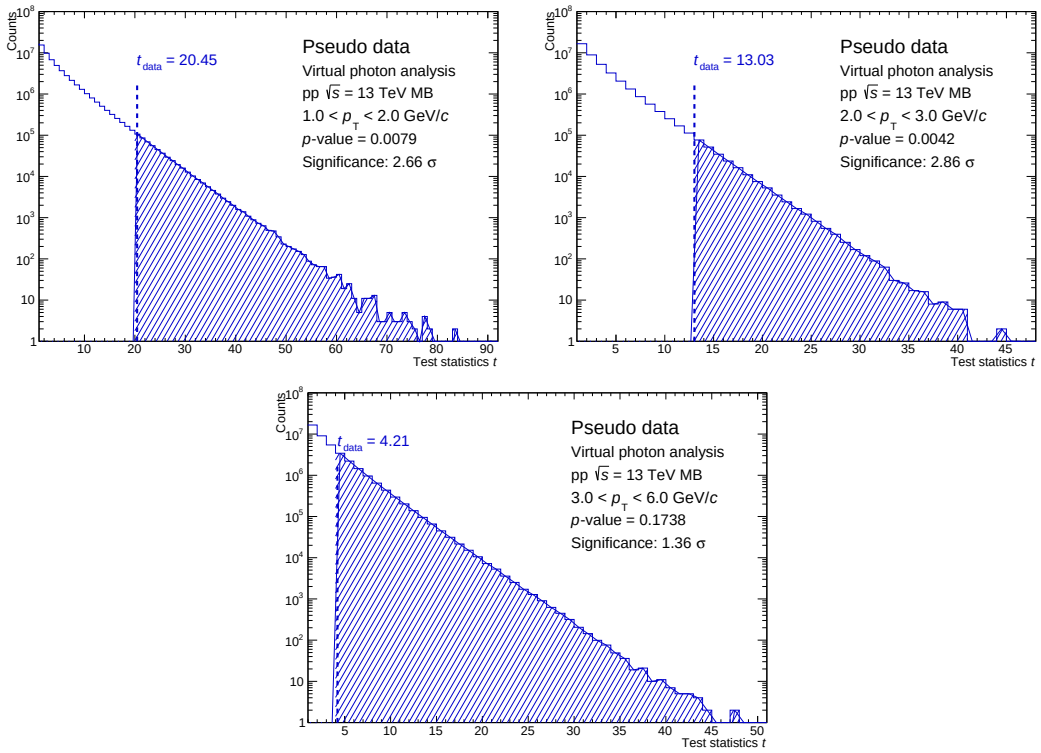

Figure D.1: Distribution of the test statistic t for the direct-photon fraction r in each p_{T} interval in minimum-bias events. Pseudo-experiments performed under the null hypothesis $H_0 : r = 0$.

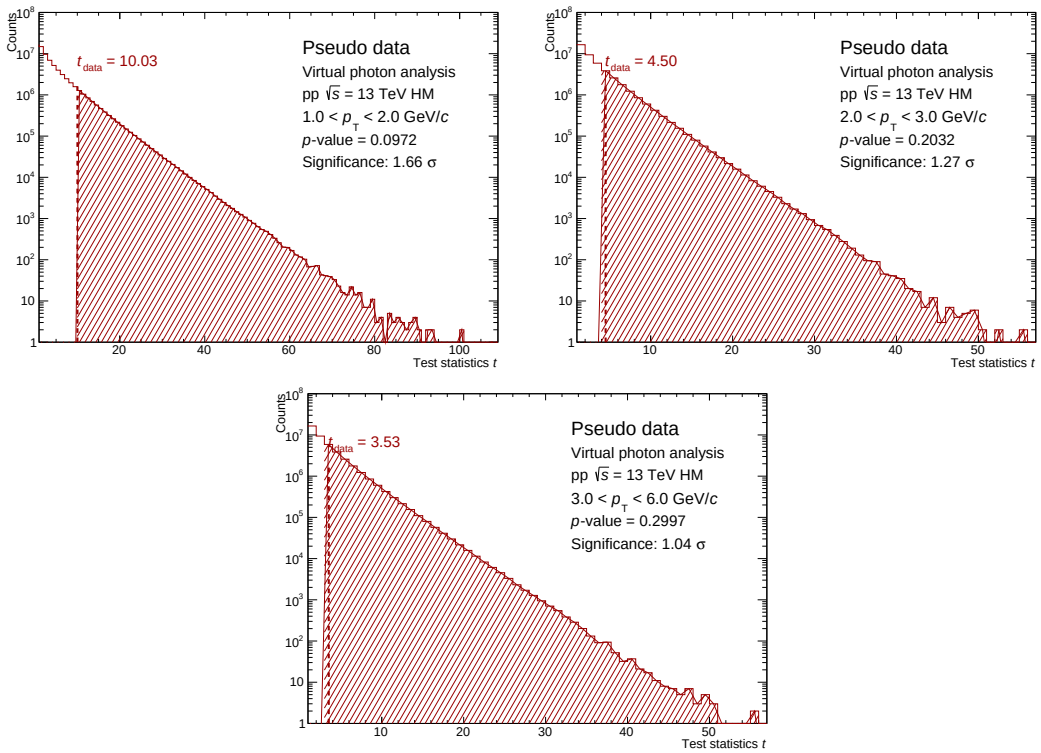

Figure D.2: Distribution of the test statistic t for the direct-photon fraction r in each p_{T} interval in high-multiplicity events. Pseudo-experiments performed under the null hypothesis $H_0 : r = 0$.

Bibliography

[1] F. Wilczek, "Quantum field theory", *Rev. Mod. Phys.* **71** (1999) , arXiv:hep-th/9803075. Cited on page(s) 1

[2] D. J. Gross and F. Wilczek, "Ultraviolet Behavior of Nonabelian Gauge Theories", *Phys. Rev. Lett.* **30** (1973) . Cited on page(s) 1

[3] H. D. Politzer, "Reliable Perturbative Results for Strong Interactions?", *Phys. Rev. Lett.* **30** (1973) . Cited on page(s) 1

[4] B. L. Ioffe, V. S. Fadin, and L. N. Lipatov, *Quantum chromodynamics: Perturbative and nonperturbative aspects*. Cambridge Univ. Press, 2010. Cited on page(s) 1

[5] **Particle Data Group** Collaboration, R. L. Workman *et al.*, "Review of Particle Physics", *PTEP* **2022** (2022) . Cited on page(s) vii, x, 1, 2, 34, 92, 96, 126

[6] J. Greensite, *An introduction to the confinement problem*, vol. 821. Springer Berlin, Heidelberg, 2011. Cited on page(s) 1

[7] J. Goldstone, A. Salam, and S. Weinberg, "Broken Symmetries", *Phys. Rev.* **127** (1962) . Cited on page(s) 1

[8] R. Gupta, "Introduction to lattice QCD: Course", in *Les Houches Summer School in Theoretical Physics, Session 68: Probing the Standard Model of Particle Interactions*, pp. 83–219. 7, 1997. arXiv:hep-lat/9807028. Cited on page(s) 1

[9] S. Muroya, A. Nakamura, C. Nonaka, and T. Takaishi, "Lattice QCD at finite density: An Introductory review", *Prog. Theor. Phys.* **110** (2003) , arXiv:hep-lat/0306031. Cited on page(s) 1

[10] C. Ratti, "Lattice QCD and heavy ion collisions: a review of recent progress", *Rept. Prog. Phys.* **81** no. 8, (2018) , arXiv:1804.07810 [hep-lat]. Cited on page(s) 1

[11] S. Chatterjee, S. Rohshap, R. Schöfbeck, and D. Schwarz, "Learning the EFT likelihood with tree boosting", arXiv:2205.12976 [hep-ph]. Cited on page(s) 1

[12] G. T. Bodwin, E. Braaten, and G. P. Lepage, "Rigorous QCD analysis of inclusive annihilation and production of heavy quarkonium", *Phys. Rev. D* **51** (1995) , arXiv:hep-ph/9407339. [Erratum: Phys.Rev.D 55, 5853 (1997)]. Cited on page(s) 1

[13] N. Brambilla, A. Pineda, J. Soto, and A. Vairo, "Potential NRQCD: An Effective theory for heavy quarkonium", *Nucl. Phys. B* **566** (2000) , arXiv:hep-ph/9907240. Cited on page(s) 1

[14] K. G. Wilson, "Confinement of Quarks", *Phys. Rev. D* **10** (1974) . Cited on page(s) 1

[15] N. Cabibbo and G. Parisi, "Exponential Hadronic Spectrum and Quark Liberation", *Phys. Lett. B* **59** (1975) . Cited on page(s) 1

[16] **HotQCD** Collaboration, A. Bazavov *et al.*, "Equation of state in (2+1)-flavor QCD", *Phys. Rev. D* **90** (2014) , arXiv:1407.6387 [hep-lat]. Cited on page(s) vii, 2, 3

[17] H. Caines, "The Search for Critical Behavior and Other Features of the QCD Phase Diagram – Current Status and Future Prospects", *Nucl. Phys. A* **967** (2017) . Cited on page(s) vii, 3

[18] P. Braun-Munzinger and J. Stachel, "The quest for the quark-gluon plasma", *Nature* **448** (2007) . Cited on page(s) 2

[19] M. collaboration, "Heavy-ion collision visualizations." https://madai.phy.duke.edu/indexaae2.html?page_id=503, accessed 2023-10-06. Cited on page(s) vii, 3

[20] **PHENIX** Collaboration, K. Adcox *et al.*, "Suppression of hadrons with large transverse momentum in central Au+Au collisions at $\sqrt{s_{\rm NN}} = 130$-GeV", *Phys. Rev. Lett.* **88** (2002) , arXiv:nucl-ex/0109003. Cited on page(s) 4

[21] **STAR** Collaboration, C. Adler *et al.*, "Disappearance of back-to-back high p_T hadron correlations in central Au+Au collisions at $\sqrt{s_{\rm NN}} = 200$-GeV", *Phys. Rev. Lett.* **90** (2003) , arXiv:nucl-ex/0210033. Cited on page(s) 4

[22] **PHENIX** Collaboration, A. Adare *et al.*, "J/ψ Production vs Centrality, Transverse Momentum, and Rapidity in Au+Au Collisions at $\sqrt{s_{\rm NN}} = 200$ GeV", *Phys. Rev. Lett.* **98** (2007) , arXiv:nucl-ex/0611020. Cited on page(s) 4

[23] **CMS** Collaboration, S. Chatrchyan *et al.*, "Observation of Sequential Upsilon Suppression in PbPb Collisions", *Phys. Rev. Lett.* **109** (2012) , arXiv:1208.2826 [nucl-ex]. [Erratum: Phys.Rev.Lett. 120, 199903 (2018)]. Cited on page(s) 4

[24] **PHENIX** Collaboration, A. Adare *et al.*, "Enhanced production of direct photons in Au+Au collisions at $\sqrt{s_{\rm NN}} = 200$ GeV and implications for the initial temperature", *Phys. Rev. Lett.* **104** (2010) , arXiv:0804.4168 [nucl-ex]. Cited on page(s) vii, 4, 5

[25] **ALICE** Collaboration, J. Adam *et al.*, "Direct photon production in Pb-Pb collisions at $\sqrt{s_{\rm NN}} = 2.76$ TeV", *Phys. Lett. B* **754** (2016) , arXiv:1509.07324 [nucl-ex]. Cited on page(s) vii, viii, xviii, 4, 5, 8, 19, 125, 139

[26] S. A. Voloshin, A. M. Poskanzer, and R. Snellings, "Collective phenomena in non-central nuclear collisions", *Landolt-Bornstein* **23** (2010) , arXiv:0809.2949 [nucl-ex]. Cited on page(s) 4

[27] **PHENIX** Collaboration, S. S. Adler *et al.*, "Centrality dependence of direct photon production in $\sqrt{s_{\rm NN}} = 200$ GeV Au + Au collisions", *Phys. Rev. Lett.* **94** (2005) , arXiv:nucl-ex/0503003. Cited on page(s) vii, 5, 19

[28] **PHENIX** Collaboration, S. S. Adler *et al.*, "Measurement of direct photon production in p + p collisions at $\sqrt{s} = 200$ GeV", *Phys. Rev. Lett.* **98** (2007) , arXiv:hep-ex/0609031. Cited on page(s) vii, 5

[29] S. Turbide, R. Rapp, and C. Gale, "Hadronic production of thermal photons", *Phys. Rev. C* **69** (2004) , arXiv:hep-ph/0308085. Cited on page(s) vii, ix, 5, 17, 18

[30] **CMS** Collaboration, V. Khachatryan *et al.*, "Observation of Long-Range Near-Side Angular Correlations in Proton-Proton Collisions at the LHC", *JHEP* **09** (2010) , arXiv:1009.4122 [hep-ex]. Cited on page(s) vii, 4, 6

[31] **CMS** Collaboration, S. Chatrchyan *et al.*, "Multiplicity and Transverse Momentum Dependence of Two- and Four-Particle Correlations in pPb and PbPb Collisions", *Phys. Lett. B* **724** (2013) , arXiv:1305.0609 [nucl-ex]. Cited on page(s) vii, 6

[32] T. Sjostrand, S. Mrenna, and P. Z. Skands, "A Brief Introduction to PYTHIA 8.1", *Comput. Phys. Commun.* **178** (2008) , arXiv:0710.3820 [hep-ph]. Cited on page(s) viii, 7

[33] T. Pierog, I. Karpenko, J. M. Katzy, E. Yatsenko, and K. Werner, "EPOS LHC: Test of collective hadronization with data measured at the CERN Large Hadron Collider", *Phys. Rev. C* **92** no. 3, (2015) , arXiv:1306.0121 [hep-ph]. Cited on page(s) viii, 7

[34] C. Bierlich and J. R. Christiansen, "Effects of color reconnection on hadron flavor observables", *Phys. Rev. D* **92** no. 9, (2015) , arXiv:1507.02091 [hep-ph]. Cited on page(s) viii, 7

[35] **ALICE** Collaboration, B. B. Abelev *et al.*, "Multi-strange baryon production at mid-rapidity in Pb-Pb collisions at $\sqrt{s_{\rm NN}} = 2.76$ TeV", *Phys. Lett. B* **728** (2014) , arXiv:1307.5543 [nucl-ex]. [Erratum: Phys.Lett.B 734, 409–410 (2014)]. Cited on page(s) viii, 7

[36] **ALICE** Collaboration, B. B. Abelev *et al.*, "Multiplicity Dependence of Pion, Kaon, Proton and Lambda Production in p-Pb Collisions at $\sqrt{s_{\rm NN}} = 5.02$ TeV", *Phys. Lett. B* **728** (2014) , arXiv:1307.6796 [nucl-ex]. Cited on page(s) viii, 7

[37] **ALICE** Collaboration, J. Adam *et al.*, "Multi-strange baryon production in p-Pb collisions at $\sqrt{s_{\rm NN}} = 5.02$ TeV", *Phys. Lett. B* **758** (2016) , arXiv:1512.07227 [nucl-ex]. Cited on page(s) viii, 7

[38] **ALICE** Collaboration, B. Abelev *et al.*, "Long-range angular correlations on the near and away side in p-Pb collisions at $\sqrt{s_{\rm NN}} = 5.02$ TeV", *Phys. Lett. B* **719** (2013) , arXiv:1212.2001 [nucl-ex]. Cited on page(s) 4

[39] **ATLAS** Collaboration, G. Aad *et al.*, "Observation of Associated Near-Side and Away-Side Long-Range Correlations in $\sqrt{s_{\rm NN}} = 5.02$ TeV Proton-Lead Collisions with the ATLAS Detector", *Phys. Rev. Lett.* **110** no. 18, (2013) , arXiv:1212.5198 [hep-ex]. Cited on page(s) 4

[40] **PHENIX** Collaboration, A. Adare *et al.*, "Measurement of long-range angular correlation and quadrupole anisotropy of pions and (anti)protons in central d+Au collisions at $\sqrt{s_{\rm NN}} = 200$ GeV", *Phys. Rev. Lett.* **114** no. 19, (2015) , arXiv:1404.7461 [nucl-ex]. Cited on page(s) 4

[41] **PHENIX** Collaboration, A. Adare *et al.*, "Measurements of elliptic and triangular flow in high-multiplicity ^{3}He+Au collisions at $\sqrt{s_{\rm NN}} =$ GeV", *Phys. Rev. Lett.* **115** no. 14, (2015) , arXiv:1507.06273 [nucl-ex]. Cited on page(s) 4

[42] **ALICE** Collaboration, J. Adam *et al.*, "Enhanced production of multi-strange hadrons in high-multiplicity proton-proton collisions", *Nature Phys.* **13** (2017) , arXiv:1606.07424 [nucl-ex]. Cited on page(s) 4, 132

[43] **ALICE** Collaboration, S. Acharya *et al.*, "Multiplicity dependence of J/ψ production at midrapidity in pp collisions at $\sqrt{s} = 13$ TeV", *Phys. Lett. B* **810** (2020) , arXiv:2005.11123 [nucl-ex]. Cited on page(s) xiv, 4, 92, 96, 97, 132

[44] **ALICE** Collaboration, J. Adam *et al.*, "Measurement of charm and beauty production at central rapidity versus charged-particle multiplicity in proton-proton collisions at $\sqrt{s} = 7$ TeV", *JHEP* **09** (2015) , arXiv:1505.00664 [nucl-ex]. Cited on page(s) xiv, 4, 97, 98, 132

[45] P. Stankus, "Experimental overview on small colliding systems at RHIC", *Nucl. Phys. A* **956** (2016) . Cited on page(s) 5

[46] C. Loizides, "Experimental overview on small collision systems at the LHC", *Nucl. Phys. A* **956** (2016) , arXiv:1602.09138 [nucl-ex]. Cited on page(s) 5

[47] **ALICE** Collaboration, S. Acharya *et al.*, "Multiplicity dependence of charged-particle jet production in pp collisions at $\sqrt{\mathbf{s}} = \mathbf{13}$ **TeV**", *Eur. Phys. J. C* **82** no. 6, (2022) , arXiv:2202.01548 [nucl-ex]. Cited on page(s) 5

[48] **PHENIX** Collaboration, T. Sakaguchi, "Overview of latest results from PHENIX", *PoS* **HardProbes2018** (2019) , arXiv:1901.01951 [nucl-ex]. Cited on page(s) viii, 8

[49] **PHENIX** Collaboration, N. J. Abdulameer *et al.*, "Low-p_{T} direct-photon production in Au+Au collisions at $\sqrt{s_{\mathrm{NN}}} = 39$ and 62.4 GeV", *Phys. Rev. C* **107** no. 2, (2023) , arXiv:2203.12354 [nucl-ex]. Cited on page(s) viii, xviii, 8, 139

[50] **PHENIX** Collaboration, A. Adare *et al.*, "Centrality dependence of low-momentum direct-photon production in Au+Au collisions at $\sqrt{s_{\mathrm{NN}}} = 200$ GeV", *Phys. Rev. C* **91** no. 6, (2015) , arXiv:1405.3940 [nucl-ex]. Cited on page(s) viii, xviii, 8, 139

[51] **ALICE** Collaboration, S. Acharya *et al.*, "Dielectron and heavy-quark production in inelastic and high-multiplicity proton–proton collisions at $\sqrt{s} =$ 13 TeV", *Phys. Lett. B* **788** (2019) , arXiv:1805.04407 [hep-ex]. Cited on page(s) viii, 8, 99, 110, 111

[52] G. J. Feldman and R. D. Cousins, "A Unified approach to the classical statistical analysis of small signals", *Phys. Rev. D* **57** (1998) , arXiv:physics/9711021. Cited on page(s) viii, 8

[53] B. Jager, A. Schafer, M. Stratmann, and W. Vogelsang, "Next-to-leading order QCD corrections to high p(T) pion production in longitudinally polarized pp collisions", *Phys. Rev. D* **67** (2003) , arXiv:hep-ph/0211007. Cited on page(s) viii, 8, 131, 142

[54] **ALICE** Collaboration, S. Acharya *et al.*, "Neutral meson production in Proton-Proton Collisions at $\sqrt{s} = 13$ TeV." Manuscript in preparation. Cited on page(s) viii, xiv, 7, 9, 91, 92, 93, 94, 132

[55] T. Sjöstrand, S. Ask, J. R. Christiansen, R. Corke, N. Desai, P. Ilten, S. Mrenna, S. Prestel, C. O. Rasmussen, and P. Z. Skands, "An introduction to PYTHIA 8.2", *Comput. Phys. Commun.* **191** (2015) , arXiv:1410.3012 [hep-ph]. Cited on page(s) viii, 9, 58, 75

[56] P. Skands, S. Carrazza, and J. Rojo, "Tuning PYTHIA 8.1: the Monash 2013 Tune", *Eur. Phys. J. C* **74** no. 8, (2014) , arXiv:1404.5630 [hep-ph]. Cited on page(s) viii, 9, 75

[57] T.-J. Hou *et al.*, "New CTEQ global analysis of quantum chromodynamics with high-precision data from the LHC", *Phys. Rev. D* **103** no. 1, (2021) , arXiv:1912.10053 [hep-ph]. Cited on page(s) viii, 9

[58] **NNPDF** Collaboration, V. Bertone, S. Carrazza, N. P. Hartland, E. R. Nocera, and J. Rojo, "A determination of the fragmentation functions of pions, kaons, and protons with faithful uncertainties", *Eur. Phys. J. C* **77** no. 8, (2017) , arXiv:1706.07049 [hep-ph]. Cited on page(s) viii, 9

[59] C. A. Aidala, F. Ellinghaus, R. Sassot, J. P. Seele, and M. Stratmann, "Global Analysis of Fragmentation Functions for Eta Mesons", *Phys. Rev. D* **83** (2011) , arXiv:1009.6145 [hep-ph]. Cited on page(s) viii, 9

[60] S. Dulat, T.-J. Hou, J. Gao, M. Guzzi, J. Huston, P. Nadolsky, J. Pumplin, C. Schmidt, D. Stump, and C. P. Yuan, "New parton distribution functions from a global analysis of quantum chromodynamics", *Phys. Rev. D* **93** no. 3, (2016) , arXiv:1506.07443 [hep-ph]. Cited on page(s) viii, 9

[61] G.-Y. Ma, W. Dai, B.-W. Zhang, and E.-K. Wang, "NLO Productions of ω and K^0_S with a global extraction of the jet transport parameter in heavy-ion collisions", *Eur. Phys. J. C* **79** no. 6, (2019) , arXiv:1812.02033 [nucl-th]. Cited on page(s) viii, 9

[62] **ALICE TPC** Collaboration, J. Adolfsson *et al.*, "The upgrade of the ALICE TPC with GEMs and continuous readout", *JINST* **16** no. 03, (2021) , arXiv:2012.09518 [physics.ins-det]. Cited on page(s) 11

[63] **ALICE** Collaboration, S. Acharya *et al.*, "Data-driven precision determination of the material budget in ALICE", arXiv:2303.15317 [physics.ins-det]. Cited on page(s) 11

[64] C. Shen, J.-F. Paquet, G. S. Denicol, S. Jeon, and C. Gale, "Collectivity and electromagnetic radiation in small systems", *Phys. Rev. C* **95** no. 1, (2017) , arXiv:1609.02590 [nucl-th]. Cited on page(s) ix, xvii, 13, 14, 15, 131, 133, 135, 137, 138, 142

[65] J.-F. Paquet, C. Shen, G. S. Denicol, M. Luzum, B. Schenke, S. Jeon, and C. Gale, "Production of photons in relativistic heavy-ion collisions", *Phys. Rev. C* **93** no. 4, (2016) , arXiv:1509.06738 [hep-ph]. Cited on page(s) 13, 14

[66] P. Aurenche, P. Chiappetta, M. Fontannaz, J. P. Guillet, and E. Pilon, "Next-to-leading order bremsstrahlung contribution to prompt photon production", *Nucl. Phys. B* **399** (1993) . Cited on page(s) 14

[67] S. Campbell, "Photon production from gluon-mediated quark–anti-quark annihilation at confinement", *Phys. Rev. C* **92** no. 1, (2015) , arXiv:1504.01654 [nucl-ex]. Cited on page(s) ix, 16

[68] P. Aurenche, M. Fontannaz, J.-P. Guillet, E. Pilon, and M. Werlen, "A New critical study of photon production in hadronic collisions", *Phys. Rev. D* **73** (2006) , arXiv:hep-ph/0602133. Cited on page(s) 16

[69] M. Klasen and F. König, "New information on photon fragmentation functions", *Eur. Phys. J. C* **74** no. 8, (2014) , arXiv:1403.2290 [hep-ph]. Cited on page(s) ix, 16

[70] L. E. Gordon and W. Vogelsang, "Polarized and unpolarized prompt photon production beyond the leading order", *Phys. Rev. D* **48** (1993) . Cited on page(s) ix, xvii, 16, 135, 137, 138

[71] C. Gale, "Photon Production in Hot and Dense Strongly Interacting Matter", *Landolt-Bornstein* **23** (2010) , arXiv:0904.2184 [hep-ph]. Cited on page(s) 17

[72] L. D. McLerran and T. Toimela, "Photon and Dilepton Emission from the Quark - Gluon Plasma: Some General Considerations", *Phys. Rev. D* **31** (1985) . Cited on page(s) 17

[73] H. A. Weldon, "Simple Rules for Discontinuities in Finite Temperature Field Theory", *Phys. Rev. D* **28** (1983) . Cited on page(s) 17

[74] C. Gale and J. I. Kapusta, "Vector dominance model at finite temperature", *Nucl. Phys. B* **357** (1991) . Cited on page(s) 17

[75] C. Song, "Photon emission from hot hadronic matter described by an effective chiral Lagrangian", *Phys. Rev. C* **47** (1993) . Cited on page(s) 17

[76] O. Linnyk, V. Konchakovski, T. Steinert, W. Cassing, and E. L. Bratkovskaya, "Hadronic and partonic sources of direct photons in relativistic heavy-ion collisions", *Phys. Rev. C* **92** no. 5, (2015) , arXiv:1504.05699 [nucl-th]. Cited on page(s) ix, 17, 19

[77] C. Gale, J.-F. Paquet, B. Schenke, and C. Shen, "Multimessenger heavy-ion collision physics", *Phys. Rev. C* **105** no. 1, (2022) , arXiv:2106.11216 [nucl-th]. Cited on page(s) ix, xviii, 17, 19, 134, 139

[78] G. Basar, D. Kharzeev, D. Kharzeev, and V. Skokov, "Conformal anomaly as a source of soft photons in heavy ion collisions", *Phys. Rev. Lett.* **109** (2012) , arXiv:1206.1334 [hep-ph]. Cited on page(s) 17

[79] G. Basar, D. E. Kharzeev, and E. V. Shuryak, "Magneto-sonoluminescence and its signatures in photon and dilepton production in relativistic heavy ion collisions", *Phys. Rev. C* **90** no. 1, (2014) , arXiv:1402.2286 [hep-ph]. Cited on page(s) 17

[80] B. Muller, S.-Y. Wu, and D.-L. Yang, "Elliptic flow from thermal photons with magnetic field in holography", *Phys. Rev. D* **89** no. 2, (2014) , arXiv:1308.6568 [hep-th]. Cited on page(s) 17

[81] **PHENIX** Collaboration, U. A. Acharya *et al.*, "Nonprompt direct-photon production in Au+Au collisions at $\sqrt{s_{\rm NN}} = 200$ GeV", arXiv:2203.17187 [nucl-ex]. Cited on page(s) 17

[82] S. Turbide, C. Gale, S. Jeon, and G. D. Moore, "Energy loss of leading hadrons and direct photon production in evolving quark-gluon plasma", *Phys. Rev. C* **72** (2005) , arXiv:hep-ph/0502248. Cited on page(s) 17

[83] M. R. Whalley, "A Compilation of data on hadronic total cross-sections in e+ e- interactions", *J. Phys. G* **29** (2003) . Cited on page(s) ix, 19

[84] P. Dasgupta, S. De, R. Chatterjee, and D. K. Srivastava, "Photon production from Pb+Pb collisions at $\sqrt{s_{\rm NN}} = 5.02$ TeV at LHC and at $\sqrt{s_{\rm NN}} = 39$ TeV at FCC", *Phys. Rev. C* **98** no. 2, (2018) , arXiv:1804.02828 [nucl-th]. Cited on page(s) ix, 19

[85] H. van Hees, M. He, and R. Rapp, "Pseudo-critical enhancement of thermal photons in relativistic heavy-ion collisions?", *Nucl. Phys. A* **933** (2015) , arXiv:1404.2846 [nucl-th]. Cited on page(s) ix, 19

[86] H.-L. Lai, M. Guzzi, J. Huston, Z. Li, P. M. Nadolsky, J. Pumplin, and C. P. Yuan, "New parton distributions for collider physics", *Phys. Rev. D* **82** (2010) , arXiv:1007.2241 [hep-ph]. Cited on page(s) ix, 19, 131

[87] J. Gao, M. Guzzi, J. Huston, H.-L. Lai, Z. Li, P. Nadolsky, J. Pumplin, D. Stump, and C. P. Yuan, "CT10 next-to-next-to-leading order global analysis of QCD", *Phys. Rev. D* **89** no. 3, (2014) , arXiv:1302.6246 [hep-ph]. Cited on page(s) ix, 19, 131

[88] M. Guzzi, P. Nadolsky, E. Berger, H.-L. Lai, F. Olness, and C. P. Yuan, "CT10 parton distributions and other developments in the global QCD analysis", arXiv:1101.0561 [hep-ph]. Cited on page(s) ix, 19, 131

[89] D. Stump, J. Huston, J. Pumplin, W.-K. Tung, H. L. Lai, S. Kuhlmann, and J. F. Owens, "Inclusive jet production, parton distributions, and the search for new physics", *JHEP* **10** (2003) , arXiv:hep-ph/0303013. Cited on page(s) ix, 19, 131

[90] M. Gluck, E. Reya, and A. Vogt, "Parton fragmentation into photons beyond the leading order", *Phys. Rev. D* **48** (1993) . [Erratum: Phys.Rev.D 51, 1427 (1995)]. Cited on page(s) ix, 19, 131

[91] L. Bourhis, M. Fontannaz, and J. P. Guillet, "Quarks and gluon fragmentation functions into photons", *Eur. Phys. J. C* **2** (1998) , arXiv:hep-ph/9704447. Cited on page(s) ix, xviii, 19, 131, 134, 139

[92] M. Klasen, C. Klein-Bösing, and H. Poppenborg, "Prompt photon production and photon-jet correlations at the LHC", *JHEP* **03** (2018) , arXiv:1709.04154 [hep-ph]. Cited on page(s) ix, 19

[93] **NNPDF** Collaboration, R. D. Ball, V. Bertone, S. Carrazza, L. Del Debbio, S. Forte, A. Guffanti, N. P. Hartland, and J. Rojo, "Parton distributions with QED corrections", *Nucl. Phys. B* **877** (2013) , arXiv:1308.0598 [hep-ph]. Cited on page(s) ix, 19

[94] **WA98** Collaboration, M. M. Aggarwal *et al.*, "Observation of direct photons in central 158-A-GeV Pb-208 + Pb-208 collisions", *Phys. Rev. Lett.* **85** (2000) , arXiv:nucl-ex/0006008. Cited on page(s) 19

[95] **ALICE** Collaboration, S. Acharya *et al.*, "Direct photon production at low transverse momentum in proton-proton collisions at $\sqrt{\mathbf{s}} = \mathbf{2.76}$ and 8 TeV", *Phys. Rev. C* **99** no. 2, (2019) , arXiv:1803.09857 [nucl-ex]. Cited on page(s) 19

[96] **PHENIX** Collaboration, A. Adare *et al.*, "Detailed measurement of the e^+e^- pair continuum in $p+p$ and Au+Au collisions at $\sqrt{s_{\rm NN}} = 200$ GeV and implications for direct photon production", *Phys. Rev. C* **81** (2010) , arXiv:0912.0244 [nucl-ex]. Cited on page(s) 20

[97] N. M. Kroll and W. Wada, "Internal pair production associated with the emission of high-energy gamma rays", *Phys. Rev.* **98** (1955) . Cited on page(s) 20, 91

[98] L. G. Landsberg, "Electromagnetic Decays of Light Mesons", *Phys. Rept.* **128** (1985) . Cited on page(s) 20

[99] R. H. Dalitz, "On an alternative decay process for the neutral pi-meson, Letters to the Editor", *Proc. Phys. Soc. A* **64** (1951) . Cited on page(s) 22

[100] E. Norrbin and T. Sjostrand, "Production and hadronization of heavy quarks", *Eur. Phys. J. C* **17** (2000) , arXiv:hep-ph/0005110. Cited on page(s) x, 23

[101] L. Evans and P. Bryant, "Lhc machine", *Journal of Instrumentation* **3** no. 08, (Aug, 2008) . https://dx.doi.org/10.1088/1748-0221/3/08/S08001. Cited on page(s) 25

[102] E. Mobs, "The CERN accelerator complex. Complexe des accélérateurs du CERN",. https://cds.cern.ch/record/2197559. General Photo. Cited on page(s) x, 25, 27

[103] J. Wenninger, "Operation and Configuration of the LHC in Run 2",. https://cds.cern.ch/record/2668326. Cited on page(s) 26

[104] B. Salvachua, "Overview of Proton-Proton Physics during Run 2",. https://cds.cern.ch/record/2750272. Cited on page(s) 1, 26

[105] **ALICE** Collaboration, B. B. Abelev *et al.*, "Performance of the ALICE Experiment at the CERN LHC", *Int. J. Mod. Phys. A* **29** (2014) , arXiv:1402.4476 [nucl-ex]. Cited on page(s) xi, xii, 1, 26, 32, 39, 41, 42, 51, 54

[106] **ALICE** Collaboration, A. Collaboration *et al.*, "Alice: Physics performance report, volume i", *Journal of Physics G: Nuclear and Particle Physics* **30** no. 11, (2004) . Cited on page(s) 26

[107] **ALICE** Collaboration, A. Collaboration *et al.*, "Alice: Physics performance report, volume ii", *Journal of Physics G: Nuclear and Particle Physics* **32** (2006) . Cited on page(s) 26

[108] K. Aamodt, A. A. Quintana, R. Achenbach, S. Acounis, D. Adamová, C. Adler, M. Aggarwal, F. Agnese, G. A. Rinella, Z. Ahammed, *et al.*, "The alice experiment at the cern lhc", *Journal of Instrumentation* **3** no. 08, (2008) . Cited on page(s) x, 26, 31, 38, 39, 42

[109] **ALICE** Collaboration, K. Aamodt *et al.*, "The ALICE experiment at the CERN LHC", *JINST* **3** (2008) . Cited on page(s) x, 27, 28

[110] L. Betev and P. Chochula, "Definition of the alice coordinate system and basic rules for sub-detector components numbering", *ALICE Offline, Geneva* (2003) . Cited on page(s) x, 28

[111] J. Alme *et al.*, "The ALICE TPC, a large 3-dimensional tracking device with fast readout for ultra-high multiplicity events", *Nucl. Instrum. Meth. A* **622** (2010) , arXiv:1001.1950 [physics.ins-det]. Cited on page(s) 29

[112] W. Blum, W. Riegler, and L. Rolandi, *Particle detection with drift chambers*. Springer Science & Business Media, 2008. Cited on page(s) 32

[113] **ALICE** Collaboration, P. Cortese, "ALICE transition-radiation detector: Technical Design Report",. Cited on page(s) 33

[114] **ALICE** Collaboration, S. Acharya *et al.*, "The ALICE Transition Radiation Detector: construction, operation, and performance", *Nucl. Instrum. Meth. A* **881** (2018) , arXiv:1709.02743 [physics.ins-det]. Cited on page(s) xi, 34, 41

[115] A. Akindinov *et al.*, "Performance of the ALICE Time-Of-Flight detector at the LHC", *Eur. Phys. J. Plus* **128** (2013) . Cited on page(s) 34

[116] A. Akindinov *et al.*, "The multigap resistive plate chamber as a time-of-flight detector", *Nucl. Instrum. Meth. A* **456** (2000) . Cited on page(s) 34

[117] **ALICE** Collaboration, J. Adam *et al.*, "Determination of the event collision time with the ALICE detector at the LHC", *Eur. Phys. J. Plus* **132** no. 2, (2017) , arXiv:1610.03055 [physics.ins-det]. Cited on page(s) 34

[118] M. Bondila *et al.*, "ALICE T0 detector", *IEEE Trans. Nucl. Sci.* **52** (2005) . Cited on page(s) 36

[119] **ALICE** Collaboration, E. Abbas *et al.*, "Performance of the ALICE VZERO system", *JINST* **8** (2013) , arXiv:1306.3130 [nucl-ex]. Cited on page(s) 36

[120] **ALICE** Collaboration, "ALICE luminosity determination for pp collisions at $\sqrt{s} = 5$ TeV",. https://cds.cern.ch/record/2202638. Cited on page(s) 39

[121] M. Arslandok, E. Hellbär, M. Ivanov, R. H. Münzer, and J. Wiechula, "Track Reconstruction in a High-Density Environment with ALICE", *Particles* **5** no. 1, (2022) , arXiv:2203.10325 [physics.ins-det]. Cited on page(s) 39

[122] R. Fruhwirth, "Application of Kalman filtering to track and vertex fitting", *Nucl. Instrum. Meth. A* **262** (1987) . Cited on page(s) 39

[123] M. Ivanov, I. Belikov, P. Hristov, and K. Safarik, "Track reconstruction in high density environment", *Nucl. Instrum. Meth. A* **566** (2006) . Cited on page(s) 39

[124] A. Maire, "Track reconstruction principle in ALICE for LHC run I and run II. Principes de reconstruction de traces dans ALICE pour les runs I et II du LHC." General Photo, 2011. Cited on page(s) xi, 40

[125] **ALICE** Collaboration, C. W. Fabjan, L. Jirdén, V. Lindestruth, L. Riccati, D. Rorich, P. Van de Vyvre, O. Villalobos Baillie, and H. de Groot, *ALICE trigger data-acquisition high-level trigger and control system: Technical Design*

Report. Technical design report. ALICE. CERN, Geneva, 2004. https://cds.cern.ch/record/684651. Cited on page(s) 42

[126] D. Evans, S. Fedor, G. Jones, P. Jovanovic, A. Jusko, L. Kralik, R. Lietava, L. Sandor, J. Urban, and O. Villalobos-Baillie, "The alice central trigger system", in *14th IEEE-NPSS Real Time Conference, 2005.*, pp. 5–pp, IEEE. 2005. Cited on page(s) xi, 43

[127] J. Alme *et al.*, "RCU2 - The ALICE TPC readout electronics consolidation for Run2", *JINST* **8** (2013) . Cited on page(s) 43

[128] **ALICE** Collaboration, S. Acharya *et al.*, "Real-time data processing in the ALICE High Level Trigger at the LHC", *Comput. Phys. Commun.* **242** (2019) , arXiv:1812.08036 [physics.ins-det]. Cited on page(s) xi, 43, 44

[129] R. Lietava, "Alice trigger run2 & run3." https://indico.cern.ch/event/835790/contributions/3513813/attachments/1902705/3141441/TriggerRun23.pdf, accessed 2023-11-09. Cited on page(s) 1, 44

[130] **ALICE** Collaboration, S. Acharya *et al.*, "Multiplicity dependence of light-flavor hadron production in pp collisions at $\sqrt{s} = 7$ TeV", *Phys. Rev. C* **99** no. 2, (2019) , arXiv:1807.11321 [nucl-ex]. Cited on page(s) 48

[131] **ALICE** Collaboration, S. Acharya *et al.*, "Multiplicity dependence of (multi-)strange hadron production in proton-proton collisions at $\sqrt{s} = 13$ TeV", *Eur. Phys. J. C* **80** no. 2, (2020) , arXiv:1908.01861 [nucl-ex]. Cited on page(s) 48

[132] I. Vorobyev, *Low-mass dielectron production in proton–proton collisions at $\sqrt{s} = 13$ TeV with ALICE*. PhD thesis, Munich, Tech. U., 2018. Cited on page(s) xi, 52, 57, 66, 69, 83, 99, 110, 113, 141

[133] ALICE, "aliqaevs." https://aliqaevs.web.cern.ch/aliqaevs/data/, accessed 2023-11-10. Cited on page(s) xii, 55

[134] S. van der Meer, "Calibration of the effective beam height in the ISR", tech. rep., CERN, Geneva, 1968. https://cds.cern.ch/record/296752. Cited on page(s) 57

[135] **ALICE** Collaboration, "ALICE 2016-2017-2018 luminosity determination for pp collisions at $\sqrt{s} = 13$ TeV",. Cited on page(s) 57

[136] T. Sjostrand, S. Mrenna, and P. Z. Skands, "PYTHIA 6.4 Physics and Manual", *JHEP* **05** (2006) , arXiv:hep-ph/0603175. Cited on page(s) 58, 75, 92, 97

[137] R. Brun, F. Bruyant, F. Carminati, S. Giani, M. Maire, A. McPherson, G. Patrick, and L. Urban, "GEANT Detector Description and Simulation Tool",. Cited on page(s) 58, 76

[138] ALICE Internal Note, "Definitions of TPC related track properties", 2016. https://github.com/alisw/AliRoot/blob/master/TPC/doc/Definitions/Definitions.pdf, accessed 2023-06-01. Cited on page(s) 62

[139] A. Caliva, *Low-mass dielectron measurement in Pb-Pb collisions at* $\sqrt{s_{\mathrm{NN}}}$ *= 2.76 TeV with ALICE at the LHC*. PhD thesis, Utrecht U., 2017. Cited on page(s) 72

[140] P. Z. Skands, "Tuning Monte Carlo Generators: The Perugia Tunes", *Phys. Rev. D* **82** (2010) , arXiv:1005.3457 [hep-ph]. Cited on page(s) 75, 97

[141] **ALICE** Collaboration, "Momentum transformation matrix for dielectron simulations in Pb-Pb collisions at $\sqrt{s_{\mathrm{NN}}} = 2.76$ TeV",. Cited on page(s) 77

[142] E. Barberio and Z. Was, "PHOTOS: A Universal Monte Carlo for QED radiative corrections. Version 2.0", *Comput. Phys. Commun.* **79** (1994) . Cited on page(s) 83

[143] A. Dashi, "Constraining Open Charm and Bottom Production with Dielectrons in proton–proton collisions at $\sqrt{s} = 13$ TeV with ALICE", 2018. Cited on page(s) 83, 110

[144] **ALICE** Collaboration, S. Acharya *et al.*, "Dielectron production in proton-proton collisions at $\sqrt{s} = 7$ TeV", *JHEP* **09** (2018) , arXiv:1805.04391 [hep-ex]. Cited on page(s) 91, 111

[145] **NA60** Collaboration, R. Arnaldi *et al.*, "Precision study of the $\eta \to \mu^+\mu^-\gamma$ and $\omega \to \mu^+\mu^-\pi^0$ electromagnetic transition form-factors and of the $\rho \to \mu^+\mu^-$ line shape in NA60", *Phys. Lett. B* **757** (2016) , arXiv:1608.07898 [hep-ex]. Cited on page(s) 91

[146] **NA60** Collaboration, R. Arnaldi *et al.*, "Study of the electromagnetic transition form-factors in $\eta \to \mu^+\mu^-\gamma$ and $\omega \to \mu^+\mu^-\pi^0$ decays with NA60", *Phys. Lett. B* **677** (2009) , arXiv:0902.2547 [hep-ph]. Cited on page(s) 91

[147] G. J. Gounaris and J. J. Sakurai, "Finite width corrections to the vector meson dominance prediction for $\rho \to e^+e^-$", *Phys. Rev. Lett.* **21** (1968) . Cited on page(s) 91

[148] J. Knoll, "Transport dynamics of broad resonances", *Prog. Part. Nucl. Phys.* **42** (1999) , arXiv:nucl-th/9811099. Cited on page(s) 91

[149] **PHENIX** Collaboration, A. Adare *et al.*, "Dilepton mass spectra in p+p collisions at $\sqrt{s}$ = 200-GeV and the contribution from open charm", *Phys. Lett. B* **670** (2009) , arXiv:0802.0050 [hep-ex]. Cited on page(s) 91

[150] **ALICE** Collaboration, S. Acharya *et al.*, "Multiplicity dependence of π, K, and p production in pp collisions at $\sqrt{s} = 13$ TeV", *Eur. Phys. J. C* **80** no. 8, (2020) , arXiv:2003.02394 [nucl-ex]. Cited on page(s) 91

[151] A. A. Bylinkin and A. A. Rostovtsev, "Parametrization of the shape of hadron-production spectra in high-energy particle interactions", *Phys. Atom. Nucl.* **75** (2012) . Cited on page(s) 91

[152] A. Bylinkin, N. S. Chernyavskaya, and A. A. Rostovtsev, "Predictions on the transverse momentum spectra for charged particle production at LHC-energies from a two component model", *Eur. Phys. J. C* **75** no. 4, (2015) , arXiv:1501.05235 [hep-ph]. Cited on page(s) 91

[153] **ALICE** Collaboration, S. Acharya *et al.*, "Production of the $\rho(770)^0$ meson in pp and Pb-Pb collisions at $\sqrt{s_{\mathrm{NN}}} = 2.76$ TeV", *Phys. Rev. C* **99** no. 6, (2019) , arXiv:1805.04365 [nucl-ex]. Cited on page(s) 92, 93

[154] **ALICE** Collaboration, S. Acharya *et al.*, "Omega meson production in Proton-Proton Collisions at $\sqrt{s} = 13$ TeV." Manuscript to be submitted. Cited on page(s) 92, 93

[155] **ALICE** Collaboration, S. Acharya *et al.*, "Production of light-flavor hadrons in pp collisions at $\sqrt{s} = 7$ and $\sqrt{s} = 13$ TeV", *Eur. Phys. J. C* **81** no. 3, (2021) , arXiv:2005.11120 [nucl-ex]. Cited on page(s) 92, 95

[156] **ALICE** Collaboration, S. Acharya *et al.*, "Multiplicity dependence of $\mathrm{K}^*(892)^0$ and $\phi(1020)$ production in pp collisions at $\sqrt{s} = 13$ TeV", *Phys. Lett. B* **807** (2020) , arXiv:1910.14397 [nucl-ex]. Cited on page(s) 92, 95

[157] **ALICE** Collaboration, S. Acharya *et al.*, "Inclusive J/ψ production at midrapidity in pp collisions at $\sqrt{s} = 13$ TeV", *Eur. Phys. J. C* **81** no. 12, (2021) , arXiv:2108.01906 [nucl-ex]. Cited on page(s) 92, 96

[158] **ALICE** Collaboration, S. Acharya *et al.*, "Soft-Dielectron Excess in Proton-Proton Collisions at $\sqrt{s} = 13$ TeV", *Phys. Rev. Lett.* **127** no. 4, (2021) , arXiv:2005.14522 [nucl-ex]. Cited on page(s) 93

[159] L. Altenkämper, F. Bock, C. Loizides, and N. Schmidt, "Applicability of transverse mass scaling in hadronic collisions at energies available at the CERN Large Hadron Collider", *Phys. Rev. C* **96** no. 6, (2017) , arXiv:1710.01933 [hep-ph]. Cited on page(s) 93

[160] M. Bourquin and J. M. Gaillard, "A Simple Phenomenological Description of Hadron Production", *Nucl. Phys. B* **114** (1976) . Cited on page(s) 93

[161] R. Hagedorn, "Statistical thermodynamics of strong interactions at high-energies", *Nuovo Cim. Suppl.* **3** (1965) . Cited on page(s) 95

[162] **ALICE** Collaboration, "ALICE luminosity determination for pp collisions at $\sqrt{s} = 13$ TeV",. Cited on page(s) 95

[163] **TOTEM** Collaboration, G. Antchev *et al.*, "First measurement of elastic, inelastic and total cross-section at $\sqrt{s} = 13$ TeV by TOTEM and overview of cross-section data at LHC energies", *Eur. Phys. J. C* **79** no. 2, (2019) , arXiv:1712.06153 [hep-ex]. Cited on page(s) 96

[164] **CTEQ** Collaboration, H. L. Lai, J. Huston, S. Kuhlmann, J. Morfin, F. I. Olness, J. F. Owens, J. Pumplin, and W. K. Tung, "Global QCD analysis of parton structure of the nucleon: CTEQ5 parton distributions", *Eur. Phys. J. C* **12** (2000) , arXiv:hep-ph/9903282. Cited on page(s) 97

[165] **ALICE** Collaboration, S. Acharya *et al.*, "Charm-quark fragmentation fractions and production cross section at midrapidity in pp collisions at the LHC", *Phys. Rev. D* **105** no. 1, (2022) , arXiv:2105.06335 [nucl-ex]. Cited on page(s) 110

[166] **ALICE** Collaboration, S. Acharya *et al.*, "Addendum Dielectron production in proton-proton and proton-lead collisions at $\sqrt{s_{\rm NN}} = 5.02$ TeV." Manuscript in preparation. Cited on page(s) 110

[167] **ALICE** Collaboration, S. Acharya *et al.*, "Dielectron production in proton-proton and proton-lead collisions at $\sqrt{s_{\rm NN}} = 5.02$ TeV", *Phys. Rev. C* **102** no. 5, (2020) , arXiv:2005.11995 [nucl-ex]. Cited on page(s) 111

[168] M. Cacciari, M. Greco, and P. Nason, "The p_T spectrum in heavy-flavour hadroproduction.", *JHEP* **05** (1998) , arXiv:hep-ph/9803400. Cited on page(s) 111

[169] **ALICE** Collaboration, "Supplemental figures: Direct photon production in Pb-Pb collisions at $\sqrt{s_{\rm NN}} = 2.76$ TeV",. https://cds.cern.ch/record/2102398. Cited on page(s) 125

[170] G. D. Lafferty and T. R. Wyatt, "Where to stick your data points: The treatment of measurements within wide bins", *Nucl. Instrum. Meth. A* **355** (1995) . Cited on page(s) 131

[171] **ALICE** Collaboration, J. Adam *et al.*, "Pseudorapidity and transverse-momentum distributions of charged particles in proton–proton

collisions at $\sqrt{s} = 13$ TeV", *Phys. Lett. B* **753** (2016) , arXiv:1509.08734 [nucl-ex]. Cited on page(s) 133

[172] P. Aurenche, M. Fontannaz, J. P. Guillet, B. A. Kniehl, E. Pilon, and M. Werlen, "A Critical phenomenological study of inclusive photon production in hadronic collisions", *Eur. Phys. J. C* **9** (1999) , arXiv:hep-ph/9811382. Cited on page(s) xviii, 134, 139

[173] K. Kovarik *et al.*, "nCTEQ15 - Global analysis of nuclear parton distributions with uncertainties in the CTEQ framework", *Phys. Rev. D* **93** no. 8, (2016) , arXiv:1509.00792 [hep-ph]. Cited on page(s) xviii, 134, 139

[174] **STAR** Collaboration, L. Adamczyk *et al.*, "Direct virtual photon production in Au+Au collisions at $\sqrt{s_{\rm NN}} = 200$ GeV", *Phys. Lett. B* **770** (2017) , arXiv:1607.01447 [nucl-ex]. Cited on page(s) xviii, 139

[175] **PHENIX** Collaboration, A. Adare *et al.*, "Beam Energy and Centrality Dependence of Direct-Photon Emission from Ultrarelativistic Heavy-Ion Collisions", *Phys. Rev. Lett.* **123** no. 2, (2019) , arXiv:1805.04084 [hep-ex]. Cited on page(s) xviii, 139

[176] **ALICE** Collaboration, A. Marin, "Measurements of direct-photon production in Pb-Pb collisions at $\sqrt{\rm s_{NN}} = 5.02$ TeV and $\sqrt{\rm s_{NN}} = 2.76$ TeV with the ALICE experiment", in *11th International Conference on Hard and Electromagnetic Probes of High-Energy Nuclear Collisions: Hard Probes 2023*. 8, 2023. arXiv:2308.02401 [nucl-ex]. Cited on page(s) xviii, 139

Acknowledgments

I would like to acknowledge the persistent guidance of many people in carrying out the research presented in this thesis. First of all, I would like to thank Prof. Kyoichiro Ozawa for his guidance throughout all my research activities in graduate school. I have been encouraged and inspired by his words many times. His clear thinking guided me to solutions when I was stuck on how to proceed with my research.

I am grateful to Prof. Taku Gunji, who gave me the opportunity to participate in the ALICE experiment. He always looked into the distance and consistently provided precise observations and advice on how this research could be improved. He was always supportive of participating in activities in ALICE, the TPC upgrade project, and others. He taught me the pleasure of getting close to discoveries.

I would like to thank Prof. Hideki Hamagaki for his support of my work on the ALICE experiment. His little advice at meetings was useful and helped me a lot.

This study was sustained by the inexhaustible curiosity and passion of the individuals participating in the ALICE experiment. I would like to give special thanks to Ivan Vorobyev for his invaluable contributions. He generously shared the experience and knowledge gained from previous experiments, actively contributing to the smooth progress of this research. Additionally, he consistently offered words of encouragement.

I would also like to express my gratitude to the members of the dielectron physics analysis group. Raphaelle Bailhache, provided detailed insights into the analysis, pinpointing issues and offering valuable feedback. Sebastian Scheid proposed various ideas based on the knowledge accumulated by the LMEE-PAG thus far. Jerome Jung also aided in improving the quality of the research by applying his analysis experience to this study. Daiki Sekihata was very helpful in the early days of dielectron analysis, providing invaluable assistance from basic knowledge to the latest status of the dielectron group.

I would also like to express my sincere thanks to the neutral meson group. Mike Sas, as an expert in photon measurements, provided valuable advice based on his abundant knowledge and experiences. I am very grateful for his support and guidance. Joshua König, Ana Marin, and Adrian Mechler, who were involved in the measurement of π^0 and η mesons in pp collisions at $\sqrt{s} = 13$ TeV, which is extremely important for this analysis. The measurement of ω meson was also an important input for making the hadronic cocktail. In this regard, I would also like to express my gratitude to Jens Lühder, and Florian Jonas. In addition, I would like to mention the precise determination of the ALICE material budget, conducted by the Photon Conversion Group. I

am pleased to have contributed, albeit in a modest way, to checking the detector position via gamma tomography. These studies could not have been completed without the collaboration of Mario Sitta and Andrea Dainese, experts in the ITS detector, and Marek Kowalski who is an expert in the TPC. Above all, I must express my gratitude to Friederike Bock, who introduced me to photon physics in ALICE. Through the measurement of direct photons, I was able to learn the importance of precision that she wanted to convey.

The TPC upgrade project in which I was involved as a service task must be mentioned: Alexander Deisting, Renato Negrao, Anastasia Berdonikova, Lilit Karayan, Prof. Raghava Varma, Sohaib Hassan, and Maria Gul, it was a very impressive moment for me to see people from different nationalities and cultures working together. It is also a great pleasure for me to see TPC being operated successfully on Run 3. I would like to thank Chilo Garabatos and Prof. Harald Appelshäeuser for giving me this opportunity.

I would like to extend my sincere thanks to Prof. Nobuaki Imai, Prof. Kentaro Yako, Prof. Toshinori Mori, Prof. Junichi Tanaka, and Prof. Osamu Morimatsu, for their careful reading and for providing valuable feedback to refine the manuscript.

I would also like to express my gratitude to the members of Gunji Laboratory, Yuko Sekiguchi, Ryotaro Kohara, Hitoshi Baba, and Shujiro Shindo. The casual conversations we shared daily proved invaluable in maintaining the mental well-being of what can be an isolating research life.

I would like to thank Hideto En'yo for his financial support through RIKEN Junior Research Associate (JRA) program. His wonderful smile always cheered me up.

I would also like to thank Ikuko Yamamoto, Yukino Kishi, Aki Kotaka, and Takeo Hoso, in the CNS Secretariat for their support of my research activities at CNS. Thanks to them, I was able to carry out my research smoothly.

Last but not least, I would like to express my gratitude to my family, who patiently waited and supported me throughout the long journey of my research career. They always believed me and offered warm encouragement.